Cluster-light interaction and imaging of cluster growth processes

vorgelegt von
Diplom-Physiker
Marcus Michael Adolph
aus Berlin

von der Fakultät II - Mathematik und Naturwissenschaften
der Technischen Universität Berlin
zur Erlangung des akademischen Grades

Doktor der Naturwissenschaften
- Dr. rer. nat. -

genehmigte Dissertation

Promotionsausschuss:

Vorsitzender:	Prof. Dr. Mario Dähne
Berichter/Gutachter:	Prof. Dr. Thomas Möller
Berichter/Gutachter:	Priv. Doz. Dr. Tim Laarmann

Tag der wissenschaftlichen Aussprache: 19. Juni 2014

Berlin 2014

D 83

Die selbständige und eigenhändige Anfertigung versichere ich an Eides statt.

Datum / Unterschrift

Abstract

This work presents findings on the growth process of rare gas clusters and their interaction with highly intense x-ray radiation. Using the "Freie Elektronen Laser in Hamburg" (FLASH), a light source producing coherent electromagnetic radiation with a short wavelength in the vacuum ultraviolet (VUV) regime, studies of the growth dynamics of single particles on the nanometer scale were performed on a single shot basis. The Linac Coherent Light Source (LCLS) opened the hard x-ray regime as a new range of the electromagnetic spectrum available for the study of ionization dynamics of krypton clusters. In order to realize statistic preparation and analysis of the data a variety of especially designed computer programs were developed. Additionally, the data acquisition software FoxIT has been developed based on a multi-threading concept introducing a HDF5 based file format of high storing performance. FoxIt will help simplify data acquisition for future imaging experiments at FLASH.

For experiments performed at FLASH the experimental setup was improved by including in-vacuum motorization of the back focusing mirror in combination with a build-in time-of-flight ion detector for the online characterization of the focal spot. With these modifications the peak power density of the FEL could be used more effectively. As a result, the contrast in the scattering patterns could be increased, enhancing the resolution limit of the scattering images. The image quality was further improved by an optimization of the detectors' positions. The upgraded setup enabled the determination of the cluster size distribution in the cluster beam with single cluster scattering patterns, allowing comparison to well established scaling laws. In addition, the setup enabled imaging of the process of two clusters coalescing and forming a twin cluster during cluster growth. Based on analysis of the cluster temperature, a theoretical model was developed, describing the formation of twin clusters. This model was tested using a numerical computer simulation of the growth process, which shows good agreement with the experimental data.

The worlds first free-electron laser (FEL) for the hard x-ray regime, the LCLS, allows in-depth studies of smaller structures due to it's short wavelength. The research presented here discusses the ionization dynamics of rare gas clusters with x-rays. The interaction between the highly intense x-ray radiation and the clusters has been investigated at the krypton L-absorption edge at 1.7 keV. Using single cluster scattering techniques it was found that the ionization efficiency is virtually independent of the excitation energy with respect to the L-edge. This can be explained with the almost complete saturation of the absorption of the cluster. A combination of single cluster scattering with time-of-flight ion spectroscopy is presented enabling single cluster ion spectroscopy. These coincidence measurements reveal extremely high charged krypton ions while low charged residuals from recombination processes are almost absent. The experimental findings give evidence to an efficient heating mechanism of the plasma suppressing recombination. These results can be of great help for future plasma simulations discussing the development of the laser-induced nanoplasma on a theoretical basis.

Kurzfassung

In dieser Arbeit wird der Wachstumsprozess von Edelgasclustern und deren Wechselwirkung mit hochintensiver Röntgenstrahlung untersucht. Experimente am „Freie Elektronen Laser in Hamburg“ (FLASH) ermöglichten durch die kohärente Strahlung und die kurze Wellenlänge im Vakuumultravioletten die für die Untersuchung der Wachstumsdynamik von Clustern wichtigen Abbildungen einzelner Cluster. Die Erschließung des Regimes der harten Röntgenstrahlung durch die „Linac Coherent Light Source“ (LCLS) erlaubte die Untersuchung der Ionisationsdynamik von Kryptonclustern in diesem Regime. Zur statistischen Datenaufarbeitung und Auswertung wurden für beide Experimente speziell angepasste Computerprogramme entwickelt. Die Messsoftware „FoxIT“ konnte darauf basierend entwickelt werden. „FoxIT“ verwendet Multithreading sowie ein auf HDF5 basierendes Dateiformat zur effektiven Bündelung der Messdaten. Die Software kann somit die Steuerung und Datenerfassung zukünftiger Streuexperimente vereinfachen.

In den am FLASH durchgeführten Experimenten wurde die Methode zur Einzelclusterstreuung weiterentwickelt. Die Integration von Invakuum-Motoren zur Spiegeljustage sowie die Installation eines Flugzeitmassenspektrometers zur Charakterisierung der Fokusintensität ermöglichten erhöhte Präzision bei der Justierung und damit Messungen bei höherer Photonendichte in der Interaktionszone. Somit konnten weitere Optimierungen der Positionen der Streulichtdetektoren durchgeführt werden, was in verbessertem Kontrast der Einzelcluster-Streubilder und somit einer verbesserten Auflösung der Streuexperimente resultierte. Auf diese Weise ließ sich aus den Streudaten eine Größenverteilung der Cluster im Clusterstrahl bestimmen, die sich mit den Skalierungsgesetzen der Clusterphysik vergleichen ließ. Mithilfe der erweiterten Messapparatur konnte das für die Clusterbildung wichtige Verschmelzen von einzelnen Clustern zu einem Zwillingscluster abgebildet werden. Basierend auf der Temperaturänderung der Cluster wurde ein Modell entwickelt, welches diese Bildung von Zwillingsclustern erklärt. Das Modell diente als Grundlage für die Erstellung einer Computersimulation des Wachstumsprozesses, die gute Übereinstimmung mit den experimentellen Ergebnissen zeigt.

Die kurze Wellenlänge des FEL-Lichts an der LCLS, dem ersten FEL für harte Röntgenstrahlung, erlaubt die Untersuchung immer kleinerer Strukturen und ist daher ein weiterer Schritt auf dem Weg zur Entwicklung abbildender Verfahren bis hin zu atomarer Auflösung. In dieser Arbeit ist die Ionisationsdynamik von Edelgasclustern bei diesen Photonenenergien untersucht worden. Die Analyse der Wechselwirkung an der Krypton L-Kante bei 1.7 keV mit der Einzelclusterstreumethode zeigt, dass die Ionisation nur schwach von der Photonenenergie abhängt. Dies kann durch eine nahezu vollständige Sättigung der Absorption des Clusters erklärt werden. Eine Kombination der Einzelcusterstreuung mit Flugzeit-Spektroskopie ermöglichte Ionenspektroskopie an einzelnen Clustern. Bei diesen Koinzidenzmessungen konnten extrem hoch geladene Fragmente von Kryptonclustern sowie das Fehlen von niedrig geladenen Rekombinationsprodukten nachgewiesen werden. Dies deutet auf einen effizienten Erhitzungsprozess des Nanoplasmas hin, welcher die Rekombinationen innerhalb des Plasmas stark unterdrückt. Diese im Experiment gewonnen Erkenntnisse können somit die Basis für weitere theoretische Betrachtungen auf der Basis von Plasmasimulationen bilden.

Contents

1. Introduction

Since the first basic experiments in cluster physics have been realized in the 1950s [1], this discipline has become a dynamic and fast-growing field over the last 60 years. Cluster physics focus on the link between atomic physics on the one side and solid state physics on the other side[2, 3]. In this context the term cluster denotes an object consisting of $N = 3$ up to $N = 10^7$ atoms or molecules. While small clusters show molecular-like properties the larger ones are more solid-like. By varying the size of clusters from very small to microscopic solids, various transitions of properties have been observed in many experiments, e.g. [4, 5, 6, 7].

In general, the condensation processes leading to the formation of larger ensembles are the origin of the complex shapes of all kinds of matter. The formation of colloids, the accumulation of clouds, the crystallization of solids, and even larger aggregates up to planets are affected by the details of aggregation of atoms and molecules. Thus, by analyzing the growth process of small particles, i.e., clusters and nano crystals, one can gain insight into various aspects of particle formation, which is playing an important role in physics and chemistry, as well as biology.

The direct observation of particle formation is very difficult due to experimental limitations resulting from the small size of the objects. In this thesis a technique is presented, which allows direct imaging of individual particles (in this case rare gas clusters) and allows drawing conclusions on their growth process. Some insights into the growth process can already be obtained from the size distribution of particles, such as the transition from successive monomer attachment to coalescence [8]. Over the years, a variety of different techniques has been developed in order to determine the size distribution of atomic clusters in gas jets.

With the development of short-wavelength free-electron lasers (FEL) a new tool for the study of small particles became available [9]. The short wavelength combined with long coherence and ultra-short pulses allows single-shot imaging experiments of individual nanometer-sized objects, where the ultimate goal is imaging with atomic resolution [10, 11]. Due to the low scattering cross-section in the x-ray regime and the need for at least one scattered photon per atom, high photon densities are mandatory to obtain usable scattering patterns of single nano objects. In general, the absorption cross-section is larger then the scattering cross-section, which results in highly ionized atoms and coulomb-exploding molecules on ultra-short time scales. A detailed study and understanding of the interaction effects of high-intense FEL radiation and the samples is a very relevant aspect of current research and is intensively studied within the scope of cluster experiments, e.g. [12, 13, 14]. The identification of different mechanisms of absorption and ionization are the driving force behind this field of science. In addition, the timescales of the interaction as well as relaxation processes are of special interest.

In this thesis, a tool for cluster analysis based on single particle imaging was developed and improved [15, 16, 17]. The intense light pulses from free-electron lasers are used to produce a scattering pattern from one single, nanometer-sized rare gas cluster. The scattering images give insight into the ultrafast changes of the electronic structure of the cluster during the interaction [18] as well as information of the geometric shape of the object. Both aspects are the focus of

this work. This scattering technique allows direct observation and imaging of one single free, i.e. unsupported, rare gas cluster. Based on the acquired data the growth process of the clusters is further discussed. It becomes apparent that almost spherical and rather complex shapes of clusters coexist in the expanded cluster beam. As part of the cluster growth process complex shapes occur which originate from binary cluster-cluster collisions. These are analyzed in detail. A simulation was developed in order to compare theoretical conclusions with the experiments.

Furthermore, the cluster imaging technique is used to push the limits of conventional time-of-flight ion-spectroscopy (cf. [15, 16]). Using ion-spectroscopy and imaging in parallel, charge state distributions from one single cluster can be obtained under very well defined conditions, namely cluster size and intensity of the FEL pulse. These experiments were carried out at the Linac Coherent Light Source (LCLS), the worlds first FEL in the x-ray regime. They revealed highly charged cluster fragments pointing to a heating mechanism [14].

Enhancing the quality of the experimental data was critical for the success of these experiments. In particular, solutions for the reduction of straylight and improvements of the alignment of the scattering setup had to be identified and applied. Further characterization of the focal intensity was possible by including a time-of-flight ion detector into the experiment. This characterization is a main factor for the success of the experiments because it increases the reliability of the experiment and the accuracy of the alignment, which enables analysis of smaller clusters.

Scattering experiments generate a enormous amount of data with thousands of scattering images per experimental parameter. In order to obtain statistically relevant conclusions this data has to be analyzed. Therefore, special emphasis was put on the development of software for data analysis. A new data acquisition software was designed, meeting the challenge of faster data analysis in future scattering experiments.

This thesis is organized in three main parts covering the theoretical background, details of the realization of the experiments, and a discussion of the results. The theoretical discussion in chapter 2 is giving an overview on the physics of cluster light interaction and scattering theory with the focus on FEL radiation. In chapter 3 the experimental aspects of this work are presented. It features the improvement of the scattering experiment together with the software development. Finally, the experimental findings are presented and discussed in chapter 4. A summery of this work can be found in chapter 5.

2. Theoretical background

This chapter gives a brief introduction into the basics of cluster physics. It focuses on two aspects, namely cluster growth and formation processes as well as the interaction of clusters with light. Both aspects are the basis of the work explored in this thesis.

Experimental and theoretical findings in the field of cluster growth are presented in section 2.1 based on the historical progress in cluster physics. The formation of clusters from rare gases as well as the characteristic properties of cluster jets are presented. The different shapes of clusters observed in single shot measurements of single clusters can be regarded as products of the cluster growth process. The following section 2.2 focuses on cluster light interaction and presents the background of the cluster scattering experiments carried out in the vacuum ultraviolet and x-ray light regime. The section outlines the interaction of clusters and intense laser fields and closes with a theoretical description of the scattering process, which is the basis for the analysis performed in the context of this thesis.

2.1. Introduction to cluster theory

Cluster formation was reported for the first time by Becker *et al.* in 1956 during experiments with dense gas jets [20]. The corresponding experiment is depicted in figure 2.1a. A chopped gas beam passed a light barrier, which allowed measuring the flight time of the gas atoms to an ionization manometer. It was expected that the gas atoms thermalize and travel with a certain speed through the experiment. However, due to the formation of clusters, a splitting of single flight-time distribution was observed, in which the second peak became predominant (c.f. figure 2.1b). This velocity slip was interpreted as a difference between the uncondensed gas and the slower clusters because the appearance of this peak depends on the pressure and the temperature of the expanded gas in contrast to the other peak, which remained constant. The rapid expansion of the gas beam caused a drop of the temperature of the molecules resulting in cluster formation, which increased the moment of inertia of the clusters compared to there interaction cross-section. This results in a velocity slip, illustrated by figure 2.1b, showing three photographs from an oscilloscope used to measure the flight-time of the gas jet for three different gas-nozzle temperatures as denoted in the figure.

One of the main goals in cluster physics is to gain insight into the relationship between material properties and their relation to cluster size, showing the transition from atomic- or molecular- to solid state behavior [7]. It implies that the size of the clusters has to be known as accurate as possible during the experiments. Metal clusters can be ionized and size selected based on their mass-charge ratio [21]. A special class of carbon-clusters, so called diamondoids, are selectable by size and structure using chromatographic methods [22]. However, similar methods did not apply for weakly-bond aggregates, especially rare gas clusters which are typically produced with a log-normal size distribution [8]. Therefore, different analytical methods are helpful in order to determine the size of rare gas clusters. Typically, size determination of clusters can be obtained

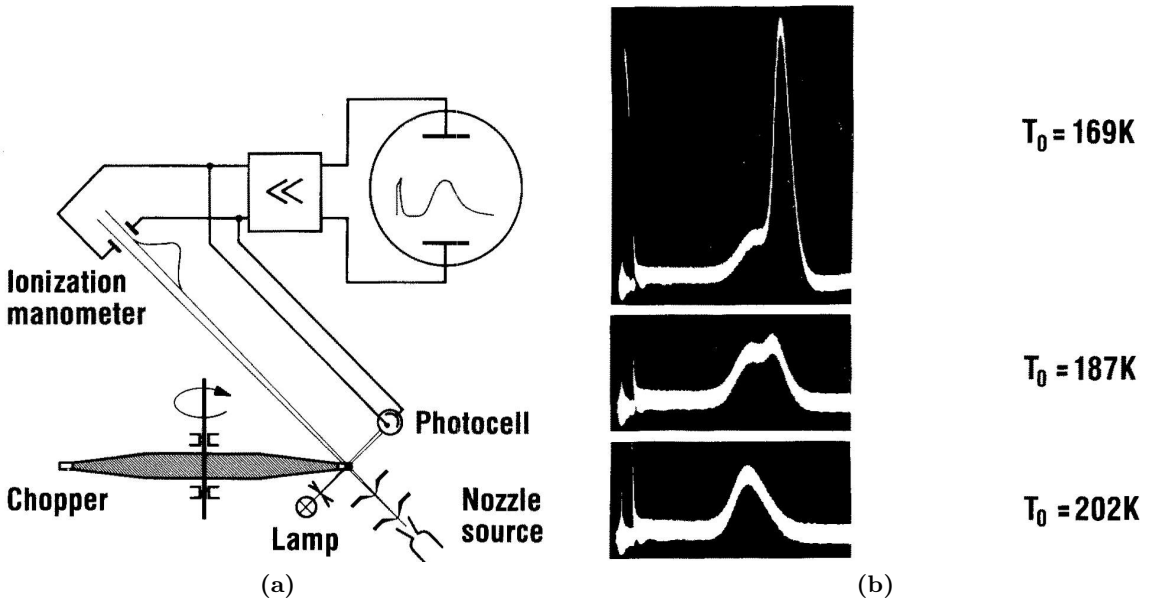

Figure 2.1.: First detection of clusters using time-of-flight measurements. 2.1a Experimental setup based on the time-of-flight of clusters. 2.1b Measured distribution recorded for different nozzle temperatures. The appearance of the second peak is strongly pressure and temperature dependence and indicates cluster formation. [19, 20]

using scattering with helium atoms for small cluster sizes or using mass spectroscopy for larger clusters [7]. Especially for rare gas clusters the scattering imaging method was developed which is used throughout this work [23]. In the context of this thesis, rare gas clusters were studied as model systems. The usage of rare gas clusters has several advantages. For one they are inert, have a uniform internal structure, and they are easy to prepare in a large size range.

Rare gas clusters can be generated by supersonic expansion of atomic gas through a nozzle into vacuum [7]. During the expansion, the temperature of the gas drops rapidly and the atoms can condensate to form clusters. This is a statistic process, which results in a wide range of clusters sizes. The mean cluster size $\langle N \rangle$ achieved during the production of rare gas clusters depends on the gas used (e.g. He or Xe), the geometry of the nozzle for the expansion, the initial temperature, and the pressure of the gas. The so-called "scaling laws" developed by Hagena [24] correlate $\langle N \rangle$ with these parameters and are widely used to calculate the mean cluster size for given experimental settings. The scaling laws are discussed in more detail in section 2.1.2. By using imaging techniques it is possible to detect single rare gas clusters and determine the size of every individual cluster for the first time. This method allows a detailed study of the growth behavior of clusters as performed in the context of this work.

The next section addresses the background of cluster formation and presents an overview of experiments determining the mean cluster size of rare gas cluster beams. In section 2.1.2 a short introduction into the thermodynamic fundamentals of cluster creation is presented leading to a sketched derivation of the mean cluster size.

2.1.1. Experimental characterization of cluster beams

Since the first observation of clusters, a variety of different experiments as been performed to study their generation. In this section, a selection of experimental approaches will be presented, giving an overview over the different experimental techniques available. The experimental techniques applied in cluster physics are for the most part adopted from the fields of atomic or solid state physics.

One of the first observations of the structure and temperature of rare gas clusters was made by Farges *et al.* using Debye-Scherrer diffraction. In this experiment, 50 keV electrons were scattered by a cluster beam and detected by a photographic plate. This made it possible to determine the mean cluster size based on the width of the diffraction lines, reconstructing the lattice constant from the Debye-Scherrer rings of clusters, and the mean square atomic displacement from the damping of the diffraction lines with the increase diffraction angle [25]. With the lattice parameter the temperature of the clusters could be determined.

A different approach was presented by Cuvellier *et al.* [26]. Here, the cluster size distribution of argon clusters was measured by sending the cluster beam through a buffer gas before the clusters were detected. By measuring the flight time of the clusters though the gas the average cluster beam velocity could be determined as a function of the buffer gas pressure, which revealed the mean cluster size. However, the size determination can be affected by fragmentation of the clusters.

Another method for the determination of cluster size distributions is Rayleigh scattering [27, 28]. Bell *et al.* overlapped an argon cluster beam perpendicular with an optical laser beam and recorded the Rayleigh scattering signal $\mathcal{R}$ [27]. This signal depends on the number of scattering particles N and the cross-section for scattering σ: $\mathcal{R} \propto N\sigma$. N is proportional to the flux of the clusters and was determined by the authors by measuring the pressure in a Pitot tube after surface dissociation of the clusters. The cross-section for Rayleigh scattering is given by [29]

$$\sigma = \frac{128\pi^5 r^6}{3\lambda^4}\left(\frac{n^2-1}{n^2+2}\right),$$

with the radius of the clusters $r < \lambda$, the wavelength λ, and the refractive index n. With that experiment an easy to perform, non-destructive method for the determination of the mean cluster size was established. This method is not limited to argon clusters and can be used for a wide range of cluster sizes depending on the wavelength of the laser.

In addition to Rayleigh scattering, molecular scattering can be used as a non-destructive method for studying the size distribution of clusters. For example, helium atoms can be used in a cross beam setup to study the size distribution of argon clusters [30]. A cluster beam is perpendicularly overlapped with a secondary atomic beam (usually helium atoms) under single collision conditions. The atoms are scattered at the clusters described by the Lennard-Jones potential, characterized by long-range attractive force and a short-range repulsive one with a minimum in between. The angular distribution of the scattered atoms shows an interference pattern similar to the scattering of light at small objects. Figure 2.2a shows the measured scattering cross-section of helium atoms scattered at argon clusters performed by Buck *et al.* [30]. The solid lines are quantum mechanic calculations of the cross-section used for the determination of the mean cluster size, which is also denoted in the figure. The oscillations in the diffraction pattern can be approximated using $\Delta\Theta = \pi/(kb_0)$, where $k = mg/\hbar$ is the wavenumber and b_0 the corresponding impact parameter [31]. With $kb_0 \approx kR_0$, where R_0 is the reach of the repulsive

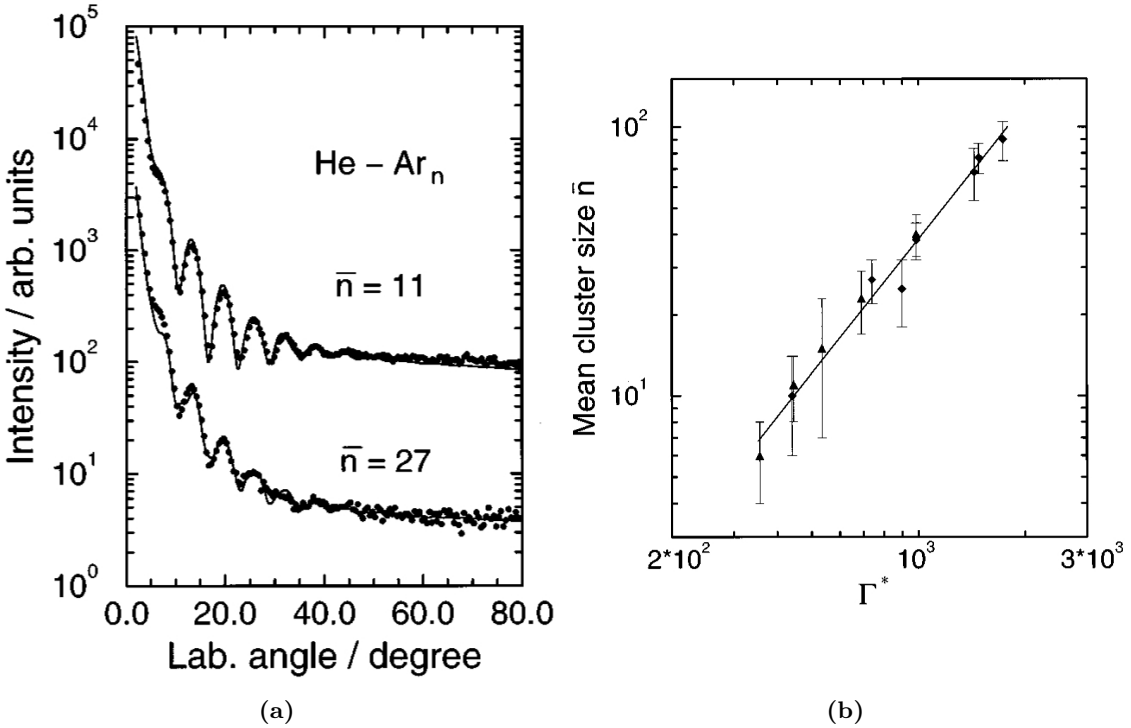

Figure 2.2.: Cluster size determination using atomic scattering. (a) Measured scattering cross-section compared to calculations to obtain the mean cluster size [30]. (b) Mean cluster size (in this work: $\bar{n} \mathrel{\hat{=}} \langle N \rangle$) measured with helium scattering for different scaling parameters Γ^* (see equation 2.12 on page 14). The measurements were performed for two different nozzle types (▲ sonic, ◆ conical) [30].

wall of the scattering potential, the cluster size could be determined. However, this equation only gives an approximation for the oscillation period of the structure, while the amplitudes of the modulation are not described properly. The experimental approach of scattering helium atoms is also used to produce size selected cluster beams [32].

The atomic scattering process can also be described by modeling the cluster potential following Gspann and Vollmer [33]. The measured results are compared to a calculation for a single cluster size until the number and periodicity of the oscillations match. The authors improved this match by taking the cluster size distribution together with monomer scattering cross-section into account: $\sigma_{\text{meas}} = \sum_N g_N \sigma_N + \sigma_1$ where g_N is a fitting parameter. The mean cluster size $\langle N \rangle$ for the cluster beam is then obtained by

$$\langle N \rangle = \frac{\sum_N g_N \sigma_N}{\sum_N g_N}. \tag{2.1}$$

$\langle N \rangle$ is shown in graph 2.2b where it is depicted for different values of the scaling parameter Γ^*, which is a function of stagnation pressure and temperature of the expanding gas dependent on the nozzle geometry [24]. Small values of Γ^* correspond to small cluster sizes and vice versa. This scaling parameter is frequently used in cluster physics and was first introduced by Hagena. It will be introduced and discussed in detail at the end of the following section.

2.1.2. Formation of rare gas clusters

While in the last section experimental methods used to characterize cluster beams were presented, this section will focus on the theoretical background of cluster formation. Because rare gas clusters are easily prepared as samples, they were used in the experiments this thesis is based on. Therefore, the focus of this section is exclusively on rare gas cluster formation.

Rare gas clusters are usually generated from a supersonic expansion. Gas with the stagnation pressure p_0 and a temperature T_0 is expanded through a nozzle into a low pressure background environment. During this expansion the gas cools down and condenses into clusters.

In order to understand the process of cluster formation, some basic properties of atomic beams will be presented first. However, this approach neglects any coagulation or accumulation processes leading to cluster formation, which will then be discussed in detail in the subsequent paragraphs. The presented discussion follows the work of Scoles [31].

Atomic beams

The initial state of a gas in order to produce an atomic gas beam, is that it is in a reservoir with a constant stagnation pressure p_0 and a constant temperature T_0 [31]. The velocities of the gas atoms follow a Boltzmann distribution with a mean velocity $\bar{v} = (2k_\mathrm{B}T/m)^{1/2}$ with the Boltzmann constant k_B and the atomic mass m. The gas in equilibrium state is then expanded through a nozzle into a volume with a low background pressure $p_\mathrm{B} \ll p_0$ (vacuum). During this expansion, the unidirectional thermal motion of the gas atoms is converted into a directed movement along the expansion axis. While the velocity in this direction is high for each gas atom, the relative velocity distribution of the entire gas beam becomes very narrow which corresponds to a drop of the gas temperature. The expansion of a gas beam evolves in a characteristic manner shown in figure 2.3. Here, a schematic drawing and a Schlieren photography illustrate the expansion process. The subsequent discussion of the expansion follows the expansion path in figure 2.3a, beginning inside the nozzle on the left-hand side of the figure.

Towards the nozzle's exit the gas is accelerated due to the pressure difference between gas reservoir and vacuum. At the nozzle exit the speed of sound c is reached. Due to the decreasing background pressure, c is dropping. At a certain point, usually the nozzle exit, the speed of the gas molecules equates the local speed of sound ($v \sim c$). Here, the Mach number $M = v/c$ is equal to one and the pressure ratio p_0/p_B exceeds a critical value $G \equiv ([\gamma + 1]/2)^{\gamma/(\gamma-1)}$ with $\gamma = C_\mathrm{p}/C_\mathrm{v}$ being the ratio of the isobaric heat capacity to the isochoric heat capacity [31]. For mono-atomic gases, which will be considered here, $\gamma = 5/3$, results in $G \approx 2.1$. If the ratio between the pressure in the gas reservoir and the background pressure is less then G, the gas will expand subsonically with an exit pressure close to P_B. For p_0/p_B exceeding G the exit pressure becomes independent of p_B and the flow is considered under-expanded. This results in a subsequent expansion shown in figure 2.3a.

The rapid expansion of the gas behind the nozzle leads to a conversion of the inner energy of the gas into kinetic energy. At the same time, adiabatic cooling reduces the inner temperature of the gas. Following a steam line, the temperature drops from T_0 at the nozzle exit to a value T while the enthalpy per unit mass (H) is partially converted into kinetic energy [31]:

$$H_0 = \frac{v^2}{2} + H. \tag{2.2}$$

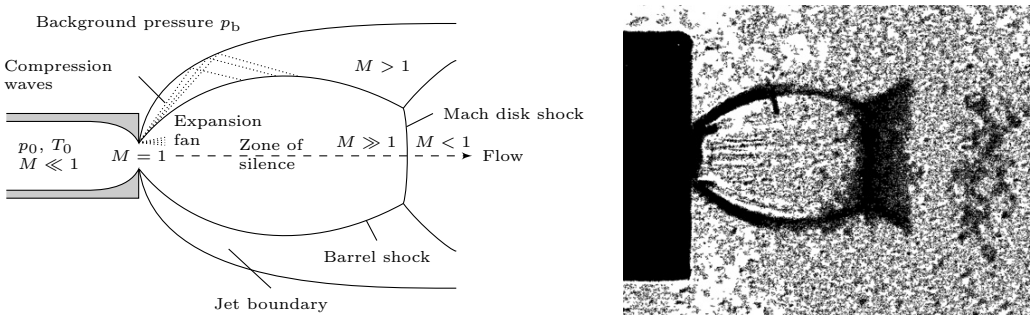

Figure 2.3.: Free jet expansion from a continuous source. Figure (a) schematically shows a supersonic expansion into vacuum with the formation of shockwave boundaries and the Mach disk, adapted from [31]. See text for details. For comparison, figure (b) shows a Schlieren photography of a supersonic expansion [34].

As a result, the now directed velocity of the gas molecules further exceeds c and the Mach number becomes $M \gg 1$. Information about surrounding conditions are transported with the speed of sound into the beam. Because the propagation of the atoms in the beam exceeds c, atoms in the center of the beam are not affected by the surrounding background. A so-called "zone of silence (ZOS)" is formed in the center of the beam where the beam is propagating undisturbed. The ZOS is surrounded by boundary layers of shock waves, containing high density, pressure, and velocity gradients as it is illustrated in figure 2.3a, which shows a continuous expansion with $p_0/p_B \sim 10^6$ schematically. The boundary layer in direction of the expansion is called Mach disk. It denotes the end of the undisturbed expansion in the ZOS, located at a distance $(x_M/d) = 0.67(p_0/p_B)^{1/2}$ relative to the nozzle diameter [31].

Figure 2.3b shows a schlieren photography of an expanding nitrogen gas jet [34]. The pressure ratio for this image was $p_0/p_B = 56$ expanded through a cylindrical nozzle with a diameter of 1.43 mm. The boundaries and the Mach disc surrounding ZOS are clearly visible. The constriction of the beam at the Mach disk shows how the shock waves change the direction of the expansion.

In the respective literature it has been pointed out that the mach number M can be used for calculating the properties of the expanding gas jet [31]. The properties being propagation velocity, temperature, local pressure, and local density. Using M all of them can be described as a function of the distance from the nozzle. But the derivation of M is verbose, however straight forward and outlined in reference [31]. Following that reference, the properties of a free jet expansion can be described by the fluid mechanics equations:

$$\text{conservation of mass:} \quad \nabla \cdot (\rho \mathbf{v}) = 0 \tag{2.3a}$$

$$\text{conservation of momentum:} \quad \rho \mathbf{v} \cdot \nabla \mathbf{v} = -\nabla p \tag{2.3b}$$

$$\text{conservation of energy:} \quad \mathbf{v} \cdot \nabla H_0 = 0 \Leftrightarrow H_0 = \text{const. along steamline} \tag{2.3c}$$

$$\text{equation of state:} \quad p = \rho(R/W)T \tag{2.3d}$$

$$\text{thermal equation of state:} \quad \mathrm{d}h = \hat{C}_\mathrm{p}\,\mathrm{d}T \tag{2.3e}$$

with $\mathbf{v}$ the velocity vector, ρ density, p pressure, H_0 stagnation enthalpy, as well as W the molar

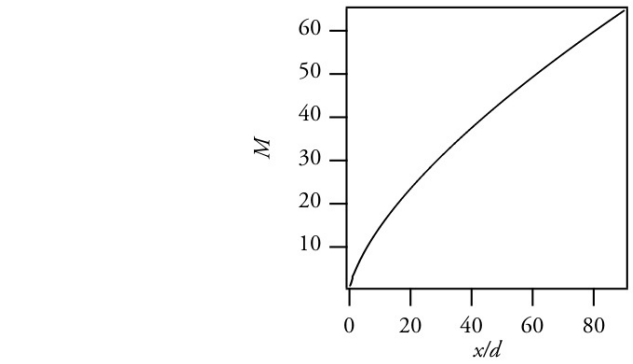

(a) Mach number

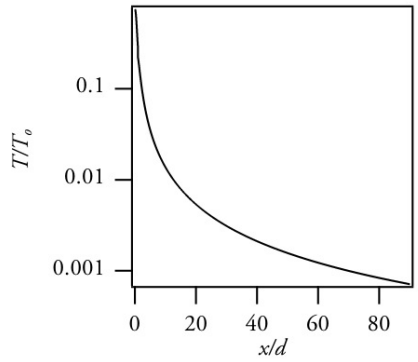

(b) Temperature

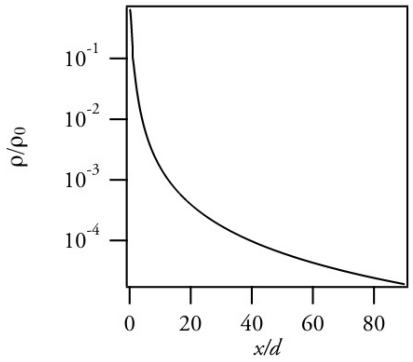

(c) Density

Figure 2.4.: Mach number, temperature, and density of a supersonic expansion of a molecular beam. The calculations for the Mach number M are based on the approximation formula given in [31] (figure (a)). With the obtained M (b) and (c) could be calculated. The results show the remarkable temperature drop during the expansion. Calculations are only valid for stream lines close to the center of the beam.

weight and $R = 8.3145\,\mathrm{J}\cdot\mathrm{mol}^{-1}\mathrm{K}^{-1}$ the molar gas constant. $\hat{C}_\mathrm{p} = (\gamma/\gamma - 1)(R/W)$ represents the molar heat capacity. The equations 2.3a to 2.3e describe the two-dimensional, isentropic, and compressible flow of an ideal gas with constant molecular weight and specific heat ratio. In order to solve these equations, a variety of different numerical methods has been used, as outlined in [31]. By performing an integration among characteristic steam lines using a suitable variable transformation, an expression for the Mach number can be derived. This is shown in figure 2.4a for the normalized distanced from the nozzle (x/d). For example, the temperature and the density in an expansion can be calculated using

$$(T/T_0) = \left(1 + \frac{\gamma - 1}{2} M^2\right)^{-1} \tag{2.4a}$$

$$(\rho/\rho_0) = (n/n_0) = (T/T_0)^{1/(\gamma-1)} = \left(1 + \frac{\gamma - 1}{2} M^2\right)^{-1/(\gamma-1)}. \tag{2.4b}$$

In figure 2.4 these properties are plotted versus the fraction of the nozzle distance x and the nozzle diameter d. The rapid drop in the temperature at the beginning of the gas expansion can be clearly seen. The ratio T/T_0 drops by two orders of magnitude, which indicates a drop

below $\sim 10\,\mathrm{K}$ gas temperature. Simultaneously, the density drops several orders of magnitude, showing that the interaction of gas atoms is limited to the first part of the expansion.

At this point it has to be emphasized that the calculations shown in figure 2.4 neglect cluster formation processes. Clustering affects almost all beam properties, e.g. one can expect faster dropping of the density or a less distinctive drop of the beam temperature due to cluster-cluster interactions.

Cluster formation

In a dense atomic or molecular beam, the atoms or molecules interact with each other in the form of collisions. Figure 2.5 shows calculations for the atom-atom collision rates in an expanding gas jet [31]. The calculations are based on a hard-sphere model for the two-body collisions and a soft-sphere model for the three-body collisions, respectively. For the simulation, gas with an initial temperature of $T_0 = 300\,\mathrm{K}$ and an initial pressure of $p_0 = 13\,\mathrm{mbar}$ was expanded through a nozzle with a diameter of $d = 2.5\,\mu\mathrm{m}$. The collisions cross-section for the atoms was $\sigma = 3.5\,\text{Å}$. Following [31], it takes about 10 collisions for a thermally stable final state ("freezing") to be reached. In the example shown in figure 2.5 this would occur at a distance of $x/d \sim 3$, considering the three-dimensional expansion or at least at $x/d \sim 10$ for a two-dimensional expansion. However, during these collisions the particles inside the beam have the opportunity to stick together, forming clusters.

At the beginning of the expansion, when the temperature of the expanding gas drops rapidly, three body collisions dominate the cluster formation and growth process, see e.g. [31]. From any given gas A a dimer A_2 forms in a two step mechanism that involves a virtual state A_2^*. This

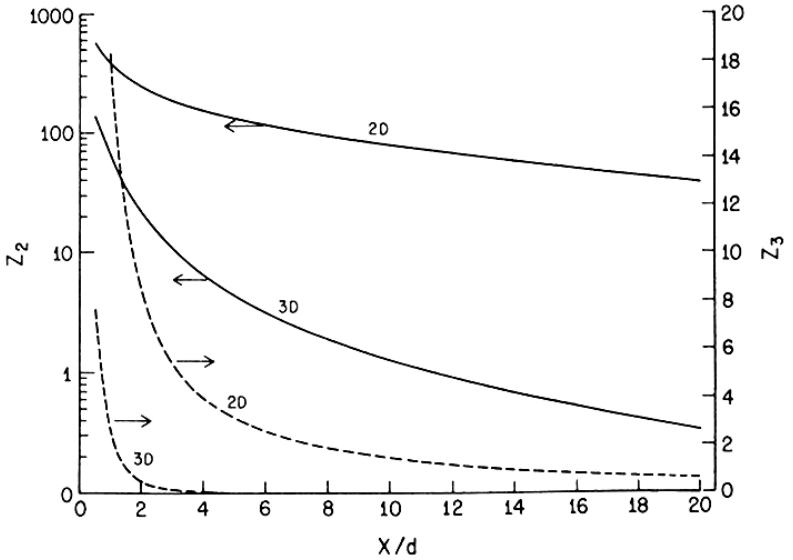

Figure 2.5.: Two- (Z_2) and three-body (Z_3) collisions per molecule in an molecular beam. The amount of collisions is shown versus the distance for axisymmetric (3D) and planar (2D) expansions. Source conditions for this simulation are $P_0 d = 10\,\mathrm{torr}\cdot\mathrm{cm} \approx 13.3\,\mathrm{mbar}\cdot\mathrm{cm}$, $T_0 = 300\,\mathrm{K}$, $d = 2.5\,\mu\mathrm{m}$ and $\sigma = 3.5\,\text{Å}$. From [31].

virtual state stabilizes when an additional monomer collision occurs:

$$\begin{aligned} A + A &\rightleftharpoons A_2^* \\ A + A_2^* &\underset{k_d}{\overset{k_s}{\rightleftharpoons}} A_2 + A. \end{aligned} \tag{2.5}$$

Here k_s and k_d are the rate constants for stabilization and destabilization, respectively. For the dimer formation rate equations can be formalized, which can be integrated along steam lines, as discussed in the last section. However, this model gives only an approximation for small dimer concentrations.

The energy removed from the virtual state A_2^* during the atomic collision increases the local temperature, which again decreases the local Mach number M. This influences other dimer formations and the further expanding gas cannot provide an isothermal enviroment for dimer formation. The density, temperature, and pressure of the expanding gas are evolving over several orders of magnitude during the expansion and the processes that are leading to dimer formation are strongly temperature dependent. In the same way, the cluster density ρ_n is affected by the monomer density ρ_1. These effects combined make the analytical thermodynamic description of the cluster growth process a difficult task.

Several different approaches for the description of clustering processes are already available, such as a classical nucleation rate theory (NRT) (e.g. [35]), a direct microscopic approach based on molecular dynamics (MD) (e.g. [36]), and a phenomenological microscopic approach [37].

NRT is based on a microscopic theory for surfaces and gives a classical steady-state nucleation rate J [31]:

$$J = \left(\frac{p_\mathrm{s}}{kT}\right)^2 \left(\frac{2\sigma}{\pi m}\right)^{1/2} V_\mathrm{c} \exp\left(-\frac{\Delta G^*}{kt}\right),$$

where σ is the macroscopic surface tension, V_c is the condensed phase atomic volume, and p_s the saturation vapor pressure. ΔG^* is the Gibbs free energy of formation of a condensation nucleus with a critical size [31]. As an approximation, which neglects translational and rotational degrees of freedom of the nuclei, the Gibbs energy is given by: $\Delta G^* = 16\pi\sigma^3/3\{\rho_\mathrm{L} \cdot kT \cdot \ln(p/p_\mathrm{s})\}^2$, where ρ_L is the bulk liquid density. However, the rapid changes in the Knudsen and the Mach number during the expansion of the gas may violate the assumptions inherent in NRT. Also, the derivation from surface theory and the use of bulk variables ρ, V,c, and ρ_L is not adequate for the small clusters with less than 100 atoms. These problems can be avoided by using "effective" macroscopic variables as pointed out in [31]. While this theory works for expansions with low temperature and density gradients ($\mathrm{d}T/\mathrm{d}t < 10^7\,\mathrm{K/s}$) problems arise for fast expansions ($\mathrm{d}T/\mathrm{d}t > 10^9\,\mathrm{K/s}$ to $10^{11}\,\mathrm{K/s}$).

MD or Monte-Carlo simulations have also been applied to analyze the clustering formation (e.g. [36]). In addition to successive monomer addition as used in NRT or the phenomenological approach, MD has to take cluster-cluster coagulation among other things into account to give proper results for clusters with $N > 7$. The formation rate of a cluster with the size k is given by [31]:

$$\frac{\mathrm{d}\rho_k}{\mathrm{d}t} = \frac{1}{2}\sum_{i=1}^{k-1} K(i, k-i)\rho_i\rho_{k-i} - \sum_{j=1}^{\infty} K(k, j)\rho_j\rho_k,$$

with rate coefficients K. The first sum is the rate at which clusters with k atoms are formed. The second one marks the loss of k-sized clusters for the corresponding size due to the growth

to larger sizes. At the beginning of the expansion, ρ_1 the monomer concentration, is very high, which results in a domination of the monomer addition channel $K(1, k-1)\rho_1\rho_{k-1}$ as the most important channel leading to a cluster size k. During the formation of larger clusters the number of cluster creation channels increases with $k/2$. This results in a domination of the residual channels $\sum_{i>1}^{k-1}(\ldots)$. This transition from single-channel to multi-channel cluster growth is observed at about $N > 7$.

A more intuitive approach is the phenomenological description of the cluster growth as presented by [37]. For the formation of small clusters, the growth process can be considered to be similar to the formation of dimers. The cluster with k atoms grows successively by the attachment of monomers. With the attachment of every monomer the inner energy of the cluster increases. At a certain point atoms evaporate from the cluster surface to ensure thermal stability. The ongoing cluster formation leads to a decrease of the monomer and dimer density. As a result, the growth process shifts from monomer absorption to coagulation of clusters. A cluster with i atoms and a cluster with j atoms are merging together and forming a cluster with $s = i + j$ atoms: $A_i + A_j \rightarrow A_s$. This can be described by four rate equations, covering the formation and dissociation of virtual states (collision, dissociation), as well as the activation and deactivation of these states [37]:

$$\begin{aligned}
A_i + A_j &\xrightarrow{K_{\mathrm{co}}} A^*_{i+j} && \text{collision,}\\
A^*_{i+j} &\xrightarrow{K_{\mathrm{di}}} A_i + A_j && \text{dissociation,}\\
A^*_{i+j} + M &\xrightarrow{K_{\mathrm{de}}} A_s + M && \text{deactivation,}\\
A_s + M &\xrightarrow{K_{\mathrm{ac}}} A^*_{i+j} + M && \text{activation.}
\end{aligned}$$

Here, the asterisk indicates a short lived, excited cluster in a transient state. M is a third body involved in the collision and $K_{(\ldots)}$ is the corresponding rate. Assuming that $A^*_{(i+j)=s}$ reaches a state of equilibrium quickly, the net rate (R) of A_s formed from A_i and A_j is calculated:

$$R(i,j) = \left(\frac{K_{\mathrm{co}}\rho_i\rho_j + \rho_s \sum_M K_{\mathrm{ac}}\rho_M}{K_{\mathrm{di}} + \sum_M K_{\mathrm{de}}\rho_M} \right) \cdot \sum_M K_{\mathrm{de}}\rho_M - \rho_i \sum_M K_{\mathrm{ac}}\rho_M. \tag{2.7}$$

Here, $\rho_{(\ldots)}$ are the corresponding concentrations. In line with the MD method, temporal changes

	rate constants
collision	$K_{\mathrm{co}} = \left(\frac{\pi kT}{2\mu_{i,j}}\right)^{1/2} (r_i + r_j)$ for $i \neq j$.
dissociation	$K_{\mathrm{di}} = \left(\left(\frac{\pi kT}{2\mu_{i,j}}\right)^{1/2} + \left(\frac{2E}{\mu_{i,j}}\right)^{1/2} \right) \cdot \left(2(\sigma_2 - \sigma_1)\right)^{-1}$.
deactivation	$K_{\mathrm{de}} = \left(\frac{\pi kT}{2\mu_{(i+j),M}}\right)^{1/2} (r_{i+j} + r_M)$.
activation	$K_{\mathrm{ac}} = \frac{K_{\mathrm{de}} K_{\mathrm{co}} \rho_i^\infty \rho_j^\infty}{K_{\mathrm{de}} \rho_i^\infty}$.

Table 2.1.: Summary of rate constants of cluster formation as presented by Lippmann *et al.*[37]. $\mu_{i,j}$ is the reduced mass of A_i and A_j, $r_{(\ldots)}$ the collision radius of the particle, σ_1 the radius of the core, σ_2 the radius of the potential well, and E the equilibrium energy. E and r are tabulated in the reference.

of the concentration of an s-sized cluster is given by the sum of all reactions that lead to the formation of A_s subtracted the sum of all the reactions that consume A_s:

$$\frac{\mathrm{d}\rho_s}{\mathrm{d}t} = \sum_{i=1}^{s/2,(s-1)/2} R(i, s-i) - \sum_{j=1}^{\infty} R(j, s) - R(s, s).$$

The expressions necessary for the rate constants are summarized in table 2.1. The rate constant for collision and deactivation directly follows from binary two-dimensional collision theory. The dissociation rate is assumed to be the inverse of the life time of state A^*_{i+j}. This can be estimated by the time A_i spends in the mutual potential well of A_j beginning with the approach and ending with the rebound. Finally, activation follows from the three other rate constants.

Deriving the mean cluster size from experimental parameters

With the rate equations or molecular dynamics simulations the growth process can be described mathematically on a microscopic scale. However, from an experimental point of view these descriptions are inefficient, because experimental parameters or conditions are hardly represented. Before mathematical descriptions of the cluster growth were formulated, empirical formulas were established referred to as scaling laws. They combine the experimental parameters with statistical averages over the observed mean cluster size $\langle N \rangle$. Here, the cluster beam is treated in its entirely instead of analyzing individual clusters.

Based on time-of-flight measurements of clusters [20] (see page 4) Hagena was able to deduce empirical scaling laws, which used the basic parameters of the cluster generation (nozzle type, pressure, gas, and temperature) and correlate them with the mean cluster size [38]. The experimental parameters are summarized using the scaling parameter Γ [39]:

$$\Gamma := n_0 \, d^q \, T_0^{(0.25\,q-1.5)} \qquad \text{with } 0.5 < q \leq 1 \tag{2.8}$$

with particle density in the reservoir $n_0 = p_0/(k_\mathrm{B} T_0)$. The parameter q was determined experimentally to be $q = 0.85$ for monoatomic gases by performing cluster beam measurements with constant T_0 and varying the nozzle diameter d.

The scaling parameter Γ in equation 2.8 strongly depends on the used expanded gas, hence a more general expression was needed. Hagena used a characteristic length r_ch (distance of the atoms in the cluster) and a characteristic temperature T_ch (heat of sublimation) [39]:

$$r_\mathrm{ch} = (m/\rho)^{1/3}, \tag{2.9}$$

$$T_\mathrm{ch} = \Delta h^0_0 / k_\mathrm{B}, \tag{2.10}$$

with m the atomic mass, ρ the density of the solid, and Δh^0_0 the sublimation enthalpy per atom at 0 K, e.g. for argon one obtains $r_\mathrm{ch} = 0.339\,\mathrm{nm}$ and $T_\mathrm{ch} = 927\,\mathrm{K}$. Equations 2.9 and 2.10 combined define a characteristic pressure for a specially considered material $p_\mathrm{ch} = k_\mathrm{B}\, T_\mathrm{ch}/r^3_\mathrm{ch}$, which is $p_\mathrm{ch} = 3.29\,\mathrm{Mbar}$ for argon. Using the reduced variables

$$n^*_0 = n_0 \, r^3_\mathrm{ch} \qquad T^*_0 = T_0/T_\mathrm{ch}$$

$$d^* = d/r_\mathrm{ch} \qquad p^* = p/p_\mathrm{ch}$$

the dimensionless scaling parameter Γ^* can be written as:

$$\Gamma^* = n_0^* \, d^{*\,q} \, T_0^{*\,(0.25\,q-1.5)} = \frac{n_0 \, d^q \, T_0^{(0.25\,q-1.5)}}{r_{\mathrm{ch}}^3 \, r_{\mathrm{ch}}^q \, T_{\mathrm{ch}}^{(0.25\,q-1.5)}} = \frac{\Gamma}{r_{\mathrm{ch}}^{(3-q)} \, T_{\mathrm{ch}}^{(0.25\,q-1.5)}}.$$

Here $\Gamma_{\mathrm{ch}} = r_{\mathrm{ch}}^{(q-3)} \, T_{\mathrm{ch}}^{(0.25\,q-1.5)}$ can be used together with $q = 0.85$ to obtain:

$$\Gamma^* = \Gamma/\Gamma_{\mathrm{ch}} = \frac{1}{k_{\mathrm{B}} \, \Gamma_{\mathrm{ch}}} \cdot \frac{p_0 \, d^{0.85}}{T_0^{2.2875}} = K_{\mathrm{ch}} \frac{p_0 \, (\mathrm{mbar}) \, d^{0.85} \, (\mu\mathrm{m})}{T_0^{2.2875} \, (\mathrm{K})}. \tag{2.12}$$

The factor K_{ch} is characteristic for different substances and indicates the ability of forming clusters. A high value identifies a chemical element that forms big clusters and vice verca. In table 2.2 the K parameters for rare gases are summarized. As K_{ch} is element specific, d is given by the experimental setup, just as p_0 and T_0. The parameter Γ^* summarizes the experimental conditions for a particular gas jet expansion. For values of $\Gamma^* < 200$ no cluster formation is observed [39]. In the range up to $\Gamma^* < 1000$ the transition from atomic beam to incipient clustering is detected. If the value for Γ^* exceeds 1000 massive cluster formation with more then one hundred atoms per cluster are feasible.

In addition to the diameter of the nozzle, the shape of the nozzle has a considerable impact on the cluster formation process. In figure 2.6 different nozzle geometries are shown. Up to this point, the sonic nozzle shape (see: 2.6a) was used to discuss the cluster formation process. Depending on the nozzle geometry the steam lines of the expanding gas are guided, compressed and decompressed. This leads to an increase in the particle collisions and therefore changes the generated cluster size. For the creation of large clusters, the use of a conical nozzle (figure 2.6d) is common, since it allows undisturbed expansion of the gas with a slight compression of the steam lines in direction of the expansion. This compression leads to the formation of larger clusters, due to the increase in the interaction of the gas atoms in the jet. In other words, the stagnation pressure p_0 can be reduced to obtain a similar cluster size compared to a sonic nozzle [41], which makes this type of nozzle an excellent choice for the experiments in this work.

In order to handle the particular nozzle shape in equation 2.12 the nozzle diameter is replaced by the equivalent nozzle diameter d_{eq}. A derivation of the equivalent nozzle diameter is found in [40]. It is based on an analogy of the continuous equations for the expansion through a conical nozzle and a free jet. The equivalent nozzle diameter reads[a]:

$$d_{\mathrm{eq}} = 0.719 \, \frac{d}{\tan\theta} \tag{2.13}$$

[a] Depending on the accuracy of the derivation the coefficient is sometimes as 0.74, cf. [24] and [40].

		He	Ne	Ar	Kr	Xe
Γ_{ch}	$(10^{16}\,\mathrm{m}^{-2.15}\,\mathrm{K}^{-1.2875})$	1494	31.07	3.495	1.931	1.036
K_{ch}	$(\mathrm{K}^{2.2875}\,\mathrm{mbar}^{-1}\,\mu\mathrm{m}^{0.85})$	3.85	185	1646	2980	5554

Table 2.2.: Characteristic parameter Γ_{ch} and K_{ch} for rare gases, adapted from [40]. K_{ch} is proportional to the condensation properties of the material. A higher value indicates higher clustering probabilities.

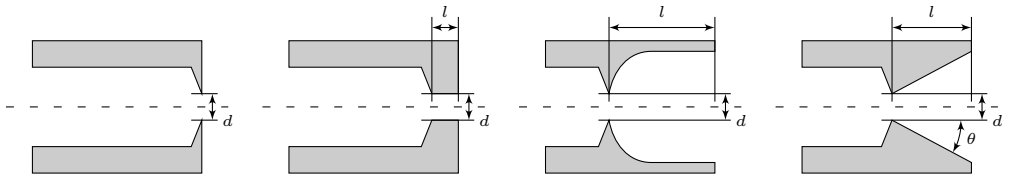

(a) Sonic **(b)** Cylindrical **(c)** Laval nozzle **(d)** Conical

Figure 2.6.: Cross sections of different nozzle shapes. Conical nozzles showed best results for producing large clusters, for pulsed and continuos beams. See text for further details. Adapted from [31].

with the diameter of the nozzle d and the opening angle θ as denoted in figure 2.6d. As it is pointed out in the references, equation 2.13 is only valid for conical nozzles with $l \geq d_{\mathrm{eq}}$. In case of $l < d_{\mathrm{eq}}$ a second expansion is taking place at the exit of the nozzle, destroying the formed clusters [40].

The experimentally mean cluster size obtained in an experiment using a supersonic expansion jet can be calculated from the scaling parameter Γ^*. Hagena presented an equation (cf. 2.14a) that was verified using mass spectrometer measurements [24], high-energy electron diffraction [25], Rayleigh scattering [27, 28], and Helium scattering [30]. The equation was found to be valid in a range of $1800 < \Gamma^* \leq 10^4$. In a lower regime ($350 < \Gamma^* \leq 1800$) Buck and Krohne presented a modification of Hagenas empirical equation for the cluster size [30] using cluster-helium-scattering as described on page 6. For $\Gamma^* > 10^4$ Dorchies *et al.* presented another adaptation of Hagenas scaling law [42]. Here, argon clusters where produced and analyzed using Mach-Zehnder interferometry and Rayleigh scattering. In the end, Hagenas empirical formula was slightly modified to fit the results. The results for the mean cluster size $\langle N \rangle$ can be summarized as follows:

$$\langle N \rangle = 38.4 \left(\frac{\Gamma^*}{1000} \right)^{1.64} \qquad 350 < \Gamma^* \leq 1800 \qquad [30], \tag{2.14a}$$

$$\langle N \rangle = \quad 33 \left(\frac{\Gamma^*}{1000} \right)^{2.35} \qquad 1800 < \Gamma^* \leq 10^4 \qquad [24], \tag{2.14b}$$

$$\langle N \rangle = 100 \left(\frac{\Gamma^*}{1000} \right)^{1.8} \qquad 10^4 < \Gamma^* \qquad [42]. \tag{2.14c}$$

Up until now, the formation of clusters from atomic beams has been discussed. The single cluster scattering method performed in this work enables a direct measurements of single cluster sizes and a direct verification of the scaling laws for the considered cluster sizes. Additionally, the shape of the clusters is revealed by this technique enabling snapshots of cluster growth. A comparison between the experimental findings and the theory presented in this section can be found in chapter 4.

2.2. Cluster light interaction

Besides the determination of the cluster size, the second important aspect forming the theoretical background for this work is the interaction between a cluster and high-intense light pulses. The theory of this interaction is presented in this chapter.

The interaction between high-intense laser sources and matter is an active field of research. Especially clusters can serve as an ideal model system to study this interaction. Clusters have the density of a solid state and their characteristics can be changed by varying their size. Starting with small clusters the interaction processes are dominated by intra-atomic and surface effects, while with larger cluster size interatomic and bulk effects start to dominate. However, in contrast to solid states, free clusters are isolated which means deposited energy is not able to dissipate into a surrounding medium.

A growing community studies the interaction between high-intense light pulses and clusters which generates a variety of reaction products. From the clusters highly charged and high energetic ions (e.g. [43, 12]) and electrons remain (e.g. [44]). In addition to that, x-rays and neutrons from deuterium fusion effects [45] are to be found in corresponding clusters. These effects indicate an efficient transfer of energy from the light field to the cluster [46].

The ionization and disintegration of clusters occurring as a result of cluster laser interaction proceed on different time scales [46, 23]. The effects are very specific and strongly depend upon excitation energy, intensity of the laser beam, cluster size, and cluster material. Yet, it is possible to derive a general three step-based schema for the cluster-light interaction, even though slightly different definitions of steps exist [12, 46, 47, 48].

1. This step occurs right at the beginning of the cluster-light interaction. The atoms inside the cluster can be treated as if they were isolated. Depending on the wavelength of the laser beam different ionization processes cause emission of electrons leaving the cluster. These electrons referred to be outer ionized.

2. During the light pulse further electrons are ionized, which are trapped inside the growing Coulomb potential of the cluster. These inner ionized electrons form a nanoplasma. Subsequent plasma processes can cause electrons to gain additional energy and outer ionize by leaving the cluster potential.

3. The disintegration of the cluster usually appears a long time after the light pulse. Additional recombination and relaxation effects might take place during this step.

The concept of outer and inner ionization was developed by Last and Jortner[49]. The following chapter present the different ionization processes at different excitation energies.

2.2.1. The infrared regime

The interaction of intense light pulses and clusters was first studied in the infrared regime (IR), simply because of the availability of high-power lasers in this regime. As a result of the interaction, highly charged ions and the total fragmentation of the clusters could be observed, even though the photon energy is not sufficient to produce the corresponding charges in direct ionization with the absorption of a single photon [50, 51]. Instead, multi-photon absorption and bending of the cluster potential allowing above-barrier ionization (AI) and tunnel ioniza-

tion (TI) have been identified as reasonable ionization channels in intense IR fields [52]. The regimes for multi-photon absorption and TI can be distinguished using the Keldysh parameter $\gamma = (\Delta E/2E_\mathrm{p})^{(1/2)}$ [53], where E_p denotes the ponderomotive energy and ΔE the ionization potential of the atom. For $\gamma \gg 1$ the perturbative multi-photon regime is reached while $\gamma \lesssim 1$ denotes non-perturbative TI regime.

Within the cluster, further effects become important. Electrons trapped in the cluster potential form a "nanoplasma" [43], interacting with the quivering laser potential. These charges are accelerated by the laser field and collide with the ions gaining momentum from that interaction. This enables them to leave the cluster potential (inverse Bremsstrahlung, IBS) [52]. Depending on the cluster size, further ionization mechanisms have been reported, such as enhanced ionization (EI) or resonant ionization (RA) [54, 55], where typical cluster radii are $R_0 < R_\mathrm{EI} < R_\mathrm{RA}$ [56].

The presence of the atomic ions and the nanoplasma result in a suppression of the interatomic barriers, the so-called plasma screening effect [57]. This effect causes a shifting of all energy levels and therefore a decrease of the binding energy. This suppression can cause direct inner ionization of valence electrons in extremely dense plasmas (barrier suppression).

2.2.2. Clusters in intense VUV pulses

With the development of free-electron lasers (FEL, see section 3.1 for details), a new regime for the interaction of light and matter has become accessible [9]. These sources produce very intense, coherent radiation from the vacuum ultraviolet (VUV, $\lesssim 100\,\mathrm{nm}$ wavelength) down to the soft and hard x-ray regime. In the VUV domain, the photon energy is only sufficient for single ionization. Collective effects like EI and RA are not expected due to the high laser frequencies and the cross-section of inverse Bremsstrahlung (IBS), which is proportional to $\propto \omega^{-2}$, is much lower compared to the IR regime.

Surprisingly however, high charged fragments from xenon clusters were recorded at 93 nm wavelength, as shown by the measurements from Wabnitz *et al.* which are presented in figure 2.7 [12]. The observed charge states vary with the size of the cluster denoted with the number of atoms per cluster N (figure 2.7a). As a reference a measurement of atomic xenon is given at the bottom of the figure. Here, only single charged ions were observed due to the low photon energy ($93\,\mathrm{nm} \approx 12.6\,\mathrm{eV}$), which is only sufficient to overcome the first ionization potential of xenon (12.1 eV). Higher ionization potentials are inaccessible (second ionization potential: 21.2 eV) with this photon energy. With increasing cluster size, more and higher charge states were observed in the measurements, with up to Xe^{8+} for clusters with $N = 30\,000$ atoms. These charge states show high kinetic energies, which can be seen by the shift towards shorter flight times compared to the calculated charge states indicated in the uppermost part of the figure. The kinetic energies are depicted in the inlay in 2.7a for $N = 1\,500$ atoms. In 2.7b the ion yield with increasing power density of the FEL is depicted. At $10^{13}\,\mathrm{W/cm^2}$ kinetic energies are appearing, which were interpreted as a signature for hydrodynamic explosion of the cluster [48]. This threshold is much lower compared to the threshold observed during IR-laser experiments [12].

For the understanding of the enhanced ionization in the clusters, collective effects based on IBS have been proposed [58, 59]. Here, IBS acts as a heating process within the inner ionized electrons, which could be verified for high intense laser fields by Laarmann *et al.* [60].

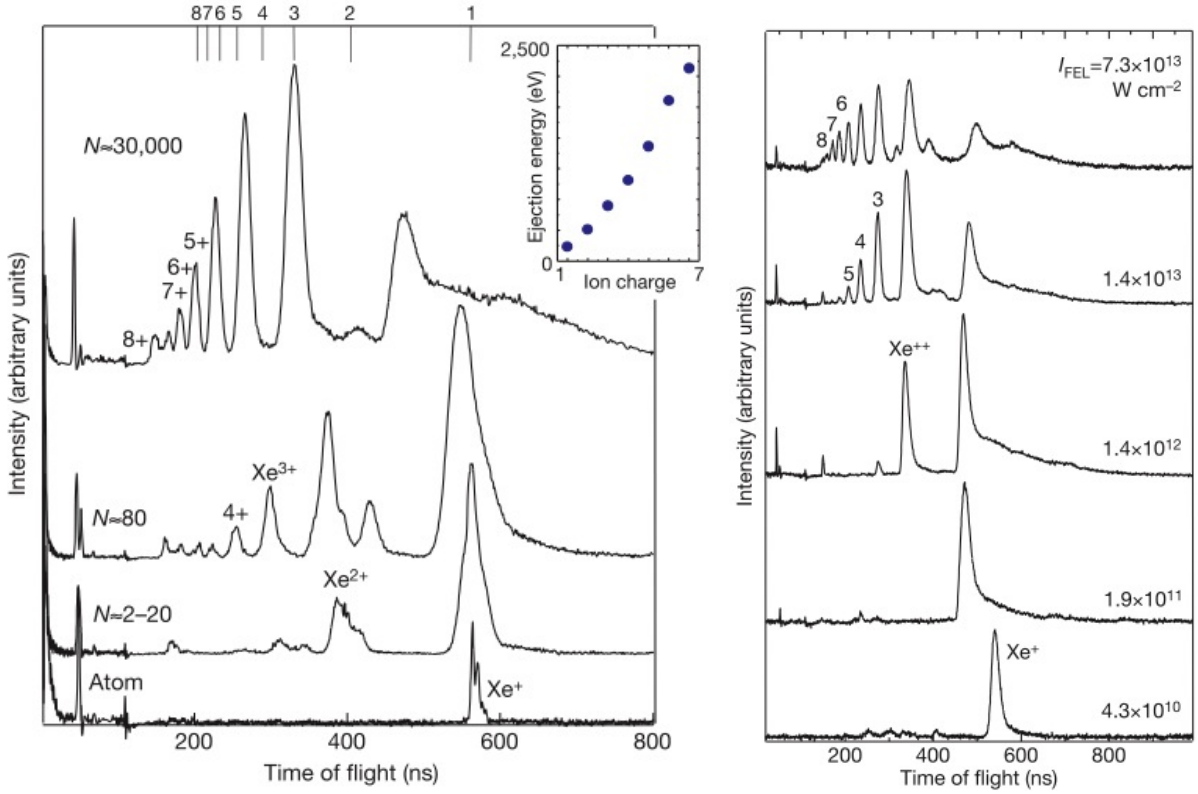

Figure 2.7.: (a) Time-of-flight (TOF) ion mass spectra for xenon clusters (cluster size N) irradiated with 98 nm high power ($2 \cdot 10^{13}\,\mathrm{W/cm^2}$) VUV-light. The observed charge states are a function of the cluster size. (b) TOF mass spectra for $Xe_{1\,500}$ clusters recorded at different power densities. [12]

During a 10 fs VUV-pulse with a power density of $10^{13}\,\mathrm{W/cm^2}$ all atoms inside the cluster become ionized due to the large photoionization cross section of about 50 Mb at this wavelength [58]. However, the majority of the atoms become inner ionized which results in a high-density nanoplasma moving freely through the cluster with a high probability for electron-electron and electron-ion collisions. A free electron can not absorb photons from the VUV pulse, nor can electron-electron collisions absorb energy [61]. Electron-ion collisions extract energy from the light pulse via IBS, which leads to effective plasma heating. However, the ionic scattering potential, which is usually given by the coulomb potential, is not sufficient for the description of the observed heating process. For the explanation of the enhanced energy absorption a more realistic atomic potential was proposed [58]:

$$V_i(r) = -\frac{1}{r}\Big(i + (Z-i)e^{-\alpha_i r}\Big)e^{-r/\lambda_\mathrm{D}},$$

where i is the ionic charge state, Z the nuclear charge (for xenon $Z = 54$), and λ_D the Debye length of the nanoplasma. The factor α_i controls the transition from the exterior to the interior of an ion where colliding electrons face a charge greater i. α_i was adjusted by the authors so that the binding energy of a $5p$ electron in the potential $V_1(r)$ ($\lambda_\mathrm{D} \to \infty$) equates the ionization potential for neutral xenon. $V_i(r)$ represents the attractive potential of a charged nucleus shielded by the surrounding electrons. Kinetic electrons from the nanoplasma, which are passing the potential, are scattered at the effective space charge of the ions which increases the scattering cross-section

compared to a free ion. This enhances IBS explains the large amount of absorbed energy form the laser field. But additional ionization processes, such as impact ionization of the electrons, are not taken into account by this model. In addition to that, cluster size effects were not considered as the cluster was assumed to be infinitely extended. Furthermore, the beam profile of the FEL and cooling/recombination processes are neglected due to the fact that the ions are detected far away from the cluster. All together this leads to an overestimation of the IBS influence on the cluster ionization.

For the explanation of the observed high charge states a modification of the approaches used in the IR regime was presented [62]. For the inner ionization of one single ion (eg. Xe^{1+}) using VUV light two photons are needed as depicted in figure 2.8. But since inside a cluster the interatomic barriers are lowered due to the neighboring atoms (2.8 (b)), the energy needed for inner ionization is lowered and the absorption of one photon (black arrows in the picture) is sufficient for (inner) ionization. These ionization processes happen during the first femtoseconds of the light pulse as predicted by calculations [62]. During most of the interaction time the clusters consist of a nano-plasma, highly changed ions and quasi free electrons. Corresponding calculations based on a slightly modified momentum-dependent potential [63, 64] by Siedschlag and Rost showed very good agreements with related experiments [62].

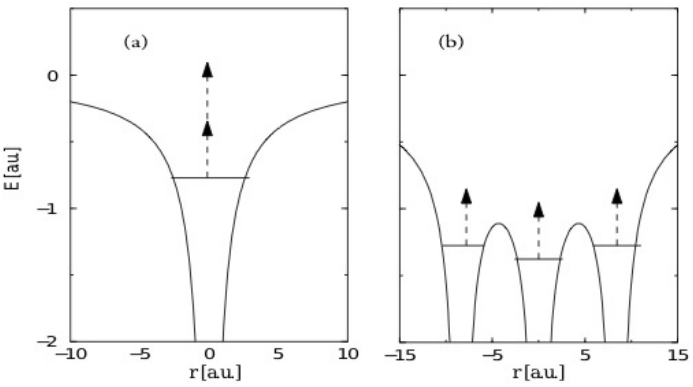

Figure 2.8.: Schematic (inner) ionization processes of an ion (e.g. Xe^{1+}) (a) and a Xe^{3+} cluster (b) [62].

In the simulations one can was observe that a high fraction of the ions are able to recombine to neutral charge states after the ionization. But due to the experimental limitations, these neutral cluster fragments could not be detected physically. Full recombination of atoms is mainly possible in the center of the cluster where the electrons in the nanoplasma are pulled back as a result of the potential of the ions. In contrast to that, the observed highly charged ions originate from the surface of the cluster.

2.2.3. Cluster light interaction in the XUV and first imaging experiments

Experiments in the extreme ultraviolet regime (XUV) below 40 nm wavelength with highly intense light sources became feasible when the "Freie Elektronen Laser in Hamburg" (FLASH) came into user operation in 2005 (see section 3.1 and [9]). Besides opening this new regime for highly intense laser-matter interaction, imaging experiments of single nanometer sized samples became possible [10, 11], allowing a study of such samples on ultrafast timescales without depositing them on a surface. In this section, the first cluster experiments using electron and ion spectroscopy will be discussed. Additionally, an overview over the first cluster imaging experiment is given.

The results of the first cluster experiments performed at FLASH are summarized in figure 2.9. The spectra in 2.9a show the kinetic energy of photoelectrons (PES: photoelectron

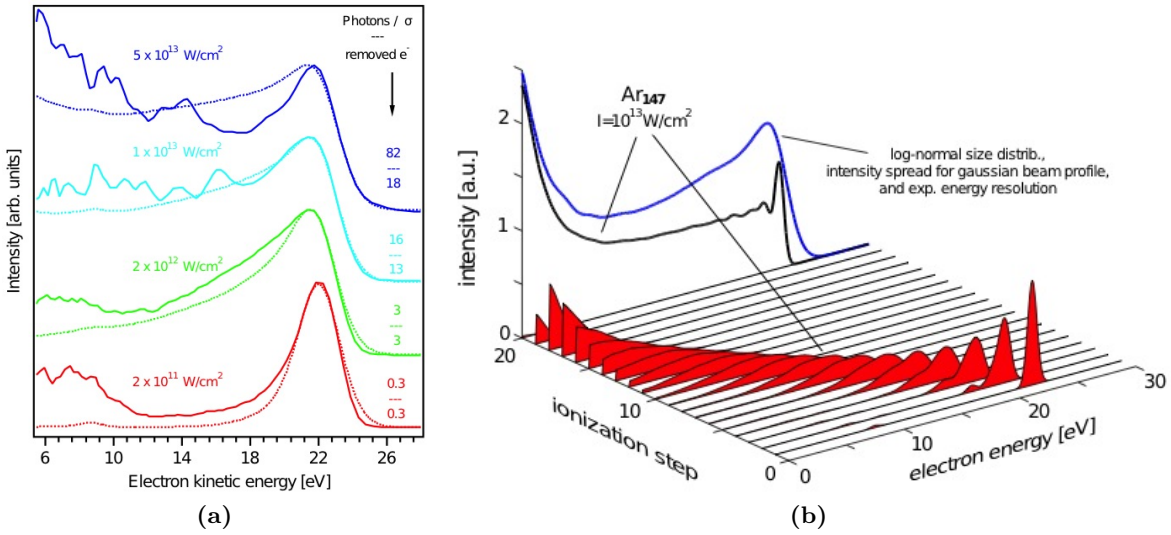

Figure 2.9.: (a) Comparison of experimental (solid) and simulated (dashed) electron spectra for Ar_{80} clusters. With increasing power density (bottom to top) the number of photons in the cross section increases together with the number of electrons overcoming the increasing Coulomb potential. (b) Monte Carlo simulation of stepwise electron emission from Ar_{147} clusters (red filled curves). For every ionization step, the electron spectrum changes significantly due to the growing Coulomb field of the ions. The sum of the spectra is given by the black line. A comparison with measured data is possible by taking relevant broadening effects into account (blue line). [65]

spectroscopy) obtained from argon clusters ($N = 80$ atoms) at a wavelength of $\lambda = 32.2\,\mathrm{nm} \mathrel{\hat{=}} 38.5\,\mathrm{eV}$. The FEL power densities are denoted in the figure. The measurements (solid lines) are compared to simulations (dotted lines). For the lowest intensity ($2 \cdot 10^{11}\,\mathrm{W/cm^2}$) on average 0.3 photons are in the absorption cross-section of the cluster, which is similar to experiments at Synchrotrons [66]. The peak around 22 eV represents the $3p$-photoemission line. The measurement at $2 \cdot 10^{12}\,\mathrm{W/cm^2}$ shows the transition from single-photon to multi-photon absorption, where on average three photons are in the ionization cross-section. This leads to an asymmetric broadening of the $3p$-line because outer ionized electrons are more and more pulled back by the increasing cluster potential. The broadening continues towards higher FEL energies. Beginning at 18 absorbed photons per cluster with 147 atoms, this trend comes to an end. At this point any further outer ionization is saturated, which is indicated by the plateau in the data. For the highest observed FEL energies ($5 \cdot 10^{13}\,\mathrm{W/cm^2}$) the increase in the low-kinetic photo electrons can be interpreted as an indicator for thermalization of the ions [65].

The theoretical model used for the depicted calculations in figure 2.9b is based on stepwise ionization. Based on the Argon $3p$ and $3s$ photoionization cross-section, the different ionization steps are calculated for an Ar_{147} cluster irradiated with $3 \cdot 10^{13}\,\mathrm{W/cm^2}$ XUV light. With every ionization step the increasing attractive forces of the cluster ions reduce the kinetic energy of the photo-ionized electrons. The sum off all ionization steps is given by the black curve in the figure. With the introduction of a log-normal cluster size distribution and a gaussian distribution for the intensity, that represents the focus of the FEL beam, the blue line is obtained. Taking these effects into account, the multistep ionization simulation is in good agreement with the measurements.

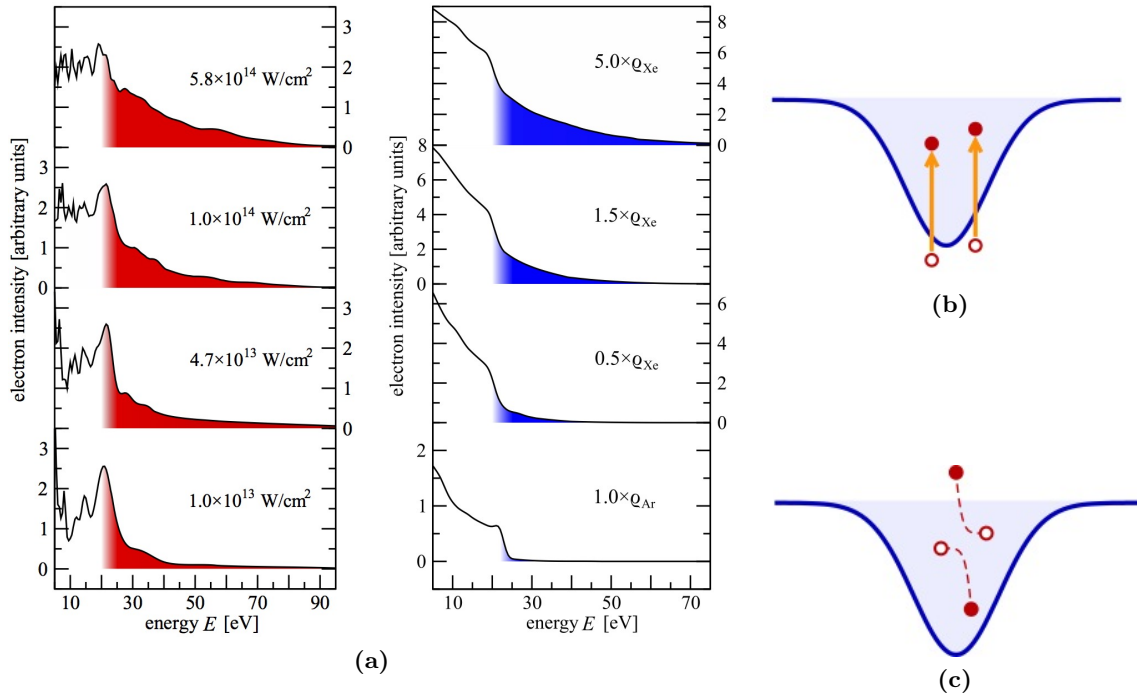

Figure 2.10.: Electron spectra of Xe_n clusters recorded at FLASH with 90 eV photon energy and 10 fs pulses with varied pulse energies. Electrons with higher energy than the photon peak at 20 eV are colored. In the theoretical model (right-hand side, blue) these electron spectra are reproduced for different electron densities ρ. (b) depicts the excitation of electrons (red) from the bound atomic states into the cluster potential (nanoplasma, blue). This is achieved by photon absorption of the electrons. (c) Energy-exchanging collisions in the nanoplasma allow electrons to leave the cluster potential as fast electrons, while others are slowed down.[67]

However, the influence of the increasing cluster potential is not limited to the reduction of the kinetic energies of the outer ionized electrons. Experiments show electrons with kinetic energies beyond the photoemission line [67]. These electrons can be interpreted as products of plasma heating processes. Figure 2.10 shows the corresponding results from xenon clusters, again irradiated with high intense 90 eV femtosecond pulses. The left-hand side of the figure depicts the photoelectron spectra with red-marked photoelectrons with high kinetic energy above the photoemission line of xenon. With increasing laser power density (from bottom to top) the amount of fast electrons increases. The associated simulations (right-hand side) are taking simplified inner and outer ionization into account. The power density of the FEL influences the density of the electrons in the nanoplasma. For the highest power density ($I_0 = 5.8 \cdot 10^{14}\,\mathrm{W/cm^2}$) the initial electron density ρ is five times higher than the atomic density of xenon ρ_{Xe}. The trapped electrons efficiently exchange energy by multiple collisions in the nanoplasma [47]. During the collisions, energetic electrons are produced by slowing down other electrons. The fast electrons can leave the cluster and contribute to the measured tail in the spectra while the slow electrons remain trapped in the potential. This is illustrated in figure 2.10b and 2.10c.

A deeper understanding of the interaction of XUV radiation and clusters can be obtained by determining the origin of the highly charged ions. Experiments with "core-shell clusters" allow corresponding conclusions. Such experiments were performed by Hoener *et al.*, allowing observation of the charge transfer in the exited clusters [68]. For these experiments different

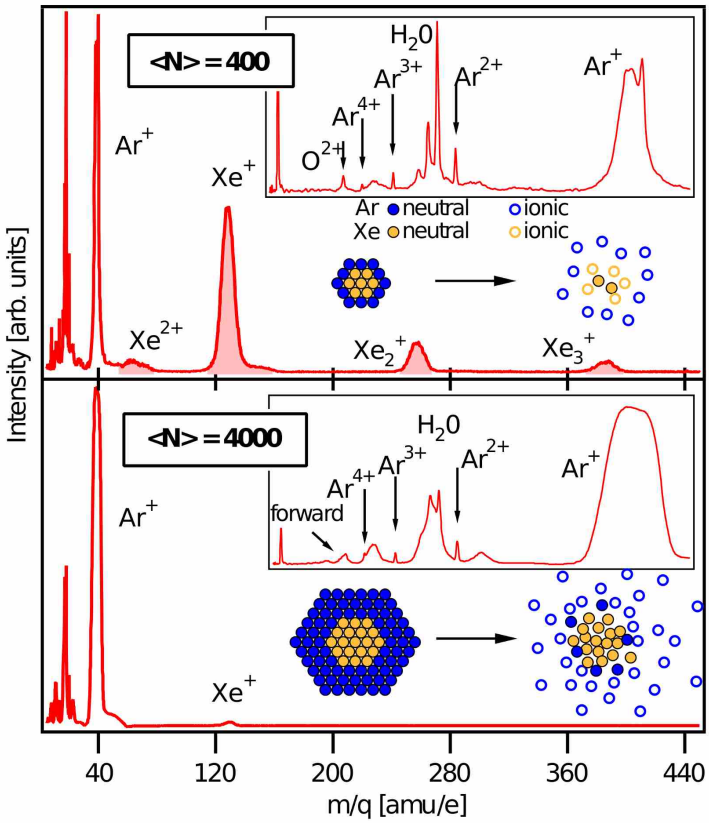

Figure 2.11.: Ion spectra of clusters with xenon core and argon shell for two different cluster sizes. A thick argon shell reduces the amount of charged xenon fragments measured which indicates charge transfer from the exited xenon core to the surrounding argon matrix allowing relaxation for the xenon. [68]

mixtures of argon and xenon gas were co-expanded, which results in xenon clusters with a layer of argon atoms surrounding a xenon core like a shell, hence the term "core-shell clusters". For ionization of the clusters with 90 eV photons it was expected to find highly charged xenon fragments, because of the coherent absorption of xenon at this photon energy regime. However, beginning at a particular cluster size charged xenon fragments were absent altogether while the argon signal increased. This is interpreted as an ion charge transfer from the core to the shell. The results of this experiment are presented in figure 2.11, where two ion spectra from two different cluster sizes are compared. For the smaller clusters (Xe/Ar_{400}) charged xenon and argon fragments are visible. But with larger cluster sizes (Xe/Ar_{4000}) the charged xenon fragments are virtually non-existent.

Due to the electron-electron interactions in the nanoplasma the electrons thermalize and recombination takes place, resulting in a charge separation in the cluster, which in turn is compensated by spalling the outer layers of the cluster. Therefore charged fragments are visible only from the shell of the cluster. Calculations show that this charge redistribution together with the recombination in the nanoplasma slows down the cluster fragmentation from fast Coulomb explosion to slower hydrodynamic expansion [69]. As Hoener *et al.* point out, these effects are not limited to heterogeneous clusters like the argon-xenon core-shell systems observed, but appear in all types of clusters.

The effect of slowing down the fragmentation of nano-particles is important for imaging

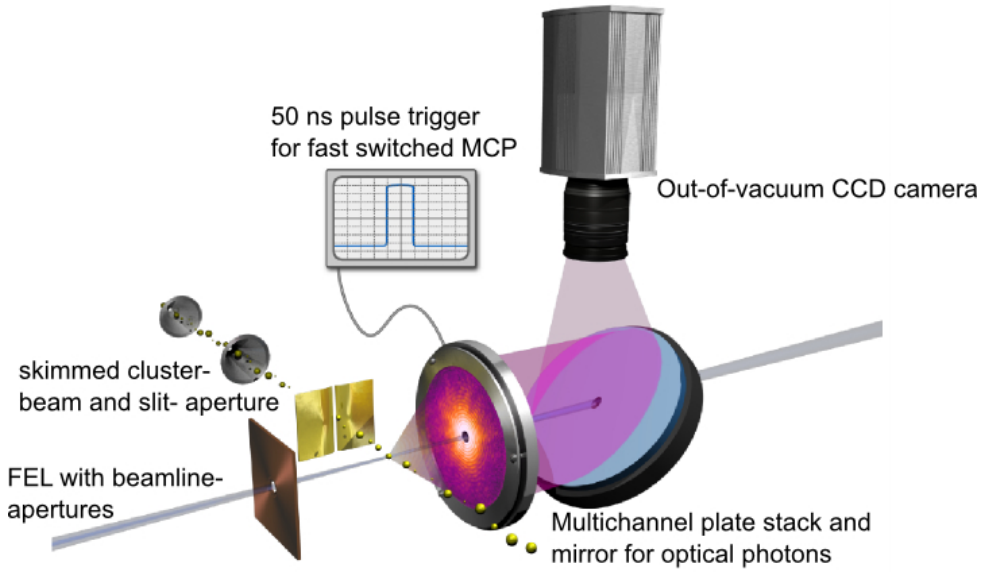

(a)

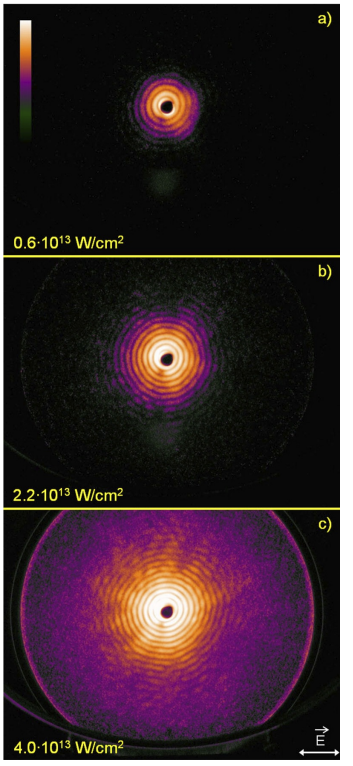

(b)

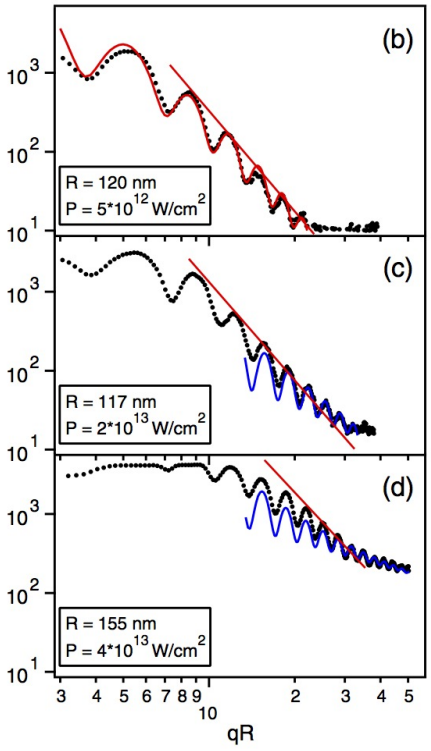

(c)

Figure 2.12.: Single cluster scattering experiment performed at FLASH. (a) depicts the experimental setup as it is described in the text. (b) scattering recorded from single xenon clusters ($r \approx 150\,\mathrm{nm}$). From top to bottom, the intensity of the FEL is increasing. (c) The corresponding scattering profiles from the scattering patterns in comparison to simulations to determine the absorption (slope and shape of the minima) of the scattering particle. An increase in the absorption with higher FEL intensity is observed. [18]

experiments as discussed by Neutze *et al.* [10]. A sample can be embedded into an atomic matrix, which is used as a surrounding shell but has to have little to no effect to the scattering image. The shell will explode while the expansion of the sample is delayed. This increases the quality and resolution of scattering patterns achievable during imaging experiments with x-ray lasers.

But even without using core-shell samples, first cluster imaging experiment were successfully performed using the FLASH as light source by Bostedt *et al.* in 2008 [18]. The experimental setup is outlined in figure 2.12a. A cluster beam (yellow balls) is skimmed until one single cluster is in the focus of the FEL at a time. The irradiation with the FEL light produced scattering photons that hit a fast gated multi-channel-plate (MCP) with an attached phosphor screen. This MCP stack was used to convert the x-ray photons into photons in the visible regime, which could be reflected out of the vacuum chamber and were detected with a conventional CCD camera.

Figure 2.12b displays three recorded scattering patterns from three individual nanometer sized clusters ($r \approx 150\,\mathrm{nm}$). The data is sorted from top to bottom according to the FEL intensity interacting with the clusters. Figure 2.12c shows the three corresponding scattering slopes generated from the scattering patterns by radial integration. Colored are corresponding simulations based on Mie theory that will be further discussed in the next section. Changes in the scattering slope indicate ultrafast electron rearrangement during the light interaction. From the simulation the absorption of the particle during the interaction can be determined, by comparing the slopes and the shape (or definition) of the minima. The data reveals an increase in the absorption of the particles with increasing FEL intensity. Effects such as this are only visible by using imaging technique, which allows gathering information during the matter-light interaction. The reaction product (the scattered photons) is produced immediately and detected on an ultrafast timescale, where conventional spectroscopy is inherently "blind". The experience and insights gained from this experiment are the basis for the experiments presented in this work. Therefore, the theoretical background of this scattering experiment (the Mie theory) is discussed in the next section.

2.3. Scattering of light by small particles

2.3.1. Introduction to scattering theory

During the research for this thesis, scattering experiments at single rare gas clusters have been performed extensively. As a light source free-electron lasers (FEL) were used (see page 39 ff.). For the means of the theoretical description in this chapter, the clusters can be considered as spherical and the FEL light as fully polarized and monochromatic with a wavelength in the regime of the cluster's diameter. The scattering patterns produced by the clusters were analyzed by simulating the scattering process with computer programs. Based on the simulations the analysis of the scattering data is presented in the upcoming chapter 4. The following description is based on the book of Bohren and Huffman "Absorption and Scattering of Light by Small Particles" [70].

The starting point for the discussion of the scattering process following Mie, as for all problems of classical electrodynamics, are the macroscopic Maxwell equations. In differential

form the Maxwell equations read:

$$\nabla \cdot \mathbf{D} = \rho, \tag{2.15a}$$
$$\nabla \cdot \mathbf{B} = 0, \tag{2.15b}$$
$$\nabla \times \mathbf{E} = -\frac{\partial \mathbf{B}}{\partial t}, \tag{2.15c}$$
$$\nabla \times \mathbf{H} = \mathbf{J} + \frac{\partial \mathbf{D}}{\partial t}. \tag{2.15d}$$

Here, $\mathbf{E}$ is the electric field, $\mathbf{B}$ the magnetic induction, $\mathbf{D}$ the electric displacement, $\mathbf{H}$ the magnetic field, ρ the charge density, and $\mathbf{J}$ the current density. Maxwell's equations summarize the properties of electro-magnetic fields, and are valid for every point in space where the physical properties are continuous. The equations can be interpreted in the following way. An electric displacement is caused by the presence of an electric charge (2.15a). Free magnetic poles are absent (2.15b) [71]. The other two equations are showing the connection between electric and magnetic fields. Changes in time of the magnetic induction imply an electric field (2.15c) and changes in time of the electric displacement imply a magnetic field (2.15d).

The electric displacement $\mathbf{D}$ and the magnetic field $\mathbf{H}$ are defined by

$$\mathbf{D} = \epsilon_0 \, \mathbf{E} + \mathbf{P},$$
$$\mathbf{H} = \frac{\mathbf{B}}{\mu_0} - \mathbf{M},$$

with the electric polarization $\mathbf{P}$ and the magnetization $\mathbf{M}$. The constants ϵ_0 and μ_0 refer to the permittivity and the permeability of free space. In addition to the Maxwell equations (2.15) constitutive relations ($\mathbf{D} = \epsilon_0 \mathbf{E} + \mathbf{P}(\mathbf{E})$ and $\mathbf{H} = \mathbf{B}/\mu_0 + \mathbf{M}(\mathbf{H})$, with $\mathbf{P}$ the electric and $\mathbf{M}$ magnetic polarizetion) are taken into account with the phenomenological constants σ (conductivity), μ (permeability), and χ (susceptibility), which are assumed to be independent of the considered fields, direction, and position, but depend on the considered medium. In other words: the medium has to be isotropic and homogenous. These relations can be formalized as:

$$\mathbf{P} = \epsilon_0 \, \chi \, \mathbf{E}, \tag{2.17a}$$
$$\mathbf{J} = \sigma \, \mathbf{E}, \tag{2.17b}$$
$$\mathbf{B} = \mu \, \mathbf{H}. \tag{2.17c}$$

Note that the equations 2.17 are not universal but have to be adopted in every individual case.

Lorentz model

The classical Lorentz model can be used to give insights to the underlying physics of the wavelength or frequency dependence of the scattering processes. It describes the interaction of light and matter based on harmonic oscillators and allows a derivation for resonant scattering. In principle, the results obtained with the help of the Lorentz model are formally identical with a quantum mechanical treatment of the interaction of light and matter, even if several quantities are interpreted differently [70]. The susceptibility χ, as presented in equation 2.17a, can serve as an example for the derivation.

The electric polarization of a material is connected with the electric field of the incident light

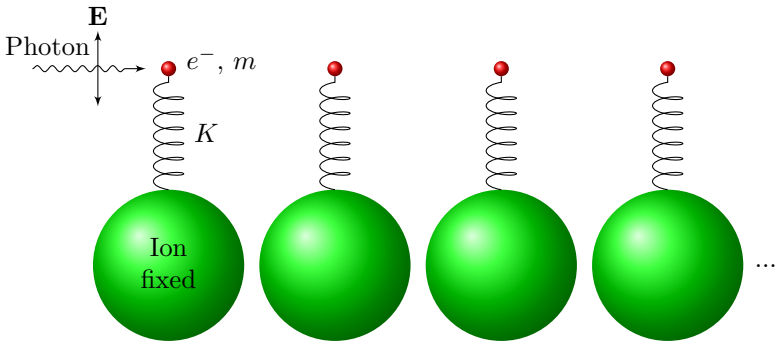

Figure 2.13.: Lorentz model of light matter interaction: a driven harmonic oscillator with damping. The ions are considered fixed. A spring with a spring constant K binds the electrons with mass m and charge e^- to them. The electric part of the incident light wave induces an oscillation of the electrons.

as shown in equation 2.17a. A single piece of unpolarized matter is described by $\mathbf{P} = 0$. When it is placed in a periodic electric field, it becomes polarized. The χ factor describes the response of the material to the electric light field. A mechanical equivalent is the mass m that is forced to oscillate due to an external driving force. The factor χ then equates to the damping in the system. In a quantum mechanical context this picture corresponds to the dipole approximation.

Considering the mechanical system that is introduced in figure 2.13, the electric field $\mathbf{E}$ of the incident photon ($h\nu$) drives the electron e^- with the mass m that is coupled with a spring (spring constant K) to a stationary ion. May $\mathbf{x}$ be the displacement from equilibrium, then the equation of motion for that particular case would be

$$m\frac{\partial^2 \mathbf{x}}{\partial t^2} + b\frac{\partial \mathbf{x}}{\partial t} + K\,\mathbf{x} = e\,\mathbf{E}, \tag{2.18}$$

where b were the (arbitrary) damping constant. The driving force in this system, that has to be treated locally for every atom, can be written as a periodic force:

$$\mathbf{E} = \mathbf{E}_0\, e^{i\omega t}.$$

The solution for the displacement $\mathbf{x}$ of the driven harmonic oscillator (eq. 2.18) is known from classical mechanics. By using $\omega_0^2 = K/m$ (resonant frequency) and $\gamma = b/m$ (damping) one obtains:

$$\mathbf{x} = \frac{e\,\mathbf{E}_0}{m(\omega_0^2 - \omega^2 - i\,\gamma\,\omega)}\, e^{i\omega t}. \tag{2.19}$$

For any damping ($\gamma \neq 0$) the factor between the displacement $\mathbf{x}$ and the electric field is complex which means that there is a phase shift between these two quantities. Therefore, the displacement can be rewritten as $Ae^{i\Theta}(e\mathbf{E}/m)$ with the amplitude A and the phase Θ:

$$A = \left((\omega_0^2 - \omega^2)^2 + \gamma^2\,\omega^2\right)^{-1/2},$$
$$\Theta = \tan^{-1}\frac{\gamma\,\omega}{\omega_0^2 - \omega^2}.$$

In figure 2.14a A and Θ are plotted as a function of ω. The maximum of the amplitude is reached at $\omega = \omega_0 = \sqrt{K/m}$ having a maximum displacement that is proportional to $1/\gamma$.

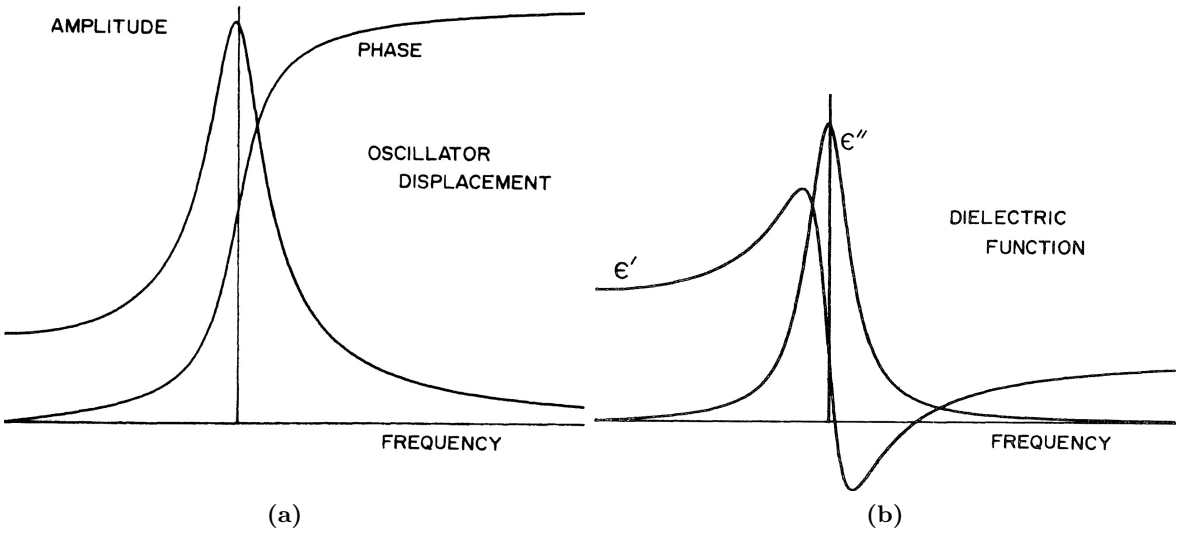

Figure 2.14.: Characteristics of the amplitude A and phase Θ of the harmonic oscillator model or Lorentz model (a). (b) shows the real and imaginary parts of the dielectric function. Both graphs are plotted as a function of the frequency ω [70].

With the obtained response of a single harmonic oscillator to a given driving force (electric field), the response of a macroscopic system can be seen as a superposition of harmonic oscillators. The induced dipole moment of a single oscillator is

$$\mathbf{p} = e\,\mathbf{x}.$$

Following the principle of superposition, the polarization per unit volume $\mathbf{P}$ can be written as $\mathbf{P} = N\,\mathbf{p}$, where N is the number of oscillators per unit volume. With the displacement of the oscillator (equation 2.19) this leads to:

$$\mathbf{P} = \frac{\omega_\mathrm{p}^2\,\mathbf{E}_0}{\omega_0^2 - \omega^2 - i\,\gamma\,\omega}\,e^{i\omega t}, \tag{2.21}$$

with the plasma frequency $\omega_\mathrm{p}^2 = N\,e^2/m\,\epsilon_0$. Using equation 2.21 and equation 2.17a the coupling constant between the polarization and the electric field, the susceptibility χ, can be determined:

$$\chi = \frac{\omega_\mathrm{p}^2}{\omega_0^2 - \omega^2 - i\,\gamma\,\omega}.$$

Figure 2.14b shows the real and the complex part of the dielectric function ε for the harmonic oscillator system:

$$\varepsilon' = 1 + \chi' = 1 + \frac{\omega_\mathrm{p}\left(\omega_0^2 - \omega^2\right)}{\left(\omega_0^2 - \omega^2\right)^2 + \gamma^2\omega^2} \tag{2.22a}$$

$$\varepsilon'' = \chi'' \quad = \quad \frac{\omega_\mathrm{p}\gamma\omega}{\left(\omega_0^2 - \omega^2\right)^2 + \gamma^2\omega^2}, \tag{2.22b}$$

with χ' and χ'' the real part and imaginary part of the susceptibility, respectively. The results for the dielectric function obtained from the Lorentz model are in very good agreement with experimental observations and also satisfy the Kramers-Kronig Relations (see for example [70]).

Light in medium – refractive index

With the aid of the dielectric function (equation 2.22), the behavior of the scattering medium can be described. A more convenient description can be gained by using the complex refractive index:

$$n = c\sqrt{\epsilon\mu} = \sqrt{\frac{\epsilon\mu}{\epsilon_0\mu_0}}, \tag{2.23}$$

where $c = (\epsilon_0\mu_0)^{-1/2}$ represents the speed of light. This expression allows rewriting the wave vector $\mathbf{k}$ for a electro-magnetic (EM) propagating through a medium (here in scalar form)

$$k = k' + ik'' = n\,\frac{\omega}{c}. \tag{2.24}$$

For $n = 1$ the well known expression for an EM wave propagating through vacuum is obtained:

$$k = \frac{\omega}{c}.$$

While the wave vector is complex, an equivalent relation is found for the refractive index with $n = n' + i\,n''$. With that and the separation of equation 2.24 in real and imaginary part one gets:

$$n' = k'\,\frac{\omega}{c}, \tag{2.25a}$$

$$n'' = k''\,\frac{\omega}{c}. \tag{2.25b}$$

With the refractive index, the equation for the plain electrical field can be rewritten. Here the wave number in free space $\omega/c = 2\pi/\lambda$ is used, where λ is the wavelength in vacuum. Now the electric field can be given as:

$$\mathbf{E}_c = \mathbf{E}_0 \exp\left(-\frac{2\pi n'' z}{\lambda}\right) \exp\left(\frac{i2\pi n' z}{\lambda} - i\omega t\right).$$

where $z = \hat{\mathbf{e}} \cdot \mathbf{x}$ and similar for the magnetic part of the EM wave. The complex part of the refractive index (n'') affects the attenuation of the wave that is propagating through a medium while n' determines the phase velocity of the propagating wave. However, the real and the complex part of the refractive index (or optical constants[b]) are not independent. They satisfy the Kramers-Kronig-Relations [70]:

$$n'(\omega) = 1 + \frac{2}{\pi}\,P\int_0^\infty \frac{\Omega k(\Omega)}{\Omega^2 - \omega^2}\,\mathrm{d}\Omega, \tag{2.26a}$$

$$n''(\omega) = -\frac{2\omega}{\pi}\,P\,\omega\int_0^\infty \frac{n'(\Omega)}{\Omega^2 - \omega^2}\,\mathrm{d}\Omega, \tag{2.26b}$$

where P is the value of the Cauchy-integral. From the measurement of $n'(\Omega)$ for any given $\Omega = \Omega_0$ the complex part of the refractive index (n'') can be obtained by integration and vice versa. Figure 2.15 shows an example for the refractive index of solid xenon in an energy regime

[b] This expression is sometimes found in the literature and is misleading, because the refractive index is not constant, but frequency dependent (dispersion).

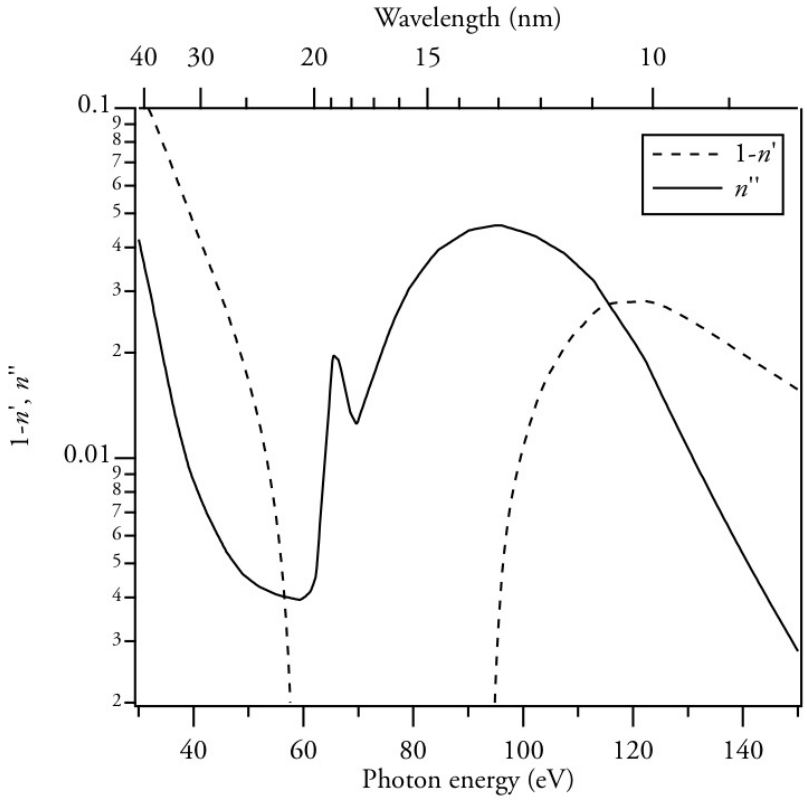

Figure 2.15.: Reflective index n of solid xenon ($\rho = 3.640\,\mathrm{g/cm^3}$) in the XUV regime address during the measurements at FLASH. [72].

accessed during the FLASH experiments.

The absorption of the electro-magnetic energy in a medium can be described by a decrease of the Pointing vector **S**. The time-averaged magnitude of the Pointing vector is proportional to $|\mathbf{E}|^2$. For an electro-magnetic wave propagating in z-direction this gives

$$\mathbf{S} \propto |\mathbf{E}_0|^2 \exp\left(\frac{-4\pi n''}{\lambda}\right) \mathbf{z}. \tag{2.27}$$

The magnitude of the Pointing vector I, called the intensity or irradiance, is $I = I_0 e^{-\alpha z}$, where I_0 is the irradiance at $z = 0$. α denotes the absorption coefficient:

$$\alpha = \frac{4\pi n''}{\lambda}, \tag{2.28}$$

that is proportional to the complex part of the refractive index. By measuring the ratio of the incoming and transmitted intensity (I_t) at the position $z = 0$ and $z = h$,one can determine the absorption of a material. With the relation $\alpha h = \ln(I_0/I_\mathrm{t})$ and equation 2.28 the complex part of the refractive index can be obtained.

2.3.2. Mie theory

In 1908, Gustav Mie published a mathematical description for the scattering of light by small gold colloids leading to the well known size depending ruby color of the dilute gold solution [73].

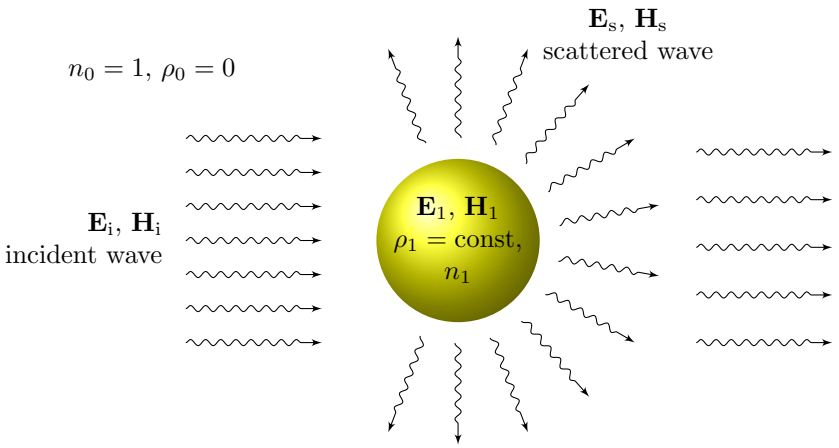

Figure 2.16.: The Mie theory describes the scattering of an electro-magnetic wave from a homogeneous sphere embedded in a non-absorbing homogeneous medium. The fields outside the sphere are the superposition of the incident and the scattered field: $\mathbf{E}_2 = \mathbf{E}_i + \mathbf{E}_s$ and $\mathbf{H}_2 = \mathbf{H}_i + \mathbf{H}_s$.

His assumption for the mathematical description of the scattering process was that the gold particles have an ideal spherical shape. He neglected multi scattering and assumed that the particles are homogeneous and non-magnetic. Although Mie derived the formalism for the diffraction of light from one single spherical particle, it also applies to any number of spheres randomly distributed in a homogenous medium, as long as they all have the same diameter a and a distance between each other, which is considered large compared to their radius. Today, Mie's theory is a description for a variety of scenarios ranging from the mentioned variations of colors of metallic suspensions to the analysis of atmospheric dust, interstellar particles, as well as the formal description of rainbows, clouds, and fogs appearances [71].

The analysis of the data recorded during this work as presented in chapter 4 will show, that a large percentage of the clusters produced during the experiments can be considered spherical with a good approximation. The thickness of the cluster surface is in the order of a monolayer. Compared to a cluster size of 10^6 atoms, or a diameter d of several nanometers, this is rather small and the influence can be neglected. The wavelength of the incident light produced by free-electron lasers is in the order of the diameter of the clusters and it can be considered monochromatically and fully polarized. Therefore, a modeling of the scattering process using Mie's theory is appropriate[c]. In this section Mie's scattering theory is briefly derived following the description given by Bohren and Huffman [70].

For a functional mathematical description of the scatting process a solution has to be found for Maxwells equations describing the scenario depicted in figure 2.16. A plane monochromatic wave is impacting on a spherical surface. Across the surface the properties of the surrounding medium are changing instantly. The incident field causes a field inside the sphere as well as a

[c]The experiments were performed at FLASH and LCLS with a wavelength of $\lambda = 13.5\,\text{nm}$ and $\lambda = 0.8\,\text{nm}$ respectively. As Mie's Theory is a general solution for the scattering process, these variations in wavelength do not make any difference for the mathematical description. However, for the case of $d > \lambda$ Fraunhofer diffraction is sufficient as it will discussed in section 2.3.4.

scattering field surrounding the particle. The fields will be denoted with $\mathbf{E}_\mathrm{i}$, $\mathbf{H}_\mathrm{i}$ for the incident field, $\mathbf{E}_1$, $\mathbf{H}_1$ for the field inside the sphere, and $\mathbf{E}_\mathrm{s}$, $\mathbf{H}_\mathrm{s}$ for the scattered field. Figure 2.16 shows the notations of the different fields. To ensure energy conservation and therefore the absence of sinks or sources of electro-magnetic energy in the particle the fields outside and inside the sphere must be continuous at the surface of the particle. This boundary condition is a critical claim for the mathematical modeling of the problem. Denoting the fields outside the sphere with $\mathbf{E}_2 = \mathbf{E}_\mathrm{i} + \mathbf{E}_\mathrm{s}$ and $\mathbf{H}_2 = \mathbf{H}_\mathrm{i} + \mathbf{H}_\mathrm{s}$ the boundary condition can be expressed as

$$\Big\{\mathbf{E}_2(x=a) - \mathbf{E}_1(x=a)\Big\} \times \hat{\mathbf{n}} = 0, \tag{2.29a}$$

$$\Big\{\mathbf{H}_2(x=a) - \mathbf{H}_1(x=a)\Big\} \times \hat{\mathbf{n}} = 0, \tag{2.29b}$$

where a is the radius of the sphere and $\hat{\mathbf{n}}$ is the outward directed normal vector on the surface. For A being the surface of the particle and the Pointing vector $\mathbf{S} = \mathbf{E} \times \mathbf{H}$ implies:

$$\oint_A \mathbf{S}_1 \cdot \hat{\mathbf{n}} \, \mathrm{d}A = \oint_A \mathbf{S}_2 \cdot \hat{\mathbf{n}} \, \mathrm{d}A.$$

Again, the indices "1" and "2" denote the inside and the outside of the sphere respectively.

In order to simplify the problem, a suitable coordinate system is used for the description of the involved waves which could be a cartesian one for the propagating plain waves. However, as the scattering of a sphere is considered, the scattered wave and the waves inside the sphere are easier to handle in spherical polar coordinates. This is the reason why it is convenient to choose spherical polar coordinates for the description of the scattering process, even though it is more complicated to find a formulation for the plain incident wave. The representation of this wave can be split into components parallel and perpendicular to the scattering plane (see figure 2.17):

$$\mathbf{E}_\mathrm{i} = E_{\parallel\mathrm{i}} \hat{\mathbf{e}}_{\parallel\mathrm{i}} + E_{\perp\mathrm{i}} \hat{\mathbf{e}}_{\perp\mathrm{i}}$$

with $\hat{\mathbf{e}}_{\parallel\mathrm{i}}$ and $\hat{\mathbf{e}}_{\perp\mathrm{i}}$ being the unity vector in the corresponding direction. Analog, the scattered fields can be written as

$$\mathbf{E}_\mathrm{s} = E_{\parallel\mathrm{s}} \hat{\mathbf{e}}_{\parallel\mathrm{s}} + E_{\perp\mathrm{s}} \hat{\mathbf{e}}_{\perp\mathrm{s}}.$$

The orientation of the different unity vectors $\hat{\mathbf{e}}$ is depicted in figure 2.17. Note that the incident and the scattered field are defined relative to a different set of base vectors. The boundary condition connecting the incident and the scattered field is a linear function (see equation 2.29). Therefore, the relation between the incident and the scattering field can be written in matrix form:

$$\begin{pmatrix} E_{\parallel\mathrm{s}} \\ E_{\perp\mathrm{s}} \end{pmatrix} = \frac{e^{i\mathbf{k}(r-z)}}{i\mathbf{k}r} \begin{pmatrix} S_2 & S_3 \\ S_4 & S_1 \end{pmatrix} \begin{pmatrix} E_{\parallel\mathrm{i}} \\ E_{\perp\mathrm{i}} \end{pmatrix}, \tag{2.30}$$

where S_i $(i = 1, \ldots, 4)$ denotes the amplitudes of the so-called scattering matrix. The prefactor in equation 2.30 represents the asymptotic behavior of the scattered wave in the far-field (cf. [74]). For incident light, that is 100% polarized to an arbitrary scattering plain, the scattered light is also fully polarized [70]. Therefore, the matrix elements that correlate parallel and perpendicular part of the scattered wave have to be zero: $S_3 = S_4 = 0$.

Now one has to determine the scattering matrix elements with respect to the scattering angles ϕ and θ. In an experimental setup it is difficult to measure the real and imaginary part of the scattering matrix amplitudes as they depend on the amplitude and the phase of the light

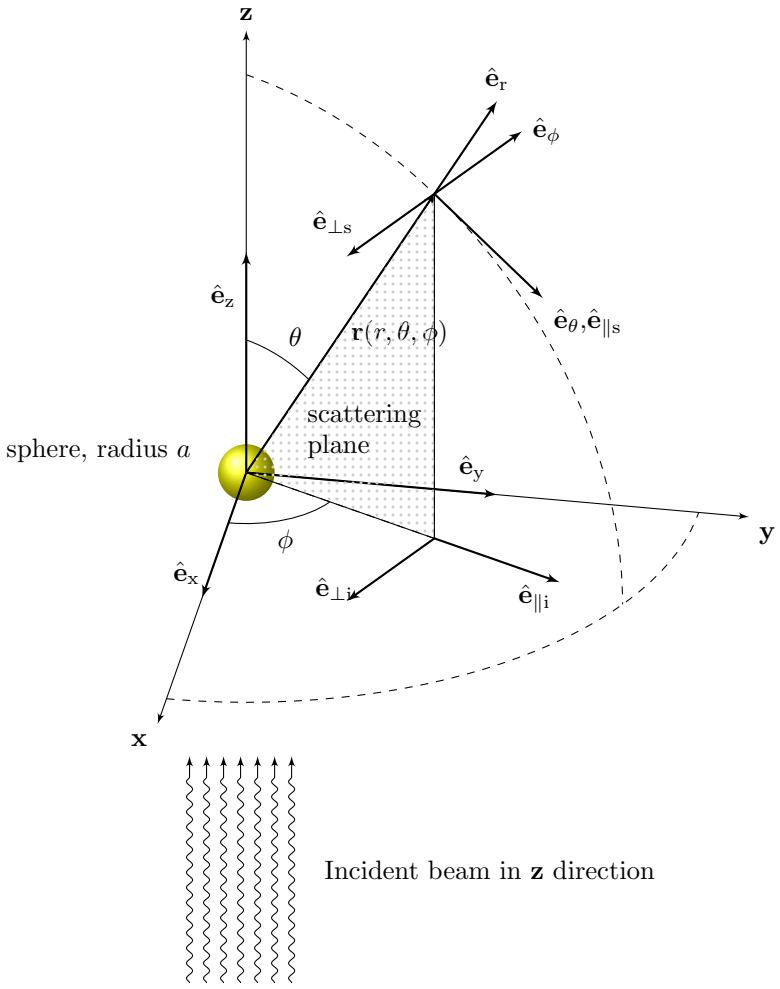

Figure 2.17.: Spherical polar coordinates and unit vectors for the incident and scattered wave. The direction of the incident beam defines the $\hat{\mathbf{e}}_\mathrm{z}$ direction. Scattering occurs in direction of $\mathbf{r}$ defining the scatting plane. In the origin O a sphere with the radius a is centered. Adapted from [70].

scattered in all directions for two incident orthogonal states of the incident light. The intensity for the scattering light with respect to a scattering plane with $\phi =$ constant reads:

$$I_{\parallel\mathrm{s}}(\theta) = \frac{1}{\mathbf{k}^2 r^2} |S_2(\theta)|^2 \, I_{\parallel\mathrm{i}}, \tag{2.31a}$$

$$I_{\perp\mathrm{s}}(\theta) = \frac{1}{\mathbf{k}^2 r^2} |S_1(\theta)|^2 \, I_{\perp\mathrm{i}}, \tag{2.31b}$$

The determination of S_1 and S_2 is tedious but straightforward and presented in detail in the literature [70]. The task is, to find a solution for the Maxwell equations for the incoming, the scattering, and the field inside the sphere which satisfy the boundary condition (2.29). One solution is a scalar wave equation ($\nabla^2\psi + k^2\psi = 0$). In order to solve this equation in spherical polar coordinates the ansatz of separating the variables by using a combination of spherical Bessel function and Henkel functions can be used. This is analog to the solution of the Schrödinger equation for the hydrogen atom. One ends up with the following expression for the diagonal

elements of the scattering matrix:

$$S_1 = \sum_n \frac{2n+1}{n(n+1)} (a_n \pi_n + b_n \tau_n), \tag{2.32a}$$

$$S_2 = \sum_n \frac{2n+1}{n(n+1)} (a_n \tau_n + b_n \pi_n). \tag{2.32b}$$

Here a_n and b_n represent the scattering coefficients obtained from the boundary condition. With the definition of a size parameter $x = k\,a = 2\pi N a/\lambda$, the introduction of the relative refracting index $m = N_1/N_0$ and the Riccati-Bessel function ψ_n and ξ_n of degree n the scattering parameters read:

$$a_n = \frac{m\,\psi_n(mx)\psi_n'(x) - \psi_n(x)\psi_n'(mx)}{m\,\psi_n(mx)\xi_n'(x) - \xi_n(x)\psi_n'(mx)}, \tag{2.33a}$$

$$b_n = \frac{\psi_n(mx)\psi_n'(x) - m\,\psi_n(x)\psi_n'(mx)}{\psi_n(mx)\xi_n'(x) - m\,\xi_n(x)\psi_n'(mx)}. \tag{2.33b}$$

π_n and τ_n are angle-dependent functions

$$\pi_n = \frac{P_n}{\sin\theta}, \qquad \tau_n = \frac{\mathrm{d}P_n}{\mathrm{d}\theta}, \tag{2.34}$$

with the associated Legendre function P_n (degree n). A plot of the first five orders of the angular functions π_n and τ_n is given in figure 2.18 for $n = 1, \ldots, 5$. The larger the scattering sphere becomes compared to the wavelength of the incident light, the higher orders of n must be taken into account. The angular characteristic of the scattered wave is represented by the superposition of π_n and τ_n. Beginning with $n = 3$, the symmetry of the angular functions is broken and the loop in forward direction becomes narrower. This represents the transition from Rayleigh scattering (dipole characteristic) to Mie scattering (forward directed).

2.3.3. Fraunhofer diffraction and Airy pattern

With the Mie theory a tool for the mathematical description of light scattering processes by spheres (or, in this case: clusters) has been introduced on the previous pages. However, if the distance between scattering source and the detector plane is quite large in comparison to the wavelength (far field) and the cluster is considerable smaller then the wavelength, the interaction is described well by Fraunhofer diffraction. In terms of a cluster, which has a diameter in the nm regime, illuminated with the light from the LCLS operating in the hard x-ray regime with Å-wavelength, and observed with detectors at a distance of several centimeters, the requirements for Fraunhofer diffraction are fulfilled. In the following, Fraunhofer diffraction for a sphere will be introduced as it has been used for the analysis of scattering data obtained at the LCLS facility. This is a simplified two dimensional approach suitable for the determination of the cluster size based on the scattering patterns. However, no information about the optical properties of the scattering clusters can be revealed using this method because the refractive index of the clusters is not included in this model.

The starting point for the Mie theory were the Maxwell equations and the simplification of the wave equation $\nabla^2\psi + k^2\psi = 0$, which has to be fulfilled for all fields involved in the scattering process. The wave equation is also the starting point for the derivation of Fraunhofer diffraction, which is described in-depth in [71]. Again, the task is to find a value for the scalar

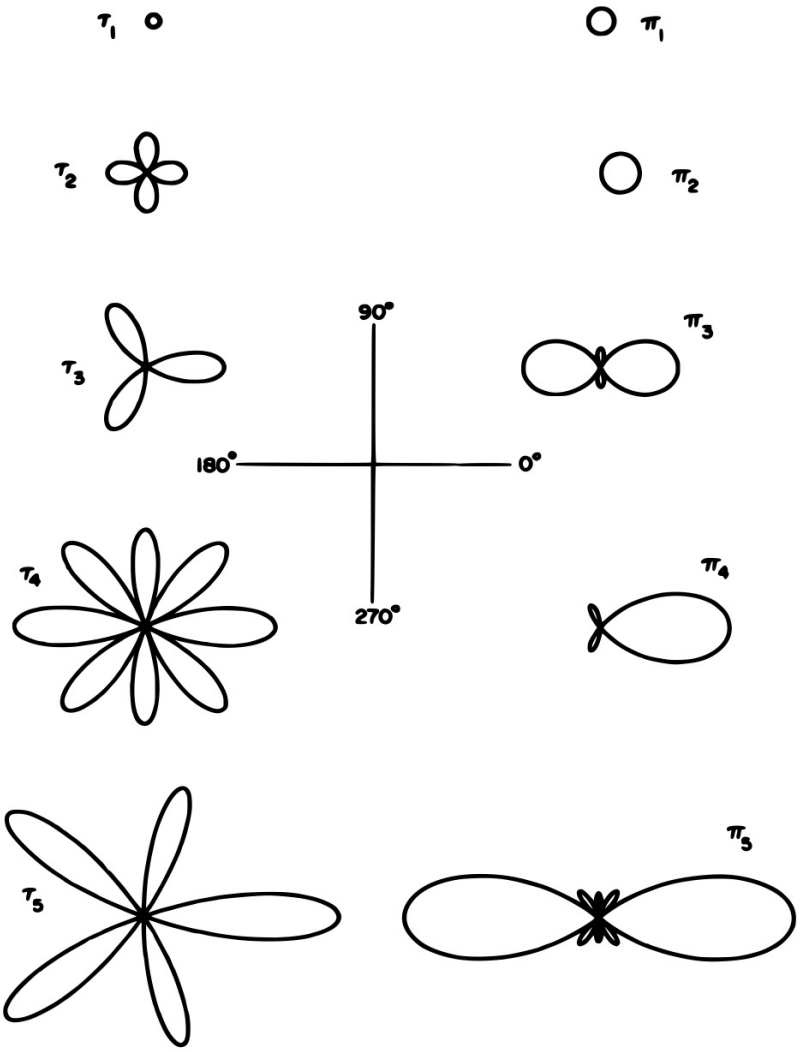

Figure 2.18.: Polar plots for the first five modes of the angle-dependent functions π_n and τ_n. All functions are plotted in the same scale. See Text for explanations. [70].

wave function ψ at a point P given by ψ and $\nabla\psi$ at a surface S surrounding P. As an ansatz the integral theorem of Helmholtz and Kirchhoff is suitable which reads:

$$\psi(P) = \frac{1}{4\pi} \iint_S \left(\psi \nabla \left(\frac{e^{i\mathrm{k}R}}{R} \right) - \frac{e^{i\mathrm{k}R}}{R} \nabla\psi \right) \mathrm{d}S,$$

with the use of Green's Theorem[d]. In the equation, R is the distance from P to a point on S with the normal vector of S directed inside. Now, the simplifications required for Fraunhofer diffraction can be used to obtain a solution.

Corresponding to Babinet's principle the scattering of a sphere can be seen as the scattering of an aperture with the same shape as a two dimensional simplification of the scattering problem. Therefore, the discussion of the scattering from an aperture, which is denoted with A in the

[d] A surface integral over a surface A is equal to the closed path integral over the border of A [75].

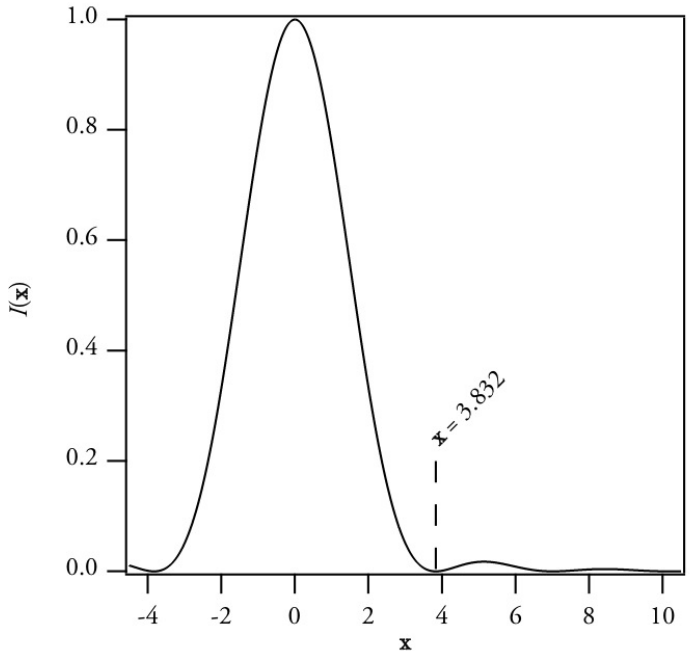

Figure 2.19.: Fraunhofer diffraction at circular aperture ("Airy Pattern"). The graph was calculated using equation 2.35.

following, is sufficient. From a physical point of view, one notices that the only contribution to $\psi(P)$ is due to the aperture A where Kirchhoff's boundary conditions are valid. This means that ψ equates the incident wave function ψ_0 and similar for the divergence of ψ and ψ_0. With that condition the Fresnel-Kirchhoff diffraction formula is established:

$$\psi(P) = -\frac{Ai}{2\lambda} \iint_A \frac{e^{i\mathrm{k}R}}{R} \big(\cos\theta - \cos\theta_0 \big) \, \mathrm{d}S.$$

Here, θ_0 is the angle of the incident wave with respect to the normal of the aperture and θ is the scattering angle.

Considering the detection of the scattered light in the far-field, it can be assumed that $\mathrm{k}R \gg 1$. Here, R denotes the distance of the point P to the aperture. For every point $P(x, y)$ and a point on the aperture with the coordinates ξ, η the following expression for R is found:

$$R^2 = r^2 - 2(x\xi + y\eta) + \xi^2 + \eta^2,$$

where r is the distance between the center of the aperture and P. Because the aperture is small compared to the distance r, the expression for R can be expanded as a power series of ξ/r and η/r. If $a^2/(R\lambda) \ll 1$, higher orders of the series can be neglected which results in Fraunhofer diffraction[e] [71]. For the derivation of Fraunhofer diffraction in the case of a circular aperture, polar coordinates (ρ, ϕ) are appropriate: $\rho\cos\phi = \xi$ and $\rho\sin\phi = \eta$. With the integral representation of the Bessel function $J_n(\mathbf{x})$ the Fraunhofer diffraction pattern from a circular aperture is described by [76]

$$I(\mathbf{x}) = \psi(\mathbf{x})^2 = I_0 \cdot \left(\frac{2J_1(\mathbf{x})}{\mathbf{x}} \right)^2, \tag{2.35}$$

[e] If higher orders have to be taken into account one speaks of Fresnel diffraction.

where $\mathbf{x}$ denotes the coordinates on a screen placed at P.

A visualization of function 2.35 is shown in figure 2.19. On a two dimensional detector a diffraction pattern comparable to the one shown in the picture would appear, characterized by a bright region in the center together with concentrical rings. This pattern is called "Airy pattern" named after G. Airy who found the first theoretical explanation of this diffraction phenomenon in 1835 [77]. To quantify the size of the Airy pattern the position of the first minima is used. The roots of equation 2.35, e.g. the minima in the diffraction pattern, are at $\mathbf{x} = ka \sin\theta$. Here a is the radius of the diffracting aperture and $k = 2\pi/\lambda$ is the wavenumber. For the first root of $I(\mathbf{x}) = 0$ one obtains $\mathbf{x} \approx 3.832$. Therefore, the correlation between the size of the diffraction object (the size of the aperture respectively) and the root of the intensity function is:

$$\sin\theta = 3.832\,\frac{1}{ka} = \frac{3.832}{\pi}\frac{\lambda}{2a} = 1.220\,\frac{\lambda}{d},$$

with the diameter of the diffraction object d and the wavelength λ of the incident beam. For a detector placed at a distance $R \gg d$ from the diffraction object and detecting small scattering angles θ this expression becomes

$$\theta = 1.22\,R\,\frac{\lambda}{d}. \tag{2.36}$$

With equation 2.36 a simple and straightforward solution for determining the size of a cluster from the scattering pattern is established.

2.3.4. Cluster size determination using Mie scattering and Fraunhofer diffraction

Depending on the experimental conditions, such as FEL wavelength and average cluster size, a rather simple approach like Fraunhofer diffraction will be a sufficient approximation for the description of the scattering process. Of course, if changes in the optical properties of the scattering object are the subject of the investigation, only the Mie theory can give any insights which shows them as changes of the refractive index that is a part of the theory. In contrast to that, an analysis biased on Airy patterns can be processed match faster for a large dataset, because it is based on the simple formula 2.36. The experiments presented in this work were performed at two different experimental facilities, operating in two different wavelength regimes: FLASH and LCLS. For the scattering pattern resulting from the LCLS experiments Fraunhofer diffraction was used, while a comparison based on a Mie theory-simulation was applied for FLASH data. This section will compare both methods in order to illustrate the reasoning behind the choice of the theoretical modeling approach used in the analysis.

The scattering angle θ, at which a minimum in the scattering pattern occurs, depends on the size of the scattering object and the wavelength of the scattered light. This statement is only true for Fraunhofer diffraction. For Mie scatting things are more complex and the positions of the minima are also influenced by the relative refractive index of the scattering sphere to the surrounding medium. Figure 2.20 on page 37 shows how the presence of a metallic sphere interacts with the field lines of the Pointing vector of the incident light. Because of the interaction between the sphere and the incident light wave at resonance, the effective scattering cross section is about a factor of four greater compared to the geometric cross section. The dashed line on the left-hand side of the figure visualizes the relative cross section. As a result the cluster would appear larger in the scattering image.

For a better illustration, the scattering patterns from two spheres are compared in fig-

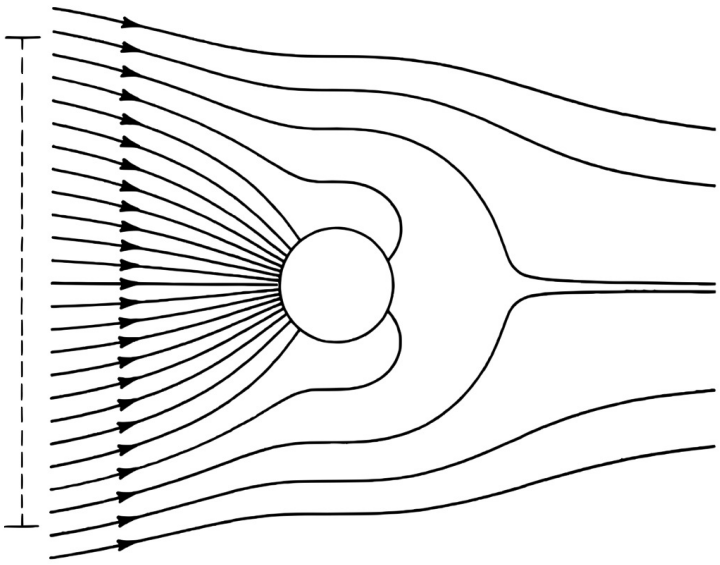

Figure 2.20.: Field lines of the Pointing vector of an incident field surrounding an aluminum sphere. The field is disturbed by the sphere, the field lines are facing the surface. As a result, the sphere appears larger. The dashed line shows the effective cross section for interaction. [70]

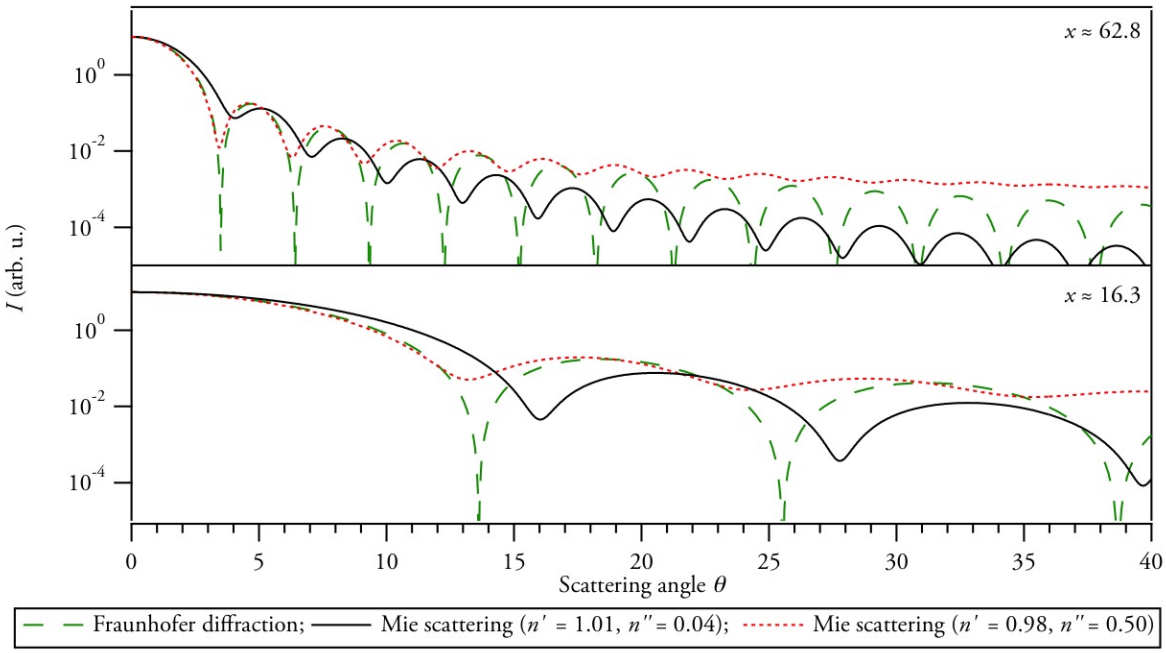

Figure 2.21.: Comparison between calculated Fraunhofer diffraction pattern and Mie scattering ($I_\perp(\theta)$) pattern. The simulation shows two spherical objects with different radii (135 nm equates $x \approx 62.8$ and 35 nm equates $x \approx 16.3$). The wavelength is $\lambda = 13.5$ nm (91.8 eV). The Mie calculation was performed for a neutral xenon sphere (refractive index $n = 1.01 + i \cdot 0.04$ [72]), as well as for a cluster with a refractive index of $n' = 0.98$, $n'' = 0.50$ which was observed during scattering experiments [18].

ure 2.21, which were calculated using Fraunhofer diffraction and Mie scattering, respectively. The calculations were performed for two xenon clusters of 35 nm and 135 nm radius with the refractive index of $n = 1.01 + i \cdot 0.04$ [72] for that wavelength. The wavelength was assumed to be $\lambda = 13.5\,\text{nm}$ (91.8 eV), which is the common wavelength used during the experiments at FLASH. In this figure 2.21 the size parameter

$$x = ka = \frac{2\pi N' a}{\lambda}$$

is used to characterize the ratio of the scattering objects diameter to the wavelength. $N' = 1$ is the refractive index of the surrounding medium. In addition, this figure shows calculations for a xenon sphere with a refractive index of $n' = 0.98$, $n'' = 0.50$. This refractive index was evaluated experimentally from scattering experiments at FLASH, where single clusters were hit with highly intense FEL pulses resulting in highly charged spheres [18].

Smaller clusters exhibit scattering patterns showing minima of the scattering angle θ at larger angles compared to the scattering patterns of bigger clusters and vice versa. Now, from the position of the first minimum the size of the scattering object should be determined. The Fraunhofer diffraction-based calculation with a size parameter of $x = 16.3$ imply a bigger cluster compared to the cluster size that is obtained from Mie simulation (both simulated using the same size parameter x). But this is only true for simulations using the refractive index of neutral solid xenon ($n = 1.01 + i \cdot 0.04$). When it comes to simulation of an "exited state" using Mie theory, the cross section of the scattering object becomes bigger, as shown in figure 2.20, and the sphere appears larger then it is in reality. The "term exited" state in this context denotes an increase in the absorption of the particle as it is described in [18]. For the "excited state" the position of the first minimum is shifted towards smaller scattering angles. Considering the size parameter for larger clusters ($x = 62.8$) as it is shown in figure 2.21, the tendency is the same. However, the differences between Fraunhofer diffraction and Mie scattering for neutral clusters and "exited state" are much smaller.

This behavior can be understood as follows. The neutral xenon cluster appears transparent to some degree and the cross-section drops. As a result, it appears smaller in the scattering profiles. For highly charged spheres, or at resonances, the cross-section for the scattering appears larger than the clusters' geometric diameters, as it is shown in figure 2.20. These states of the scattering sphere are only taken into account in the context of Mie theory. However, for scattering objects with $x \gg 1$ the influence of material properties is rather small. With regard to size determination of clusters this means that from scattering patterns, which were recorded at FLASH, Mie theory is used because this treats the changing material constants correctly. For measurements performed at LCLS Fraunhofer diffraction gives reasonable results because of the much shorter wavelength and hence the grater value of x.

3. Experimental aspects

This chapter describes experimental aspects of scattering experiments in the VUV and x-ray regime. The sections 3.1 is focused on the background and functionality of free-electron lasers. In section 3.2 the experimental equipment used for the study of the cluster-light interaction is described. Here, insights into experimental details are presented as well as improvements in scattering technique compared to previous experiments [78, 17, 18] are highlighted. Finally section 3.3 presents the description of the software development for data analysis and data acquisition.

3.1. Free-electron lasers (FEL)

The basic principle of the generation of electro-magnetic (EM) radiation in free-electron lasers (FEL) is the oscillation of relativistic electrons in a magnetic structure (undulator). The term "free-electron" implies that the electrons are not bound to atoms as in conventional lasers, e.g. solid state or gas lasers. Free-electron lasers were developed from synchrotrons, which are a widely used source for short wavelength radiation as an analytical tool in chemistry, biology, material science, and physics for several decades. With the development of FELs for short wavelengths a new regime for the interaction of light and matter has emerged. These FELs combine extreme intensities and high photon energies exceeding the peak brilliance[a] of synchrotrons by several orders of magnitude [9]. A comparison of the peak brilliance of several synchrotron and FEL facilities can be found in figure 3.1.

Table 3.1 summarizes the basic properties of the "Freie Elektronen Laser in Hamburg" (FLASH) [9] operating in the VUV regime at $\sim 90\,\mathrm{eV}$ photon energy and the Linac Coherent Light Source (LCLS) in Stanford [79] providing x-ray radiation (1.5 keV to 2.0 keV). The light from both light sources was used during the studies of the cluster light interaction.

[a] photons per (second mrad^2 mm^2 0.1% bandwidth)

		FLASH	LCLS
Charge/bunch	nC	0.5–1	0.25
Electron energy	GeV	1	3.5–15
Wavelength	Å	470–60	22–1.5
photon energy	eV	26–207	0.5k–8.2k
Photons/puls	10^{12}	1	10–20
Pulse duration (FWHM)	fs	10–100	70–500
Repetition rate	Hz	5	30
Reference		[9]	[79]

Table 3.1.: Comparison of several features of FLASH (version from 2008) and LCLS (2010) facility.

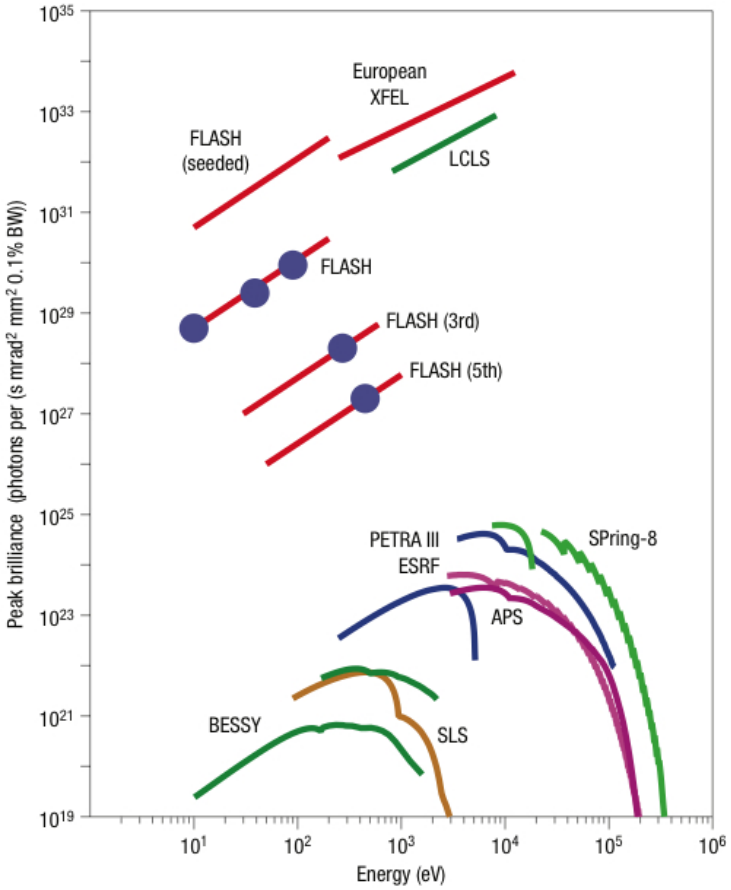

Figure 3.1.: Peak brilliance of different third generation synchrotron light sources in comparison with peak brilliance of FELs (FLASH, LCLS, planned XFEL). The blue spots show measurements of the FLASH FEL at DESY. [9]

In this section the basic principle of the generation of EM-radiation from relativistic electrons followed by an overview of the special design aspects used in FELs is discussed.

3.1.1. Electro-magnetic radiation from relativistic electrons

First synchrotron radiation sources were primarily high-energy physics facilities. The electromagnetic radiation emitted from charged particle orbiting though the bending magnets was considered to be energy leakage in the first place. A second generation of synchrotron radiation facilities was explicitly built to use the emitted radiation as a light source used for experiments. With the improvement of storage rings, retaining a huge amount of electrons for hours, quasi continuous radiation sources became feasible with radiation wavelengths from visual light to the x-ray regime.

By including straight sections equipped with so-called undulators or wigglers, the third generation of synchrotron radiation laboratories was introduced, for example the European Synchrotron Radiation Facility ESRF in Grenoble or the Advanced Light Source ALS in Berkeley. These facilities had a much higher brilliance compared to previous ones. Figure 3.2 shows a comparison of synchrotron radiation sources of the first and third generation together with schematic spectra of the emitted light.

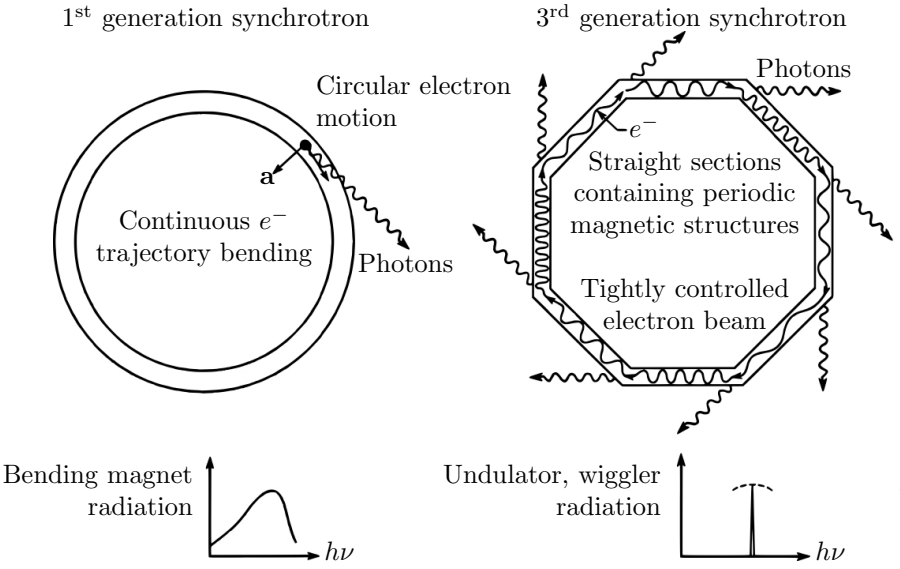

Figure 3.2.: First and third generations of synchrotron facilities. In the first generation, electrons conducting a circular motion emit a broad spectrum of radiation. By inserting straight sections with undulators (or wigglers) into the electron path the generated radiation can be optimized in terms of spectral brightness (3rd generation).[80]

The essential parts of a third generation synchrotron are the undulators or wigglers used for the generation of the electro-magnetic radiation. Figure 3.3 shows the physical principle of an undulator (or wiggler) used in a synchrotron. At this point, both expressions can be used synonymously. Later in this section the difference between wiggler and undulator will be discussed.

The undulator consists of a periodically alternating magnetic structure (grey and white boxes in the upper left corner of figure 3.3) with a periodicity of λ_u. A relativistic particle (consider electrons in this case) with charge e^- and a relativistic gamma factor $\gamma \equiv 1/\sqrt{(1-\beta^2)}$, where $\beta = v/c$, is entering the undulator[b]. The Lorentz force caused by the undulators' magnetic structure forces the electron to oscillate perpendicular to its path through the undulator. Due to the oscillation, the charge emits electro-magnetic radiation like a Hertzian dipole.

For an observer in the fixed coordinate system of the laboratory, the emission characteristics of the electro-magnetic radiation are straightened strongly in forward direction. This can be understood when considering the relativistic velocity of the charge (electron). In the coordinate system of the relativistic electron O' the periodicity of the undulator λ_u is contracted due to the speed of the electron: $\lambda'_u = \lambda_u/\gamma$. In O' the electron emits isotropic electro-magnetic radiation as it is shown in figure 3.3 on the lower right-hand side.

For an observer in the coordinate system of the laboratory O the emitted dipole radiation is again Lorentz contracted. The shape of the Hertzian dipole is becoming highly asymmetric with most of its radiation emitted in forward direction. The angle of the emitted radiation scales with $\theta = (\gamma^*\sqrt{N})^{-1}$. Here, N is the number of undulator periods. For the wavelength of the

[b] In this section γ is used to denote the relativistic factor being widely used in literature. It should not be confused with adiabatic index in the last sections which is also denoted γ for historical reasons.

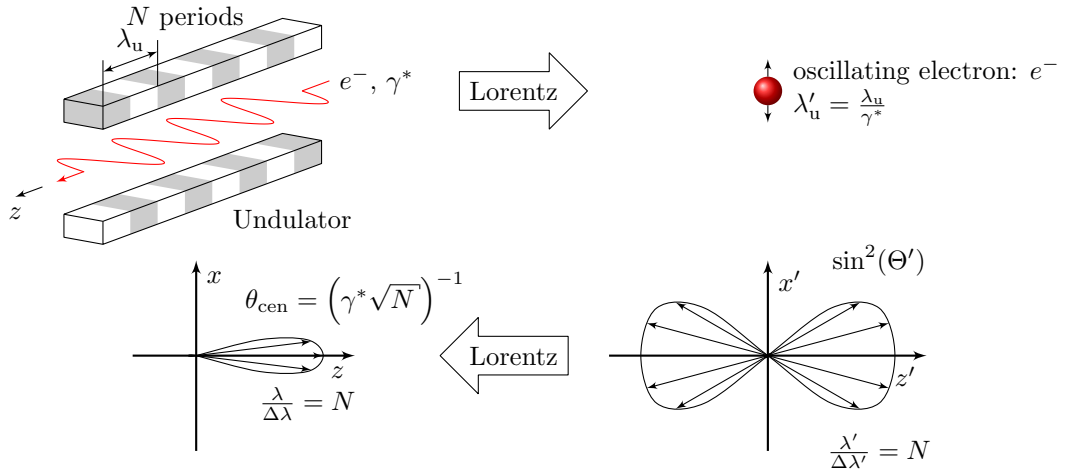

Figure 3.3.: Light emission characteristic for a relativistic electron in an undulator. In the top left corner the electron is forced on an sinusoidal shaped trajectory through an undulator. Due to its relativistic speed a Lorentz transformation in the electron coordination system O' gives the contracted undulator period λ'_u that is seen by the electron (right-hand side). The emitted em-radiation following Hertzian dipole characteristic in O' has to be transformed back into O the coordination system of the experiment. That leads to a straitened emission characteristic. Adapted from [80]

emitted radiation λ the transformation leads to [81]

$$\lambda = \frac{\lambda_u}{2\gamma^2}\left(1 + \frac{K^2}{2} + \gamma^2\theta^2\right). \tag{3.1}$$

Equation 3.1 is the so called undulator equation, where all parameters concerning the undulator are combined in the undulator parameter K:

$$K = \frac{eB\lambda_u}{2\pi mc} \tag{3.2}$$

with B as the magnetic field of the undulator. For electrons, equation 3.2 can be simplified to $K = 2.934\,\lambda_u B$ with λ_u given in centi meters and B in tesla. From equation 3.1 and 3.2 it can be seen that the wavelength of the emitted light is proportional to the inverse mass of the charged particle. With the aim of creating short wavelength radiation it is therefore beneficial to use electrons for the creation of synchrotron radiation.

The undulator equation 3.1 offers different ways to change the wavelength of the emitted radiation λ. First by changing the undulators magnetic properties, because λ is proportional to K and second, by changing the kinetic energy of the electrons (γ). Although changing the magnetic field of the undulator requires changing the magnetic gap, it is more desirable than γ-tuning. This is because γ-tuning would effect all synchrotron end-stations on a multi-undulator storage ring and not only one desired experimental end-station because the velocity of the electron in the storage ring has to be adjusted.

The difference between an undulator and a wiggler is the characteristic of the emitted radiation. While an undulator produces a sharp spike of radiation, the wavelength spectrum

of a wiggler is much broader. In a wiggler the particles are much more deflected compared to an undulator due to higher magnetic field strength. Therefore, the superposition of the emitted light is less efficient. The K parameter can be used to distinguish between both devices. $K \leq 1$ usually denotes an undulator. The emitted light in forward direction is constructively interfering and the intensity of the emitted light becomes proportional to the square of the undulator periods $I \propto N^2$. $K > 1$ indicates a wiggler, where the emitted radiation does not interfere and the intensity in forward direction is $I \propto N$. See [80] for a detailed discussion of wiggler and undulator radiation.

3.1.2. The design of free-electron lasers

A lot of research has been performed on the development of synchrotron radiation sources, especially in order to improve the storage ring technology and the brilliance of the undulators. The radiation produced in such machines is based on spontaneously emitted radiation of different electrons in the bunch with slightly differing energies. Therefore, the emitted radiation jitters in space and time. As a consequence the radiation power scales linearly with the number of electrons N_e in the bunch. In order to further increase the power and coherence of the radiation the electrons have to be forced to emit EM radiation coherently. This is achieved by compressing the electron bunch until phase-correlated electric and magnetic fields appear. An ideal point-like bunch of electrons in an undulator would lead to a power boost that scales with the number of electrons squared: N_e^2. Although an ideal point-like electron bunch is not realistic due to repulsion of the negative charges, this is the concept of an FEL as demonstrated by Mandy and his team in the 1970s [82, 83].

In order to generate an ideal point-like bunch of electrons, so-called bunch compressors are used. For the compression of the electron bunch two steps are required. First the electrons need to be accelerated by the slope of a radio-frequency field (RF-field). As a result, the charges at the end of the bunch gain more kinetic energy from the field compared to electrons at the head of the bunch, where the acceleration field is weaker. Secondly, the accelerated electrons enter a

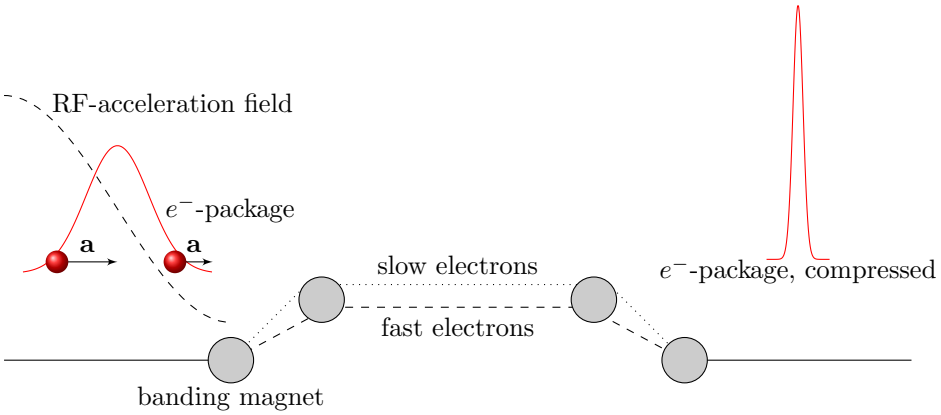

Figure 3.4.: Trajectory of an electron bunch through a bunch compressor. The electrons are accelerated by an RF-field before entering the chicane which consists of four bending magnets. The dashed lines show the path of fast and slow electrons from the beginning and the end of the bunch, respectively. See text for details. Adapted from [84].

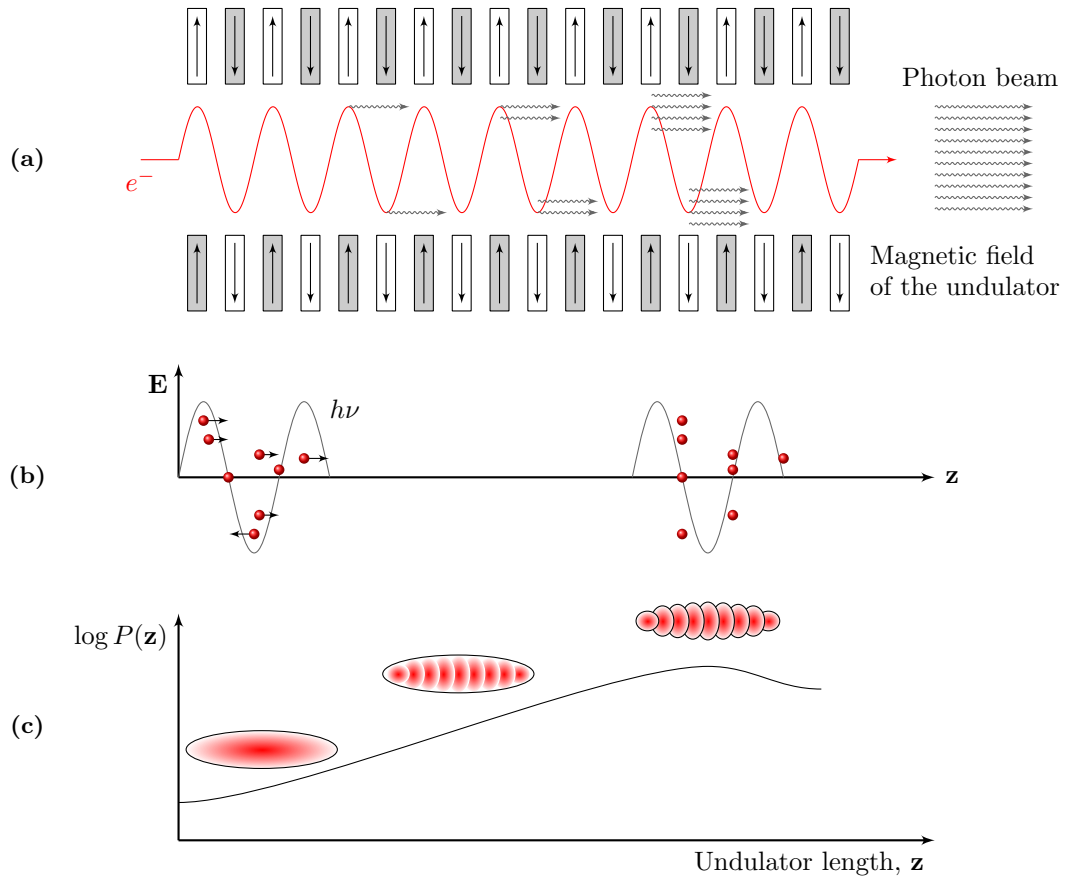

Figure 3.5.: Schematic drawing of micro-bunching in a Self-Amplified-Spontaneous-Emission (SASE) FEL. During the passage through the undulator electro-magnetic radiation is emitted from the electron bunch (a). The electric field of the radiation leads to charge density modulation (b). Here the acceleration of the electrons depending on the phase is shown in the figure. The charge modulation causes the formation of micro bunches (c) leading to an increase in the gained power density with increasing length of the undulator until saturation effects appear. Adapted from [85].

magnetic chicane as it is shown in figure 3.4. Here, slower electrons from the head of the bunch are stronger deflected by the magnets compared to the fast electrons from the tail and hence travel a longer path through the chicane (dotted line). Realigning the fast and slower electrons results in a shortening of the electron bunch. The installation of such bunch compressors prior to the undulator of an FEL leads to a huge increase in the compactness of the electron bunches showing a very narrow velocity distribution. A detailed description of the bunch compressors used at FLASH is found in [84].

Another important aspect for the emission of coherent radiation from an FEL is micro bunching. While the electrons pass the undulator of the FEL an external light field can be injected into the electron beam path in order to interact with the electrons (e.g.: [83]). This concept is widely used for IR and visible light FELs. If the use of an external field is not feasible, shot noise radiation emitted by the electrons bunch itself works too, which is used for FELs operating in the x-ray regime (Self Amplified Spontaneous Emission (SASE) FEL) [80]. The light field causes electrons to accelerate and gain energy from the field or decelerate and contribute energy to the field, depending on the phase between the electrons and the light field.

Inside the long undulator of a high gain FEL the periodic modulation of the kinetic energy of the electrons results in a density modulation of the bunch. This is because faster electrons can catch up with slower ones. The process continues until the density modulation reaches a periodicity of λ. As a result, micro bunches are formed as depicted in figure 3.5c. The formation of the micro bunches leads to the coherent emission of an FEL because each micro bunch can be assumed to emit radiation as a point-like charge with $Q = n_e \cdot e$ and a distance of λ. Due to to micro bunching, more and more electrons are contributing to the lasing process of the FEL, leading to an increase of the power density with the length of the undulator (gain length)[86]:

$$P(z) = P_0 A \exp(z/L_g). \tag{3.3}$$

with L_g being the power gain length. A is the input coupling factor and is equal to 1/9 for a one-dimensional FEL with ideal electron beam in FEL theory. After the formation of micro-bunches a saturation in the emitted power is observed, as no additional electrons for amplification of the bunching process are available. This is the case after a certain undulator length. If saturation is reached, energy from the electro-magnetic field is absorbed by the electron leading to a decrease of the emitted power. This causes a destruction of the micro-bunches, which has to be avoided for maximum power output.

3.2. Experimental setups

After discussing the physics of FELs in the last section, this section describes the two different experimental settings for the recoding of the scattering- and ion spectroscopy data presented in this thesis. The experiments were performed at two different free-electron laser facilities on two different continents. Since both of them, the FLASH in Hamburg and LCLS in Stanford, have their own specific requirements and experimental requirements, two different experimental setups were used. However, the underlying principle of the experiments and the setup in general are similar.

Both setups used pnCCD detectors (see page 49) for the detection of the scattered photons and for time-of-flight mass spectroscopy data a build-in ion detector was used (see page 56). The experimental setup that was used for the experiments at FLASH is presented in the following section 3.2.1. Central components are described in detail in the following subsections. The experiments at LCLS were performed as part of a collaboration with the Max Planck Institute of Nuclear Physics that constructed the experimental chamber. The setup is introduced in section 3.2.2 and details can be found in [87].

3.2.1. Scattering setup for VUV-light

Figure 3.6a on page 46 shows the principle of the scattering experiments. The FEL beam overlaps with a skimmed cluster beam. In the interaction zone only one single cluster is present, which scatters the FEL light. The scattered light is detected using pnCCD detectors.

The "Time resolved imaging of clusters" (TRIC) came into operation at FLASH. For the experiments the in-vacuum part of experimental setup completely redesigned compared to first measurements [78, 17]. The basic concept of the experiment was kept, but several improvements were made that increased the image quality which allowed detection of scattering frames from

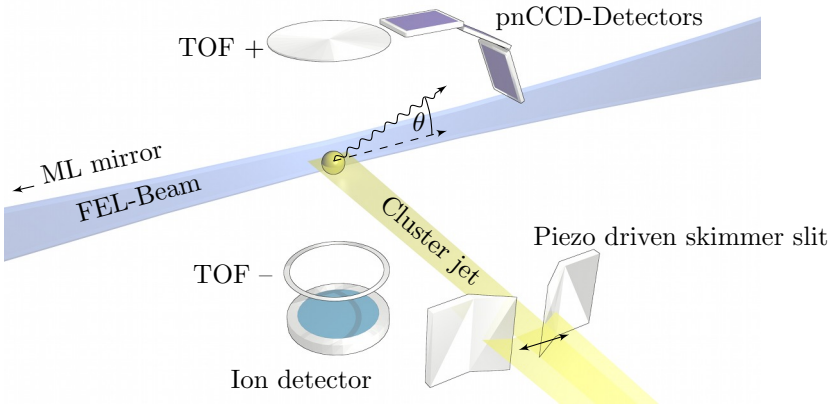

(a)

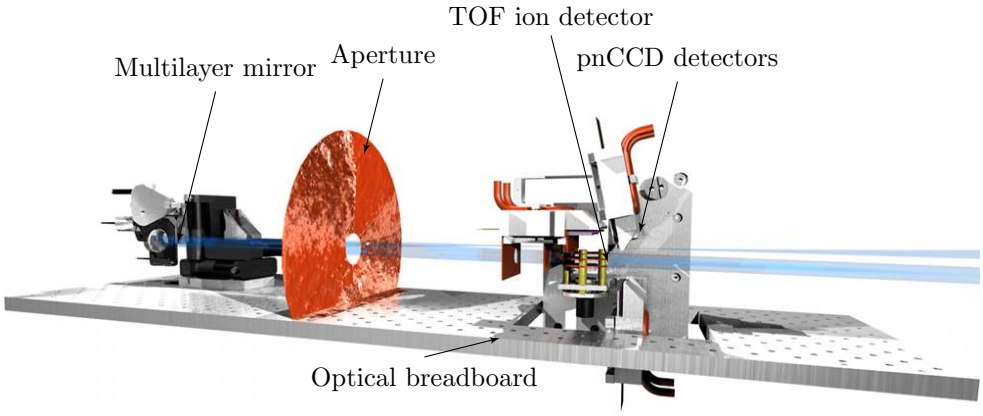

(b)

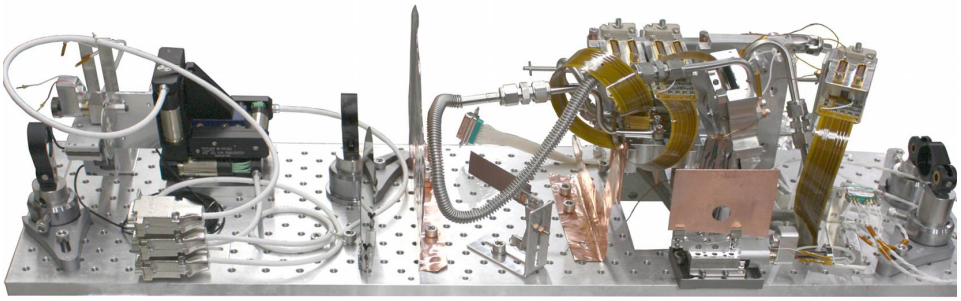

(c)

Figure 3.6.: Experimental setup used at FLASH. (a) Sketch of the interaction region of the experimental setup. pnCCD detectors are used to record scattered photons and a time-of-flight ion spectrometer (TOF) was installed to characterize the peak power in the focal spot. Xenon clusters are prepared by a supersonic expansion and intersect with the FEL beam. A piezo driven skimmer slit controls the width of the cluster beam and therefore the number of clusters in the focal volume. A focussing multilayer mirror (ML) is placed downstream (not shown here). (b) Computer generated image of the experimental setup with refocussing multilayer mirror and breadboard with pnCCD detectors mounted on top. The cluster beam and the piezo skimmer slit are omitted due to clarity. (c) Photograph of the setup with alignment crosses and piezo skimmer slit.

smaller clusters. The original concept of using an optical breadboard as a support for the detector unit was adapted to allow easy access and adjustment to be made to the optical parts outside the vacuum. The breadboard with the vacuum assembly parts is shown in figure 3.6. New to the design are a flexible, motorized mirror mount and a build-in time-of-flight ion detector for the characterization of the focal spot. Both innovations helped with in-vacuum alignment of the setup and optimizing the overlap of the cluster beam and the FEL light pulse, resulting in higher laser power densities at the imaged point. This helps for the detection of smaller clusters. Additionally, the mounts of the pnCCD detectors were redesigned and optimized with regards to their position compared to [78, 17] increasing the number of scattered photons to be detected.

At the FLASH facility the experiments were performed at beamline BL3 with a photon energy of 90 eV ($\lambda = 13.5\,\text{nm}$, pulse energy: $\sim 30\,\mu\text{J}$) [9]. A multilayer mirror was used to focus the FEL-beam on the interaction region, down to $\sim 20\,\mu\text{m}^2$ (FWHM) focal spot size yielding a power density of $P \approx 10^{15}$ W/cm^2. A built-in time-of-flight (TOF) ion detector was used to characterize the focal power density. Mirror mounting system and TOF ion detector are described in the following, corresponding sections.

Xenon clusters were prepared by a supersonic expansion of xenon gas at stagnation pressure ranging from $p_0 = 4.2\,\text{bar}$ to $p_0 = 14.0\,\text{bar}$ and a nozzle temperature of $T = 220\,\text{K}$. This combination of pressure and temperature creates conditions around the xenon vapor pressure curve which means that clusters where formed from the gas phase as well as from the liquid phase of xenon. With these parameters very large clusters could be created. For the expansion a conical nozzle with an equivalent nozzle diameter of $d_{\text{eq}} = 2056\,\mu\text{m}$ ($d = 200\,\mu\text{m}$, $\phi = 4°$ half angle of the cone) was inserted in the cluster source. The clusters travel a distance of 138 mm from the cluster source through a differential pumping stage (1 mm skimmer) to the interaction region, where the cluster beam overlaps with the FEL focus.

Right before the interaction point the cluster beam passed a piezo driven skimmer slit. By narrowing the slit width the number of clusters in the interaction volume was controlled. Since the number of clusters per volume depends on the condensation parameters the width of the slit was varied accordingly from $\sim$300 µm to $\sim$650 µm, assuring that on average only one single cluster was in the focus for every shot. The slit is described in detail on page 56.

The scattered photons were detected using three pnCCD detectors with single photon sensitivity [88]. Three small detectors are used to cover scattering angles from $\theta \approx 10\,°$ to almost $\theta \approx 90\,°$ perpendicular to the FEL polarization (see page 49).

Mirror and mirror mount

Previous experiments [78, 17] showed that an optimized FEL intensity in the focus is crucial for the success of scattering experiments. Therefore, a small focus giving high intensity is ideal for the experiments. At the time the experiments were performed at FLASH the focal length of the beamline mirrors was about 2 m. The focus of the FLASH had a total diameter (FWHM) of 20 µm to 30 µm. If the focus can be considered diffraction limited, a shorter focal length would result in a smaller focus and thereby higher intensities in the focus (cf. [71]). Therefore a mirror with a focal length of 450 mm was used. The mirror is a normal incident mirror with high reflectivity in direction of normal incident FEL light with a narrow bandwidth in reflectivity of $13.6\,\text{nm} \pm 0.1\,\text{nm}$. This is achieved by using a multilayer interference coating, often referred to as reflection coatings or multilayer mirrors [80]. The coating was manufactured by Fraunhofer IOF.

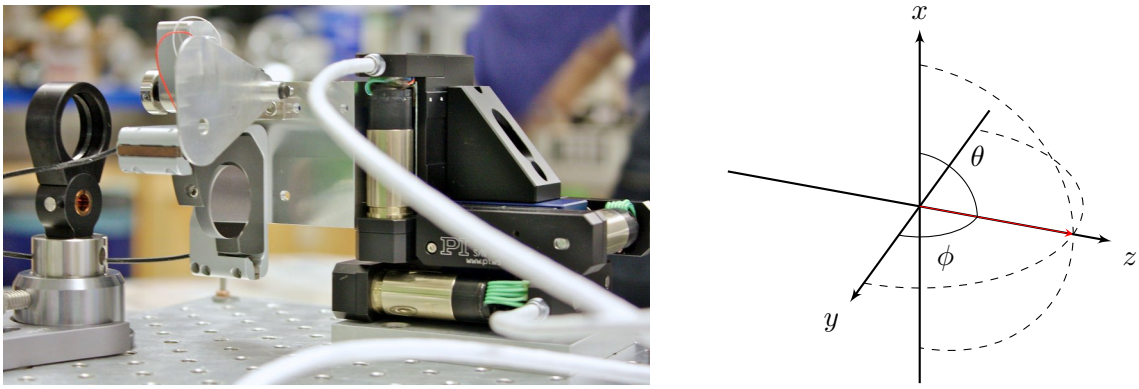

(a) (b)

Figure 3.7.: (a) Multilayer mirror and mirror mount. The mount consists of three PI linear stages and a Newport piezo mirror mount. An aluminum aperture can be moved in front of the mirror to block the incoming beam. The hole in the aperture is used to only let the center FEL beam be reflected by the mirror. (b) Degrees of freedom of the mirror. The mirror can be translated (5 mm in x and y, 25 mm in z direction) and tilted (2° in ϕ and θ direction). z marks the axes of the FEL beam, the red arrow denotes the mirrors normal.

The coating was deposited on a concave substrate of silicon with alternating layers of different reflection indices. Each layer has a thickness of $\lambda/4$, if λ denotes the wavelength of the reflected light (13.5 nm in this case). For wavelengths in the nanometer regime, each layer has a thickness of only several mono-layers. The reflection is in agreement with Bragg's law ($d = \lambda/(2\sin\theta)$) for a periodicity of d equal to the thickness of one bi-layer pair.

The multilayer mirror had a diameter of 25 mm. In figure 3.7a a photo of of the mirror is shown and table 3.2 gives an overview of its specifications. The substrate of the mirror has a diameter of curvature of 900 mm which results in the focal length of 450 mm. The diameter of the focus (FWHM) is about 5 µm. The coating was optimized during manufacturing for the wavelength of the FLASH.

For the adjustment of the focus spot in the interaction region a movable mirror mount was designed. The mount had to be motorized to change the focal position while the vacuum chamber is pumped. Figure 3.7b gives an overview of the degrees of freedom of the mirror. To align the mirror relative to the incident FEL beam three linear stage motors were used. For the movement perpendicular to the incident beam two M-110 compact micro-translation stages (PI) with a travel range of 5 mm were used. To move the focal spot along the beam axis and thus to change and optimize the power density in the interaction region (z-direction) a longer travel range of 25 mm was used that was provided by a M-112 (PI). The step width of the linear stages is at minimum 50 nm. For tilt movements a piezo driven optical mount Agilis AG-M100L (Newport) was used. These compact motors with an adjustment sensitivity of 1 µrad gave high accuracy for the positioning of the focus.

In front of the multilayer mirror an aperture which could be rotated into the beam path was attached. The purpose of this aluminum blade was to block the reflected FEL beam during the alignment of the incident beam. It was coated with fluorescent material to provide visual feedback of the FEL position on the aperture. During the scattering experiments, the aperture was moved out of the beam path.

Wavelength	$\lambda = 13.70\,\text{nm}$
Reflectivity	$R > 60\,\%$
Bandwidth	FWHM $< 0{,}5\,\text{nm}$
Angle of incidence	$\Theta = 0°$
Polarization	s-polarized
Stratification	Substrat / $[\text{Mo/Si}]^{60}$
Coating	Si
Bi-Layer period	$d = (6{,}98 \pm 0{,}01)\,\text{nm}$
Substrate	casted silicon, concave, super polished
Surface accuracy	$\lambda/20$ @ 623,8 nm
Roughness	$\sigma < 0{,}2\,\text{nm}$ rms
Diameter	25,0 mm
Thickness	6,35 mm
Focal length	$f = 450\,\text{mm}$

Table 3.2.: Technical specification of the mirror that was used during the FLASH scattering experiments. The data is taken from the data sheet.

The entire mirror mount was tilted by 1.96° parallel and 1.34° perpendicular to the breadboard, in order to assure that the incident and the reflected FEL beam did not overlap. As the incoming beam had a much wider diameter compared to the reflected one the detectors could therefore be placed closer to the FEL focus. The incident FEL beam produced by FLASH had a diameter of about 14 mm. The reason for tilting the entire mirror mount was to avoid that a movement of the mirror in z direction would move the focus in any other direction.

In order to guide the FEL beam through the vacuum chamber several apertures were used. These were made of copper which helped reduce the amount of straylight that would distract the measuring due to the high absorption of copper at 90 eV photon energy. Using the apertures the position of the focus was defined in x and y direction. The z position of the focus was determined using the built-in time-of-flight ion detector as described on page 56 ff.

pnCCDs and detector mounts

The cluster scattering patterns observed during this these experiments were recorded using pnCCD detectors developed by "Max-Planck-Institut Halbleiterlabor" (MPI HLL) and "PNSensor GmbH". During this work, two generations of the same detectors were used, one kind of pnCCD detectors operated at the FLASH experiment and a new generation used at the LCLS. However, both detectors have the same properties, the only major difference is their form factor[c]. In the beginning of this section, the functionality of the pnCCD detectors is presented, before differences in the form factor are discussed.

In principle, the pnCCD detectors operate similar to a conventional charged-coupled device (CCD). A CCD consists basically of a number of combined pn junctions. Photons generate quasi free electrons at the depleted pn junctions which are formed by applying a voltage on the front- and backside of the CCD. The charges result in an increase in the thermal cutoff current that is leaking through the depleted zone. The electric field of the external voltage accelerates

[c]The term "form factor" in this context refers to the geometry of the detectors and is widely used in the semiconductor industry.

the electrons generating further charges in the bulk material due to impact ionization.

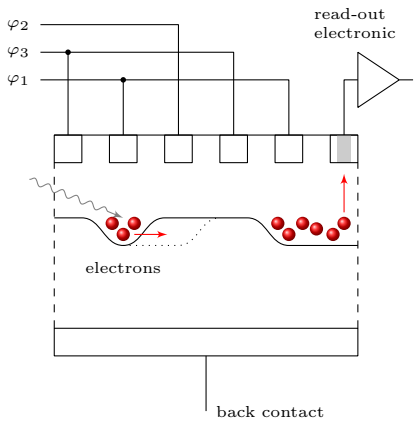

Figure 3.8.: Charge transfer in a CCD.

The electrons are moved to a read-out electronic, using a set of shift registers with their applied voltages $\varphi_{1,2,3}$ (compare figure 3.8). The transportation is realized by applying attractive potentials at neighboring pn junctions (pixels). For example, the photon generated electrons are collected by using a potential applied at φ_1. By applying an attractive potential at the neighboring pixel (φ_2) and slowly rising φ_1 afterwards, electrons are shifted towards the read-out electronic. This process is repeated with φ_2 and φ_3 while φ_1 is used as a potential barrier preventing following electrons from falling into the same potential. The electrons reaching the end of the CCD are amplified and digitized for further processing. This entire procedure is repeated until all charges per pixel row are read-out. The read-out electronic usually digitizes and serializes the produced charges before the recorded data is transmitted and further processed. The described principle is valid and widely used for CCDs operated in the visible light regime. The pnCCD[d] detectors from the MPI HLL are also based on this principle but further improvements were necessary in order to create high performance, fast read-out CCDs that work well in the X-ray regime. These improvements will be presented here and further details can be found in [89].

The design of the pnCCDs is based on the design developed for the XMM-Newton (X-ray multi mirror) space mission of the European Space Agency (ESA) [90]. The XMM-Newton design was upgraded to fit the needs for eROSITA [91] and further improve the quantum efficiency at low and high X-ray energies together with high energy resolution and a fast read-out of the data.

The compact structure of the pnCCDs is shown in the drawing in figure 3.9a. The pnCCD detector consists of 256 × 256 pixels with a side length of 75 µm. Altogether, the X-ray sensitive image area is about 3.7 cm^2 due to a fill factor of 100 %. A frame store area is attached to the image area of the detector. It is used to store the image before it is further processed by the CAMEX[e] read-out electronics. The entire pnCCD chip is fabricated from one single piece of silicon. In order to save space on the substrate the pixel size in the frame store area is reduced to 51 µm × 75 µm. The frame store area is shielded against x-ray radiation in order to ensure the integrity of the captured image. The transfer of the charges that are generated in the image area during an exposure to the frame store area takes about 5 µs. After that, a new image can be acquired while the old one is processed by the CAMEX during the exposure time of the new one. In the lab a frame rate of > 120 frames/s was achieved [89].

The pnCCDs are operated in a fully depleted mode. That means that almost all free charges are removed from the substrate with the help of external electrical fields. This results in a high quantum efficiency in the x-ray regime, as it is shown in figure 3.9b. Here, the dotted line corresponds to the quantum efficiency for an uncoated detector device. The absorption bands of the used materials (SiO_2) are denoted. The quantum efficiency of at least 0.9 in an energy

[d] The CCDs are denoted pnCCD because all components of the detector are build up using pn-junctions.
[e] CMOS (complementary metal oxide semiconductor) multichannel analog multiplexer

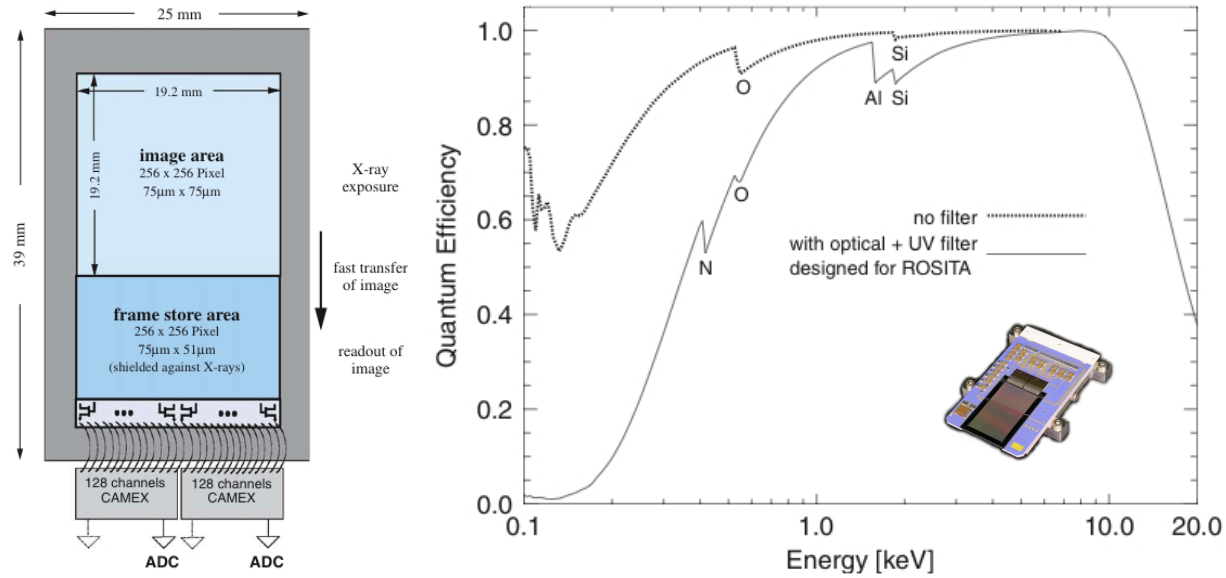

(a) (b)

Figure 3.9.: (a): Schematic drawing of eROSITA pnCCDs that were used during the FLASH experiments. The detector consist of an image and a frame store area together with an on-chip amplifier JFET. (b) shows the quantum efficiency of the pnCCD. The dotted and the solid line represents efficiencies for uncoated and coated detectors, respectively. A coated detector is equipped with an optical und UV-filter in front of the chip as used in the ROSITA space mission. The inlay displays a photography of the detector. [89]

range from 0.4 keV up to 11 keV is remarkable. For the wavelength of the FLASH ($\sim$ 90 eV) the quantum efficiency is still about 0.6. For the eROSITA mission a filter for optical and UV-radiation was applied to the detectors composed of SiO_2, Si_3N_4, and 100 nm homogeneous aluminum layer [92]. The resulting efficiency is depicted by the solid line in figure 3.9b. This filter was not used for the detectors operated at FLASH.

An additional increase in the sensitivity of the detectors is obtained by using backside illumination, as it is shown in the sectional view of the pnCCD detector in figure 3.10 on page 52. The lefthand side shows the image area with the shift registers on top ($\varphi_{1,2,3}$), which are mounted on the front side of the detector. The x-ray photons are entering from the backside and are absorbed in the depleted zone under the shift registers in a depth of 7 µm. Using the shift registers, the charges generated by the photons are transported to the right hand side through the frame store area and to the on-chip read-out anode. Here a monolithic implemented JFET[f] amplifies the signal before it is passed out to a CAMEX input. Each CAMEX chip processes 64 CCD rows in parallel. The signals are further amplified and filtered. Afterwards they are serialized and transferred to a computer using fiber optics.

The energy resolution of the pnCCDs is illustrated in figure 3.11 on page 52, showing an energy resolution measurement. The measurement was performed at FLASH operating at 90 eV photon energy recording cluster scattered photons [87]. The data was recorded in single photon regime, meaning that less then one scattered photon per pixel is detected with the pnCCD. In the detector every scattered 90 eV photon generates about 25 electron-hole pairs. When a photon is absorbed between neighboring pixels the charges are fragmented across these. This was taken into account by recombining those events into one entry for the spectrum 3.11. Also,

[f] junction gate field-effect transistor

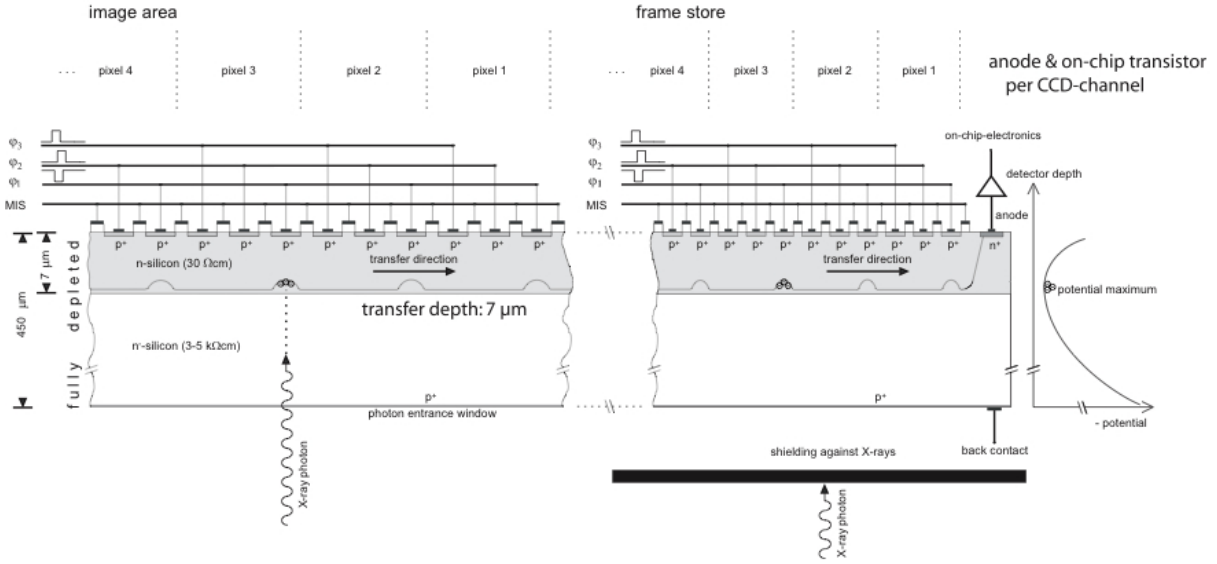

Figure 3.10.: Schematic profile of a pnCCD channel strip. Photon generated charge is stored and transported using shift registers with there applied voltages φ_1, φ_2, φ_3 in a depth of 7 µm below the front side of the pnCCD. The charge transportation is performed from left to right in this picture. The end of the transfer channel is attached to the anode of a JFET for on-chip amplification of the signal [93].

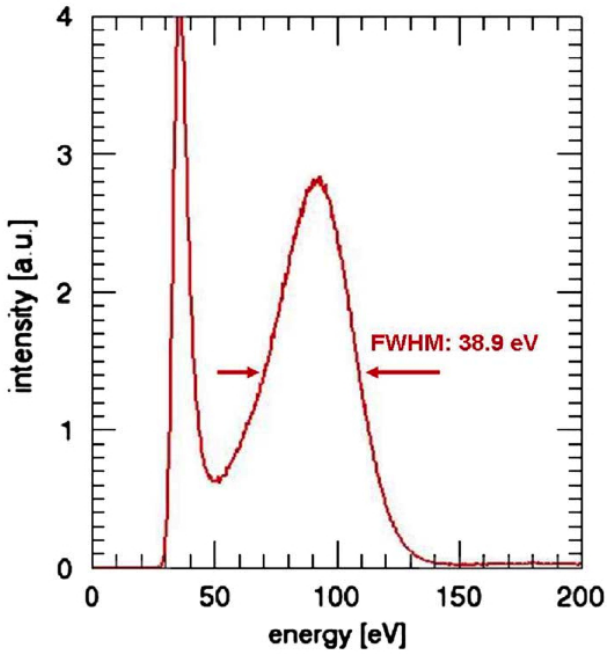

Figure 3.11.: Energy resolution of the pnCCDs measured at FLASH using cluster scattering. [87]

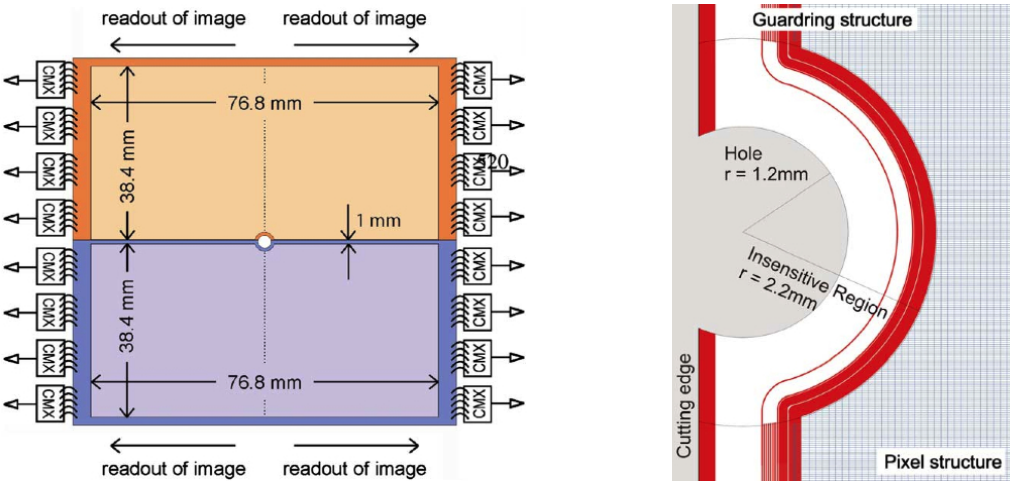

(a) (b)

Figure 3.12.: (a) Schematic layout of the pnCCD detector used during the experiments at LCLS. Each part of the detector consists of two 512×1024 pixels pnCCDs with a pixel size of $75\,\mu m \times 75\,\mu m$. In the center of the wafer a hole (radius: 1.2 mm) is cut with a laser. It is used as an exit hole for the FEL beam. (b): Geometry of the center hole. Red is the guard ring structure. Images from [87].

"pile-up effects" (two photons were absorbed in the same pixel) were removed. The spectrum shows a clearly resolved photon line with a full-width half-maximum (FWHM) of $\Delta E = 38.9\,eV$, which is close to the theoretical limit for a read-out noise of 2.5 electrons (rms). Read-out noise causes the peak at lower energies in the picture. This peak is partly suppressed via threshold discrimination at 28 eV (3σ). Further reduction of the read-out noise is obtained by operating the detectors at low temperatures between 173 K and 193 K. A small contribution of pile-up effects could be seen in a logarithmic spectrum at $\sim 180\,eV$.

For the experiments at LCLS the layout of the detectors was redesigned by the MPI-HLL. The goal was to increase the sensitive area and to move the detector closer to the FEL beam. The layout of the pnCCDs is schematically shown in figure 3.12a. The pnCCD detectors were upscaled to two times 1024×512. Both sections of the pnCCD were fabricated on the same waver that was laser-cut afterwards. The two pnCCD chips are placed above and below the FEL beam to cover a maximum scattering angle. In order to obtain imaging information from small scattering angles a hole was cut in the center of the detectors guiding the FEL beam though the experiment. The hole has a radius of $r = 1.2\,mm$ and is shown in figure 3.12b. It is surrounded by an insensitive region of 1 mm in width before the pixel structure begins. The insensitive area contains a dedicated guard structure, which reduces electric fields between the biased back constancy and the cutting edge of the detector.

Similar to the smaller pnCCDs used at FLASH all data shifting and digitalization is done in parallel. The CAMEX chips are mounted at the left and right side of the photon sensitive area. The charges are transported to the closest chip, as it is shown in figure 3.12a. As the quantum efficiency is similar to the efficiency for the pnCCDs used at FLASH, figure 3.11 is also valid for the redesigned pnCCDs. For the sake of completeness, the figure A.1 in the appendix on page 129 shows the quantum efficiency of the CAMP pnCCDs, when covered with different

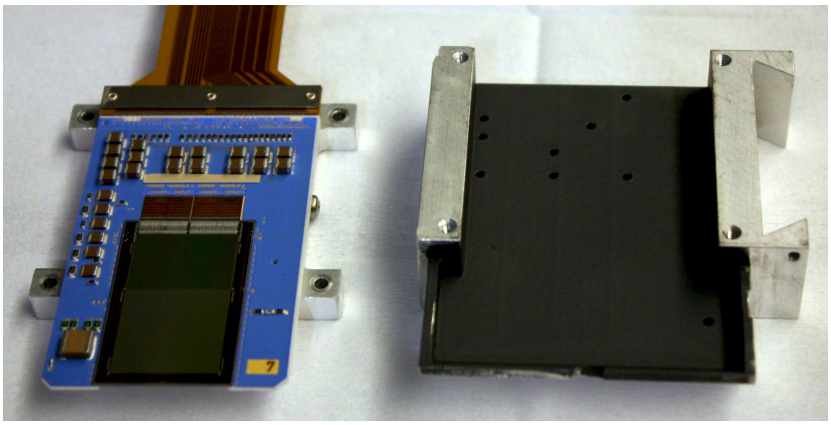

(a)

(b)

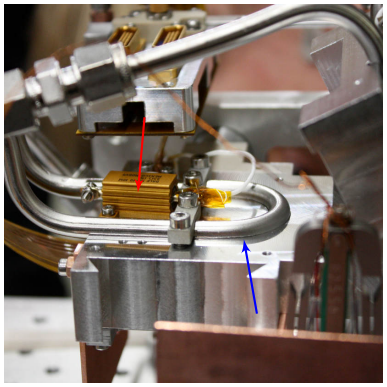

(c)

Figure 3.13.: Mounting of the pnCCD detectors. (a) shows the inside of the mounting cap next to a pnCCD detector. To avoid any straylight photons the inside is covered with graphite. (b) Pivot spindle of the detector mounting. The detector can be rotated around this point by turning the threaded bar for easy adjustment of the pnCCD. (c) shows the cooling and heating capabilities of the mounting cap that was designed for the pnCCD detectors. A pipe filled with cooled nitrogen cooled the detector to 190 K (blue arrow). A heat resistor (red arrow) and a PT1000 (on the tip of the white wire) were attached to control the temperature.

filters.

For the attachment of the pnCCD detectors to the setup special mounts were designed. They had to be stable to avoid vibrations of the detector, but at the some time they had to provide easy and precise alignment of the pnCCDs in the vacuum which is critical for the success of the scattering experiments. Therefore, the mounts had to be flexible and stable. Additionally, the mounts had to provide cooling for the pnCCDs which have to be operated at 190 K ($\sim -80°$C). The mounts provide shielding for detectors against unwanted straylight which pivotal for obtaining a good signal-to-noise ratio.

To fulfill all these design requirements for the detector mounts, they ended up being caps made from solid aluminum. The caps screen the delicate and sensitive top surface of the backside illuminated detectors from nearly all sides. To absorb straylight photons, the interior of the caps was covered with graphite (see figure 3.13a). For the adjustment of the detectors the

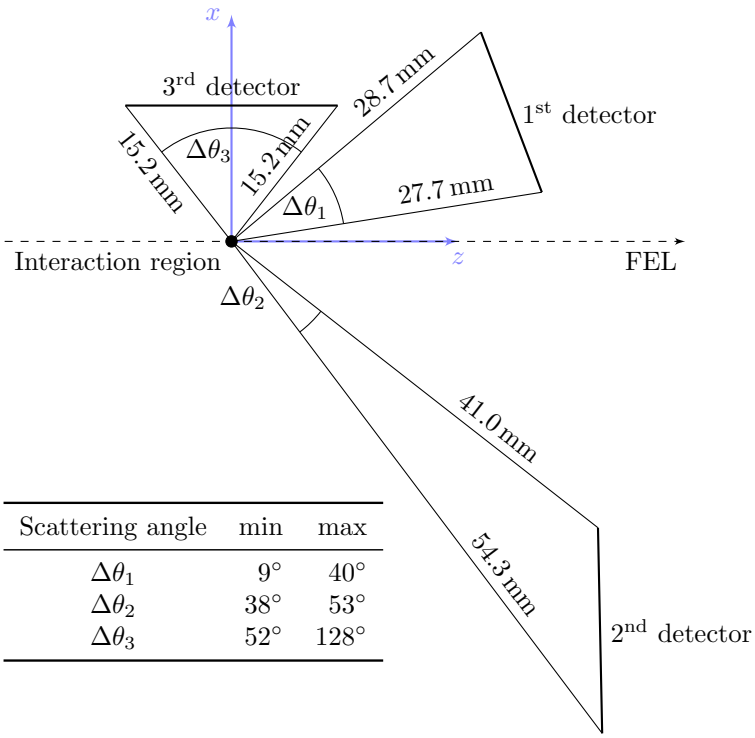

Scattering angle	min	max
$\Delta\theta_1$	9°	40°
$\Delta\theta_2$	38°	53°
$\Delta\theta_3$	52°	128°

Figure 3.14.: Illustration of the detector positions relative to the interaction region. The distances to the interaction region are shown, the table gives an overview over the scattering angles θ covered by the detectors.

mounts could be rotated around a pivot point which gave the required degrees of freedom for the alignment of the detectors on the scattering signal, i.e. in vacuum. This can be seen in figure 3.13b

In operation the pnCCDs produce heat, which needs to be cooled in such a way that the signal noise of the detectors is kept as low as possible. The aluminum caps act as thermal coupling between the heat sink of the pnCCD detectors and tubes filled with cooled nitrogen attached to the top of the caps. The gaseous nitrogen was piped through a dewar flask filled with liquid nitrogen, which cooled the gaseous nitrogen before it entered the pipes on the top of the caps. Besides the cooling pipe on top of the mounts, a heat resistor was attached to control the temperature of the detector. The temperature of the caps could be determined by measuring the resistance of a PT1000 resistor, which was also mounted on top of the detector caps. The temperature controlling mechanism can be seen in figure 3.13c.

The position of the detector mounts was chosen deliberately, so that a huge scattering angle θ perpendicular to the polarization of the FEL beam could be covered. The scattering angles covered by the three pnCCD detectors can be seen in figure 3.14. This figure shows a schematic drawing of the interaction region and the three detectors arranged around it. The scattering angle that could be detected ranges from 9° to 128° measured in relation to the FEL beam. The detectors were mounted with a certain overlap between the recorded scattering angles, in order to recover the recorded scattering pattern for later analysis.

The distance from the pnCCD detectors to the interaction region was minimized in order to compensate the expected low intensity of the scattered light. Although each FEL light pulse consists of $\sim 10^{12}$ photons the amount of scattered photons from a cluster is rather small. Previous experiments showed that the distance between the interaction region and the detectors

has to be as small as possible because then the detectors cover a larger solid angle [78, 17]. This increases the fraction of the recorded scattering pattern helping with the identification and interpretation. In consideration of the dimensions of the pnCCD detectors and the build-in TOF spectrometer the configuration shown in figure 3.14 seems to be the ideal setup.

Built-in time-of-flight ion detector

A well established tool for the detection of charged particles is a time-of-flight (TOF) ion spectrometer. The basic principle of this device is to determine the mass to charge ratio of a particle by accelerating it in a constant electric field and measuring the flight time from a start point to a detector [94]. A TOF spectrometer consists of an accelerator region and a drift region. At a time $t_0 = 0$ the ions[g] with a mass m and and charge q are created, for example, by an incident laser pulse on a neutral cluster target. By applying a voltage potential U the ions are accelerated towards the detector with the velocity $v = \sqrt{2qU/m}$. These ions fly through the field free drift region D before the are detected. The time difference between the creation of the ions and the detection is given by:

$$t_{\mathrm{TOF}} = D/v = \frac{D}{\sqrt{2U}}\sqrt{\frac{m}{q}}\,. \tag{3.4}$$

The accuracy of measurements with a TOF spectrometer depends on the exact evaluation of the field free region D, the precision of the acceleration voltage U and the accuracy of the measured time t_{TOF} as long as the generation time of the ions is very short compared to t_{TOF}. U and D can be determined with high precision, but the position where the ions are generated is rather undefined. Depending on the ion generation position x the ions gain different kinetic energies $qU(x)$. Ions generated further away from the detector traverse a larger acceleration field and therefore gain more kinetic energy compared to ions generated in vicinity of the detector. This results in a dispersion in time and a lower resolution of the recorded signal.

In order to overcome these limitations Wiley and McLaren proposed a modification for the TOF spectrometer, by introducing an acceleration of the ions in two steps [95]. They extended the TOF spectrometer concept by using three potentials ϕ_1, ϕ_2, and $\phi_3 = 0$ at distances a and d, as it is shown in figure 3.15a. This generates two acceleration potentials U_s and U_d with the homogeneous electric fields E_s and E_d, respectively. The flight time for an ion generated at x is given by the total flight times in the different potentials: $T = t_s + t_d + t_D$. The flight times read [94]:

$$x = \frac{1}{2}\frac{q\,E_s}{m}t_s^2 \Rightarrow t_s = \sqrt{\frac{2m\,x}{qE_s}}\,. \tag{3.5}$$

At the end the ions have a velocity of $v_s = \frac{\mathrm{d}x}{\mathrm{d}t} = \frac{qE_s}{m}t_s$. Similary, the velocity at the end of the second acceleration region d is given by:

$$v_d = v_s + \frac{qE_d}{m}t_d = \frac{q}{m}\big(E_s t_s + E_d t_d\big).$$

An integration gives a corresponding solution for the length of the second acceleration region:

$$d = v_s t_d + \frac{1}{2}\frac{qE_d}{m}\big(2t_s t_d + t_d^2\big). \tag{3.6}$$

[g] alternatively a TOF spectrometer can be operated to detect electrons, depending on the applied voltages.

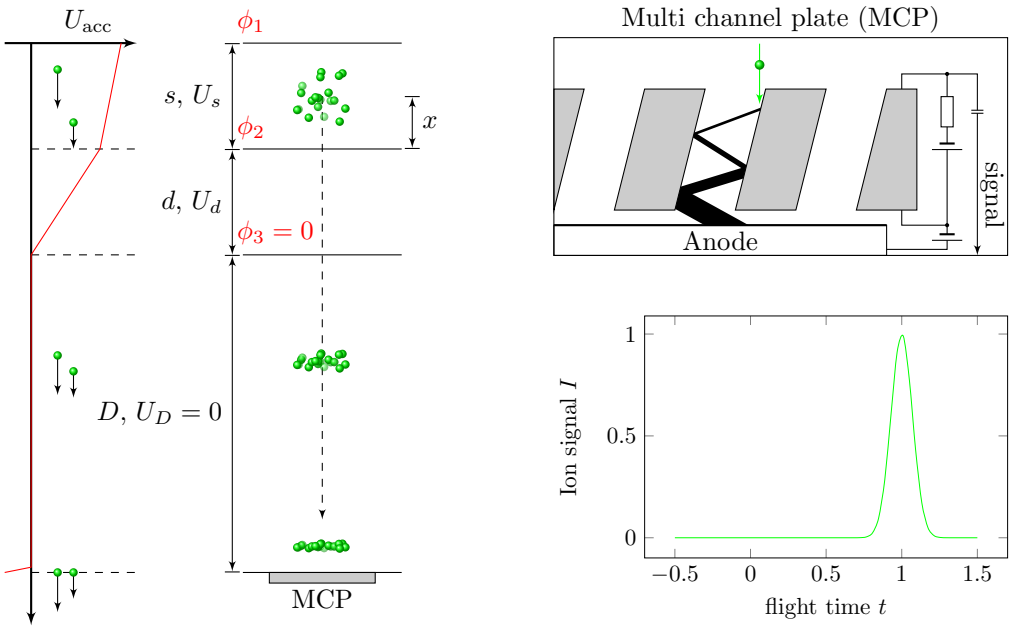

Figure 3.15.: (a) Time-of-flight (TOF) spectrometer with two acceleration regions as proposed by Wikey-McLaren [95]. Appropriate selection of the length of the field free drift region D together with the acceleration voltages U_s and U_d result in a spacial focus of ions on the detector as described in the text. (b) Multichannel plate (MCP) as it is used as ion detector in a TOF spectrometer. Ions generate secondary electrons that are amplified and detected. By plotting the MCP signal versus the flight time (bottom) ions can be identified due to there mass-charge ratio m/q.

The flight time through the field free region D is given by $t_D = D/v_d$. To obtain a total flight time T that is independent of the origin of the ions the following condition must be fulfilled:

$$\frac{\mathrm{d}T}{\mathrm{d}x} = 0. \tag{3.7}$$

With equations 3.5 and 3.6 this condition is fulfilled if the length of the field free drift region is given by

$$D = sk^{3/2}\left(1 - \frac{d}{s}\frac{1}{k+\sqrt{k}}\right)$$

with

$$k = 1 + 2\frac{d}{s}\frac{E_d}{E_s} = 1 + 2\frac{U_d}{U_s}.$$

With a given drift region and the appropriate voltage settings of U_d and U_s the flight time of all ions with the same mass is independent of their generation location x.

A multi channel plate (MCP) is used for the detection of the ions. It consists of a glass plate with various tiny holes, as it is shown in the cross-sectional view in figure 3.15b. The front- and backside of the MCP are metal-coated. The holes are coated with a low ohmic resistance material that features a negative electron affinity. Ions that hit the edge of the holes generate a bunch of secondary electrons, which are accelerated by the applied electrical field between

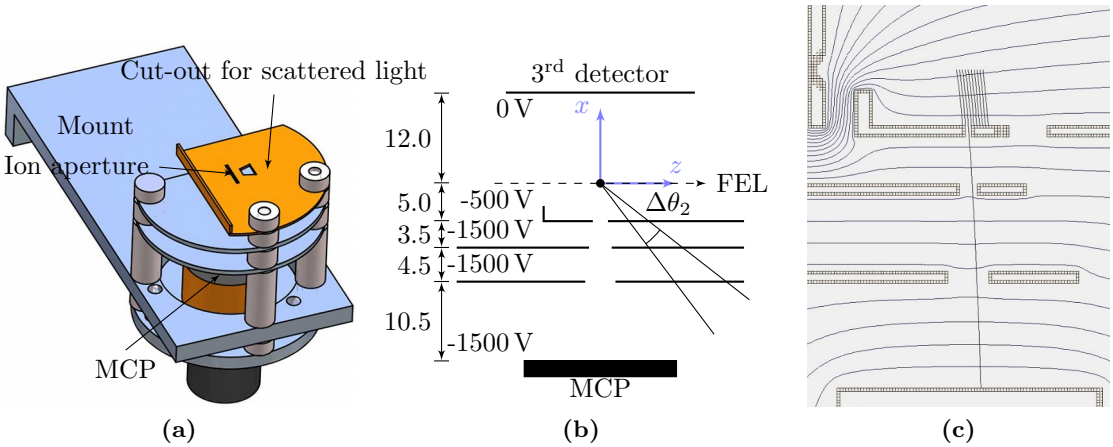

Figure 3.16.: (a) Computer generated image of the built-in TOF ion detector. In order to find the optimal focus position of the FEL focus a slit-like ion aperture was used. Holes were cut into the anodes to avoid blocking of scattered photons. (b) Schematic of the TOF detector with voltage settings for homogenous electrical fields. Dimensions and position of the interaction region can be seen in this draft. To keep the TOF compact, the third detector surface was used as the grounded top anode. Distances are in mm. (c) Simulation of field lines with SIMION. Scanning of the FEL focus spot across the interaction region produces ions at different starting points. The slit ion aperture can only be passed by ions generated in the interaction region. Additionally, the homogeneous potentials of the TOF detector setup are visible.

the front and the backside of the MCP. The electrons generate further electrons due to impact ionization of the walls as it is implied by the picture. Therefore, from one single ion an avalanche of secondary electrons is created that exits the MCP on the back-side and hits an anode where it is detected.

During the experiments the time-of-flight ion detector was used for the characterization of the overlap between the focus of the FEL beam and the cluster beam. The overlap between cluster beam and FEL focus has to be positioned at the interaction region, which was defined during experimental planning and used as a reference for adjusting the setup. The TOF detector was designed to collect only ions that were generated in the interaction region. This was realized by cutting a slit-like aperture with a width of 0.5 mm in the top anode.

To overlap the FEL focus with the interaction region xenon gas was injected into the vacuum chamber via the cluster source. Then the FEL focus was adjusted in z direction through the interaction region by moving the multilayer mirror accordingly. Simultaneously, the ions generated in the interaction region were detected with the TOF spectrometer. The highest charge states (up to Xe^{14+}, see below) indicated an optimized position of the FEL focus in the interaction region.

Because the TOF ion detector was used as an alignment tool its influence on the scattering experiment had to be minimized. In particular, no scattered photons should be blocked by the TOF detector anodes. This is the reason for the compact design of the TOF detector. Its diameters are shown in figure 3.16b. In this picture it can be seen that the TOF detector had no grounded repeller top anode. Instead, the surface of the switched-off third scattering detector ($\Delta\theta_3$ from 52° to 128°) was used as a grounded reference potential. Due to the setup design, the first and the third scattering detector were not blocked by the anodes of the TOF detector

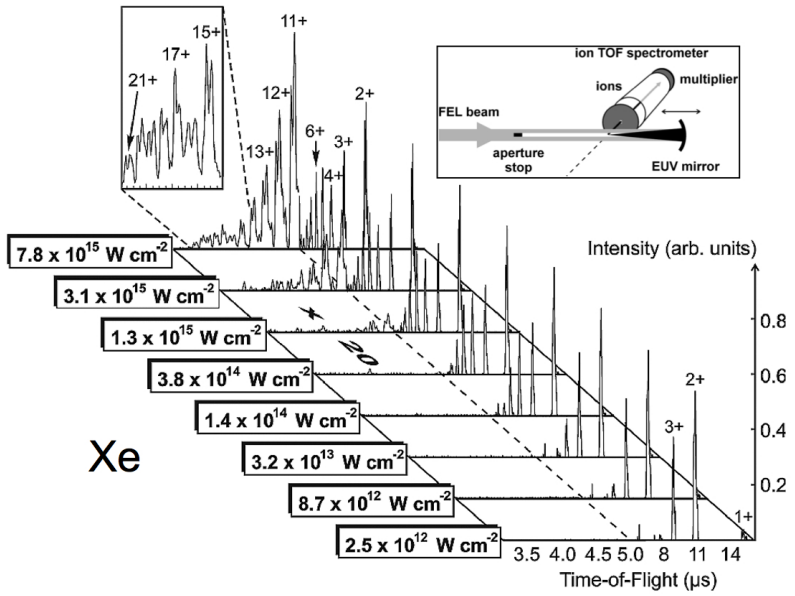

Figure 3.17.: Multistep ionization of xenon atoms at 90 eV photon energy. In the ion spectroscopy data higher charge states appear with increasing laser power density. Charge states on the right hand side of the dashed line can be achieved with linear ionization processes. [96]

(cf. figure 3.14) but the second detector was shadowed. Therefore, cut-outs were made in the TOF detector anodes to avoid blocking the second pnCCD detector. The solid lines in figure 3.16b show the scattering angle $\Delta\theta_2$ recorded with the second pnCCD detector.

Nevertheless, the electrical field had to be sufficiently homogenous to record ions from the interaction region. Especially the copper apertures from the FEL beam, which were close to the TOF detector, could disturb the fields. Therefore, the layout of the TOF detector was simulated using "SIMION" [97]. The result is shown in figure 3.16c. In order to reduce the effect of the copper aperture (upper left corner of the image) the top TOF detector anode was L-shaped, providing much more homogenous electrical fields in the interaction region. The inhomogenity caused by the scattered light holes in the anodes could be minimized by moving the anodes closer together. It has to be mentioned, that the design of the TOF detector was not perfect for the detection of highly charged ions with high kinetic energy. The detection rate for these types of ions is very small compared to singly charged ions with no kinetic energy. This is a consequence of the slit-like ion entrance in the top anode.

The built-in TOF was used to determine the power density in the interaction region by comparing the measured ion distribution to literature, as depicted in figure 3.17 [96]. This reference experiment was performed by Sorokin *et.al.* and showed highly charged xenon ions after interaction with intense FLASH radiation of 13.5 nm wavelength (90 eV) in a very similar experiment using a 300 mm focal length multilayer mirror. In this regime the photon energy matches the giant $4d$ resonance of xenon. With increasing photon energy, more and higher charge states are observable. Up to Xe^{7+} sequential absorption of single photons is sufficient to obtain the charge state, but at $10^{14}\,W/cm^2$ a transition to multi-photon ionization is reached. Charge states up to Xe^{21+} were recored for the highest power densities ($8 \cdot 10^{15}\,W/cm^2$).

Sorokins experiment was repeated with the scattering setup. In figure 3.18 the measured

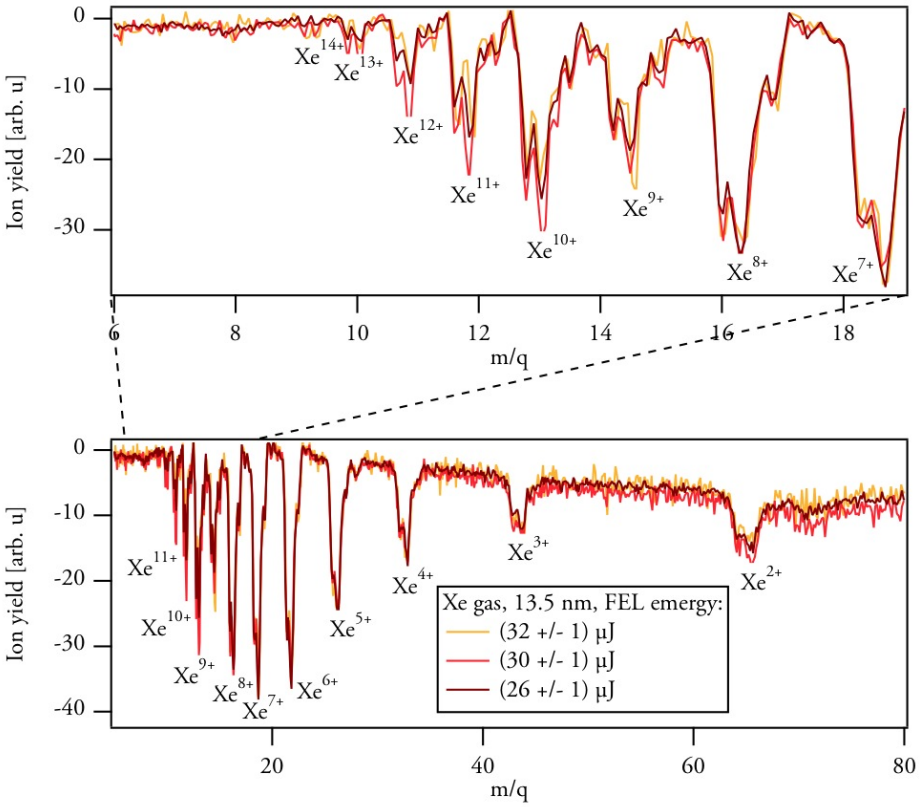

Figure 3.18.: Ion yield measured with built-in time-of-flight spectrometer for different FEL intensities. In the magnification (upper spectrum) charge states up to Xe^{14+} are seen, indicating high power densities of up to $2 \cdot 10^{15}\,W/cm^2$ in the focal spot.

ion spectra are shown for three different FEL energies at 13.5 nm photon wavelength. From the comparison of the highest verified charge states (Xe^{14+}), with the charge states given in [96], a power density of $2 \cdot 10^{15}\,W/cm^2$ in the focal spot could be determined. However, this value can only serve as an approximation. The construction design of the built-in TOF spectrometer with the complicated electrical fields results in a non ideal detection probability for high charged ions. Therefore, the actual power densities in the focus can be assumed higher compared to the measured power densities.

Piezo driven skimmer slit

Measuring scattering patterns from single clusters requires a method to isolate single clusters from the surrounding cluster beam. During previous experiments [18, 78, 17] a technique was developed that allows single cluster scattering. It was shown, that it is sufficient to narrow the cluster jet perpendicular to the FEL beam until statistically less than one cluster per FEL light pulse is in the focus of the beam. While data recorded with no cluster present can be ignored during analysis, the remaining scattering data shows one single cluster with a high probability.

The narrowing of the cluster beam was realized by installing two razor blades within the path of cluster beam. The sharp edges of the blades facing each other were directed towards the cluster source. In order to be able to change the distance between the blades they were mounted

on a piezo driven shutter/slit system PZS 3 manufactured by "Piezosysteme Jena". The PZS 3 device has an opening distance of 1500 µm, which can be closed continuously. The device is based on piezo technology, therefore the resolution is in the nanometer regime. A photograph of the PZS 3 with the attached razor blades is shown in figure 3.19. The whole device is denoted as the "piezo driven skimmer slit".

By applying a voltage between 0 V and 100 V the PZS 3 can be closed depending on the applied voltage. The controller of the PZS 3 gives a reference voltage between 0 V and 10 V. In order to correlate the effective opening distance of the razor blades and the applied voltage, the maximum opening distance and the maximum reference voltage at which no cluster was able to pass the piezo skimmer slit, were measured. By assuming a linear closing behavior of the piezo device the following calibration function was found:

$$d_\mathrm{s} \mathrel{\hat{=}} -0.17\, U_\mathrm{s} + 1.50, \tag{3.8}$$

where d_s is diameter of the piezo skimmer and U_s denotes the reference voltage of the voltage applied to the skimmer. The value for d_s needed to reach single cluster mode depends on the cluster density in the cluster beam. As the density of the clusters in the beam depend on the expansion parameters used for the cluster creation, d_s was determined experimentally for the current expansion parameters.

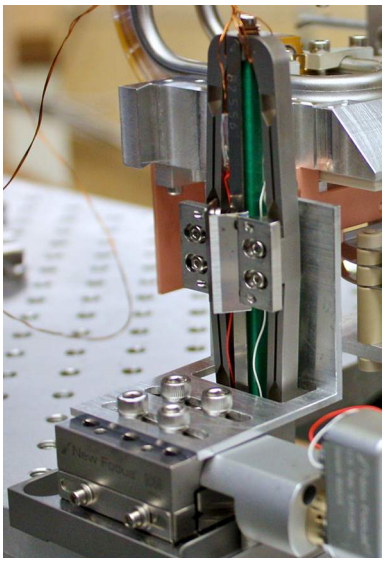

Figure 3.19.: Piezo driven skimmer slit. The slit is mounted on a transition stage and can be moved in z direction.

In order to allow the adjustment of the piezo driven skimmer slit depending on the given cluster source position and the FEL focus it was mounted on a linear motor stage. The stage was motorized for in-vacuum adjustment of the position of the skimmer slit and enabled movement of the slit parallel to the incoming FEL beam.

Cluster source

The clusters were prepared using supersonic expansion of rare gas clusters as discussed in chapter 2.1. For the scattering experiments performed at FLASH and LCLS very large clusters ($N \geqslant 10^6$ atoms) were needed. Therefore, a cooled and pulsed cluster source was used, which was build by Heiko Thomas and is described in detail in [98]. A technical drawing of the cluster source is shown in figure 3.20.

The cluster source is mounted on a CF100 flange with attached x, y, and z manipulator and has a total length of 596 mm. Several feedthroughs are attached at the flange. A gas feedthrough for the experimental gas which is used as a seed for the clusters and two feedthroughs for the cooling fluid. In addition to these, electrical feedthroughs are used for the temperature sensors and the heater of the source.

At the tip of the cluster source the nozzle is attached to an electro-mechanic pulsed valve ("Parker S99"). The magnetic field of a coil pulls a magnetic core with an attached gasket (poppet) away from the nozzle and against a spring. The gas can now pass the valve, expand

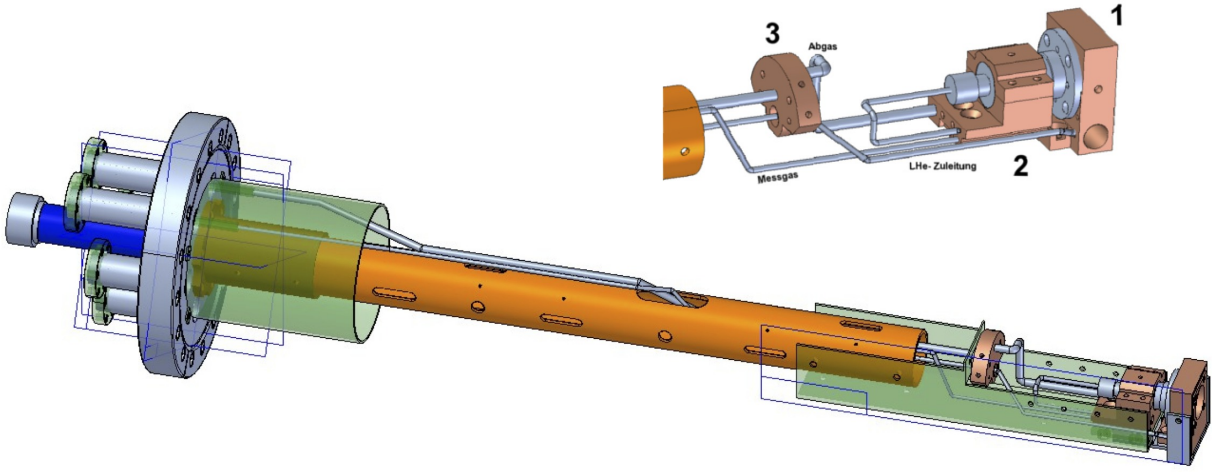

Figure 3.20.: Cluster source used in the experiments. The source is pulsed and can be cooled using liquid nitrogen. The cryostat at the front of the source is shown in the inlay. 1: Heat sink of the nozzle made from solid copper with temperature sensors and heater. 2: Mounting device for the pulsed valve and pre-cooling of the experimental gas. 3. Cooled heat shield. [98]

in the nozzle and form clusters. When the current that induces the magnetic field in the coil is switched of the force that opens the valve drops down. As a result, the magnetic core and the gasket are pushed backed by the spring and the pressure of the gas against the exit of the valve. Thus the valve is sealed again. The opening and closing of the valve was synchronized to the FEL main trigger (5 Hz at FLASH and 10 Hz at LCLS). The opening duration of the valve was set to 5 ms which long was enough for the production of clusters, however saves gas and reduces pumping load.

The cluster source can be cooled down to 5.7 K [98] by using liquid helium as a cooling medium when used for helium and neon clusters. During the presented experiments liquid nitrogen was used for the cooling in order to achieve nozzle temperatures of $\sim$ 200 K for the production of xenon clusters. The cooling medium is pumped through the cluster source and cools the nozzle (1 in figure 3.20). Here the copper block which is attached to the nozzle holder is cooled using evaporation heat. A temperature sensor is attached close to the nozzle in order to measure the nozzle temperature. The outgoing cooling medium is used for pre-cooling of the gas and cooling of the valve (2). Furthermore, a heat shield is cooled to screen the tip of the cluster source from heat radiation (3).

3.2.2. Coincident measurements in the x-ray regime

The experiments at LCLS were performed in the CFEL-ASG[h] Multipurpose (CAMP) chamber, which is presented in detail in reference [87]. The design of CAMP aims to record a complete dataset from one single target, similar to high-energy physics experiments. This dataset includes correlated detection of ions and electrons together with scattered and fluorescent light. Furthermore, CAMP is designed to be a flexible end station for the soft x-ray beamline at LCLS, allowing a large variety of different experiments to be carried out.

The entire CAMP setup is remote-controlled. The traveling range is 50 mm in x and y

[h]Center for Free Electron Laser Science, Advanced Study Group

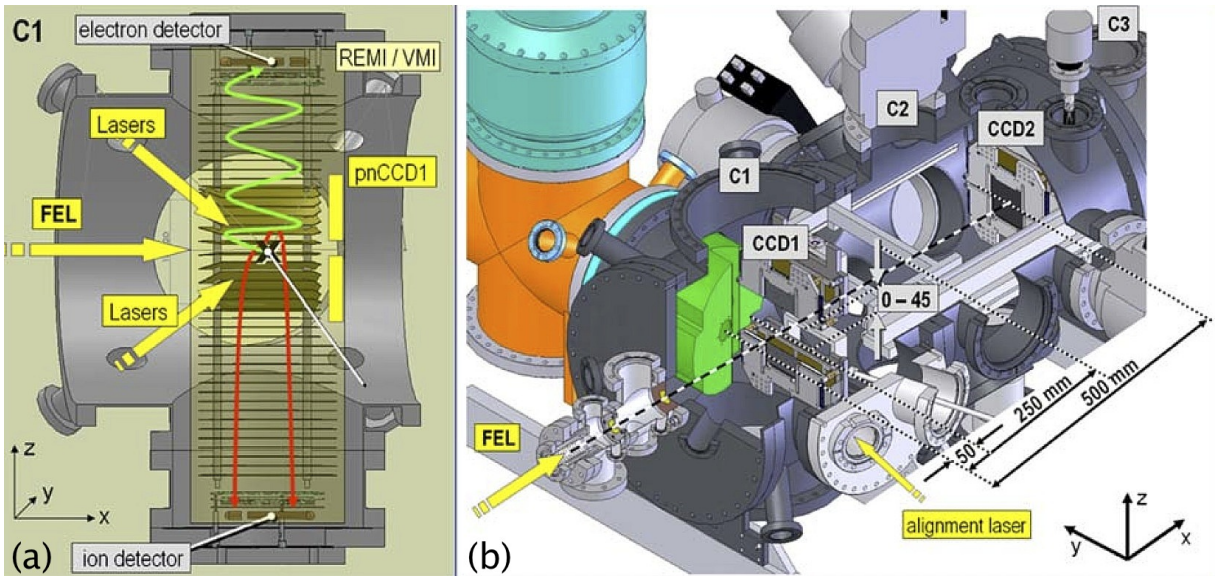

Figure 3.21.: Schematic drawing of the CAMP chamber. In figure (a) CAMPs reaction microscope (REMI) setup is shown. This setup was used as a time-of-flight ion detector. In order to clear the line of sight to the pnCCD detectors, the electrode of the REMI/VMI are conically shaped. In figure (b), the position of the REMI/VMI is denoted with C1 in the draft. The front and back pnCCD detector (CCD1 and CCD2) are mounted in the second part of the CAMP chamber (C2). [87]

direction. Parallel to the FEL beam (z direction) the chamber can move 150 mm. The chamber can be rotated vertically and horizontally by 6°. This allows precise alignment and overlapping of the FEL beam with the target cluster beam.

Figure 3.21 shows the detectors of the CAMP setup. For the detection of charged particles a reaction microscope (REMI) [99] or a velocity map imaging (VMI) [100] system can be installed (figure 3.21a shows the installed REMI). The electrodes of the REMI and the VMI are conically shaped, allowing an unrestricted view into the interaction volume for the pnCCDs. In the figure the cluster beam enters the chamber in y direction, perpendicular to the FEL beam. Additional optical or infrared lasers can be focussed in the interaction volume through the electrodes of the REMI/VMI (optional, not used here). During the experiments presented in this thesis, the VMI was used as a time-of-flight ion detector. The VMI was modified by installing a slit aperture similar to the aperture that was used in the TOF detector used during the FLASH experiments (see page 56 ff).

Figure 3.21b shows the interior of the second vacuum tube attached to the REMI/VMI detector, which contains two large-format pnCCD detectors (See figure 3.12 on page 53) for the detection of scattered light and fluorescence photons. The pnCCDs are two-parted with one part mounted above the FEL beam and one part below. As a beam guide, the detectors contain a half hole in the center as described in section 3.2.1. Both parts are mounted movable to change the distance between the detector parts. Additionally, the first detector set (CCD1) is movable parallel to the FEL beam. The travel distance for this detector is 250 mm with a starting point being 50 mm from the interaction region.

The scattering angles that can be recorded using the CAMP pnCCD detectors are depicted in figure 3.22. The small yellow cluster denotes the interaction region and the green cones indicate the scattered photons, which are detected by CCD1 and CCD2, respectively. By moving CCD1

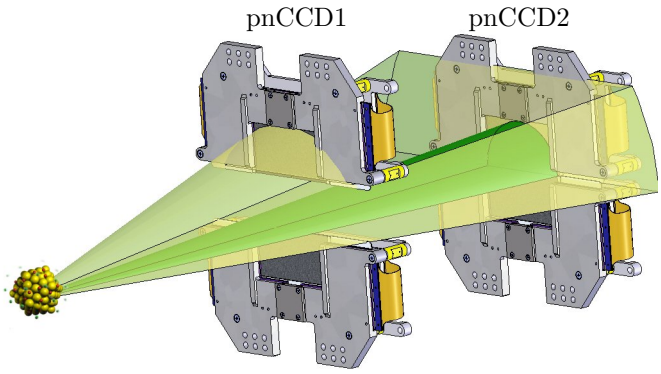

Figure 3.22.: Computer generated image of the scattering angle detected using the CAMP pnCCD detectors. The front detector records scattering photons in large scattering angles while the back detector records small scattering angles. The distance between the pnCCDs can be changed up to 250 mm by moving pnCCD1 along the beam axis. [87]

to the front and opening the detector parts scattered photons at larger scattering angles can be detected. By narrowing the gap between the parts of CCD2 very small scattering angles can be detected, only limited by the diameter of the outgoing FEL beam, which has to pass the hole in the center of CCD1 and CCD2. For the experiments described in this thesis only the second detector was analyzed (CCD2). Therefore, the halves of CCD1 were moved 45 mm away from the beam, allowing the scattered photons to reach CCD2. CCD2 is mounted in a distance of 500 mm to the interaction region as depicted in figure 3.22.

3.3. Data analysis and software development

In the context of this thesis a variety of different programs and routines were developed and used for the analysis of the recorded data. Data acquisition (DAQ) software is used for the controlling and read-out of the pnCCD detectors. Handling the huge data volume generated by the pnCCDs and avoiding data loss is the main challenge for DAQ software. The analysis of the data requires searching of the database for individual cluster hits as well as averaging over particular events. Due to the fact that the data was recorded at different FEL facilities, the developed programs had to fit in both given environments. For example, at LCLS the data acquisition program had to run on the server farm provided by SLAC, while for the experiments at FLASH responsibility for data security and integrity was with the experimentalist themselves.

In the following part the tools and programs that were developed and used for data acquisition and analysis are presented. First, a general view of the data analysis is given, before the corrections and reductions of typical image artifacts and detector errors are discussed. Detailed informations about the workflow and functionality of the analysis tools are provided in section 4.1.1 for the programs used at FLASH and section 4.6.1 for the LCLS tools. This is because the discussion overlaps with the analysis of the data. In this section common parts of the analysis are presented in order to provide the background for the understanding of the upcoming chapter.

This section closes with a description of the data acquisition tool, which was developed based on the experiments gathered during this work. This tool aims to allow novel single cluster scattering experiments at the FLASH facility as performed in [15].

3.3.1. Outline of data analysis

Figure 3.23 shows the general pre-analysis steps that were carried out in order to prepare the data for further analysis. In principle, the experimental procedures at LCLS and FLASH were identical, but the software tools performing the analysis had to be implemented specifically for the measurements.

The working process starts with the recorded raw data, which contains the pnCCD frames saved for every shot of the FEL. In addition, FEL parameters like e.g. pulse energy and wavelength, were collected and correlated with the scattering data. This allows reconstruction of the physical conditions that led to a specific scattering pattern. From this data pool the pnCCD frame data is further processed before it is used in analysis.

The raw frame data readout from the pnCCDs is dominated by the influence of the readout electronic and noise generated from the pnCCD array. The scattered x-ray photons are initially covered by the noise, which has to be removed ("Image correction" in figure 3.23) The different noise types in the frame data are presented and correction techniques are explained in section 3.3.2. The result of the image correction is the so-called "frame data". At this point the scattering patters are visible in the data.

Next, the large amount of recorded data had to be reduced since that can be handled more confortablily. This is done by applying different filters on the data sets, e.g. by filtering for a certain FEL intensity or particular cluster sizes. These filter techniques are described in section 4.1.2. For the experiments performed at LCLS data filtering also included filtering of the recorded time-of-flight ion spectroscopy data, which was also recorded on a shot-to-shot basis in parallel to the scattering data.

Based on the filtered data the frames are analyzed. The results can be found in chapter 4.

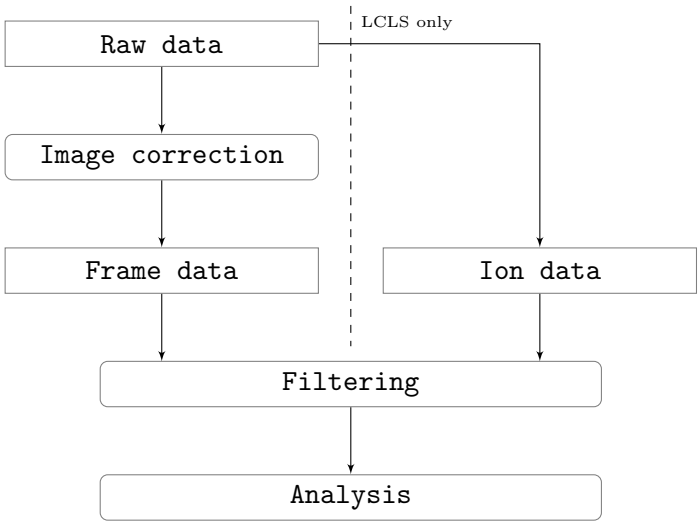

Figure 3.23.: Outline of the data pre-analysis and analysis. The raw data is recorded during the experiments. The first step is the correction of the image data, see section 3.3.2 before the data gets filtered which means removing of data sets with no scattering signal (see section 4.1.2). Corresponding scattering frames and the time-of-flight ion spectra are then prepared for further analysis.

3.3.2. Processing of scattering images

Before analyzing the scattering data collected with the pnCCD detectors, it has to be processed as outlined in the previous section. This step requires the elimination of all detector related unwanted side effects like readout noise, charge transfer effects, and thermal noise. The removal of these effects is descried in this section. The result is a high quality scattering image showing the full potential of the 90% quantum efficiency of the pnCCD detectors. Details on this correction can be found in [101].

The Linux based computer system used for detector readout stores the initial frame from each detector and every FEL shot. Up until this point no corrections are performed on the data, allowing different methods for data correction in the analysis process. The data, (frames) is stored in a binary file format defined by MPI-HLL called FRMS6. In addition to the binary frames data, a file header tracks all detector settings for the offline analysis. An example of a raw image extracted from a FRMS6 file taken at FLASH is shown in figure 3.24a. This example shows a scattering pattern with a rather weak signal caused but a medium sized cluster hit by the wings of the FEL. This image was chosen to emphasize the importance of image processing performed in post analysis. Basically, the entire information visible in figure 3.24a is noise and other unwanted signal. At this point no VUV photons are visible in the frame.

The first step carried out in order to remove noise is subtraction of the so-called "offset map". Leakage current and thermal noise shift the baseline of the signal in each pixel, even for low operation temperatures. Additionally, each readout channel of the detectors has its individually offset. In order to determine these effects, data without any scattered light is recorded as a reference, so-called "dark frames". An average over this data would result in a suitable correction for the data frames. However, cosmic radiation can influence the dark frames by generating a large amount of charges on a small spot (mips) in the frame. These mips stand out very brightly from the rest of the frame and have to be removed before any averaging takes place. Therefore, a threshold M can be defined in order to identify them. The offset map is then calculated according to [101]

$$\overline{v_{x,y}} = \frac{1}{D - 2\,M}\left(\sum_{i \in \text{Frames}} v_{i,x,y} - \sum_{i \in I_{\text{high}}} v_{i,x,y} - \sum_{i \in I_{\text{low}}} v_{i,x,y} \right), \tag{3.9}$$

where $\overline{v_{x,y}}$ is the value for the x-th column in the y-th row. D is number of dark frames and $v_{i,x,y}$ marks the i value of the frame. The factor $2M$ represents the removal of the brightest pixels and, due to symmetry, the removal of the darkest pixels. I_{high} and T_{low} are the frames containing the largest and lowest amount of signal, respectively. The offset map for the image example is shown in figure 3.24b. The variations between the different channels dominating it can be seen from the picture. The offset map is subtracted from the raw image which results in figure 3.24c. Although still only little information is visible in the frame so far, the first scattering photons are visible in the upper part.

The vertical bars in figure 3.24b are due to the parallel readout of the pnCCDs. Any induced noise, such as cross talk, affects the different channels of the pnCCD and leaves the same amount of imprint on all pixels in a row. This "common-mode" can be reduced by performing corrections on a line-to-line basis. First, each row of the frame is searched for the five to ten (user defined) least intense pixels. Their mean value is subtracted from the entire row. Second, a histogram is generated from the frame and a Gaussian fit of the histogram is used to determine its maximum.

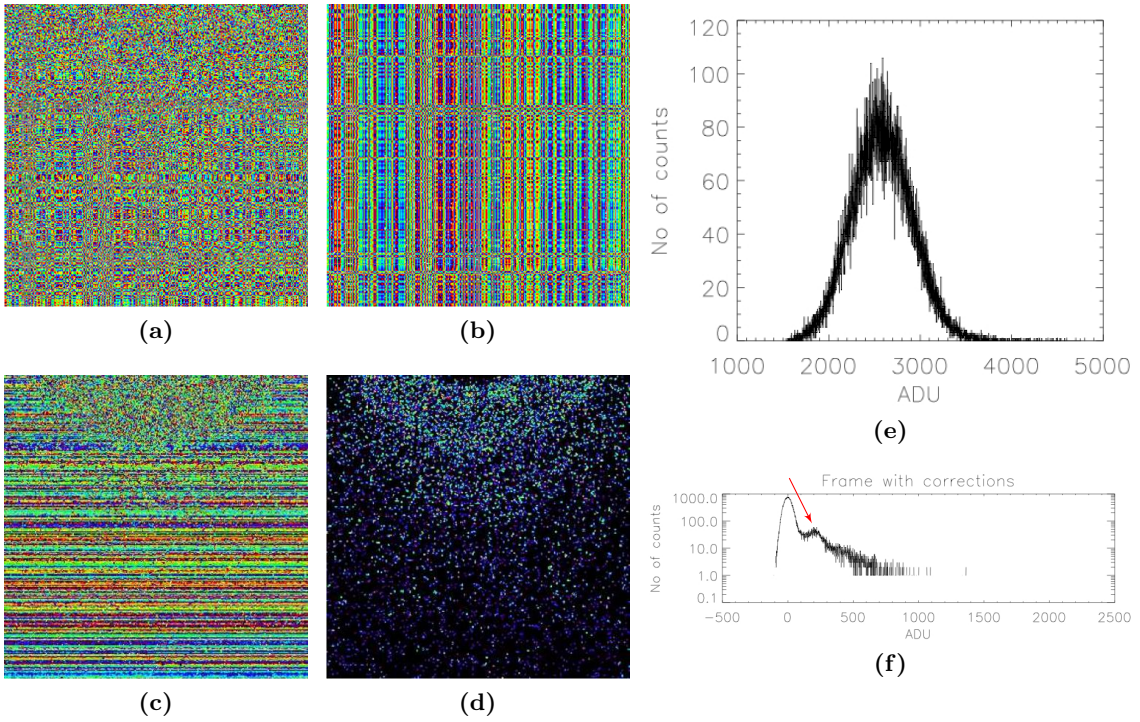

Figure 3.24.: Processing steps for the pnCCD detector images. (a) A raw image as it is read out from the pnCCD detectors. Noise and common-mode cover the desired scattering data. (b) Offset data that is gained from dark images. This is subtracted from the scattering pattern resulting in (c). Here first detected scattering photons are visible (top), however common-mode still disturbs the image. (d) Corrected image with only VUV-photons left. (e) Histogram the raw image shown in (a) plotted versus detector units (ADU). (f) Histogram of the corrected image. The red arrow indicated 90 eV photons which are scattered and detected by the pnCCD. Only photons which contributed to the 90 eV peak in (f) are shown in figure (d).

This maximum is used as the constant offset for the frame and is removed by subtracting it from the pixel values. This method gives satisfying results assuming a sufficient number of pixels per row are "dark", which means that they detected no photons. This assumption is fulfilled for most of the measured scattering patterns.

Since noisy pixels (so called "bad pixels") can spoil the image, these pixels needed to be masked. This exceeds the mean noise of the surrounding pixels which hence are marked and removed from the frame. This is done within the MPI-HLL software. It is also possible to define bad pixels manually in the graphical user interface. However, the appearance of bad pixels in the recorded data is extremely rare and can therefore be neglected for the presented study.

Figure 3.24e shows a histogram of the raw image as it is read-out from the pnCCDs. The axis of abscissas is given in terms of atomic digitizer units (ADU), which are proportional to the amount of charges stored in the pixels. The histogram is dominated by one single peak that is caused by detector noise. In figure 3.24f the histogram of the fully corrected frame is shown. Notice that the histogram is shifted towards lower values of ADU due to the offset calibration and commode-correction. Additionally, more structure is visible in the histogram, e.g. the red arrow marks a peak caused by 90 eV photons scattered from the cluster. By applying a discrete filter around that energy regime, the scattered photons of interest can be further isolated and analyzed. Figure 3.24d shows the corrected sample image ready for further analysis. The only

values appearing in this frame are pixels with values corresponding to ∼90 eV. Therefore, this final figure shows only scattering data.

3.3.3. Data-aquisition software "FoxIT"

The experiments performed at LCLS and FLASH showed that a customized data acquisition software (DAQ) greatly facilitates the data recording process and allows novel experiments. Therefore, the experience gathered during this thesis was used to design and develop a suitable software named FoxIT (**F**emtosecond **O**ptical and **X**-ray **I**maging of clus**T**ers). First successful measurements were performed in Summer 2011 at the FLASH facility. The results can be found in [15].

The aim of these experiments were coincident measurements, which means that different reaction products (scattered photons, charged fragments) originating from one single cluster are detected at the same time. Similar concepts are used in high energy physics. Therefore, the requirements of a DAQ system can be summarized with performance and reliability. Requirements for the performance arise from the amount of data that has to be processed in a given time frame. Processing of the data required combining the datasets obtained from different detectors into one single data point in order to obtain a complete representation of the reaction products. The amount of data to be processed is made up of a CCD image representing the scattering data and data acquired from a time-of-flight (TOF) ion detector. It accumulates to 1.4 MB for the CCD frame (1040 × 1392 pixel with 8-bit resolution) and ∼0.2 MB for the TOF ion detector. This data has to be acquired, processed, and stored before the next data set can be recorded without loosing data. For the FLASH experiments a repetition rate of 10 Hz was required, resulting in moderate 16 MB processed per second. For the reliability of the software it is essential that the performance requirements are fulfilled and no loss of data occurs during the measurements.

The software has to be intuitive, allowing the user to focus on the experiments, e.g., the software has to track edited parameters and apply them automatically when the editing is done. All parameters had to be saved in a configuration text file for easy editing and backup. In order to allow a flexible configuration in a multi-monitor setup non-modal program windows had to be used. This means that a configuration dialog can be opened while other dialogs display the recored data without blocking the user input. In order to give intuitive access to the configuration, tools provided by the software had to be based on established laboratory equipment, e.g., the control interface for digitizers had to be based on conventional oscilloscopes. These requirements are accomplished with the introduction of FoxIT.

For the recording of the ion spectroscopy data an Agilent Acqiris digitizer is used and controlled with FoxIT. A Basler CCD camera (1040 × 1292 pixels) images the scattering pattern in a similar setup as described in [18]. In addition to controlling the instruments FoxIT displays the recorded data providing immediate feedback for the user. The displaying of the camera data is hardware accelerated using OpenGL technology. The user feedback is combined with FEL related data for instance a unique identification number (bunch ID) for every electron bunch producing an FEL pulse and control data for a femto-second laser provided by DESY. All the different data sources are combined into one single file for later analysis.

In order to ensure sufficient performance of the software, it was developed in C++ with extensive use of the Qt4.7 framework [102]. A major increase in performance could be achieved by

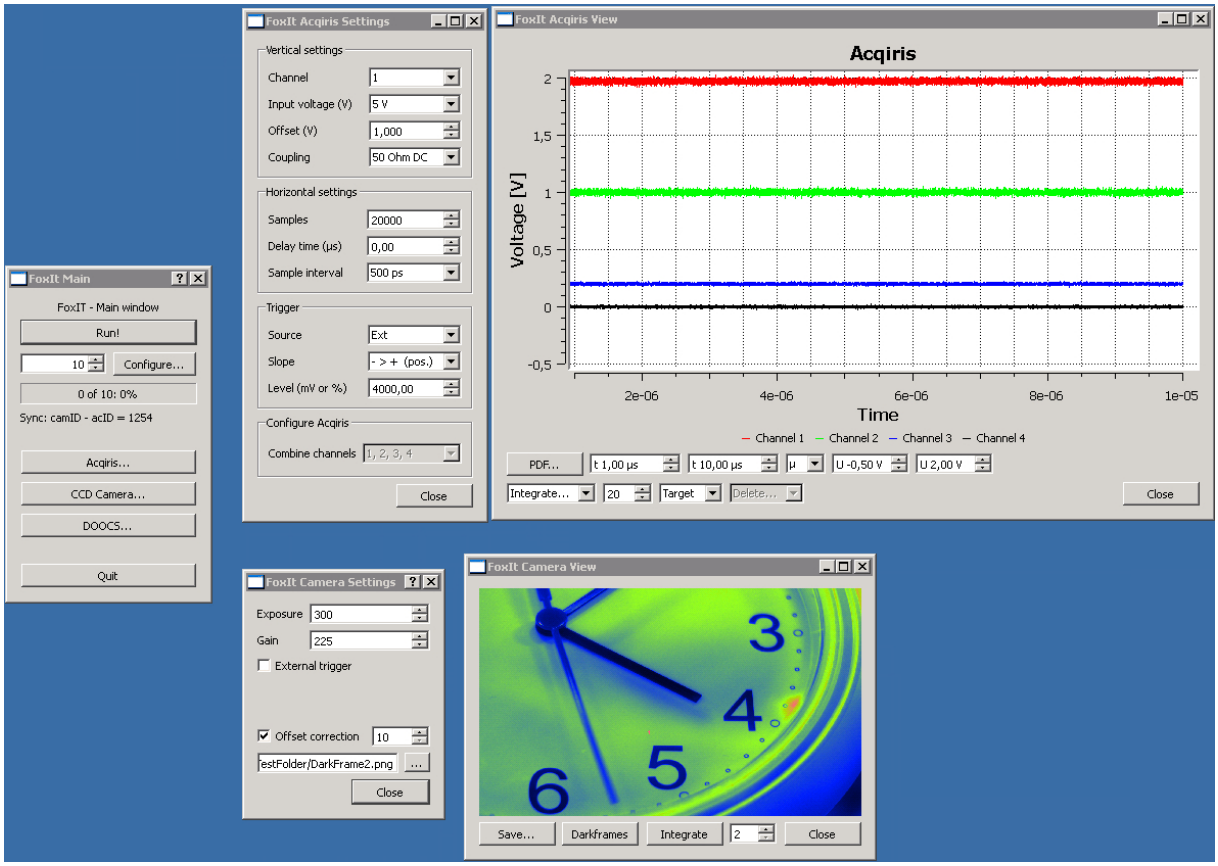

Figure 3.25.: Screen shot of the FoxIT data acquisition program running on Windows XP. On the left hand side the main window is visible, the right hand side shows the currently recorded Acqiris data (top) and the recorded CCD frame (bottom). This screenshot shows a test setup of the software. The acquires data shows noise recorded from open Acqiris channels. In this example, the image recorded with the CCD camera is a ticking clock in order to have movements in different frames.

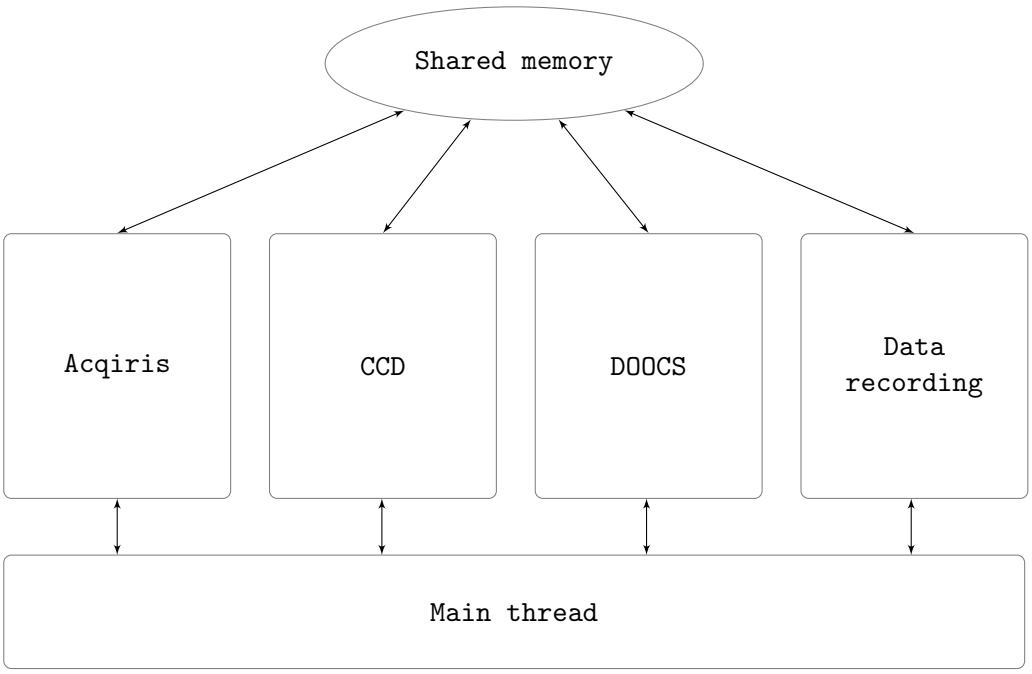

Figure 3.26.: FoxIT threads structure. The basis is the main thread. It configures and starts four individual threads each capable of another aspect of the experiment. Data exchange between the threads is realized using a shared memory buffer. See text for further details.

using multi-threading techniques[i]. Excessive testing was done to ensure stability and reliability. Object-oriented programming techniques allowed strict differentiation between different parts of the program, which helps servicing the code and simplifies the implementation of new features. A class based documentation using Doxygen [103] was created in order to help implementing expansions in the future. As required, the use of blocking dialog windows was reduced and editing of parameters is directly applied and stored. Figure 3.25 shows a screen shot of the software in a test environment. The Acqiris digitizer records random noise in this example. In order to have movement between different frames recorded with the CCD camera, the seconds hand of a clock is imaged. Even though the control interface for the Acqiris digitizer does not have the visual appearance of an oscilloscope, the parameters are similar. During the development a variety of features were implemented, e.g., digitizer graphs can be exported as PDFs for a quick reference, integration features for the displayed camera frame provide online-analysis and -background reduction. A floating integration can be performed on the data acquired with the digitizer.

The general outline of the FoxIT program is depicted in figure 3.26. After launching the program the main thread is created, which features the main event loop of the program together with the graphical user interface (GUI). It starts up to four different threads, which handle different aspects of the experiment. One thread is capable of the Acqiris data acquisition, one of recording CCD frames, another handles interaction with the FEL facility using the DOOCS interface [104], and lastly a thread deals with data storage. The data format used for storing the data is presented in detail on page 73 ff. The exchange of data between the different threads is realized by using a shared memory buffer. This denotes an address range within the computer's main memory (RAM) with read-write access for the different threads. Communication between the threads is realized using function calls and Qt's "Signal And Slot" mechanism. Parts of the program are emitting signals, which can be received by other parts of the software. Further information can be found in the corresponding Qt documentation [105]. The inter-thread communication is suppressed in the figure for clarity reasons.

The principle functionality of the different threads in FoxIT can be outlined as follows: After initialization each of the different threads run independently from the main thread. That means that every thread has its own main event loop which is executed until a termination function is triggered by the main thread. Recording of the data is performed autonomously by the threads. When new data is acquired it is saved to the shared memory buffer and a signal is emitted, which informs the other threads that data is available and allows them to perform operations with that data, e.g. storing it on disk. Then, the execution of the thread is paused until a new hardware trigger event occurs, which signalizes a new recorded set of data. Stopping the threads is critical because it gives processing time back to the thread scheduler of the operation system, which can cause other threads to perform work in the meantime. While the worker threads record, analyze, and store data, the main thread handles all interaction between the user and the software. If the user changes a parameter which is important for the execution of a particular thread, the thread is informed by using a function call which causes it to obtain a new set of parameters from the shared memory.

The example of the Acqiris-Thread is used in the next section to give further insights into the thread mechanism of FoxIT.

[i]The term "thread" denotes the smallest unit of a process (instance of a program) that is scheduled by the operation system.

Example: Thread of the Acqiris Digitizer

The Acqiris-Digitizer-Thread `acqirisThread` handles the interaction of FoxIT with the digitizer and runs autonomously from the rest of the program. It is derived from the `QThread`-class: `class acqirisThread:public QThread`. This inherits thread functionality from the base class. In `QThread`, the so-called `run()` function contains the main event loop of the thread. Its implementation `acqirisThread::run()` is depicted in figure 3.27 and, for the sake of completeness, its source code can be found in appendix C. A detailed description of the thread functionality can be found in the Qt documentation [102] and in the corresponding example [106].

In the beginning of the `acqirisThread::run()` function, local copies of the desired variables are created. This includes the settings of the Acqiris Digitizer. The creation of local copies is a very important step, because these settings could be changed from another thread during the execution of the `run()` function, which would lead to serious problems. Every variable contains a certain address range in the computers memory. If two threads access the same address range at the same time, this will lead to undefined behavior of the threads, e.g., one thread writes data to the memory while the other one tries to read from that memory. The result could be a mixture of the new and the old data in that memory block, depending on the unpredictable order of the execution of the threads. In order to avoid this double memory access, the memory block can be sealed using a mutex. However, this interrupts the execution of the second thread trying to access the memory. This can result in performance issues and the loss of data events. Therefore, the creation of local copies of all required variables is critical in order to avoid these problems.

The next step in the execution of `acqirisThread::run()` is the configuration of the shared memory buffer used for the exchange of measured data with the rest of the program, especially the data saving thread. The size of the shared memory equates to the size of the data in bytes plus an overhead of 16 bytes. This overhead is used to store the unique data-shot identification number (ID), which is used to ensure consistency of the data. With this step, the recording software is configured properly for the acquisition of data. The next step is the initialization of the Acqiris Digitizer. Here, several self-tests and calibration procedures are preformed by the hardware which can take up to one minute. The last step before starting the main event loop in the `acqirisThread::run()` function is a configuration step for the Acqiris. The digitizer is configured according to the users adjustments, e.g., the activated channels, gain settings for the channels, timing configurations, and much more. All of the mentioned steps so far are only performed once upon stating of the thread. Now, the threads main event loop is started.

The main event loop is basically a "`for`"-loop executed until the thread reveals the notification to jump out of that loop. In the beginning of each iteration, the break condition is checked and therefore the execution of the loop can be terminated at this point. The break condition is set from the outside of `acqirisThread` (see figure 3.27). Similar to the break condition another condition is set, if the settings of the Acqiris Digitizer are changed. If this is the case, the shared memory buffer has to be reallocated before the digitizer is reconfigured accordingly. Reallocation of the shared memory is necessary, because the size of the recorded data could have been changed during reconfiguration.

The final steps within the main event loop handle the data recording itself. First, the Acqiris Digitizer is set into a hardware trigger state, where it waits for the occurrence of the next hardware trigger event. Then the desired data is recored and the execution of the event loop continues. The next function collects the recorded data from the digitizer before it is copied

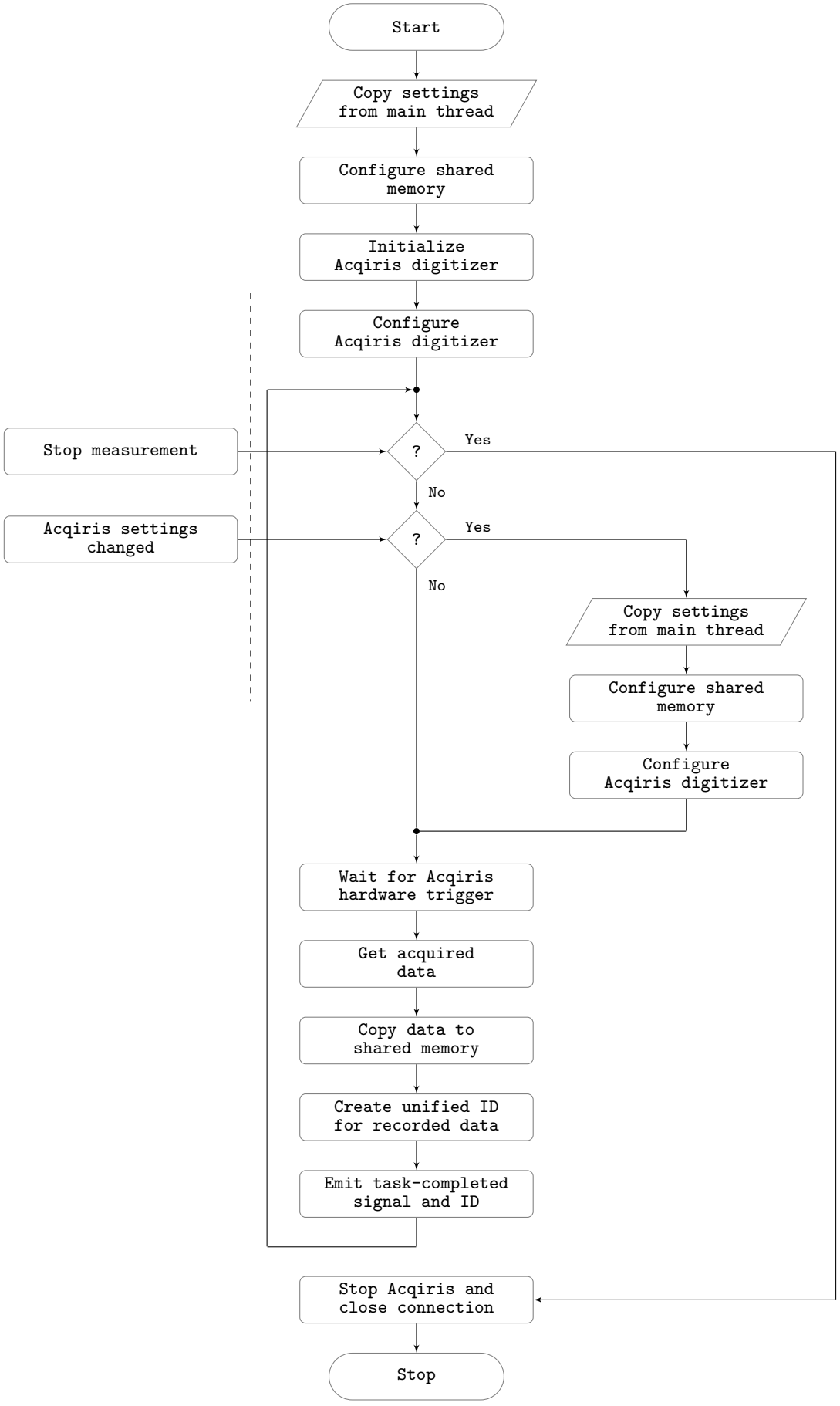

Figure 3.27.: Flowchart of the Acqiris digitizer thread

into the shared memory buffer together with the unique ID. The last step of the iteration is the emission of a task-completed signal with the ID as a reference. The recording thread receives the signal and writes the content of the shared memory to the disk. During this step, the ID handed over by the shared memory is compared with the ID that triggered the writing process. This ensures consistency of the data. In the meantime, the instance of the `acqirisThread` can start with the next iteration.

Besides the above mentioned task, the unique ID is used to ensure coherence between the recorded scattering frame and the ion data measured by the Acqiris. It can therefore be used as a tool for synchronization of the threads. While capturing the scattering data, the camera thread also generates an unique ID for its data. For each data set both IDs are increased by one, so that a constant difference between CameraID and AcqirisID ensures a sequence of matching data. Both IDs are stored in the data in order to allow comparison during the analysis. Even though asynchrony between different threads is unlikely in a scenario of low CPU load, it may occur. In this unlikely case, the stored IDs help the user to correct an offset between ion data point and scattering pattern, rendering such corrupted data still usable.

FoxIT data structure

The data recorded with FoxIT is stored in a file formate based on the hierarchical data format HDF5 [107]. HDF5 was developed by the National Center for Supercomputing Applications (NCSA) and is currently developed by the non-profit organization HDF Group. It is released using a BSD-like license for general use. HDF5 is supported by a variety of third-party applications including Matlab, Igor Pro, Python, IDL, and many more. With the task at hand the usage of HDF5 has several advantages, which are outlined in the following. Thereafter, the data format will be presented.

HDF5 was developed to store and organize a large amount of numerical data on a disk. Complex data with no limitations in terms of size and number of objects is combined into one single file. Within this file, the data is organized in a tree structure with XML-like descriptive identifiers. The application programming interface (API) provides fast random-read and -write access to the data and offers additional features like built-in data compression. Additional data can be added to a file before it is closed and uncompleted files remain usable. The format is independent of the computer platform and the existing interfaces in different programs simplify the analysis of the data.

The file size of the recorded HDF5 file is not limited by the API but it can be an issue for the handling of the data. The size of an HDF5 file recorded by FoxIT depends on the number of data points collected. For example a run of 1000 shots (equates to about 3 minutes 20 seconds of data recording at FLASH with a repetition rate of 5 Hz due to reduction of the pump load) takes about 1.6 GB disk space. In theory even file sizes beyond that are imaginable but not practical usable in all cases. Depending on the used file system such large files can be problematic. For example FAT32 formatted disks can only handle files up to 4 GB. That means that, in order to keep the files movable it is encouraged to keep the file size in a reasonable range.

The principle outline of a HDF5 file generated by FoxIT is outlined in figure 3.28. Comparable to the FRMS6 file format which is being used by MPI-HLL software (see figure 4.3 on page 80) the file contains a number of different frames, which represent the recorded data. However, in contrast to the FRMS6 file format, a frame contains not only the scattering pattern

but also all other data recorded during that particular FEL shot. This includes the Acqiris Digitizer data and the bunch ID together with unique identification numbers for the CCD frame data and the digitizer data.

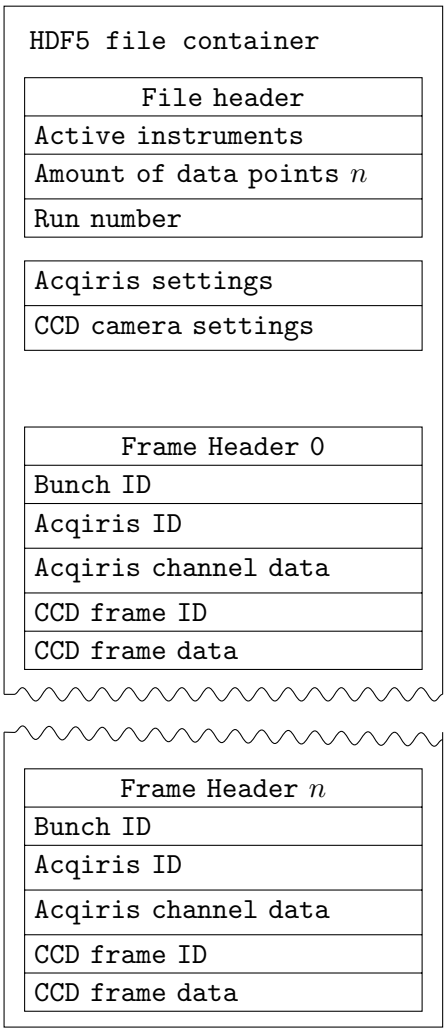

Figure 3.28.: HDF5 file format.

The first items in the file represents the status of the recording software stored for later references. Here, active parts of the program, e.g., an activated or deactivated state of the CCD camera is kept. Besides the amount of data points that will be recored, the run number is deposited in the file header. This run number serves as an identification number, which helps to distinguish the different measurements. Note, that the value for the amount of data points saved in the file header may differ from the actual number of frames in the file. This happens if a recording is canceled by the user before its completion.

Following these general items the next entires in the header of the HDF5 file are the settings of the CCD camera and the Acqiris Digitizer. While the settings for the CCD camera contain gain and exposure time only, the settings for the digitizer are more complex. The Acqiris settings contain information about the used digitizer channels such as offset, full scale settings, impedance, and coupling. Furthermore, timing information, e.g., the number of samples, delay, sample rate, and trigger modi are stored in this item. These informations are important for the data analysis. The Acqiris channel data is stored in a raw format, which contains the discrete steps from the 10-bit analog-to-digital converter of the Acqiris. Using the settings for offset, gain, and timing information in the file, the actual values can be calculated from the stored raw data.

In addition to the HDF5 API, the HDF Group provides a tool for viewing the content of an HDF5 file. This software is called HDFView and is a Java based application. A screen shot is presented in figure 3.29. Although HDFView is a multi purpose application of viewing HDF5 files and does not provide any analysis tools relevant in the context of this thesis, the application can be used for obtaining a first impression of newly recorded data. The screenshot in figure 3.29 shows on the left-hand side the tree-like organization of the data content (a). It shows the items for the Acqiris and CCD camera settings. The file header can be found as the top-level element of this list (not shown). The tree view lists the individual data frames (cf. figure 3.28). They are labeled with "Shot_" plus a consecutive number. Each entry can be expanded in order to show its content. Double-clicking on the content displays the data on the right hand side of the application. Here, HDFView offers two different views for the data: a table-view and an image view. As an example, two table-views are showing the bunch ID (d) and the raw data from the digitizer which is also displayed as a plot (b). An image-view is used to display a recored scattering pattern (c). It has to be pointed out that the screenshot shows uncorrected raw data which has to be further processed for the analysis (see

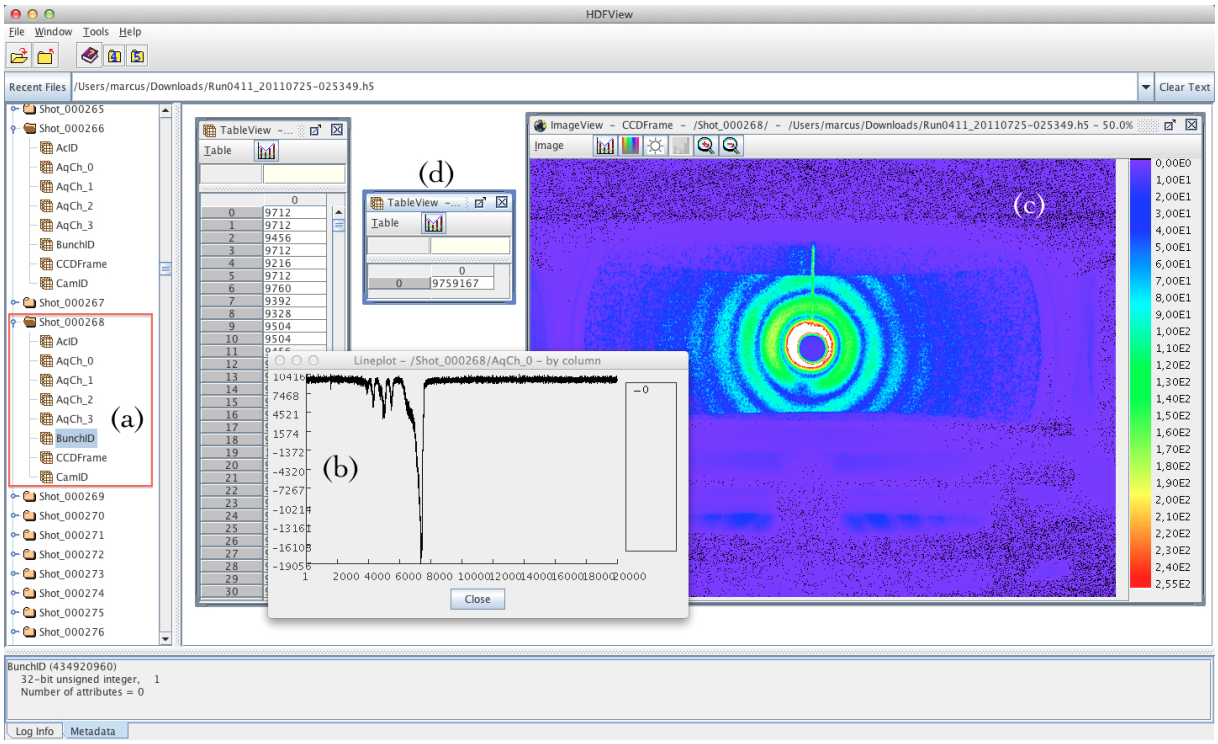

Figure 3.29.: Screen shot illustrating the usage of the HDFView program for the data analysis. A single shot scattering pattern with corresponding Acqiris data is shown. On the left hand side, the tree-like organization of the HDF5 file is visible (a). The raw data of this particular FEL shot contains a TOF ion spectroscopy data (b) and the uncorrected scattering image (c). The bunch ID (d) allows correlation of the data with the FEL parameters of that particular shot.

[15]). The figure 3.29 illustrates the correlation between TOF ion spectroscopy data and the scattering image, which combined represent the experimental results obtained from one single cluster during one single FEL pulse. By using the HDF5 file format the connection between the data of both measurement methods can be transferred to the data processing of the analysis.

Although FoxIt is a versatile application for recording of scattering data, it has to deal with new challenges for data acquisition and online analysis in future experiments, regarding new detector systems or enhanced online data analysis. Appendix D provides considerations for further developing the tool.

4. Experimental findings and discussion

This chapter presents the experimental findings and discusses them. It starts with the results obtained at the FLASH FEL in Hamburg, focussing on the scattering patterns from xenon clusters irradiated with intense 90 eV photon pulses. The measured scattering patterns are classified according to similarities and analyzed. First, the scattering data is used to perform single cluster size measurements revealing good agreement with well known scaling laws. This shows the capability of the scattering technique to characterize the clusters observed in single cluster experiments. Secondly, the imaging of clusters is used to observe residuals from the cluster growth process. These "twin clusters" are for the first time visible and show remarkable stability. Finally, a computer simulation of the cluster growth process is presented and the outcome is compared with the measurements revealing deeper insight into the cluster growth process.

This chapter closes with experimental results obtained at the LCLS facility. Here, measurements at the ionizations edge of krypton are presented extending investigations of cluster light interaction to the x-ray regime. The chapter closes with the presentation of a novel type of scattering experiments, combining imaging technique with time-of-flight ion spectroscopy. This new approach reveals new insights into the ionization process of single clusters.

4.1. Single shot, single cluster scattering

During the scattering experiments a large amount of individual scattering images were recorded. Even though every recored frame is unique, similar characteristics can be found in the data, which help to classify the scattering patterns. The figure on page 78 (figure 4.1) shows characteristic examples of the recorded data. The frames were recorded at the FLASH facility operating at 90 eV photon energy. For the generation of the clusters, xenon was expanded into the experimental setup with a stagnation pressure of $p_0 = 10.0$ bar and a nozzle temperature of $T_0 = 220$ K. The raw pnCCD data was corrected according to the procedure described in section 4.1.1. The amount of data was reduced by introducing a threshold that will be discussed in section 4.1.2

figure	Classification	Scattering intensity (ADU)			frame ID
4.1		minimum	maximum	mean	
(a)	Single	-113	1 361	26	724_8595298
(b)	Twin	-122	9 554	189	57_8594631
(c)	Double	-108	1 820	447	402_8104620
(d)	Double	-122	3 451	66	747_8104965

Table 4.1.: Summary of scattering pattern depicted in figure 4.1. The scattering intensity is given in ADU (atomic digitizer units). The mean value is an average of the entire detector.

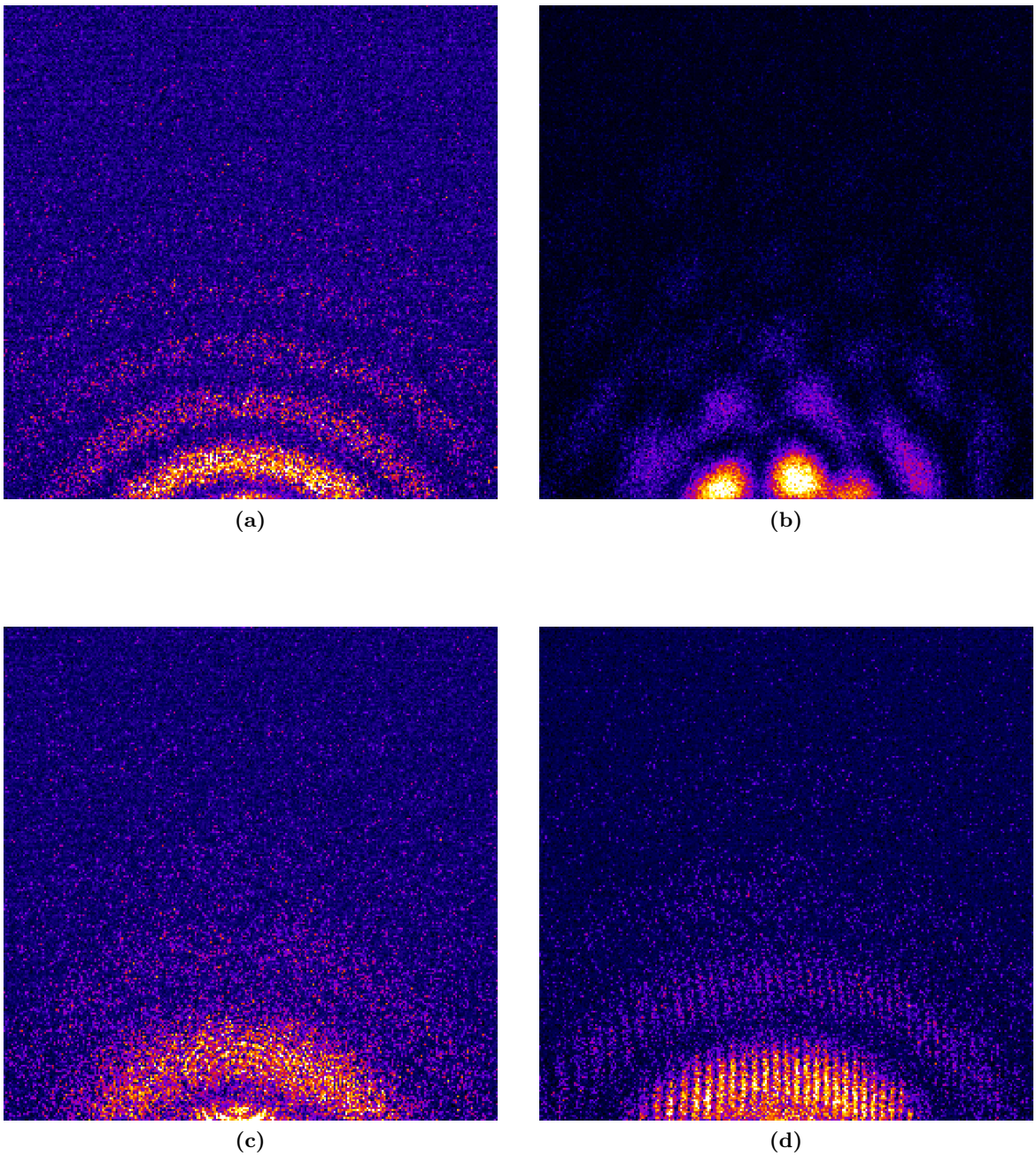

(a) **(b)**

(c) **(d)**

Figure 4.1.: Selection of scattering patterns from one data set recored at FLASH. These frames show scattering data from one or more clusters. The bright ring-like pattern in 4.1a indicates a single cluster in the interaction region. Interference fringes start to appear when two clusters are imaged at once. In 4.1b two clusters are detected being in direct contact (twin cluster). With increasing distance of two clusters newton ring scattering patterns are starting to evolve (figure 4.1c and 4.1d).

(page 81) in order to remove scattering data with no meaningful scatting signal, e.g. scattering pictures, where no cluster was in the focus of the FEL. The color scale of the images reaches from black, with the pixels with the lowest intensity, to white, referring to the pixel with the highest intensity given in ADU (atomic digitizer units). At the expense of direct comparability the color scales of the images were adjusted to fit a printable format. Table 4.1 gives the absolute values for the lightest and the darkest pixels in ADU.

The most frequent scattering pattern is shown in figure 4.1a. The data looks similar to the scattering pattern produced in a pinhole scattering experiment, which indicates that the visible ring structure is caused by on single spherical cluster, which was hit by the FEL pulse. With about 26 ADU mean scattering intensity it exceeds the threshold for analysis which was set to 10 ADU, but at least six rings can be seen in the figure. In the top half of the figure, photons even form a seventh ring. The scattering pattern shows a relatively small ring structure. This indicates, that it originates from a very large cluster. Using Mie theory, this type of scattering patterns can be used to determine the size of the cluster. This will be discussed in section 4.3.

The experiments were performed in such a way, that single cluster scattering events were favored. Therefore scattering patterns from single cluster (e.g. figure 4.1a) dominate the gained data. A totally different scattering pattern is shown in figure 4.1b. An interference pattern overlays the ring structure of single scattering sources. Similar structures are well known from scattering experiments performed with two pinholes arranged in double slit scattering experiments. This leads to the conclusion that two clusters in a very close distance caused this type of image. From the distance of interference fringes the distance of the scatterers can be determined, leading to the observation that the clusters must be displaced in the order of their radii or even in direct contact [18, 23, 108]. Hence, these clusters are denoted as “twin clusters”. This feature is further discussed in section 4.4.

The patterns shown in figure 4.1c and 4.1d are different from the twin cluster scattering image. In this images the fringes are very thin compared to twin cluster scattering patterns. The interference denotes that at least two clusters are in the interaction region. The light of the FEL was scattered on both clusters and interfered on the detector. This caused the formation of the monochromatic Newton-ring like fringes in the scattering patterns.

4.1.1. FLASH data processing

Critical for the success of the scattering experiments is efficient data processing and automatic reduction of the amount of data recorded. This section focuses on different scripts, programs, and algorithms developed and used during this thesis for the preparation of the recorded scattering data. General data processing aspects were already discussed in section 3.3 on page 64. Therefore, this section focusses on data related adoptions of the general workflow.

The analysis required the combination of several specialized tool: a C/C++ based recording software [101], C++ programs for data sorting, several Bash scripts for file processing, IDL programs for image corrections [109], and standard analysis tools like ImageJ [110] and IgorPro [111]. Technically it is possible to combine all needed scripts and programs in one monolithic application that performs the preparation of the data. However, the presented approach uses the advantages of the individual tools. For example Bash scripts are easily modified and adjusted to various purposes. The vector optimized programming language IDL was initially used for operations on the image data. But as IDL is proprietary software, it cannot be transferred

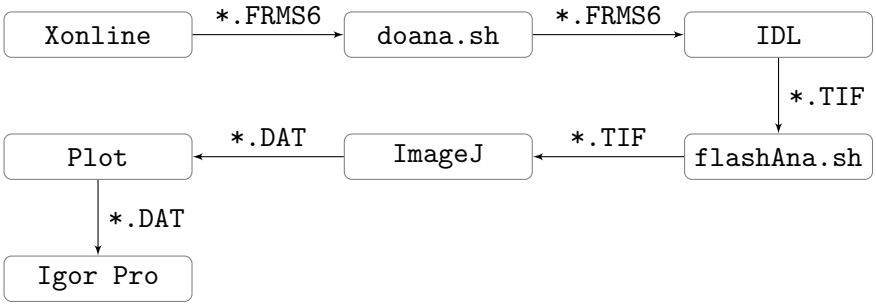

Figure 4.2.: General data flow for the analysis of the pnCCD data recorded during the FLASH experiments. The raw images are stored using the Xonline program. The doana.sh script triggers an automatic correction of the frame data using IDL. This generates TIF files from the frame data, which are further analyzed. Sorting of the data is performed using flashAna.sh. The results are viewed and exported as two-dimensional arrays using ImageJ. These are transformed to spherical coordinates and a scattering plot is generated which is analyzed using Igor Pro.

to different computers due to license restrictions. Therefore C/C++ programs were written, combining the fast data processing abilities of IDL with the flexibility to be run on different machines.

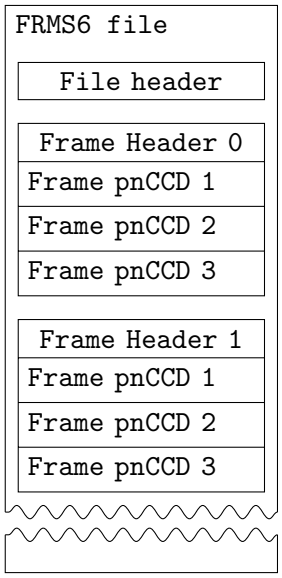

Figure 4.3.: FRMS6 file format, as defined by MPI-HLL

At FLASH the pnCCD data was recorded using Xonline [101]. This program provided readout of the pnCCDs combined with visual feedback for the data. The frames are stored in a binary file format called FRMS6. In addition to the frame data the file format provides a file header and a frame header. The file header stores information about the number of pnCCDs read out in coincidence with their number of pixel-rows and -columns and an identification number of the dataset. Furthermore, information about the format version and the size of file- and frame-header in bytes is saved. The frame-header stores the position of the frame data in the file together with a unified number, which is used to identify single FEL shots afterwards (bunch ID). The bunch ID is provided by DESY. In figure 4.3 the FRMS6 file format is illustrated schematically.

During the measurements FRMS6 files containing scattering images ("data files") and files containing background signal ("dark files") are recorded. As outlined in figure 4.2 these files are handed over to the "doana.sh" (DO ANAlysis) Bash shell script. In a shell the user calls the doana.sh script with the filenames of the data FRMS6 file and the FRMS6 file containing the dark files as arguments. The script checks their existence and generates an appropriate script to perform image corrections on the given FRMS6 files using IDL (Interactive Data Language, see [109]). Furthermore the desired commode correction (see section 3.3.2 on page 66) algorithm is set here.

The image correction within IDL starts automatically by compiling the needed routines.

Then the FRMS6 files containing the dark frames are split in three files each containing the frames of one detector. An offset correction and a commode correction is performed on the dark frames data. The data file is split into three parts, which are then corrected using the three corrected dark frame files. In the end, the IDL script produces tif- and report files for every frame.

The next step of the data preparation is the sorting of the data. The shell script "flashAna.sh" is used. This script requires the folder with the corrected tif files as a calling argument. Additionally, a threshold value can be given for reducing the amount of data to be analyzed. The script calls a C-program ("FLASH-Tiff") for every tif file in the provided folder which is used to calculate the mean value of that frame. The mean value of each tif file is compared to the threshold-argument by the flashAna.sh script (see section 4.1.2. For a frame above the threshold the corresponding tif file is exported to a new folder.

In a last step, the images are converted into 1D-scattering plots. The tif files are loaded into ImageJ [110] and exported as a two dimensional data file. This dat file is processed with a LabView program which transforms the flat images into spherical coordinates with a constant radius of the mean detector distance. Afterwards a radial integration over the detector is performed. The result of this integration is exported into Igor Pro [111]. Here, the cluster size could be determined using a comparison with a simulation of the scattering process using Mie theory. The simulation algorithm was adapted from [70] and is described in detail in [17].

4.1.2. Computer aided data filtering

The scattering experiments produced several hundreds of gigabyte of data. For example, one hour of data recording produced 18,000 scattering pattered from the same amount of single cluster events which had to be screened and classified. In oder to reduce the amount of data filtering of the data was required. The first filter method applied is an intensity filter that removes all shots with no cluster present in the focus. Due to the applied technique to dilute the cluster beam in a way that on average less than one cluster is in the FEL focus at any given time, the amount of data without scattering signal is significant.

There are different ways to remove "empty" scattering data from the data pool. The first method is to integrate the frame intensity in the recorded frame data and compare it to an experimentally determined threshold. The integration can either be performed for the entire frame or for an area of the pnCCD detector, which is expected to detect most scattered photons. The size of the integration area has to be as large as possible on the one hand to represent the total detector, but on the other hand as small as possible in order to reduce the influence of mips (see section 3.3.2 on page 66) missed by the image correction. Furthermore, extreme noisy detector regions have to be omitted as well. Typically, the size of the integration region was at least 50 pixels by 100 pixels up to 200 pixels by 200 pixels depending on the analyzed data. The integration is performed by calculating the arithmetic mean:

$$AM_{\mathrm{F}} = \frac{1}{n_{\mathrm{r}} \cdot n_{\mathrm{c}}} \sum_{i,j}^{n_{\mathrm{r}},n_{\mathrm{c}}} v_{i,j}, \tag{4.1}$$

where n_{r} and n_{c} denote the number of rows and columns per pnCCD detector or per integration area and $v_{i,j}$ is the value of one particular pixel.

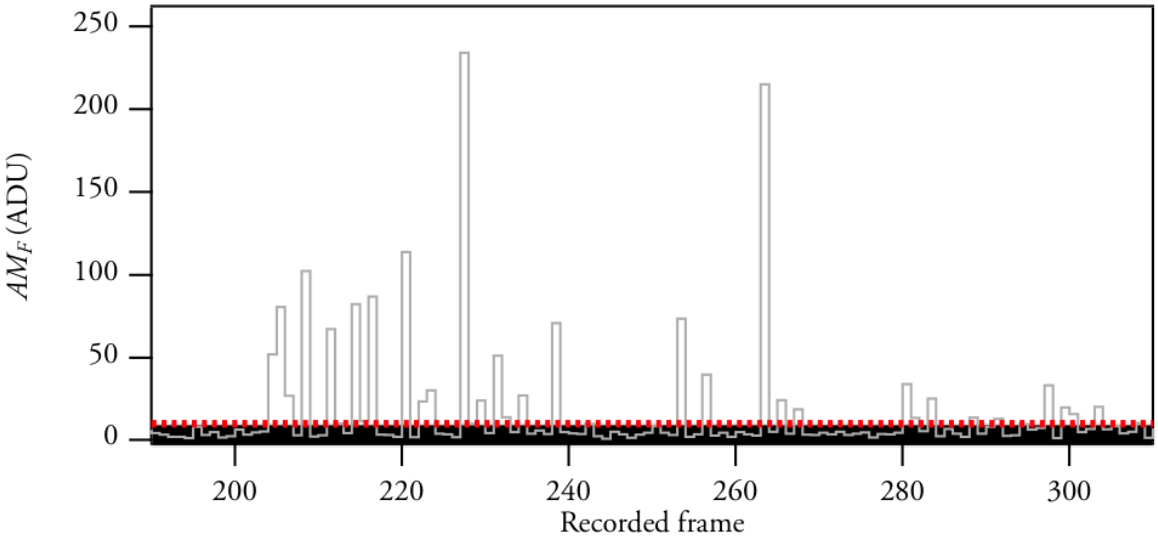

Figure 4.4.: Detail of an experimental run illustrating the filtering of the data. The graph shows a fraction of a run of data measured at FLASH. The averaged signal detected at the first CCD detector is plotted for the different recorded frames. High spikes in the spectrum correspond to frames with a large amount of scattering light. A threshold (10 ADU, red line) is used to filter the frames accordingly. Images with a lower intensity (black bar) are removed from the data pool and are not analyzed further.

In figure 4.4 an example for a filtered data set is presented. The graphic shows the AM_{F} values of patterns with xenon cluster scattering signal of an averaged cluster size of $\sim 42\,\mathrm{nm}$ in radius, produced with 10 bar, 220 K nozzle pressure and temperature, respectively. The data was recorded at FLASH with 90 eV photon energy. The spikes in the figure correspond to frames with a lot of scattering signal. The threshold, which distinguishes between a cluster hit and an empty frame, is marked with the dashed bar. Frames below this marker show no scattering signal and are removed from the data pool. The discrete bars of the frames with scattering signal indicate perfect single cluster mode. The figure illustrates the data reduction obtained by applying a 10 ADU threshold filter. The figure contains 120 data shots but for only 30 the AM_{F} is above the thread hold (red line), reducing the data by 75%.

4.2. Classification of scattering patterns

The filtering helped reduce the data in order to identify the most significant scattering pattern. Figure 4.1 on page 78 introduced recorded frames that pass the filtering threshold and showed first examples of single cluster scattering data. The results show, that the scattering patten can be classified depending on the amount of clusters in the interaction region (single cluster or multiple clusters) and the distances of the clusters (two clusters or twin clusters, respectively). Figure 4.5 compares the three types of scattering patterns and matches them with schematic drawings illustrating the corresponding origins of the images. It has to be noted that combination of the three categories are feasible. For example one can think of a twin cluster in combination of a single cluster which overlays the twin scattering pattern with newton rings. However, these events are very unlikely and were not observed in the presented data.

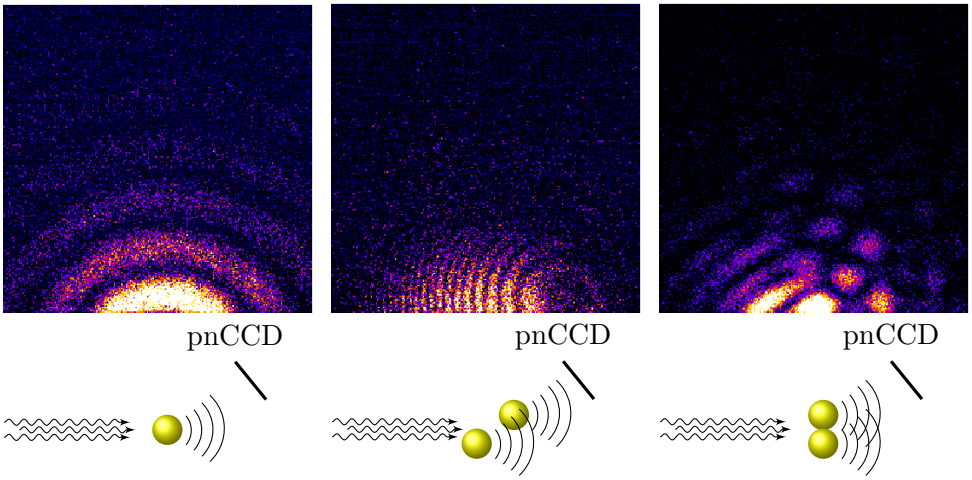

(a) Single cluster **(b)** Two clusters **(c)** Twin cluster

Figure 4.5.: Typical scattering images from the small angle detector recored during the scattering experiments at FLASH. (a) the ring structure indicates one single cluster in the focus. (b) This interference pattern shows that two clusters were in focus at the same time ("Newton Rings"). (c) This scattering pattern is produced if to clusters are in direct contact and form a "Twin Cluster". The schematic drawings indicates the underling geometry of the scattering data.

With the scattering data classified, the relative appearance of the different types of scattering patterns was examined. From the histogram presented in figure 4.6 it can be seen that the appearance of the scattering types is not uniformly distributed. This histogram shows the appearance of single clusters, two clusters, and twin clusters for five different measurements performed with five different mean cluster sizes. The cluster sizes are denoted in therms of the condensation parameter Γ^*. In order to compare the measurements, the total number of appearances of the different scattering patterns is presented in percent relative to the number of recorded scattering patterns for the particular experimental setting.

With about 80% the most frequent scattering patterns observed are the single cluster scattering images. This indicates that the single cluster scattering condition was well fulfilled, which is a critical factor for the performed experiments. The remaining percent are dominated by twin cluster images which form $\sim 20\%$ of the data. This is a larger amount than one would expect from a statistical point of view. 80% of the data show only one single cluster in the interaction region which is in the oder of several micro meters located several deci meters from the cluster source. Therefore, it is highly unlikely that, if two clusters are in the focus of the FEL, their distance is in the order of the clusters radii, which is in the order of nano meters.

This estimation is supported by the findings that two clusters in the interaction region appear to be rare with about 1% of the data. The visibility of the two cluster scatting pattern depends on the width of the piezo skimmer. Its width was adjusted until the amount of clusters in the interaction region was less then one (see section 3.2.1 on page 60). Hence, Newton-ring fringes in scattering patterns are rarely detected.

Figure 4.6 shows a slightly increase in the appearance of twin clusters at $\Gamma^* = 212 \cdot 10^3$, corresponding to $p_0 = 13\,\mathrm{bar}$, $T_0 = 220\,\mathrm{K}$. At this data point the expansion parameters are chosen in a way that is above the vapor pressure curve of xenon (For reference, the vapor

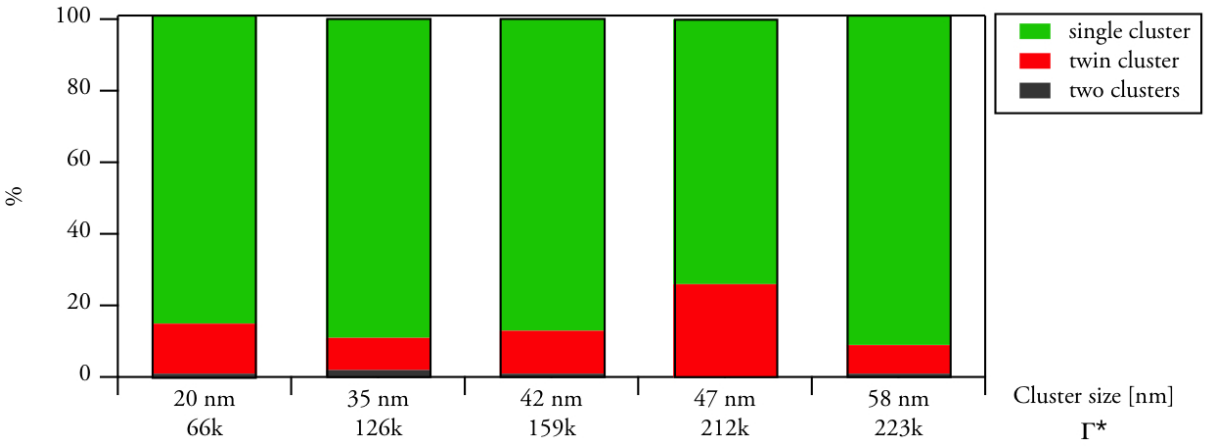

Figure 4.6.: Occurrence of the three types of scattering patterns obtained from single cluster, (see figure 4.5a), two clusters in focus (figure 4.5b), and twin clusters (figure 4.5c) plotted for various experimental conditions. Single clusters dominate the observations, which indicates single cluster scattering mode in the experiments. This is also supported by the almost absent of two clusters in the interaction region. In contrast to that, about 20% of the data shows scattering signatures from twin clusters independent of the experimental condition.

pressure curve of xenon is given in appendix B). Hence a cluster formation from the liquid phase is feasible. However, this data point lacks statistics and has to be taken into account with care. The appearance of twin clusters is discussed in section 4.4.

4.3. Determination of the mean cluster size

For the determination of the mean cluster size single shot scattering patterns from single clusters were analyzed. The tools needed for the processing of the data are described in section 3.3. Figure 4.7 on page 85 shows some scattering images obtained from processing of the raw data files. The xenon clusters that were imaged, were created using a stagnation pressure of $p_0 = 10\,\text{bar}$ and a nozzle temperature of $T_0 = 220\,\text{K}$. From figure 4.7a to figure 4.7f the frames are sorted with increasing scattering intensity. The results of the data analysis of these images are summarized in table 4.2

The images originate from one single cluster each. The pictured clusters are varied in size, resulting in different ring structures. Larger clusters lead to smaller rings and vice versa. In order to obtain meaningful information about the imaged cluster size, the scattering data was compared to Mie simulations (c.f. section 2.3.2, and [18, 73]). A radial integration of the scattering images was performed, leading to the scattering profiles presented in figure 4.8a. This enables direct comparison of the intensities of the scattering images. Additionally, radial integration increases the statistic for weak scattering frames which enables analyzing smaller clusters.

In figure 4.8a the scattering profiles from figure 4.7a to figure 4.7f are summarized. The scattering intensity is plotted versus the scattering angle with a scattering angle of 0° represents the propagation direction of the FEL beam. A logarithmic scale was used to cover the dynamic range of more then three orders of magnitude. Note that for large scattering angles ($\gtrsim 35°$) the single photon regime is reached.

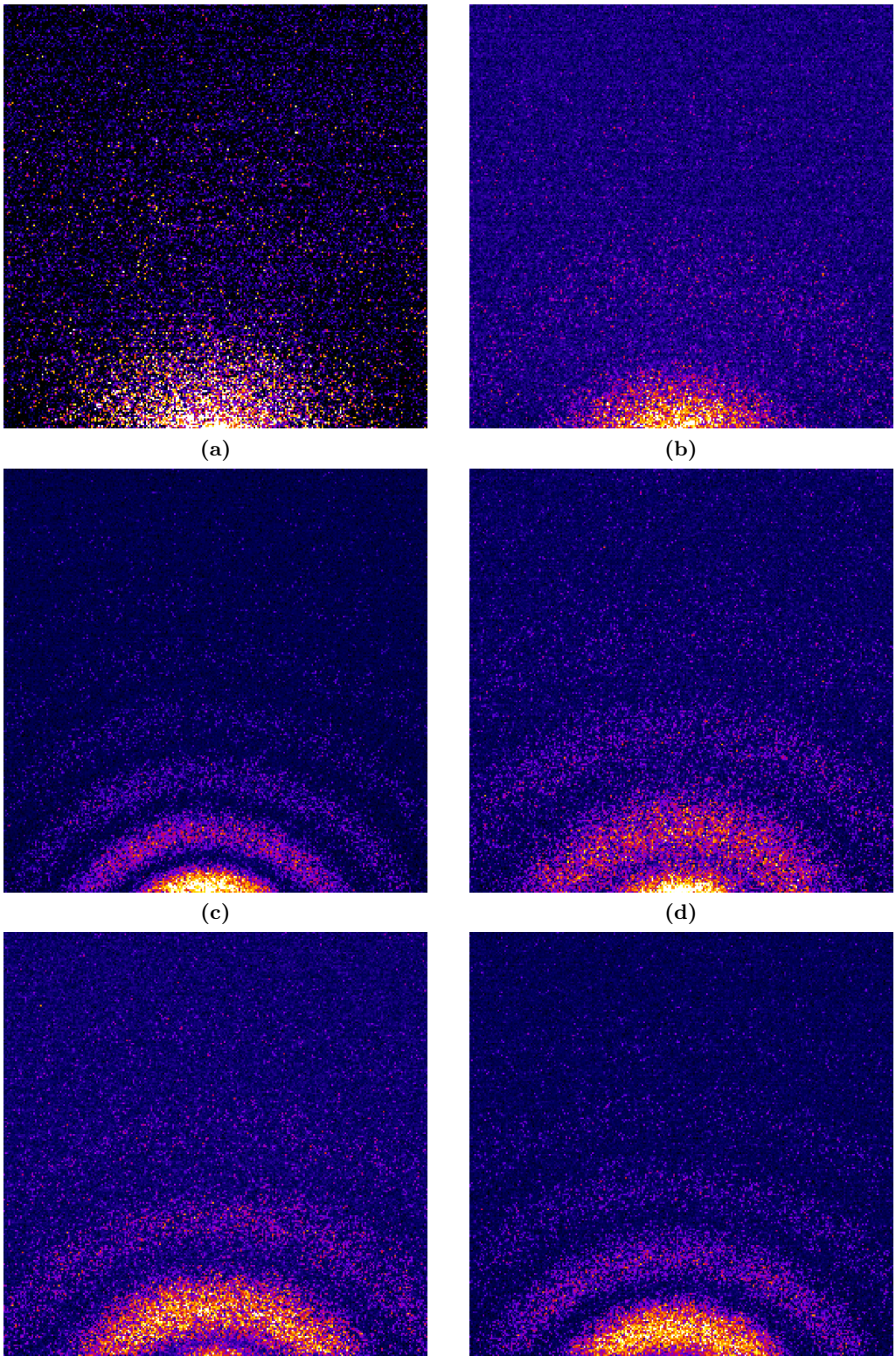

Figure 4.7.: Selection of scattering images showing single xenon cluster scattering recorded at FLASH with 90 eV photon energy ($p_0 = 10.0\,\mathrm{bar}$, $T_0 = 220\,\mathrm{K}$). The images are ordered by cluster size (small to larger), see table 4.2 for comparison.

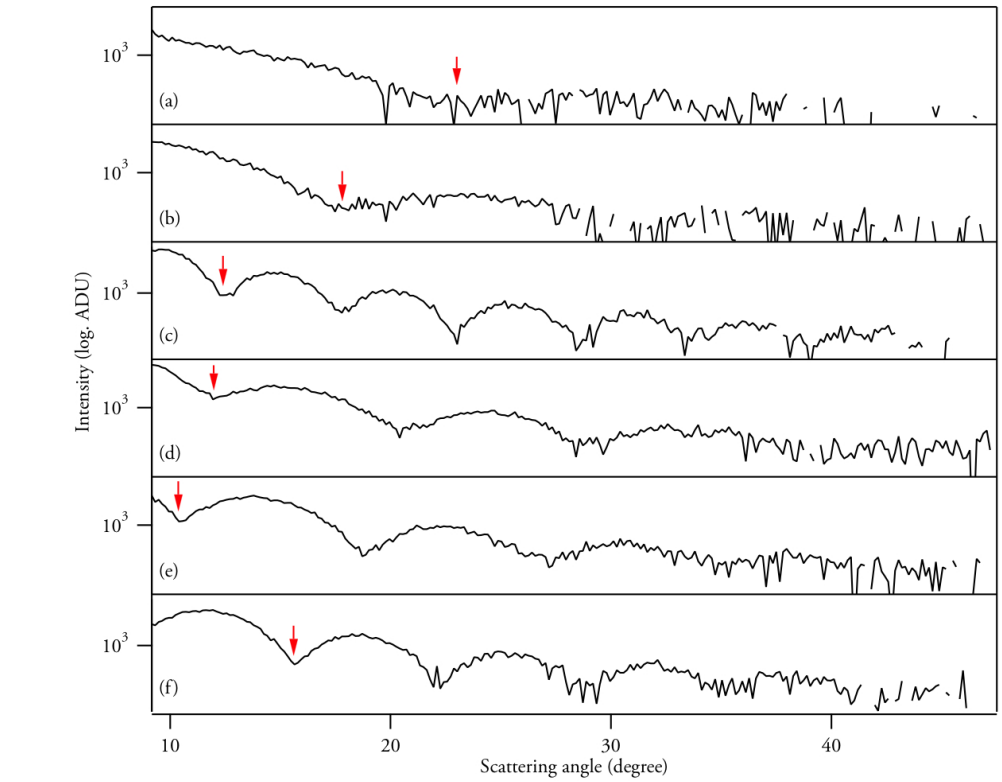

(a)

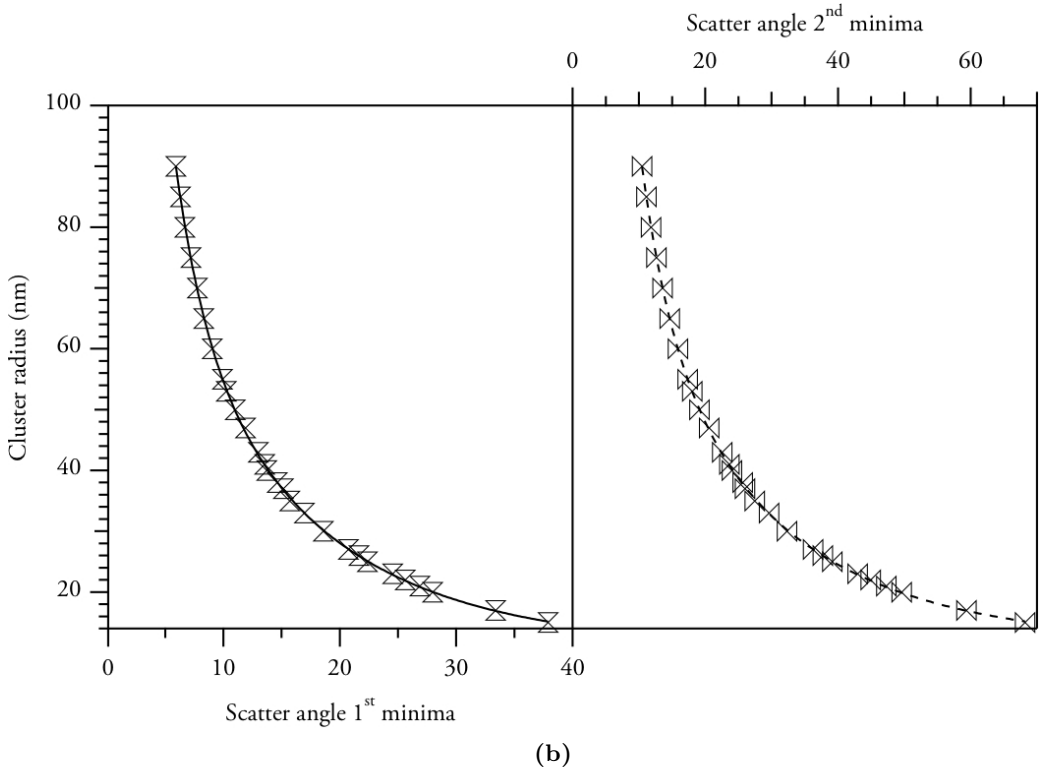

(b)

Figure 4.8.: (a) Scattering profiles obtained from figure 4.7a to figure 4.7f. The red arrows indicate the position of the first scattering minima determined. Using figure (b) the scattering angle of the first and second minima obtained from Mie simulation can be used in order to determine the cluster radius. See text for further details.

figure	position of min.	radius (nm)	Scattering intensity (ADU)			frame ID
4.1	(degree)	(Mie)	min.	max.	mean	
(a)	23.0	23	-120	1133	13	1362_8595936
(b)	17.8	31	-134	2032	20	902_8595476
(c)	12.4	44	-117	3854	47	884_8595458
(d)	12.0	46	-116	2494	53	1018_8595592
(e)	10.4	52	-121	2118	51	1079_8595653
(f)	15.7	60	-115	2274	56	991_8595565

Table 4.2.: Analysis results of scattering patterns depicted in figure 4.7. The cluster radius was obtained from Mie simulations as described in the text. The mean scattering intensity is calculated with respect to the entire detector.

For the determination of the cluster size the data is compared with a Mie calculation of the scattering profile. A first criterion for comparison is the scattering angle of the first minimum visible in the scattering plots. In figure 4.8a red arrows mark the position of the corresponding position in the profiles. Regarding the gradient of the data it has to be noted that in the scattering profiles 4.8a (c) and 4.8a (f) the first scattering minimum was not captured by the pnCCDs. This can be seen by considering the slope of the curve for a scattering angle $\varphi < 10°$. In this range, the slope starts with an increase of the scattering intensity, which points to a minimum at smaller scattering angles. Therefore the marked minima in 4.8a (c) and 4.8a (f) can be considered to be the second one. In figure 4.8b the scattering angle of the first and second minima is correlated with the corresponding cluster size.

With the cluster size obtained from the graph 4.8b Mie calculations with variation of the complex refractive index were performed until agreement between simulation and measurements was obtained. An example of the comparison is shown in figure 4.9. The presented scattering plot is obtained from the scattering frame shown in figure 4.7d. The red-dashed line represents the Mie simulation of a sphere with a radius of 46 nm and a refractive index of $N = 0.97 + 0.01\mathrm{i}$. The incident irradiation was set to 13.5 nm wavelength, a common value for the scattering experiments at FLASH. The values of the simulation were adjusted in order match the scattering profile. However, slight derivations from the measurements are visible. At small scattering angles the minimum from the simulation is hardly found in the measurement which is blurred due to saturation effects on the detector. At large scattering angles, insufficient amount of scattering photons make it difficult to compare the measurement and the simulation. But, at medium scattering angles from 15° to 27° the scattering profile can be matched with the Mie simulation leading to the given cluster size. The refractive index is in good agreement with the one obtained from former measurements at FLASH under similar conditions [18].

Following this procedure, a detailed study of single cluster scattering patterns recorded from clusters created with a variety of expansion parameters was carried out to gain insight into the statistical distribution of the cluster sizes. The cluster size determined for every recorded scattering pattern was used to create a cluster size distribution for the different experimental parameters, namely background pressure p_0 and nozzle temperature T. Based on the established histograms an average cluster size for every experimental run was determined by fitting a log-normal distribution using Igor Pros multi peak fitting algorithm [111].

Figure 4.10 shows the obtained size distributions for xenon clusters expanded with a nozzle temperature of 220 K and variated stagnation pressure p_0. From top to bottom, the clusters

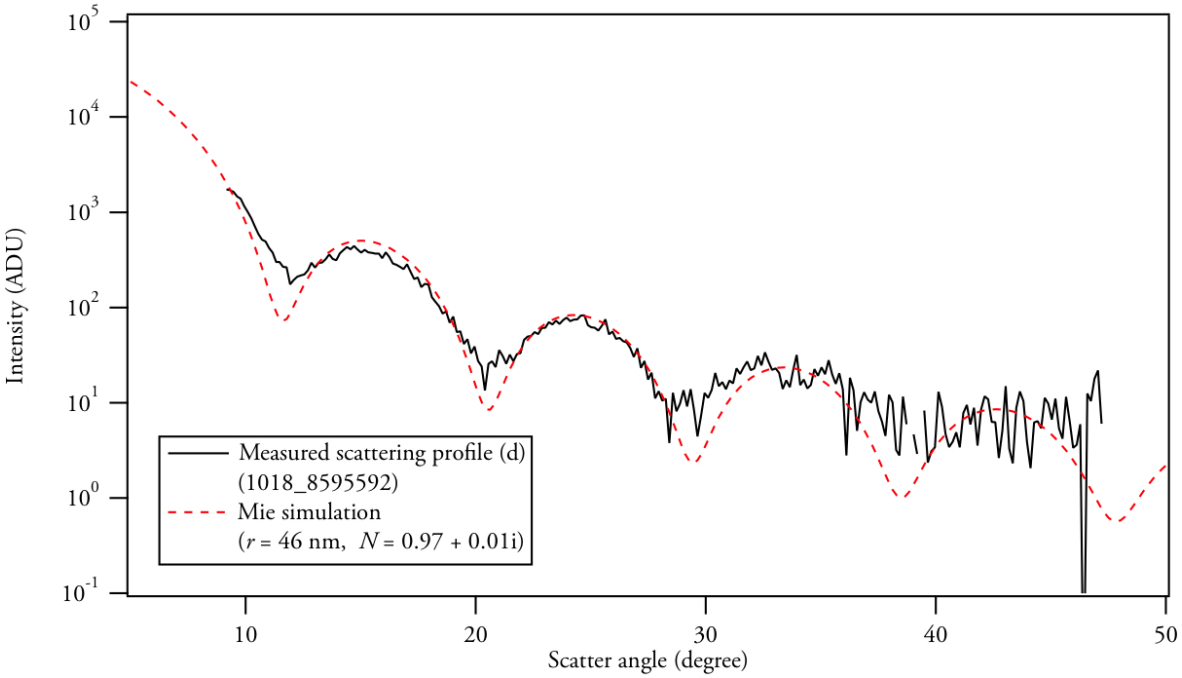

Figure 4.9.: Comparison of Mie simulation and scattering data. The solid line shows a scattering plot obtained from a cluster generated with $p_0 = 10.0\,\text{bar}$ at $T_0 = 220\,\text{K}$. The plot is compared to a Mie simulation (dashed line). The parameter for the simulation are given in the annotation.

size is increased by increasing the pressure: $p_0 = \{4.2\,\text{bar}, 7.9\,\text{bar}, 10.0\,\text{bar}, 13.3\,\text{bar}, 14.0\,\text{bar}\}$. Note that the transition from gas to liquid xenon at 220 K occurs at 10.5 bar (the vapor pressure curve of xenon is giving in appendix B), which means that the vapor pressure curve of xenon is crossed between the experiments in graph (c) and graph (d). The expansion conditions are defined by one single quantity, the scaling parameter Γ^* (see equation 2.12 on page 14, with $K_{\text{ch}}^{\text{Xe}} = 5\,554$ and $d_{\text{eq}} \approx 2\,056.44\,\mu\text{m}$) depicted in the graphs.

As expected, with increasing stagnation pressure and therefore increasing cluster size, the distribution becomes broader. This is in very good agreement with mass spectroscopy investigations performed by Soler *et al.* [8]. In the regime above the vapor pressure curve, the cluster size distribution becomes very broad and starts to dissolve. Unfortunately the measurement (d) shows a very weak statistic and can therefore be seen as an outliner, were the mean cluster size obtained from the log-normal fit of the histogram shifts towards smaller cluster sizes. For $\Gamma^* > 160 \cdot 10^5$ (e) the histogram of the single cluster sized is even broader, resulting in the fact, that one single log-normal fit cannot reproduce the histogram with reasonable accuracy. Overlapping two log-normal fits as shown in figure 4.10 (e) result in better agreement with the experimental results. The second peak is located at $\sim 27\,\text{nm}$, which is half way towards the distinct peak at $\sim 60\,\text{nm}$. This could be an evidence for fragmentation of larger clusters, e.g. $\sim 60\,\text{nm}$ clusters breaking apart and fragments are detected as parts of the second peak. However, the data is not absolutely clear on this behavior and it could also be caused by a statistical effect. Further experiments are necessary in order to clarify this theory.

In order to compare the data obtained with cluster size distributions reported in literature a conversion is needed to translate the cluster radius given in nano meters to the mean number of atoms per cluster $\langle N \rangle$, which is used throughout the literature. The following geometric

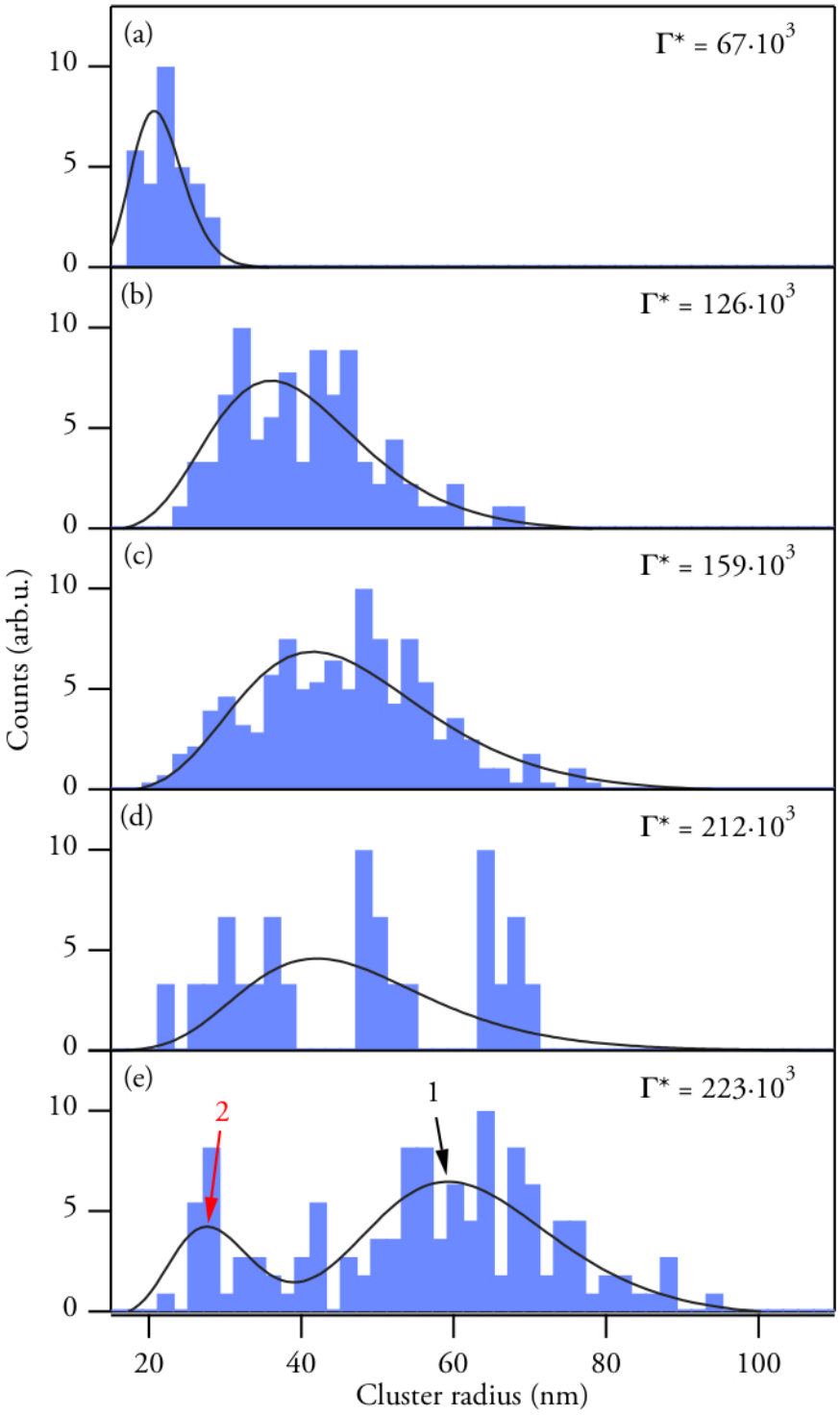

Figure 4.10.: Size distributions for different experimental parameters Γ^* (selection). The histograms are created from single shot scattering data as described in text. All distributions are fitted using a log-normal distribution. For measurements above Xenon's vapor pressure curve (e) a second peak is appears in the spectrum. For comparison reasons, the counts for the measurements were normalized to 10.

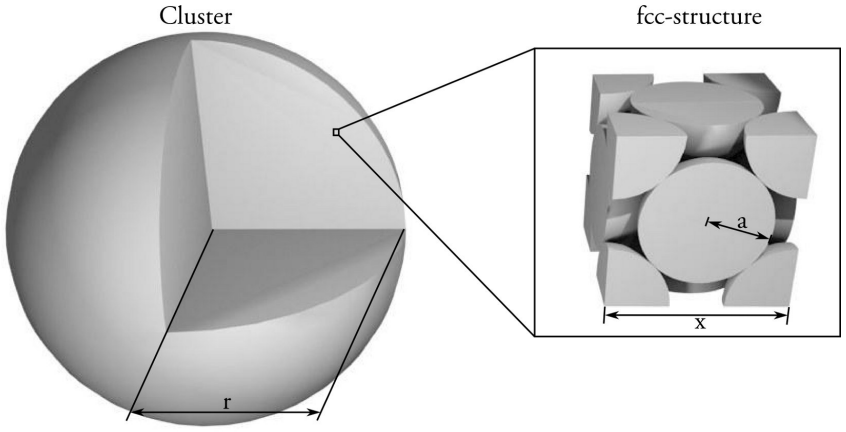

Figure 4.11.: For the determination of the number of atoms in a cluster it is considered that the clusters consists of n fcc-structures. See text for explanation.

considerations are used for the correlation of these quantities. For large rare gas clusters, in this case xenon clusters, the atomic structure is equal to the face centered cubic (fcc) structure of a solid. The cluster can be assumed to be spherical with a volume $V_{\text{Cluster}} = 4/3\,\pi r^3$ with radius r. It is constructed from n fcc unit cells as illustrated in figure 4.11. With x being the length of an edge of the unit cell and a the van der Waals radius of the atoms one finds:

$$V_{\text{Cluster}} = \frac{4}{3}\,\pi\, r^3 = n\, x^3 = 16\, n\, \sqrt{2}\, a^3,$$

with $x = 2\sqrt{2}\, a$. Every fcc unit cell consist of four atoms (eight "eighth" atom fractions in the corner and six atom "halves" on the centers, see figure), therefore the number of atoms is four times larger compared to the number of unit cells: $4n = \langle N \rangle$. With that, for the radius of the cluster

$$r \approx a \left(\frac{3\sqrt{2}}{\pi}\, \langle N \rangle \right)^{1/3} \tag{4.2}$$

is found. Alternatively one obtaines

$$\langle N \rangle \approx \frac{\pi}{3\sqrt{2}} \cdot \frac{r_{\text{Cluster}}^3}{a^3}. \tag{4.3}$$

For the van der Waals radius $a_{\text{Xe}} = 2.16\,\text{Å}$ is considered as given by [112].

The experimentally determined mean number of atoms per cluster $\langle N \rangle_{\text{exp}}$ for different scaling parameters Γ^* is compared to results from various scaling laws as shown in figure 4.12. The annotations within the figure ((a) to (e_2)) correspond the measurements shown in figure 4.10. The errors given in the figure are estimated based on the following assumptions. For pressure and temperature logged during experiments an accuracy of 500 mbar and 4 K, respectively, can be given. These values are predominately caused by pressure drops in the experiment's gas system and the stability of the temperature of the nozzle. For the determination of the cluster radius an error of ± 2 nm was assumed, which is basically caused by a uncertainty in the comparison of Mie simulation with the experimental data. In addition to that further experimental errors like imprecise distances in the setup have an influence on the reliability of the data. Especially these kinds of errors, which are independent from the cluster size, dominate the measurements.

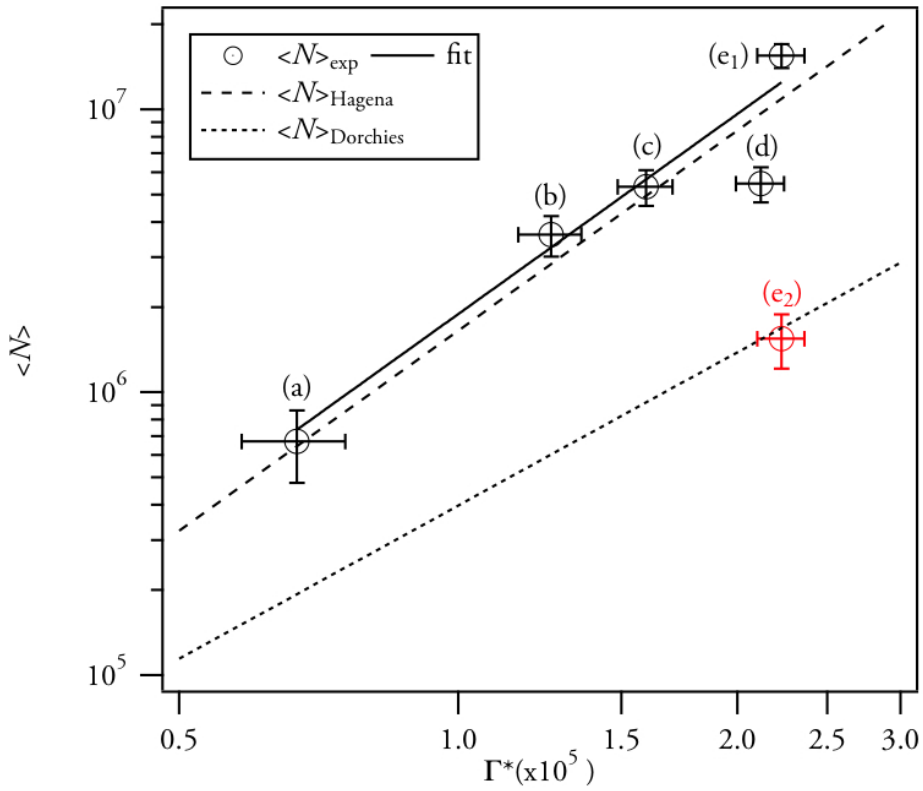

Figure 4.12.: Comparison of measured and calculated mean cluster sizes. The average number of atoms per cluster are plotted versus the cluster scaling factor Γ^*. The measured results are averaged cluster sizes from single shot scattering data, marked (a) to (e_2) corresponding to the notation in figure 4.10. The calculated cluster sizes, given as dashed lines, are performed based on [24] and [42] respectively.

In oder to verify the results for the mean cluster size they are compared to calculations based on scaling laws derived by Hagena ($\langle N\rangle_{\text{Hagena}}$, see [24]) and Dorchies ($\langle N\rangle_{\text{Dorchies}}$, see [42]). These scaling laws were chosen because both of them refer specifically to large numbers for the scaling parameter ($\Gamma^* > 1.8 \cdot 10^3$, cf. page 15). Figure 4.12 shows very good correlation of the measured data with the scaling law provided by Hagena, when the peak (e_2) is omitted from the fit. Using Hagenas scaling law as a reference the measurement can be fitted with

$$\langle N\rangle = A\left(\frac{\Gamma^*}{1000}\right)^B \tag{4.4}$$

with $A = 37.8 \pm 0.1$ and $B = 2.35 \pm 0.01$ being very close to the values given by Hagena ($A = 33.00$ and $B = 2.35$ [24]). The fit was weighted with the number of recorded frames per cluster size in order to minimize the influence of poor statistical data, as e.g. given in point (d). In the range of Γ^* considered in the experiments, Dorchies proposed $A = 100.0$ and $B = 1.8$ [42]. However, this results in significantly smaller mean number of atoms per cluster as depicted in the figure. This disagreement can be understand by taking the measurement methods into account. Different parts of the cluster beam were considered during the present measurements compared to Dorchies measurements. Dorchies used Rayleigh scattering measurements ([42]), which considers the entire cluster beam for the observation of the mean cluster size. In contrast to that, the scattering experiments presented in this thesis focus on clusters in the center of the

beam. In the case of atomic beams the center of the beam is the region with the highest density of atoms [113]. Therefore it can be assumed, that the center of a cluster beam consists of larger clusters compared to the wings of the beam. Hence, the scattering method gives an accurate measurement of the largest clusters in the beam, but it slightly overestimates the mean cluster size.

The second peak found in the measurements with $p_0 = 14.0\,\text{bar}$ and $T_0 = 200\,\text{K}$ is also displayed in figure 4.12 and denoted with (e_2). In contrast to previously discussed data, this peak shows a significant decrease in the mean cluster size compared to predictions for the mean cluster size derived from Hagenas scaling law. It rather shows good agreement with Dorchies scaling law. Therefore it is very likely that clusters from the outer wings of the cluster beam were imaged in the experiments, which results in a smaller mean cluster size. This could have happened due to a misalignment of the cluster source with respect to the FEL beam. However, this could not be verified due to weak statistic of this measurement. Hence the data point e_2 is omitted in the analysis and only presented for the sake of completeness.

4.4. Observation and discussion of twin clusters

The foregoing discussion of the scattering results revealed that two clusters in direct contact in the interaction region cause the second most common scattering pattern. The example in figure 4.5c showed that for these patterns the detector frame is dominated by a stripe-like pattern which is similar to the scattering pattern from a double slit. Similar scattering patterns can be found throughout the measurements almost independent from the expansion parameters. Figure 4.13 gives further examples of recorded scattering data originating from twin clusters. Due to the fact that single shot data is concerned, the orientation of the twin clusters vary from shot to shot. As a result, the orientation of the scattering pattern changes, too. Hence the alignment of the scattering figures depicted in 4.13a and 4.13b is a coincidence with no further meaning. However, these examples of twin cluster scattering patterns show very bright and clean fringes. Although these patterns are impressive, an example of a more common scattering pattern is shown in figure 4.13c. Here, the modulation of the scattering rings reveals the presence of a twin cluster. The interference fringes caused by twin cluster are so obvious that even frames containing very weak scattering signal can be identified as twin cluster scattering patterns. Figure 4.13d shows a corresponding example. This frame contains only a few scattered photons, but the interference caused by a twin cluster structure is clearly visible.

Scattering images of twin clusters can be found throughout an experimental measurement. The appearance of twin clusters within one experimental run is presented as an example in figure 4.14. The graphic shows the arithmetical mean of the intensity in the scattering pattern (AM_F in ADU) for every frame recorded during the run. High values of AM_F indicate a cluster that scattered a large amount of photons on the detector. The number of scattered photons is affected by the position of the cluster in the focus and the pulse intensity of the FEL. Both factors combined impact the amount of photons that hit the cluster and therefore the amount of photons potentially scattered on the pnCCD detector. This procedure is valid for all clusters regardless of their shape. Additionally, the size and scattering cross-section of the scattering objects influences the amount of scattered photons on the detector. Because twin clusters consist of two clusters sticking together, the scattering cross-section can be up to two times larger compared to a single cluster. Therefore, one would expect that on average twin clusters appear at higher AM_F values. However, figure 4.14 shows the occurrence of twin clusters at

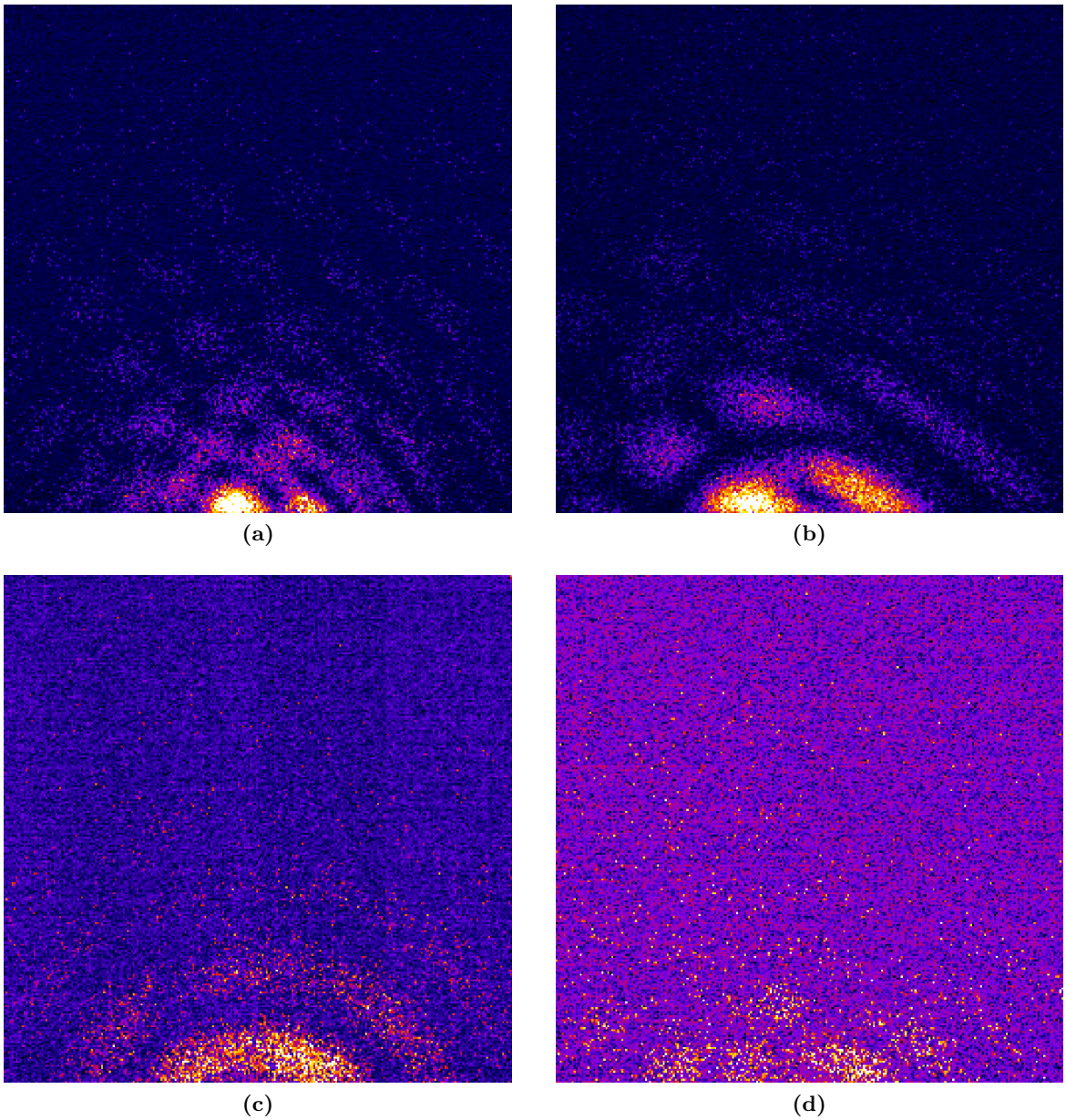

(a) **(b)** **(c)** **(d)**

Figure 4.13.: Examples of twin cluster scattering data. In most cases the scattering signal from twin clusters is obvious ((a) and (b)), but in some cases, only modulations of the ring structure reveal the origin of the scattering frame (c). Fringes from twin clusters can also be found in images where only a few photons were detected (d). (Xenon cluster, $p_0 = 13.3\,\mathrm{bar}$, $T_0 = 220\,\mathrm{K}$, $\lambda_{\mathrm{scattered}} = 13.3\,\mathrm{nm}$).

all different values and throughout the entire run, which emphasizes the uniform appearance of the twin clusters in the cluster beam. The abundance of these types of cluster formations throughout the recorded data suggests that the fundamental process of twin cluster formation is imaged, which is part of the cluster growth process.

As described in the section on the theoretical background of the formation of clusters in an expanding atomic beam, successive monomer addition by three body collisions dominates the cluster growth process. At a certain cluster size, a transition from monomer addition to cluster-

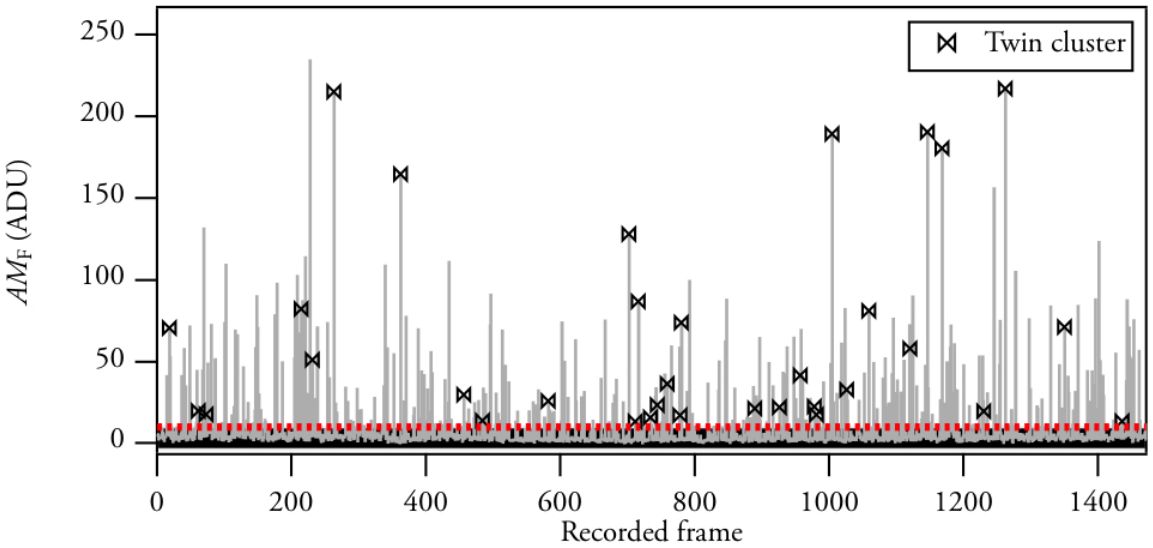

Figure 4.14.: Arithmetic mean (AM_F) of the scattering intensities of single shot images recorded during one experimental run at FLASH (xenon clusters, $p_0 = 10\,\text{bar}$, $T_0 = 220\,\text{K}$, $\Gamma^* = 159 \cdot 10^3$). The arithmetic mean of each individual frame in ADU is plotted versus the frame number. The read dashed line indicates the noise threshold. Scattering frames below it were not further analyzed. A detector image showing a twin cluster is marked ($\bowtie$). The twin cluster scattering patters appear almost constantly during the entire run.

cluster coagulation takes place. This transition between the two regimes has been studied experimentally by Soler *et al.* [8] by observing the cluster size distributions of carbon dioxide clusters with time-of-flight ion spectroscopy.

During these experiments the CO_2-clusters were produced using an adiabatic expansion. Varying the stagnation pressure changed the cluster size. An electron beam ionized the clusters in a time-of-flight detector with a beam energy set in a way that dissociation of the clusters was avoided. The time elapsed between the ionization of the clusters and there detection was recorded with a multichannel analyzer. Here, the flight time towards the detector of the clusters is proportional to their mass and therefore to the number of atoms in the clusters. The recorded mass spectra are shown in figure 4.15. With a stagnation pressure of $p_0 \geq 100\,\text{mbar}$ clusters were observed. The cluster size distribution shows an exponential decay with increasing cluster size until up to $p_0 = 700\,\text{mbar}$. For higher pressures, the distribution becomes peaked and at $p_0 \approx 2000\,\text{mbar}$ small clusters are absent in the spectra. However, the monomer peak is still present, even at high pressures due to residual gas. This transition of monomer presence to its nonappearance indicates a change in the growth process. In the scenario where monomers are detected the growth process of the clusters is dominated by monomer addition. At a certain point in the growth process the lack of small cluster sizes indicates an additional process, which consumes small clusters. Simultaneously, more and more larger clusters are visible and a significant shift of the mean cluster size towards larger cluster sizes occurs. Similar behavior can be witnessed in scenarios where the growth process is based on coagulation of smaller particles.

Soler *et al.* developed a mathematical model for the description of the observed cluster growth process. As a degree of freedom they introduced the parameter τ, which gives the degree of condensation. The core assumption of this model is that the growth process is dominated by binary collision and coagulation of clusters, while at the same time the evaporation of atoms

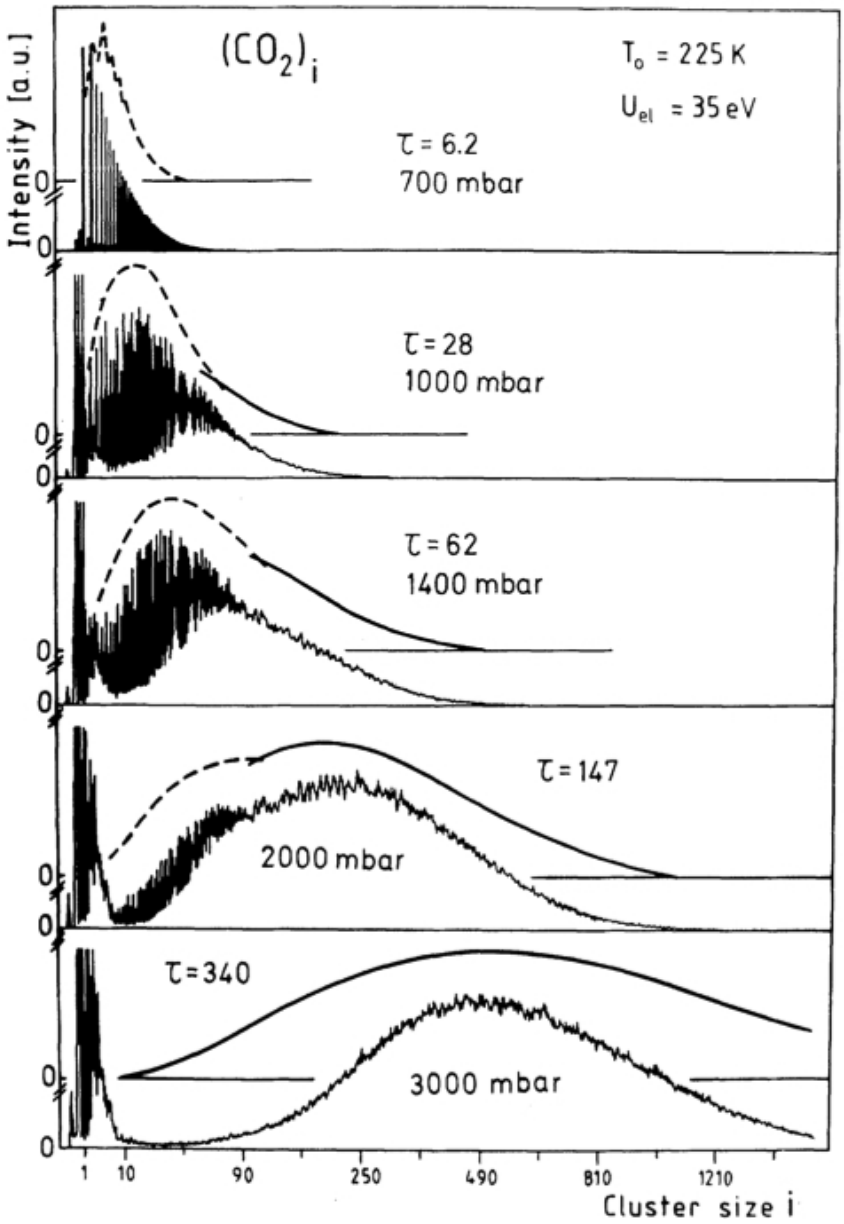

Figure 4.15.: Development of CO_2 clusters size distribution for constant temperature $T_0 = 225\,\mathrm{K}$ and different stagnation pressures p_0. This shows the transition from monomer dominated cluster growth to coalescence-dominated growth. The spectra are fitted with a function of single parameter τ that gives the degree of coagulation. See text for further details. [8]

from the clusters at all sizes is negligible. Then τ is used to solve the kinetic cluster-cluster coalescence equations, which describe the change of the concentration n_k of k-sized clusters per unit volumes over time [114],

$$\frac{\mathrm{d}n_k}{\mathrm{d}t} = \sum_{\substack{i+j=k \\ i \leq j}} C_{ij} n_i n_j - \sum_i C_{ik} n_i n_k. \tag{4.5}$$

The two sums of the equation 4.5 represent two antagonistic processes. The first term identifies

the rate at which k-sized clusters are formed by coagulation of smaller clusters. The second sum represents the loss of the k-sized clusters due to the growth of larger ones. C_{ij} and C_{ik} are the corresponding rates. For the coagulation rate C_{ij} one finds in the literature [115]

$$C_{ij} = 2\sigma_{ij}\left(\frac{2kT}{\pi}\right)^{1/2}\left(\frac{m_i + m_j}{m_i m_j}\right)^{1/2}.$$

Here, m is the mass of an i-sized cluster, k is the Boltzmann constant, and T the mean temperature in the cluster beam. σ_{ij} is the total cross-section of the coagulation. For larger clusters a simple droplet model with a sticking coefficient of unity can be assumed. The sticking coefficient is justified due to the low relative velocities of the clusters in the beam and the various vibrational modes into which the collisional energy of the clusters can be accommodated. With this assumption the coagulation cross-section equates the geometric cross-section of the clusters. Therefore, the coagulation rate can be normalized as

$$C^{\star}_{ij} = \frac{C_{ij}}{C_{11}} = \frac{\left(i^{1/3} + j^{1/3}\right)^2}{4\sqrt{2}}\left(\frac{i+j}{ij}\right)^{1/2}. \tag{4.6}$$

This function represents the experimental observation that small clusters disappear while larger cluster increase in number. For any value of $k = i + j$, the function $C^{\star}_{ij}$ becomes larger for increasing differences between i and j. For example, the increased coagulation cross-section explains the absence of small clusters for the interaction of a large cluster with a large cross-section and a small (fast moving) cluster.

With a volume $V(t)$ that contains $\mathcal{N}$ clusters in total and $\mathcal{N}_i$ i-sized clusters at any given time t the equation 4.5 can be written dimensionless:

$$\frac{\mathrm{d}n^{\star}_k}{\mathrm{d}\tau} = \sum_{\substack{i+j=k \\ i\le j}} C^{\star}_{ij} n^{\star}_i n^{\star}_j - \sum_i C^{\star}_{ik} n^{\star}_i n^{\star}_k, \tag{4.7}$$

were τ is defined by

$$\tau = \int_0^t 16\pi r_1^2 \left(\frac{kT(t')}{\pi m_1}\right)^{1/2} \frac{\mathcal{N}}{V(t')}\,\mathrm{d}t'. \tag{4.8}$$

During the expansion of the gas, for $V \to \infty$ the parameter τ reaches a maximum. This represents a frozen cluster beam with no further development of the cluster size over time.

In figure 4.15 the measured size distributions are compared to the calculations with (dashed-lines) and without (solid-lines) corrections of the ionization cross-section of the different sized clusters. Without these corrections these calculations cannot reproduce the measured spectrum for small clusters because of neglecting monomer addition. For larger clusters ($p_0 > 1000\,\mathrm{mbar}$) the agreement is much more accurate.

Following Soler *et al.*, the growth process for clusters larger than ~ 7 to 50 atoms is dominated by binary cluster-cluster collisions and coalescence of the clusters [8]. This growth process gives an explanation for the origin of the observed twin cluster scattering patterns. Twin cluster scattering patterns were found at any experimental parameters Γ^* with cluster sizes $\langle N\rangle \gg 50$. The distance of the clusters forming a twin cluster was found to be $< 2R$. Both observations support the theory that twin clusters are remnants of coalescing clusters imaged in the experiments. This statement can be supported by considering the following.

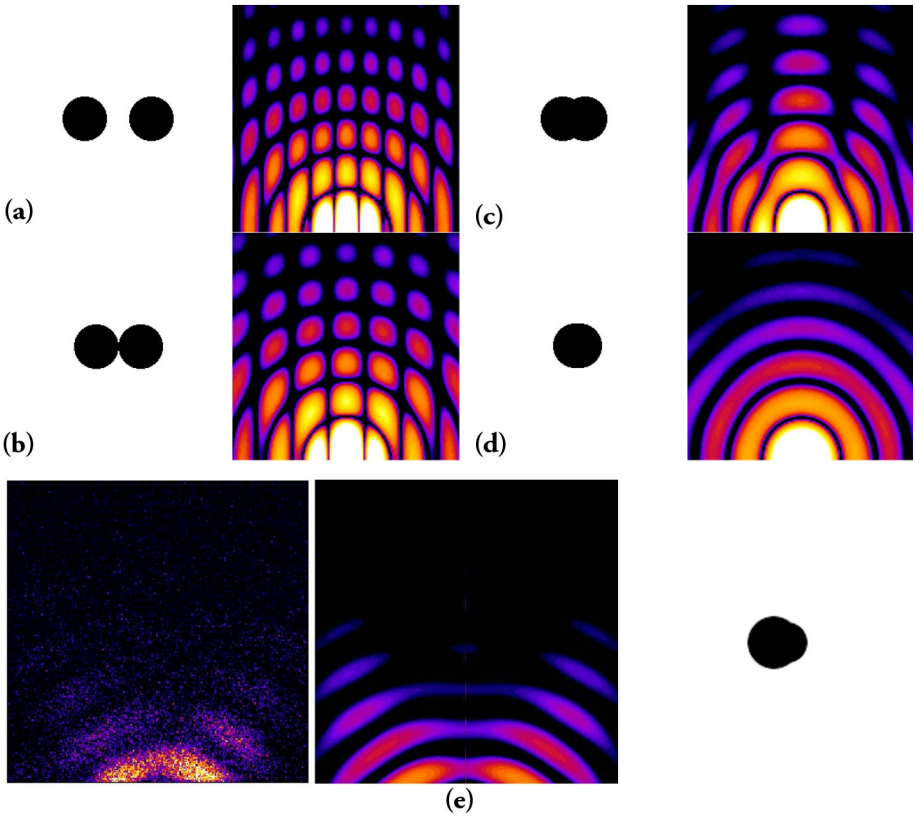

Figure 4.16.: By applying a 2D-Fast-Fourier-Transformation (FFT) on a mask with two black spheres, twin cluster like scattering patterns can be simulated. (a) to (d) are showing calculations for deceasing distance of the spheres leading to broadening of the speckles in the FFT patterns until the ring structure of a single sphere again dominates the transformation. Scattering patterns similar to the calculations can be found in the data. As an example (e) compares the FFT calculation with a recorded scattering pattern (left, xenon cluster, $p_0 = 10\,\mathrm{bar}$, $T_0 = 220\,\mathrm{K}$, $\Gamma^* = 159 \cdot 10^3$). Good agreement with the calculation is found for two spheres morphed together.

The scattering process can be compared to a Fourier transformation of the object. Figure 4.16 illustrates a two dimensional Fourier transformation of a mask containing two spherical items at a distance smaller than their radii. These transformation are showing similar structures compared to recorded scattering patterns. In 4.16 (a) to (d) a 2D-Fast-Fourier-Transformation (FFT) algorithm [110] was used to create corresponding simulated scattering patters. From (a) to (d) the distance of the center of the spheres in the mask was reduced from $d = 3\,R$ (a), $d = 2\,R$ (b), $d = R$ (c), towards $d = 0.2\,R$ (d), with R being the radius of the spheres. With decreasing distance the fringes in the FFT-image become broader until almost a complete ring structure is achieved (d). Comparable scattering patterns for all transient states were found in the experiments. As an example figure 4.16(e) shows a scattering pattern recorded from a xenon twin clusters produced at $p_0 = 10\,\mathrm{bar}$, $T_0 = 220\,\mathrm{K}$ together with a FFT simulation and the corresponding mask. The similarity of the measured data and the simulation is obvious. A detailed analysis of the comparison between simulation and twin scattering pattern was published in [108] and [15], were it was shown that almost all twin cluster scattering patterns can be understood by simulations taking size ratio, distance, degree of fusion, and rotational aspects of the simulated spheres into account.

4.4.1. Twin cluster formation - sticking of clusters

The formation of twin clusters is fundamental to the growth process of the clusters. Hence, the following shall illustrate the collision and sticking of clusters. Direct observation and imaging of coalescing clusters, as performed during this thesis, is a rather new technique. However, simulations based on molecular dynamics (MD) were performed in order to study binary collisions of clusters, e.g. [116, 117]. These simulations help to understand the conditions leading to cluster sticking and hence twin cluster formation. Figure 4.17 shows MD based simulations of the collisions of two argon clusters published by Ming *et al.*. The clusters in these simulations are formed by 1000 argon atoms with an interaction represented by a truncated and shifted Lennard-Jones potential. The initial positions of the cluster atoms were achieved by considering a close-packed sphere with an initial temperature of 10^{-4} K and minimizing the potential energy. This resulted in clusters with radii of 2.2 nm. Even though the clusters in the simulation are smaller then the clusters observed in the experiments carried out for this work, the results could be transferred because in both cases rare gas clusters composed of van der Waals bounds are considered.

The authors of the work illustrated in figure 4.17 studied the interaction between two clusters for different relative velocities ranging from $v = 100\,\mathrm{m/s}$ to $v = 1000\,\mathrm{m/s}$ in steps of $\Delta v = 100\,\mathrm{m/s}$ [116]. The studies were performed with different axial impact displacements b of the clusters, varied from 0 nm up to 4 nm. Depending on the values of v and b the outcome of the MD simulations varied drastically as shown by picture 4.17, which shows the three basic scattering channels observed. For low relative velocities, the kinetic impact energy is transferred into internal vibrational and rotational motions of the clusters. As a result the clusters seem to coalesce (a). Depending on the kinetic energy of the collisions the penetration depth of the clusters varies. For sufficiently slow relative velocities (the authors conclude less then 250 m/s) this behavior is observed for all impact parameters b. On the left hand side of figure 4.17 the limit for coalescence is illustrated. The small impact parameter combined with higher relative velocity $v = 400\,\mathrm{m/s}$ still causes coalescence, but also shows deformation of the cluster. Slightly higher velocity combined with heavy axial displacement leads to a stretching separation of the clusters (b). Even the formation fragments forming smaller clusters (denoted as "satellites") is possible. Here, the largest fragments of the impact contain 700 to 1200 atoms. On the upper end of the velocity scale shattering with the total destruction of the clusters is characteristic for all values of b (figure 4.17(c)).

For coalescing of the analyzed argon clusters, Ming *et al.* give a maximum relative velocity of 250 m/s [116]. When considering xenon, like in the presented scattering experiments, the relative velocity has to be reduced due to the mass ratio of argon and xenon in order to obtain an impact with the same momentum. Therefore, a maximum relative velocity for sticking as a result of a binary cluster-cluster collision can be given as 75 m/s for two xenon clusters similar to the clusters in the publication.

As we will see, the velocities for shattering and stretching separation will not be achieved during the formation of the clusters in the cluster beam used in the presented experiments. According to Hagena, the flow velocity of an expanding gas jet increases up to a limit v_∞ [24]:

$$v_\infty = 1.581 \sqrt{\left(\frac{2kT_0}{m}\right)} = 204 \sqrt{\left(\frac{T_0[\mathrm{K}]}{m[\mathrm{amu}]}\right)}\ \mathrm{m/s}. \tag{4.9}$$

with the atomic mass unit $1\,\mathrm{amu} \mathrel{\hat{=}} 1.660 \cdot 10^{-27}\,\mathrm{kg}$ and T_0 the temperature of the nozzle in Kelvin. For xenon at 220 K this gives a velocity of $v_\infty \sim 264\,\mathrm{m/s}$. Similar velocities are

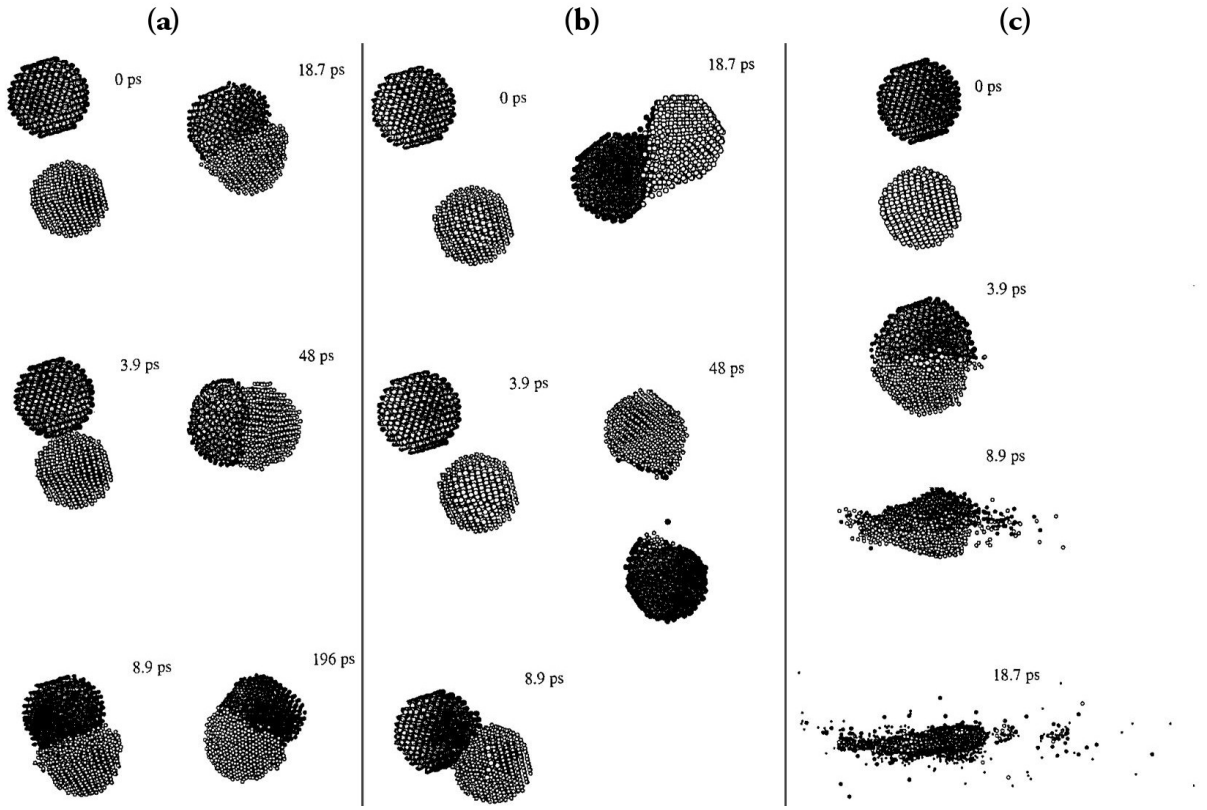

Figure 4.17.: Simulation of cluster-cluster scattering. The molecular dynamics simulation (MD) of two Ar_{1000} cluster with an initial temperature of 10^{-4} K shows the collision with different relative velocities v and off-center displacements b. Depending on v and b the outcome of the collision varies drastically. From left to right: $v = 400\,\mathrm{m/s}$, $b = 1\,\mathrm{nm}$ results in coalescence of the clusters (a), (b) shows "stretching separation" for $v = 500\,\mathrm{m/s}$, $b = 3\,\mathrm{nm}$. The high relative velocity of the simulation in (c) ($v = 1000\,\mathrm{m/s}$, $b = 0\,\mathrm{nm}$) results in shattering of the clusters. From [116]

expected to be reached when the formation of clusters comes to an end due to depletion of the beam. This is the case at a distance $x/d < 5$ where d is the distance from the nozzle and d is the equivalent nozzle diameter. At this point collisions within the expanding beam has come to an end [31] and a Mach number of $M \approx 10$ is reached (see page 9). Hence one obtains for the speed of sound in the beam at this point $c = v/M = 26\,\mathrm{m/s}$. The speed of sound determines the maximum velocity within the boundaries of the expanding gas jet. Therefore it can be assumed that relative velocities of colliding clusters are also below c and hence in the regime of sticking.

All in all, with the relative velocities, binary cluster-cluster collisions lead to sticking during the expansion of the beam. The next steps would require a more accurate analysis of the colliding clusters in the beam. First molecular dynamic (MD) simulations were performed in this field [118] and helped to shine light on the cluster growth and twin cluster formation. However, the cluster size suitable for imaging requires large clusters with more the 10^6 atoms, making numeric calculations challenging. The benefit of such simulations is that further influences of the twin formation can be examined, like the influence the shape of the cluster nozzle. A first attempt for simulating the cluster formation process is presented in the following section.

4.4.2. Simulation of cluster growth

The imaging experiments revealed a coexistence of twin clusters and spherical clusters almost independent of the experimental parameters (c.f. figure 4.6 on page 84). By considering the cluster formation process it was argued that the twin clusters originate from binary collisions during the phase of cluster growth. Therefore one could assume that dumbbell- or similar shaped clusters are the most frequent form for rare gas clusters. Twin clusters are detected quite frequently but not for every scattering pattern. On the one hand, one can argue that twins are remnants of the cluster formation and every cluster undergoes this state during its formation. This raises the question, why the twins are relatively rare (about 20% of the data show twin-like shape). On the other hand, compared to a spherical shape, the twin clusters are energetically unfavorable, which means that relaxation into spherical shape has a high probability. This puts a second question; Why are twin clusters still present milliseconds after their formation? In the following simulation a solution to this apparent contraction is proposed, considering a transition of the clusters from a dumbbell-shaped cluster to a spherical cluster. It will be discussed that this transition can be interpreted as a transition of the clusters from solid to liquid state. A solid cluster conserves its shape where as a liquid cluster will try to minimize its surface area due to surface tension and form a spherical cluster.

The developed simulation software program "ClusterSim" (CS) aims to simulate the development of a given cluster distribution based on binary cluster-cluster collisions. In order to ensure mass conservation through the entire simulation, the number of atoms is kept constant. However, due to the fact that cluster size distributions are simulated, individual atoms are not considered. Instead, a huge amount of small clusters is used as a simulation seed. CS uses collision detection based on a hard sphere cluster model to calculate the cluster interactions. During the collision, the software keeps track of all sub-clusters allowing the user to observe the formation of twin clusters or even higher orders. In the presented version of CS, cluster temperature, collision impact heating, and cooling by evaporation are not taken into account in order to increase the performance of the simulation at the expense of accuracy. The relaxation of twin clusters in spherical shape is calculated based on a (user provided) merge probability that can be adjusted to obtain agreement with the measured data. For performance reasons, CS is written in C++. A graphical user interface is realized using the Qt4.8 framework, which also enables CS to be compiled on multiple platforms. Details regarding the framework can be found in [102].

The cluster growth is described by an algorithm as depicted schematically in figure 4.18a. A pool of clusters represents the initial cluster size distribution. Several iteration steps are performed until the program terminates at a given number of steps. For every iteration, two clusters are picked from the pool randomly. With a certain probability, which will be discussed in detail later, these two clusters interact. The interaction results in a dumbbell shaped cluster having a certain probability to relax into spherical shape. The resulting cluster is returned to the pool, before a new pair of clusters is taken from the pool for the next step of the simulation. This procedure is repeated until a given number of cluster-cluster interactions are simulated.

The interaction probability is obtained from binary collision theory as outlined in [8] and corresponds to the coagulation rate derived in the paper. For two given clusters with i and j as their numbers of atoms, the rate is given by

$$C_{ij}^{\star} = \frac{(i^{1/3} + j^{1/3})^2}{4\sqrt{2}} \left(\frac{i+j}{ij}\right)^{1/2} \tag{4.10}$$

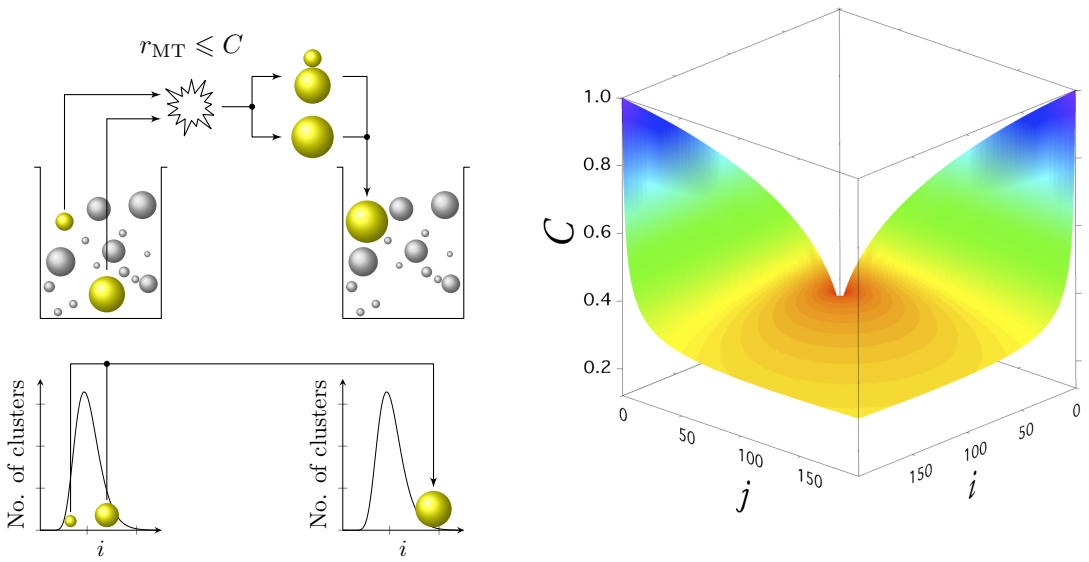

(a) (b)

Figure 4.18.: Simulation of binary cluster collisions as described in the text. (a) principle of the binary collision simulation. Two clusters are picked randomly from a pool. There interaction probability is calculated using C (see equation 4.11). If they interact, the probability of forming a twin cluster or a single cluster is calculated before the resulting cluster is returned to the pool. (b) illustrates the collision weighting function C. i and j denote the number of atoms in the colliding clusters.

where the star denotes the normalized interaction rate: $C^*_{ij} = C_{ij}/C_{11}$. For any given i and j $C^\star_{ij}$ becomes larger the smaller either i or j becomes (compare figure 4.18b). As pointed out in [8], this is due to the fact, that larger clusters have a larger cross-section, while smaller clusters are faster. A combination of both results in an increased interaction rate and in the disappearance of small clusters during the formation of larger clusters.

For the simulation of the cluster collisions the boundaries of $C^\star_{ij}$ are important because $\lim_{j\to\infty} C^\star_{1j} \to \infty$. The same is true for $i \to \infty$. Therefore $C^\star_{ij}$ was normalized by considering a cluster with $N = \mathcal{N}$ atoms where $\mathcal{N}$ denotes the total amount of atoms in the simulation. A cluster containing $\mathcal{N}$ atoms is the largest cluster achievable in the simulation. The $\mathcal{N}$-sized cluster is also formed from a binary collision. It is unlikely that binary collision occurs between two clusters with extremely different cluster size. It is much more likely that this collision happens between two equally sized cluster: $N_1 \approx N_2 \approx \mathcal{N}/2$. Even though both clusters will not be equally sized, $\mathcal{N}/2$ gives a good reference for maximum imbalance of the atomic distribution throughout the simulation. Hence it can be used as a normalization factor for $C^\star_{ij}$:

$$C = \frac{C^\star_{ij}}{C^\star_{1\mathcal{N}/2}}. \tag{4.11}$$

This function is displayed in figure 4.18b. An interaction between two randomly drawn clusters is achieved if $r_{MT} \leqslant C$, were r_{MT} is a randomly generated number in the interval $[0, 1]$[a]. Now,

[a] MT denotes the random generator used by CS: Mersenne Twister MT19937ar, a fast pseudo random number

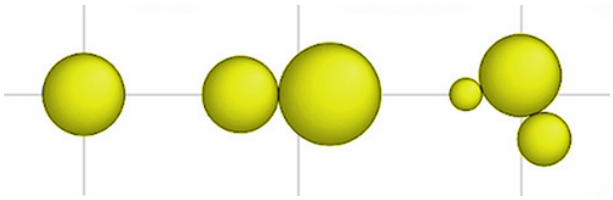

Figure 4.19.: Simulated cluster shapes with ClusterSim (CS). The different shapes are formed from binary cluster collisions. CS uses hard sphere collision detection for the simulation of these shapes. The clusters have a certain probability to reorganize in spherical shape. This probability can be adjusted in order to match experimental observations.

the two clusters are considered as colliding and a hard sphere, center-of-mass collision between the two clusters is performed under a randomly picked collision angle. For simplicity, the simulation calculates only collisions in 2D. This assumption does not limit the simulation, because the absolute positions of the sub-clusters in 3D are not important. Instead, this can be seen as the projection of the interaction on the 2D plan. However, a further improvement of the program could supply 3D simulation. During the collision any geometrical shape of the cluster is preserved, e.g. if one of the clusters consists of several sub-clusters (like a twin cluster) the simulation will retain this structure. An example of a single cluster, twin cluster, and a triple cluster is given in figure 4.19.

In order to enable the simulation to determine the merging of the cluster in a spherical shape, the user provides a "merge probability" (m_p) for the clusters. This probability (given in percent from 0 to 100) denotes the probability of a colliding cluster to merge into a spherical shape. m_p is interpreted as a mean cluster temperature relative to the melting point (T_m) of the clusters. The introduction of m_p is a simplification because the temperature as well as the melting point of a cluster are highly complex factors of the cluster formation process. Besides the cooling of the gas due to the adiabatic expansion, collisions of clusters increase the temperature of the clusters which again is reduced due to evaporation of surface atoms. The melting temperature of the clusters depends on the cluster size. The cluster temperature and the simplification introduced with m_p will be further discussed after presenting the simulated data (see section 4.4.3).

Considering the "merge probability" (m_p) as a measure for the amount of clusters exceeding the melting temperature T_m of the cluster beam. A cluster exceeding T_m becomes liquid and is able to relax into spherical shape. A high value for m_p illustrates a cluster beam with warm clusters and therefore a simulation producing only few twin clusters. By adjusting m_p, the amount of twin clusters generated by the software was matched with the amount of twins detected in the experiments.

The simulation uses a log-normal cluster size distribution as a starting point. The distribution is defined by the mean cluster size and the standard derivation. For the simulation the average cluster size has to be in a regime where cluster growth is dominated by binary collisions of clusters, meaning a mean cluster size greater 50 atoms per cluster. As a starting point for the simulation a log-normal cluster size distribution of 320 000 clusters was picked ranging from five atoms per cluster up to 280 atoms per cluster with a mean of 50 atoms per cluster. This initial starting distribution is shown as the topmost graph in the waterfall plot in figure 4.20. However, this amount of clusters in the distribution is a compromise due to computational time

generator with a period of $2^{19937} - 1$. The periodicity of a random generator denotes the number of random numbers it can produce before any repetition is observed. MT19937ar offers a sufficiently large one to simulate cluster-cluster interaction. See [119, 120] for details.

for the simulation as pointed out by the following estimation.

For a nozzle expansion, the density of atoms in the nozzle can estimate the cluster density at the beginning of the expansion. For xenon with a stagnation pressure of 10 bar and a gas temperature of 220 K one obtains a density of $\rho \approx 71.8\,\mathrm{kg/m^3} = n_0 = 3.4 \cdot 10^{26}\,\mathrm{Atoms/m^3}$. More meaningful than cubic meters is a normalization for a volume with a radius in the order of the cluster nozzle diameter: $V_{\mathrm{Nozzle}} \sim 10^4\,\mu\mathrm{m}^3$ for a nozzle with $d = 100\,\mu\mathrm{m}$. The resulting number of atoms is $n_0 = 3 \cdot 10^{12}\,\mathrm{Atoms}/V_{\mathrm{Nozzle}}$. With this amount of atoms and a condensation of 100%, $\sim 6 \cdot 10^{10}$ clusters with $\langle N \rangle = 50$ can be formed. These are five orders of magnitude more clusters then in the simulation. However, increasing the number of clusters in the simulation to $1 \cdot 10^7$ takes about 46 hours of computational time. Due to the large amount of independent cluster-cluster collisions, the program would be ideal for the use of massive parallel processing, which could reduce the computation time significantly.

The duration of the simulation is limited by computational time. In the experiments cluster sizes with 10^6 atoms per cluster have been observed. Beginning with 10^{10} clusters with 50 atoms, one can obtain 10^6 clusters with one million atoms each. This is a reduction of four orders of magnitude with respect to the initial amount of clusters. For the simulation a reduction from 320 000 cluster to 2 500 clusters was considered, as any further increase in the orders of magnitude considered increases computation time significantly. However, the first observation of the cluster growth process could be reproduced and will be presented here.

By successively increasing the simulated cluster-cluster interactions, the development of the cluster size distribution can be observed. The results of such a simulation are shown in figure 4.20. Here, the cluster distribution develops from top to bottom. For every histogram the total amount of clusters in this particular experimental step are denoted beginning with 320 000 clusters. Dividing the number of clusters in the simulation in half means, that on average every cluster has performed an interaction. Hence, the right hand side of the figure gives the average number of collisions per cluster (ANC). For better comparison, the height of the different cluster size distributions is normalized to one.

The initial distribution appears as a bell-shaped curve in the logarithmic scale. The logarithmic scaling compresses the slowly decreasing edge towards larger clusters. This edge leads to an amplification of the appearance of larger clusters, which can be seen in the increasing slope of the size distributions with increasing ANC. In parallel to that, smaller clusters are starting to vanish. Both effects lead to a shift of the mean cluster size $\langle N \rangle$ towards larger clusters. By comparing the mean cluster size to the average number of collisions per cluster one can calculate the number of collisions per cluster necessary to reach a given cluster size.

Figure 4.21 compares $\langle N \rangle$ obtained from figure 4.20 with the average number of collisions per cluster (ANC). The calculated mean cluster sizes are given in the graph. The growth of the mean cluster size is exponential and can be fitted using

$$\langle N \rangle(\mathrm{ANC}) = c_0 + c_1 \cdot 2^{\mathrm{ANC}} \tag{4.12}$$

where the fitting constants are donated by c_0 and c_1. The exponential base ("2") represents the binary collisions underlying the simulation. For the fit constants $c_0 = 10.3 \pm 2.2$ and $c_1 = 46.1 \pm 0.3$ is found. The fit agrees very well with the simulation, which can be seen in the embedded graph in figure 4.21. The fitting parameters strongly depend on the width of the initial cluster size distribution. An extrapolation of the fitting function 4.12 is shown in the figure 4.21 in blue. From that extrapolation the development of the mean cluster size

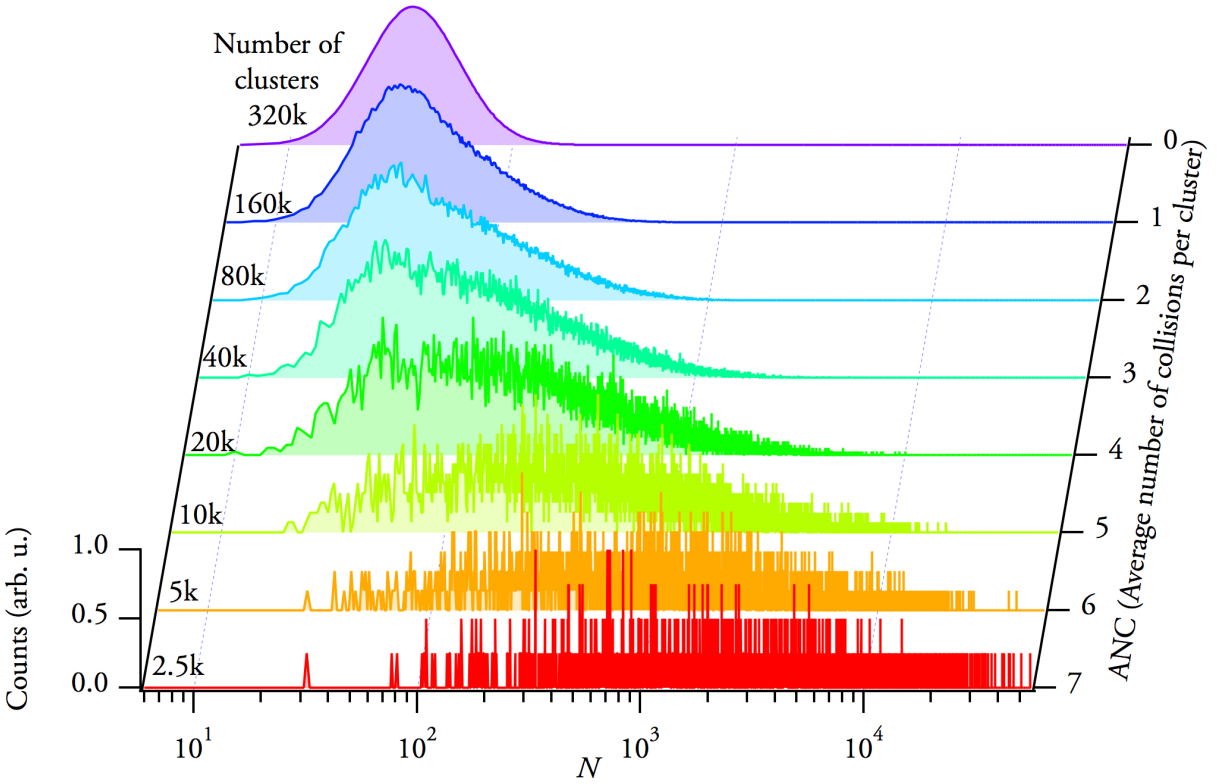

Figure 4.20.: Abundance of clusters simulated with ClusterSim (CS) (details see text). Beginning with an initial cluster size distribution of $320 \cdot 10^3$ clusters the development of the cluster size distribution is depicted. The binary collisions lead to a broadening of the distribution with a shift of the mean cluster size towers larger cluster. For better comparison the distributions are normalized to one.

with further increasing ANC can be seen. This gives an approximation of the evolution of the simulation, if it could be run for a longer time. For example, one can see, that a mean cluster size of $\langle N \rangle = 10^6$ is reached after $ANC \approx 14$. Taking into account that it takes about six binary collisions to exceed a mean cluster size of 50, the obtained 14 collisions required to reach 10^6 atoms are in good agreement with the expectation.

Before comparing the results from the single cluster and twin cluster distribution with the results from the experiments, the influence of the normalization function C (see equation 4.6 on page 96 and equation 4.11 on page 101, respectively) should be discussed. Figure 4.22 shows the cluster size distribution for ANC = 6 plotted in grey. For better comparison, the distributions are overlaid with a smoothed version of the distribution (black). The top distribution, which is calculated without using C, appears broader compared to the distribution on the bottom. The appearance of smaller clusters ($N < 10^2$) is particularly more distinct. The same observation can be made for larger cluster sizes ($N > 10^3$), although the effect is not as obvious as for small cluster sizes. Compared to cluster size distributions in other experiments, e.g. observed by Soler *et al.* [8], the simulation results appear broader. This could have various reasons. For example, the simulation omits decay of clusters or detection efficiencies for different cluster sizes. The usage of the normalization factor C (see equation 4.11) for the simulation results in more compact distributions, even though the effect could be stronger.

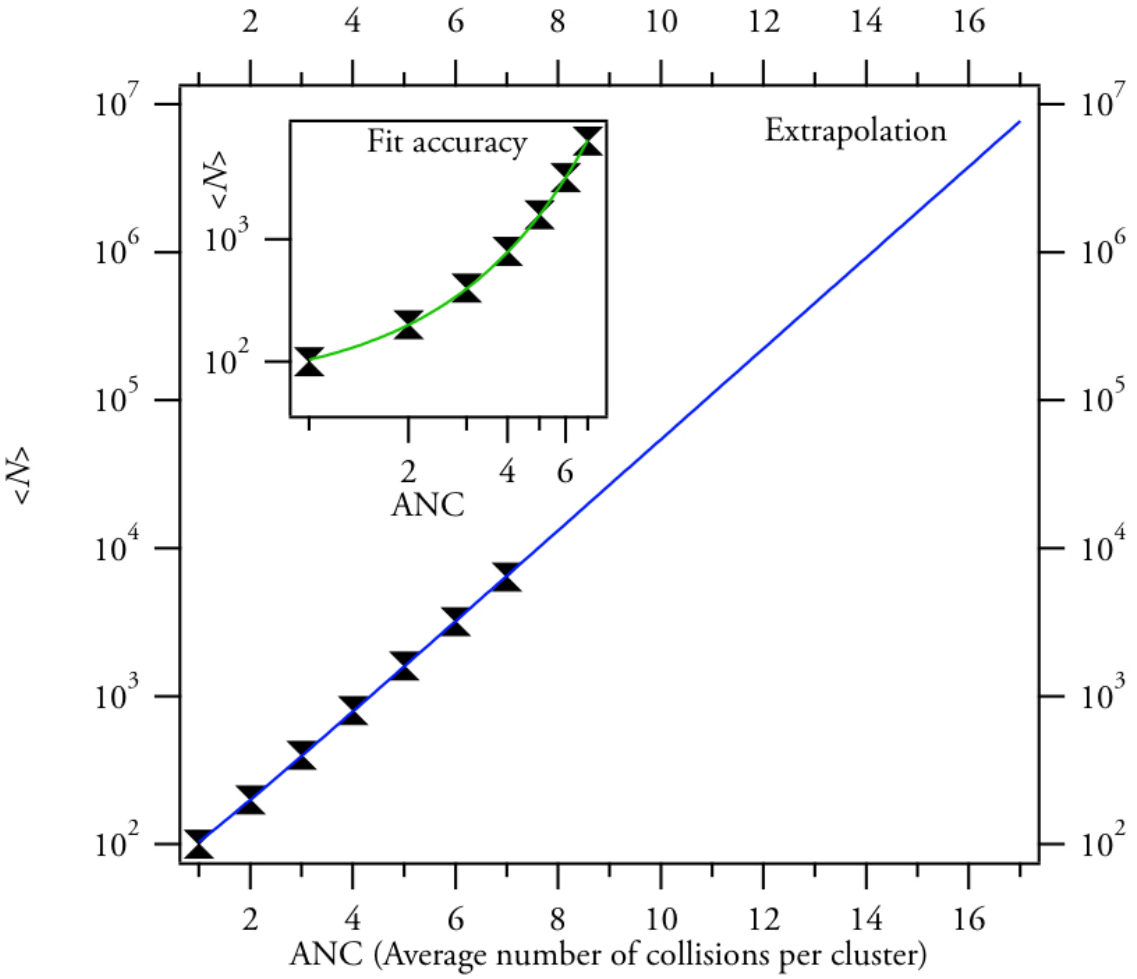

Figure 4.21.: Development of the mean cluster size $\langle N \rangle$ with increasing ANC. Marked (⧗) are the mean cluster size values obtained from the simulation shown in figure 4.20. The simulation results were fitted as described in the text. The fit is depicted in the embedded graph and extrapolated towards larger cluster sizes (blue).

The intention of the development of the simulation software CS was to reproduce the distribution of single and twin clusters as observed in the experiments (cf. figure 4.6 on page 84) in order to obtain a merge probability factor (m_p) for the given experimental parameters. During the measurement xenon clusters were produced from a stagnation pressure of $p_0 = 10\,\mathrm{bar}$ at a nozzle temperature of $T_0 = 220\,\mathrm{K}$ ($\Gamma^\star = 159\,000$). This measurement was selected, because it contains the most significant statistic of all measurements minimizing fluctuations in the data. In this measurement 87% of the recorded frames contained single cluster scattering patterns. In 12% of the data, twin clusters were found which was determined by analyzing all scattering frames by hand.

Figure 4.23 shows the comparison between simulation and measurements. The results are classified accordingly to the amount of sub clusters forming a cluster. In this context, a single cluster is denoted as “1”, a twin cluster as “2” and so on. Clusters containing more than four sub clusters are also found in the simulation data, but they are very rare. Therefore, corresponding events are summarized and marked as miscellaneous (“Misc.”). The simulation is compared

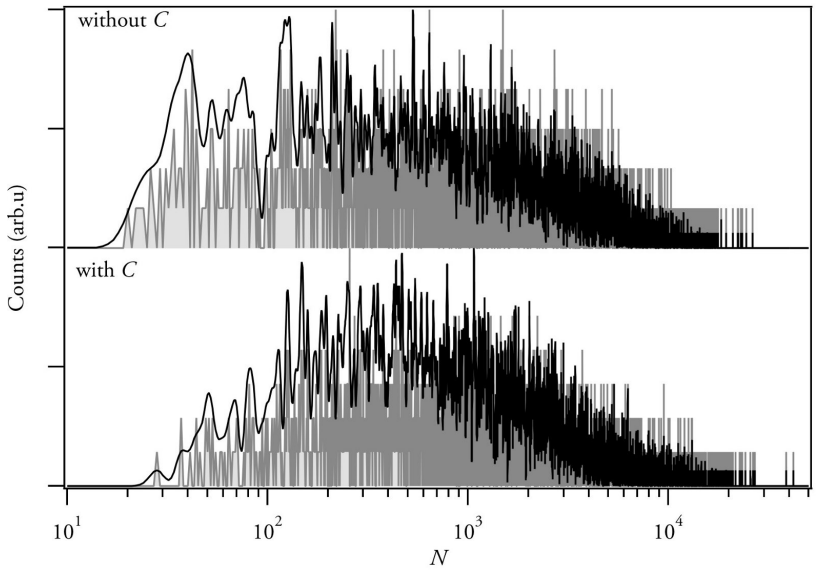

Figure 4.22.: Comparison between a simulation using the normalizing function C and a simulation without C. Shown is a histogram of the cluster sizes simulated after $ANC = 6$. The normalization function reduces the width of the cluster size distribution, which can be seen by the absence of small cluster sizes in the lower graph, although the difference is relatively small. The black line is a smoothed representation of the histogram in oder to ease comparison of the two graphs.

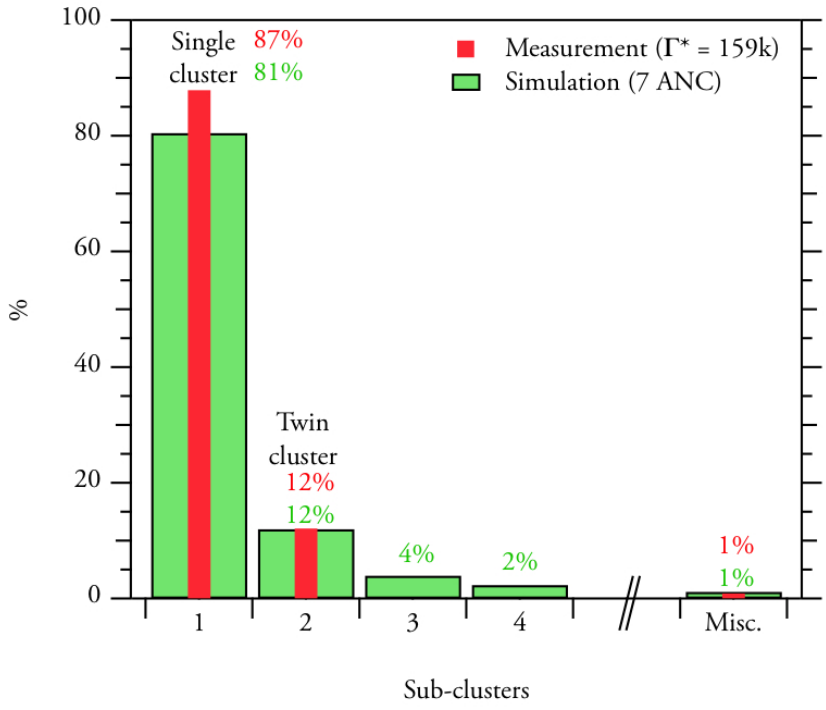

Figure 4.23.: Distribution of different cluster shapes obtained from CS in comparison with measurements. For the simulation a merging probability of 80% was assumed. Reasonable agreement with experimental data is achieved. The red and green percentage numbers give the exact result of the simulation (green) and the experiment (red), respectively. The experimental data was recorded from xenon clusters ($p_0 = 10\,\text{bar}$, $T_0 = 220\,\text{K}$). This dataset was chosen for comparison due to the reliable statistic.

to the measurements, which are shown in red in the figure. Clusters with more than two sub clusters were not identified in the data. Unidentified clusters are also counted as miscellaneous. In order to obtain the simulated data shown in the figure CS was run several times, each run was performed with a variation in the merge probability (m_p). The obtained distribution was compared to the measurements with the aim to find agreement with the amount of twin clusters measured. A very good agreement was found for a simulation with $m_\mathrm{p} = 80$ which is shown in figure 4.23. Because m_p can be interpreted as the amount of clusters over the mean melting temperature T_m of the cluster beam, the simulation indicates that on average about 80% of clusters exceed T_m. Hence, these clusters can be considered as liquid in the in the area of the nozzle marking the part of the beam where cluster formation takes place.

Even though the agreement between experimental data and simulation is satisfying, one can sees that the simulation underestimates the amount of single clusters found in the data. In contrast to that, clusters containing three or more sub clusters appear in the simulation. Corresponding cluster ensembles were not identified in the experimental data. It can be assumed that clusters with 3 or more sub clusters have a largely increased probability of merging into spherical shape in comparison to clusters with only 2 sub clusters. A simulation with the merge probability (m_p) varying in dependence of the number of sub cluster would therefore further improve the simulation of the measured data. However, the presented tool very well simulates the experimental data and especially the twin cluster formation. The general formation of larger clusters with a high amount of sub clusters was indeed observed in other experiments and represents an interesting filed for future research [15]. However, their appearance is not relevant for the work presented here because in the discussed data corresponding complex cluster structures were not identified.

The findings of the simulation have to be considered in relations to the cluster sizes found in the experiments. On average the first 7 collisions per cluster (ANC) were captured by the simulation. In contrast, clusters observed in the experiment had undergone $\sim$ 20 ANC until imaged. Certain changes of the cluster beam occur during this longer time of flight. With an increased number of collisions larger clusters are formed and the cluster density in the beam is reduced. Larger clusters collide with a higher kinetic energy due to their increased mass. However, due to the increased number of atoms in the cluster the collision energy per atom remains constant. This means that the amount of energy a cluster can absorb before melting also increases. In contrast to that, the reduced cluster density increases the time between the cluster-cluster collisions, giving the clusters time to cool down by evaporating surface atoms. The mean cluster temperature in the beam drops. As a result, the amount of liquid clusters able to reorganize their atoms in spherical shape is also reduced. Hence, more twins and more complex cluster structures should be visible, which is not the case in the presented experiments. Therefore it can be stated the cooling is overestimated in this argumentation and that the approximation made for CS are justified.

It can be concluded from the simulation that the introduced parameter m_p is a very important factor for the modeling of the experimental results, regarding the ratio of twin to single clusters. The merge probability m_p was interpreted as the amount of clusters succeeding the mean melting temperature in the cluster beam, because a liquid cluster is able to reorganize its atomic structure in an efficient way in order to translate its shape from a dumbbell structure to a spherical one. The following section discusses the cluster temperature in more detail.

4.4.3. Twin cluster appearance and cluster temperature

At a certain point the main cluster growth process undergoes a transition from successive monomer attachment to a cluster growth based on cluster-cluster collisions leading to dumbbell-shaped clusters. Even though a spherical shape is an energetic favorable state, a certain amount of energy is required in order to reorganize the atoms. This energy can originate from the kinetic energy obtained from cluster-cluster collisions during the cluster growth, increasing the internal energy of the clusters. Yet, evaporation of surface atoms reduces the internal energy. If many cluster-cluster collisions and/or collisions with high energetic impact occur, evaporation can not cool the cluster in sufficiently short time. The internal energy of the cluster increases and rises the amplitude of the thermal oscillation of the atoms in the cluster until the atoms change position in the lattice structure. The cluster melts and can reorganize and relaxes into spherical shape. Evidently, the melting temperature is a critical aspect for the observation of twin clusters.

The melting temperature T_m can be used for the quantification of the energy needed to reach the regime of reorganization. However, one has to take into account, that the melting temperature of clusters is size-dependent, e.g. [7]. Following Lindemann [121], a crystal melts if the mean thermal vibration amplitude of its atoms $\langle u \rangle^{1/2}$ exceeds $\sim 10\%$ of the distance to the nearest neighboring atoms. In case of a crystal lattice the oscillation of an atom is reduced due to the presence of the neighboring atoms. Any locally induced thermal energy is dissipated into the surrounding medium. In contrast to that, it is possible for atoms on the surface to oscillate freely perpendicular to the surface, because the overall binding energy is reduced. As a result, one finds a lower melting temperature at the surface of a crystal. For clusters this is an important characteristic because a cluster has much more surface atoms compared to its overall amount of atoms than a solid state body, illustrated in figure 4.24a. For smaller clusters the melting temperature drops because the clusters contain more surface atoms compared to the entire number of atoms in the cluster. As an example, measurements for bismuth clusters [122] or argon clusters can be found [123]. A argon cluster measurement is shown in figure 4.24b. For larger cluster, the melting temperature approaches the bulk melting temperature, scaling with $N^{-1/3}$, N is the number of atoms in the cluster as discussed by Rytkönen *et al.* [123].

During this work xenon clusters were used as targets for the scattering experiments. So that the observations of the cluster melting temperature will be adopted for this material, since no corresponding data was avalable. For solid xenon a melting temperature of $T_\mathrm{m}^\mathrm{b} \sim 161\,\mathrm{K}$ was found (e.g. [124]). Figure 4.24b shows the ratio of the cluster melting temperature to argon bulk temperature versus the number of atoms in the cluster represented by $N^{-1/3}$. The linear fit in the figure is achieved using [123]

$$T_\mathrm{m}^\mathrm{c} \propto T_\mathrm{m}^\mathrm{b} - N^{-1/3}. \tag{4.13}$$

In equation 4.13 T_m^c is the melting temperature of the cluster, T_m^b represents the melting temperature of the bulk, and N is the number of atoms in the clusters [123]. From the figure one can estimate that for clusters with more the 125 000 atoms ($N^{-1/3} = 0.02$) the melting temperature approaches the bulk value: $T_\mathrm{m}^\mathrm{c}/T_\mathrm{m}^\mathrm{b} = 0.95$. Assuming that the twin clusters image originate from the last cluster-cluster collision before they reach the interaction region, this discussion is focussed on the collision of large xenon clusters with 10^6 atoms. Hence the assumption $T_\mathrm{m}^\mathrm{c} \approx T_\mathrm{m}^\mathrm{b} = 161\,\mathrm{K}$ is appropriate, corresponding to 14 meV thermal energy.

Considering the results from the simulation of the cluster growth process (e.g. see figure 4.23

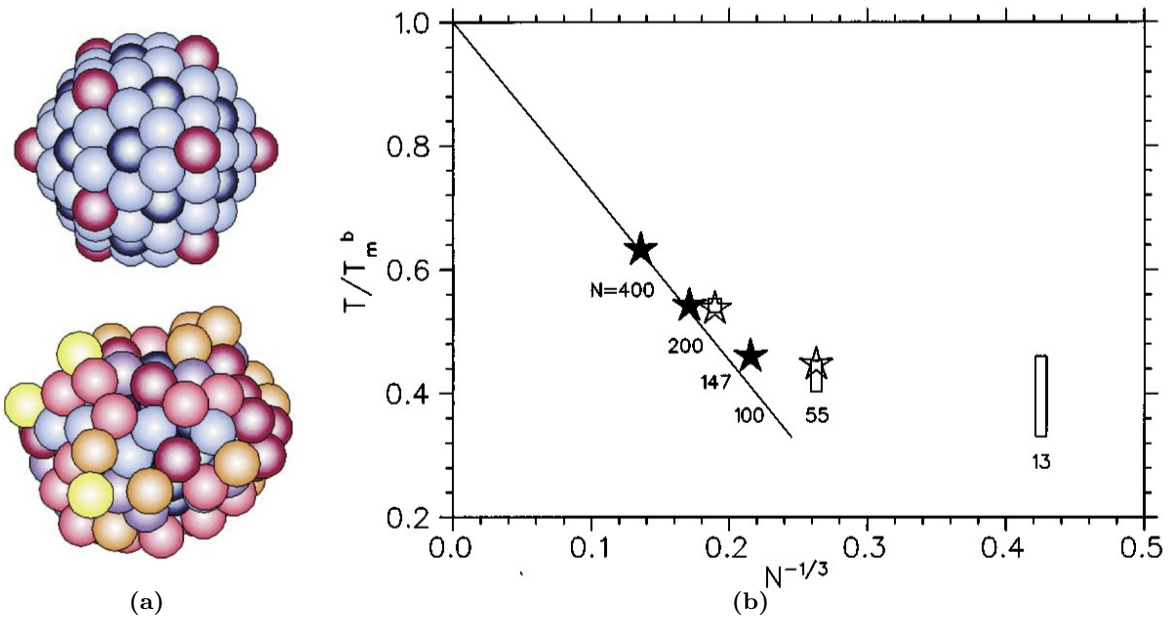

Figure 4.24.: The melting process of clusters. The left hand side (a) shows a Lennard-Jones potential simulation of a sodium cluster with 147 atoms at $T = 0$ (top) and higher temperature (bottom). A darker color indicates strongly bound atoms. Weekly bound atoms in the hot cluster can change their position. [125]. On the right hand side (b) the measured melting temperature of argon clusters for different cluster sizes N illustrate the size dependence of the melting temperature. Open stars are simulations, closed stars represent experimentally determined melting temperatures of Ar_{100}, Ar_{200}, and Ar_{400} clusters, respectively. For $N^{-1/3} \approx 0.02$ the melting temperature of the cluster is about 95% of the bulk melting temperature. [123]

on page 106), about 80% of the clusters must exceed T_m^c in order to perform the transition from twin cluster to spherical cluster. This seems to be in conflict with findings regarding the cluster temperature which will be discussed in the following.

One can consider the work of Farges *et al.*, who performed a study on the structure and temperature of rare gas clusters in a supersonic expansion [25] as a starting point for this discussion. They found that while the structure of the clusters is highly dependent on the cluster size, the temperature is size independent but characteristic for each gas. For the study rare gases were produced using the following parameters: $p_0 = 1\,\text{bar}$ to $30\,\text{bar}$, $T_0 = 100\,\text{K}$ to $300\,\text{K}$ and a nozzle diameter $d = 50\,\mu\text{m}$ to $400\,\mu\text{m}$. The xenon clusters were produced from a seeded beam of 5% xenon in 95% neon. The authors used 50 keV electrons providing Debye-Sherrer diffraction patterns in order to determine the cluster lattice parameters and from which the temperature was determined. For xenon clusters a temperature of $T = 79 \pm 8\,\text{K}$ was measured. This means that the clusters in the imaging experiments have a temperature which is about 80 K below the melting point, making shape transitions very unlikely. However, it has to be pointed out that the experiments where performed using a seeded cluster beam. This means that the carrier gas (neon in this case) increased the background pressure and helped cooling the clusters using collisions between the gas background and the clusters.

These assumptions regarding the temperature of clusters can be compared by considering the temperature model developed by Gspann [126]. This model describes the cluster temperature based on the evaporation of surface atoms and was used to analyze the phase of metal clusters.

Following [127] the residence time of an atom on the surface of a cluster τ is given by

$$\tau = \tau_0 \exp(u_0/k_\mathrm{B}T) \tag{4.14}$$

with τ_0 the period of vibration of the atom and u_0 the heat of sublimation or vaporization. Gspann estimated that the residence time of a surface atom must be greater then the mean flight time of the cluster through an experiment and set $\tau \sim 10^2\,\mathrm{s}$. With the aid of a typical period of vibration ($10^{-12}\,\mathrm{s}$) the temperature of the clusters can be calculated using equation 4.14. One obtains $T = 78\,\mathrm{K}$, which is in good agreement with the cluster temperature observed by Farges.

Although the temperatures for the clusters obtained following the methods from Farges and Gspann agree very well, the results are misleading. The reason for that is that in both cases the temperature is considered at a point where the cluster growth process is already completed. In the work of Farges *et al.* the cluster temperature was determined in an interaction region milliseconds after the creation of the clusters. The same is true for the work of Gspann where a residence time of the surface atoms was estimated to be in the same order of magnitude. However, the work of Gspann can be used to estimate the temperature of the clusters right at the point in time when the growth process is completed by setting the residence time accordingly. One can estimate that the growth of clusters has come to an end after the clusters traveled a distance of about $x/d \leq 4$ because at this point the interactions (collisions) in the beam can be neglected due to expansion and depletion (see [31] and figure 2.5 on page 10). For the presented experiments this means $x = 8\,\mathrm{mm}$. Following Hagena, the maximum flow velocity is given by $v_\infty = 204\sqrt{T_0/m} \sim 264\,\mathrm{m/s}$ (see equation 4.9 on page 98). Therefore, one can estimate the mean residence time of a surface atom to be $\tau \succeq x/v_\infty = 3 \cdot 10^{-5}\,\mathrm{s}$. With equation 4.14 the cluster temperature can be determined to be $T = 113\,\mathrm{K}$ right after the formation process has come to an end. During the time it takes the clusters to travel to the interaction region the temperature of the clusters can be reduced by the evaporation of surface atoms until the temperature of 78 K is reached.

If the temperature of $T = 113\,\mathrm{K}$ is compared to a calculation where the formation of clusters is neglected during the expansion of the atomic beam, one can see the influence of the clustering process on the temperature of the beam. Based on the calculations given in [8] as well as the calculations shown in section 2.1.2 on page 7 an atomic beam reaches a Mach number $M \approx 8$ at $x/d = 4$. With the relation [31]

$$(T_\mathrm{Beam}/T_0) = \left(1 + \frac{\gamma - 1}{2} M^2\right)^{-1}, \tag{4.15}$$

and an initial temperature of $T_0 = 220\,\mathrm{K}$ and $\gamma = 5/3$ the temperature of the beam can be determined: $T_\mathrm{Beam} = 9.9\,\mathrm{K}$. It can be seen that the formation of clusters has a strong impact on the mean temperature of the beam.

Even though the melting temperature of large xenon clusters can be assumed to be similar to the melting temperature of the bulk, the clusters melting temperature is strongly size dependent. As an example, figure 4.25 shows a Monte Carlo simulation of a small argon cluster containing 87 atoms at various temperatures. At $T > 40\,\mathrm{K}$ the cluster atoms are able to switch positions frequently and the cluster can be considered as liquid. Corresponding cluster sizes are reached within just a few collisions. With an observed cluster temperature of $T_\mathrm{Ar} = 37 \pm 5\,\mathrm{K}$ [25] and the melting temperature shown these clusters can be considered as hot. This consideration can be transferred to the xenon clusters observed in the experiments in order to explain the observation of twin clusters and spherical clusters side by side. During the cluster formation the

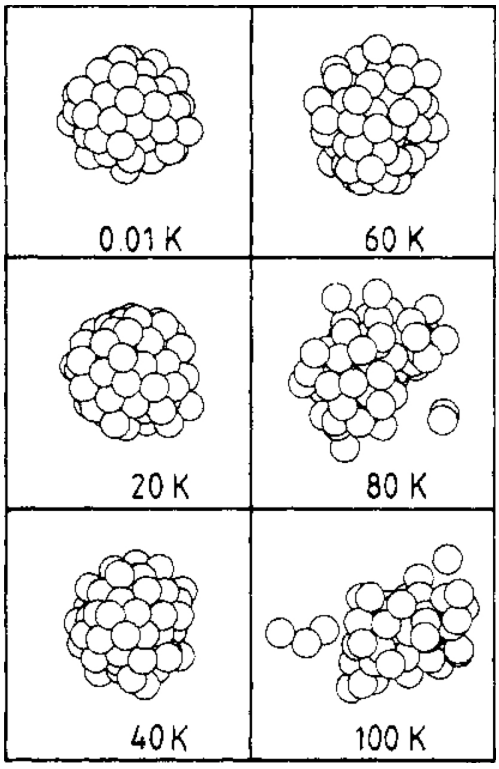

Figure 4.25.: Monte Carlo simulation of a melting end vaporizing argon clusters (87 atoms). Below $T = 20\,\mathrm{K}$ the atoms are in a steady position but with increasing temperature position changes are feasible and the cluster can be considered as liquid. At high temperature ($T = 80\,\mathrm{K}$ the cluster vaporizes. [128]

xenon clusters are very hot and close the there melting point. At the end of the formation phase at a distance from the nozzle of $x/d =\leq 4$ the temperature is still about $T = 113\,\mathrm{K}$. Due to the flight time of $10^{-5}\,\mathrm{s}$ the clusters have enough time to cool down via evaporation of surface atoms and become solid again. Therefore, most of the hot clusters are able to relax into a spherical shape after the cluster-cluster collisions. The twin clusters, however, are formed from colder clusters which collide on average with a low relative velocity and therefore remain solid. Based on the data obtained from the simulation presented in section 4.4.2 this is the case for 20% of the clusters in the experiments.

4.5. Summary of cluster growth

The experiments presented in the previous section enable imaging of free rare gas clusters and allow for a direct observation of the cluster formation and growth process. The data shows scattering from spherical clusters together with interference patterns caused due to twin clusters. The origin of this dumbbell shaped objects is the cluster formation process. It was found that this twin clusters are stable objects detected milliseconds after their creation during binary cluster-cluster collisions, which are part of the cluster growth process. For 20% of the clusters a dumbbell twin shape was identified. This finding could be explained by considering the temperature distribution in the cluster beam and it was determined that these clusters originate from the colder part of the cluster beam which prevent the clusters relaxing into spherical shape. In order to conclude the previous discussion this section summarizes the cluster growth process.

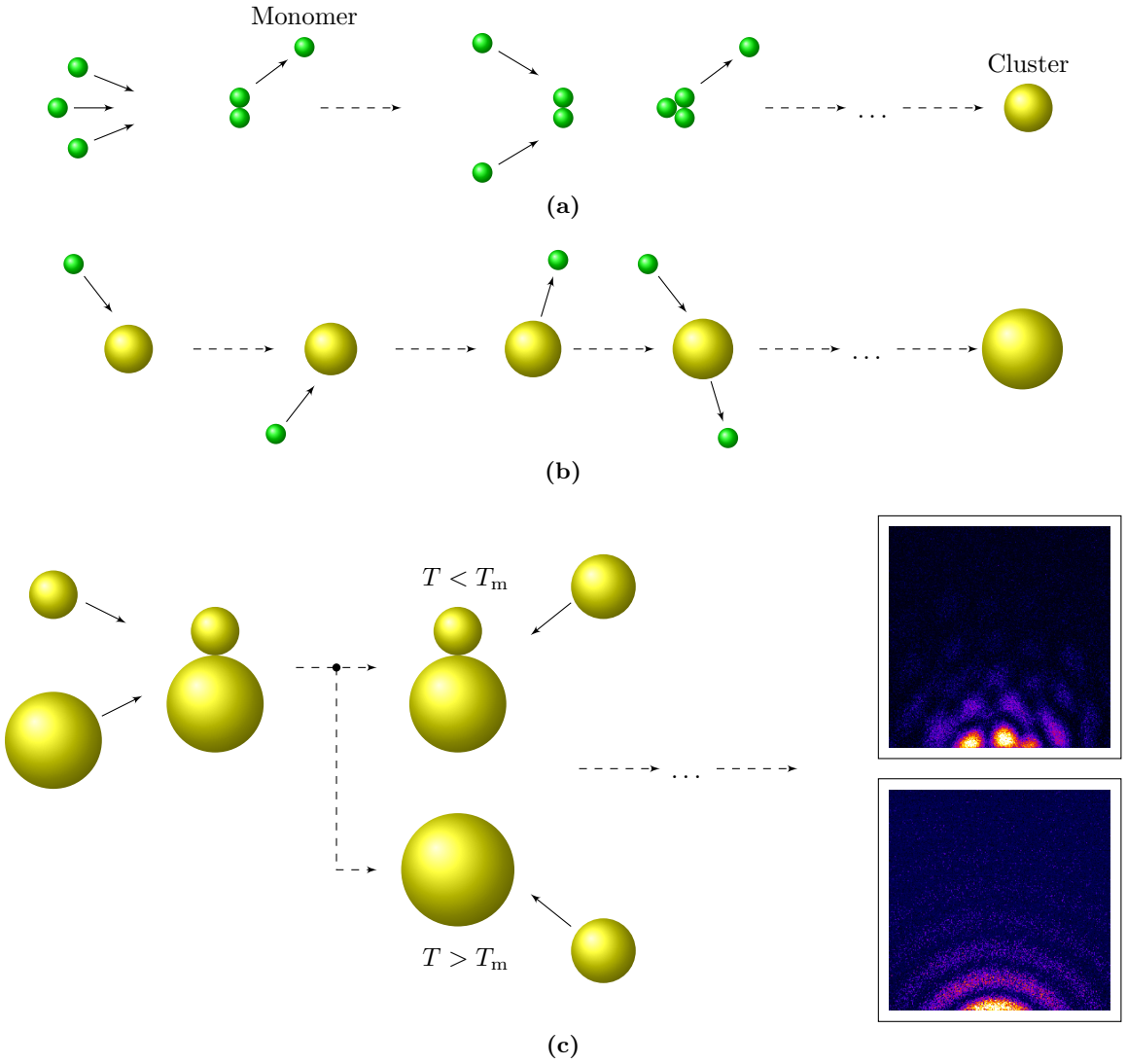

Figure 4.26.: Summary of cluster growth as described in the text. The beginning of the cluster formation process is dominated by three body collisions (a) directly followed by successive monomer addition (b). For clusters with $\langle N \rangle \gtrsim 50$ atoms binary collisions with coagulations dominate the cluster growth (c). At the end, depending on the overcome of the cluster melting temperature T_m, single or twin clusters are imaged.

Figure 4.26 visualizes the cluster formation process from atomic gas up to a cluster size sufficient for imaging experiments. In principle, the growth process can be split into three different parts labeled with (a), (b), and (c) respectively. From top to bottom the mean cluster size increases.

Part (a) of figure 4.26 shows the beginning of the cluster formation. A gas is expanded with a high stagnation pressure and low temperature into an environment with a low background pressure (see also figure 2.3a on page 8). The unordered movement of the gas atoms becomes directed in forward direction, the temperature drops, and the expansion velocity of the beam exceeds the local speed of sound. A supersonic expansion is formed. In this environment a sequence of three-body collisions leads to the formation of dimers, beeing a seed for further cluster growth. Additional three-body collisions of the dimers with the gas atoms cause successive addition of monomers. Three-body collisions are required because the third atom removes the

released binding energy of the first two atoms from the system. Otherwise the released binding energy would heat the ensemble until its disintegration. This process results in the formation of small clusters containing several atoms cooled by evaporation of single atoms. If the atom density in the cluster beam drops under a threshold were three-body collisions are no longer possible, the growth process would come to an end at this point.

The next step in cluster growth process is illustrated in figure 4.26b. More and more monomers attach to the cluster. Due to the increased amount of atomic bonds at this stage of the cluster growth process the released binding energy can be dissipate over the entire cluster, which avoids bond breaking. Again, the evaporation of single atoms from the surface of the clusters reduces the inner energy of the clusters. However, the overall temperature of the cluster beam increases.

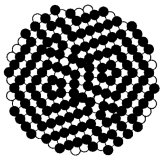

Figure 4.27.: Simulation of internal cluster structure [129].

At a cluster size of about fifty atoms per cluster the growth process changes drastically (figure 4.26c). Measurements of the cluster size distribution showed that further increase of the cluster size is caused by collision and coagulation of smaller clusters [8]. As a result, the formation of larger clusters is achieved by the consumption of smaller clusters. In contrast to the processes shown in 4.26a and 4.26b, binary collisions are a very effective growth mechanism because of the exponential increase in the number of atoms in the cluster per collision. Two clusters collide, stick together, and form a bigger one. The energy deposited during this collision is again compensated by the evaporation of surface atoms (which are omitted in the figure due to size relations). The internal cluster temperature increases as a result of the collisions. When the cluster's temperature exceeds the melting temperature the cluster becomes liquid, which allows reorganization of the atoms into an energetically favorable, spherical state. If the melting temperature is not exceeded the cluster remains in a dumbbell shape. This interaction process is repeated until no further collisions are possible due to depletion of the cluster beam caused by coagulation of the clusters. When the clusters reach a size of about 10^6 atoms, a size sufficient for imaging experiments is achieved. Depending on the energy that has been gathered during the growth process and released using evaporation of surface atoms, the melting temperature is exceeded once more and relaxation into spherical shape is possible before imaging of the clusters takes place. In this case the cluster appears as a spherical object which was observed in 80% of the recorded scattering patterns. Otherwise, the temperature of the cluster remains below the melting point and relaxation is not possible. The cluster remains in a dumbbell shape of a twin cluster identifiable by the interference pattern in the recorded scattering pattern.

This section closes with a remark regaining reconstruction of electron diffraction patterns of argon Ar_{3000} clusters, which reveal that the internal structure of the clusters is not well ordered [129]. Instead, a cluster structure was presented, which was obtained by cutting up a cluster into two parts and letting the parts reunite and relax by applying a two-body Lennard-Jones potential. This procedure resulted in the cluster structure shown in figure 4.27. A cluster growth process based on twin cluster formation can explain such an atomic structure. The reorganization of the cluster atoms as a result of overcomeing of the melting temperature would lead to a similar internal structure of the cluster. As soon as FELs with higher pulse intensity and higher photon energy are available it will be possible to even directly observe the internal cluster structure on an atomic scale.

4.6. Scattering and coincidence measurements in the x-ray regime

With the development of the ultrafast x-ray scattering a new approach for studies of the interaction between light and matter under extreme conditions has become available, allowing the study of the structure and dynamics of matter with atomic resolution [130]. In the last section the structure of the clusters was discussed revealing twin cluster formations using high intense laser pulses from FLASH. Furthermore, the scattering technique was used to study transient states of matter on a ultra fast time scale [18].

With the operation of the free electron laser LCLS a new regime for the study of high intense light matter interaction opend and for the first time high intense hard x-ray radiation from an FEL was available. This new light source allows novel experiments and was used for the research on the interaction of krypton clusters with photons of that energy regime to gain further insights in the occurring ionization processes. The experiments were performed in the CAMP chamber presented in section 3.2.2 on page 62. Details about the setup can be found in [87]. The experiments were based on the experimental experience gathered during the FLASH experiments and used single cluster imaging as well as coincidence measurements. In this context this means the simultaneous recording of diffraction patterns and ion spectra with the aim to cluster size effects and the influence for the focus distribution of the FEL. This enables analyzing of a time-of-flight (TOF) ion spectrum from a single, well-defined cluster. This reveals new effects in TOF ion spectroscopy measurements, which cannot be observed without the help of imaging. This section presents the experimental findings from the x-ray cluster interactions, showing highly

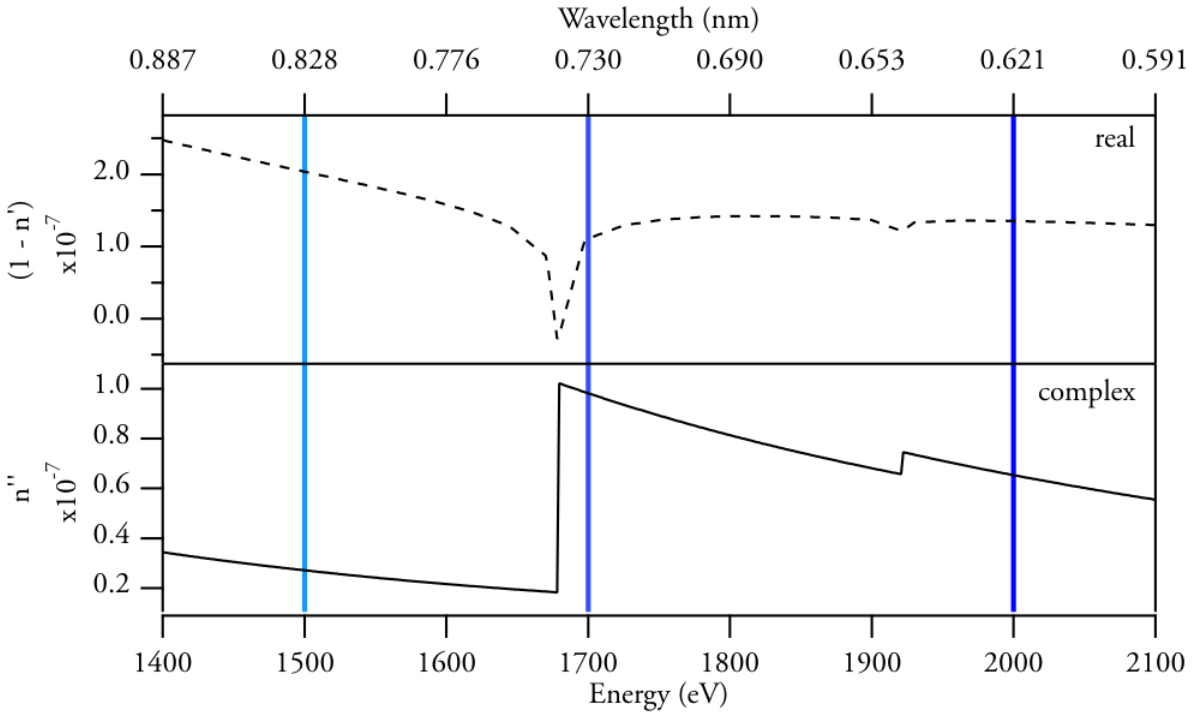

Figure 4.28.: Complex refractive index of krypton in the x-ray regime from 1.0 keV to 2,5 keV photon energy [72]. For comparison the corresponding wavelength is given on top of the diagram. The blue lines indicate the presented measurements performed at 1.5 keV, 1.7 keV, and 2.0 keV. Between these points, the complex part of the refractive index, n'', shows steps resulting in different absorption characteristics.

ionized krypton fragments in combination with missing low charged ions as an indicator for the absence of nanoplasma recombination.

The measurements were performed using krypton clusters at three different FEL photon energies: 1.5 keV, 1.7 keV, and 2.0 keV. Figure 4.28 shows the real and the complex part of the refractive index being important for the scattering experiments: $n = n' + i\,n''$. Right below 1.7 keV an absorption edge is visible, characterized by an increase in the complex part of the refractive index showing a discontinuity ranging from $2 \cdot 10^{-8}$ to $1 \cdot 10^{-7}$. A similar absorption edge is found for xenon at 90 eV, which is the photon energy of FLASH used in scattering experiments [18]. From the experiments it was observed that this edge has a strong impact on the scattering cross-section resulting in bright scattering patterns. Therefore, the influence of the krypton absorption edge at ~ 1.7 keV is studied using single cluster scattering.

Similar to the analysis of the experiments performed at the FLASH FEL (as discussed in sections 4.1 to 4.5) single shot scattering patterns were considered at first. Additionally and in order to increase the sensitivity of the scattering method during the krypton experiments, averaged scattering profiles were also analyzed. Averaging was achieved by developing specialized analysis software implemented in the data-processing tools.

4.6.1. LCLS data processing

The principle data processing follows the outline described in section 3.3.1 on page 65. Data processing and filtering have benefited from the experience gathered during the FLASH experiments. The major difference was that besides the scattering data, time-of-flight (TOF) ion spectroscopy data was acquired increasing the complexity of the data processing. For the data obtained at the LCLS facility the CFEL/ASG data acquisition software CASS [131] was used that ran on the computer grid installed at SLAC. The recorded data was stored on the grid in the form of XTC files, again sorted according to data files and calibration (dark) files. The XTC files are readable using the software tool provided by CFEL/ASG, called offlineCASS, also running on the SLACs computers. OfflineCASS provides an interface for the analysis of the measured data, called "PostProcessor". The analysis software performs a loop over user provided data files while the PostProcessor has access to each dataset that contains corrected pnCCD frame data and ion TOF spectroscopy data.

In the PostProcessor several filters are implemented. In order to distinguish cluster hits and no-hits an integral over the light peak in the ion time-of-flight data is performed. The MCP in

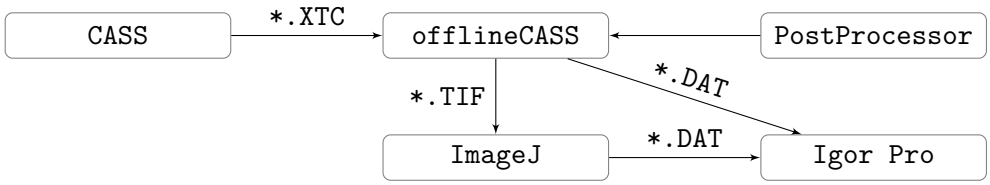

Figure 4.29.: Outline of the data analysis performed with scattering data recorded at LCLS. On the SLAC computer infrastructure the program CASS is implemented to handle the measurement of the data. The generated XTC files are further analyzed using offlineCASS. The implemented PostProcessor triggers the data analysis and sets the output of offlineCASS. Frame data is exported as TIF files and analyzed by ImageJ. Ion time-of-flight data is saved as DAT files, which can be handled with Igor Pro.

the TOF detector generates a characteristic signal peak, if scattered photons from the clusters are detected. The FEL photons are mainly scattered in forward direction but the MCP is very sensitive to x-ray photons. Therefore, even very few photons detected by the MCP result in a so-called light peak in the TOF data. As long as the light peak is not saturated, the integral of the light peak can be used to distinguish between cluster hits and shots without cluster signal.

The cluster size is determined by the PostProcessor using Fraunhofer diffraction and formula 2.36, which connects the scattering angle of the first scattering minimum with the diameter of the scattering object, as it is shown on page 36. In order to obtain the scattering angle θ of the first minima, a scattering plot was calculated by radial integration over the recorded frame. The plot was slightly smoothed and a self-developed binary-search algorithm was used for peak-finding, which searched the scattering plot for the first local minimum.

Figure 4.29 shows the outline of the analysis process performed with scattering data recorded at LCLS. OfflineCASS with the adopted PostProcessor handles the pnCCD frame- and ion-data. The data was exported as image files (tif) and data files (dat), respectively. Tif files were viewed using ImageJ in order to create scattering gradients. For the analysis of the data again Igor Pro was used.

4.6.2. Wavelength dependent absorption of krypton

With the availability of the analysis tools the data was examined for scattering patterns originating from spherical clusters with comparable cluster sizes and similar intensities of the scattering signal. The scattering slopes of these events were averaged in order to obtain statistical meaningful data. This process was repeated for the different photon energies that were recorded during the LCLS experiments.

Figure 4.30 shows a comparison of the averaged scattering profiles obtained at the three different wavelengths 1.5 keV, 1.7 keV, and 2.0 keV. The FEL operated constantly for all three wavelength with a similar pulse energy of $\sim 3\,\mu$J. In order to obtain the scattering profiles the most intense scattering patterns with identical cluster size within 0.5 nm were averaged. This ensures similar conditions for all scattering events. The downside of this strict filtering is that the amount of suitable cluster scattering patterns is very low. This means that from a single experimental run containing thousands of scattering patterns less then ten fit the required parameters and could be used for averaging. The figure presents data gained from clusters with a radius of $r \sim 25\,\text{nm} \pm 0.5\,\text{nm}$, which was the most frequent cluster size occurring in the data. The data is plotted against the dimensionless parameter $qr = 4\pi\lambda^{-1}\sin(\theta/2)r$, with the scattering angle θ and the radius r. The advantage of using this parameter is that the plots of the scattering profiles are independent of the wavelength. In consequence, the position of the minima is similar for all three wavelengths and can be compared. In order to further increase the comparability of the data, the slopes are normalized. The scaling factors for the measurements are 8.6 (2.0 keV) and 3.6 (1.7 keV), respectively. This shows that the scattering intensity at 2.0 keVwas about 8.6 times weaker compared to the measurement at 1.7 keV. This can be explained by the fluctuation in the FELs power density as well as by different scattering cross-sections of krypton at the different wavelengths.

The measurements from 1.5 keV to 1.7 keV show similar slopes of the scattering profiles, but the local minima in the 1.7 keV measurement are more distinct compared to the other two. This could imply an increase in the absorption, as distinct minima represent higher values of the

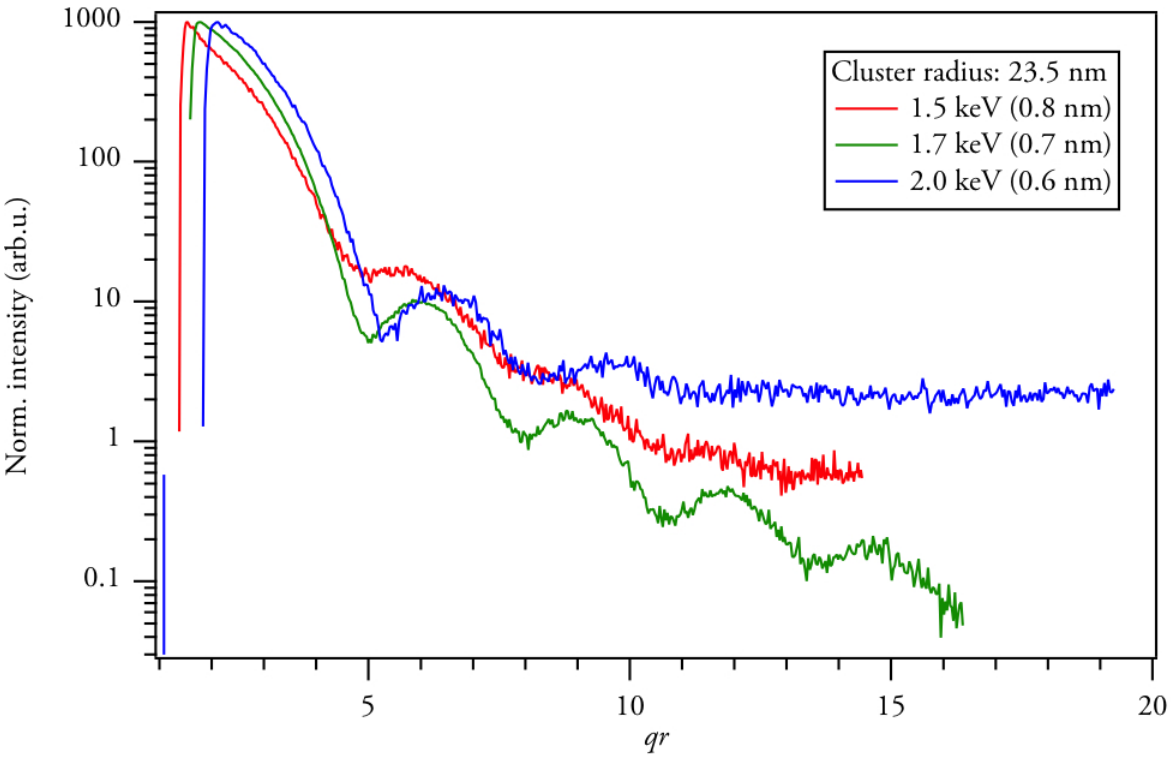

Figure 4.30.: Comparison of averaged scattering spectra recorded at different wavelength. For the cluster size 23.5 ± 0.5 nm radius was chosen. The graphs are plotted versus the dimensionless parameter $qr = 4\pi\lambda^{-1} \sin(\theta/2)r$, with the scattering angle θ and the radius r in order to compare measurements the different wavelength.

complex refractive index and hence the absorption of the scattering particle. This correlation was discussed in detail in [78, 17]. In general, this increase would be in line with the expectations derived from the refractive index shown in figure 4.28. However, these synchrotron measurements indicate a strong increase in the absorption, which could not be verified in the LCLS scattering data showing only a slight increase. An explanation for this might be a different power density of the free electron laser compared to a synchrotron. The LCLS laser pulse strips the krypton atoms in the clusters by sequentially direct photoionization. Every ionization results in Auger emissions and therefore ionized cluster atoms and the formation of a nanoplasma. Similar effects are reported for xenon clusters [132]. Every ionization step changes the absorption characteristics and shifts the absorption edge in a way that differences in the absorption did not appear in the data.

A large increase at high values of qr was detected for the measurements at 2.0 keV. This increase cannot be explained based on the material properties of krypton in that energy regime. It is assumed that this signal is a background scattering signal, as it was found at various scattering angles in all recorded patterns. This result indicates fluorescence as a source of this signal. By analyzing the amount of charges generated by the photons detected on the far edge of the CCD detector, a spectral analysis of this fluorescence signal was feasible. The analysis revealed that photons with a photon energy of ~ 1850 eV caused the signal. The only fluorescence line of krypton close to that wavelength is $L\beta_1 = 1636.6$ eV [133]. However, a more suitable candidate for the fluorescence could be found by taking silicon into account, which has a florescence line at $L\beta_1 = 1835.9$ eV [133]. During the experiments, silicon apertures were used

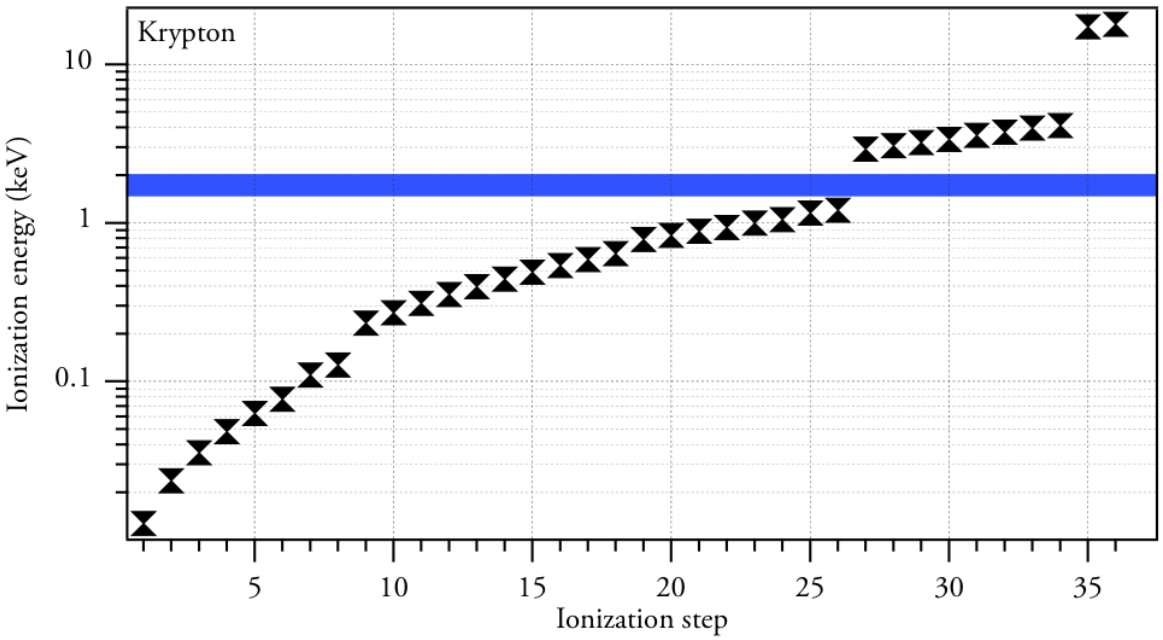

Figure 4.31.: Ionization steps of krypton achieved with single photon absorption. The blue bar marks the ionization energy addressed in the experiments. [134]

to guide the beam. At a photon energy of 2.0 keV the FEL stray light might case the aperture to fluoresce. This explains the background signal in the scattering profile.

The comparison of all the scattering profiles, as shown in figure 4.30, reveals that the profiles are all similar except from one minor difference already discussed. This similarity could be caused by a depletion of the clusters ionization process. Figure 4.31 illustrate the depletion. It shows the ionization steps of atomic krypton, which can be addressed in the x-ray regime. The blue bar in the figure represents the photon energy used in this experiment. With exception of the K-shell and L-shell all electrons can be removed from the krypton atom by single photon absorption. Each direct photoionization is followed by Auger-decays resulting in highly charged krypton fragments. This procedure is similar for all considered photon energies in the experiments. But it must be pointed out that these findings are based on averaged data. Depending on the position of the cluster in the FEL focus the amount of photons interacting with the cluster can vary exceedingly. A cluster located in the center of the FEL focus, at the point with the highest power density, is exposed to orders of magnitude more photons compared to a clusters interacting with the photons in the wings of the focus. From experiments at shorter wavelength it is known that multistep photon ionization becomes dominant for the absorption process at very high power densities [65, 135]. Therefore, in the intense x-ray focus of the LCLS with fluxes exceeding 10^5 photons per $Å^2$ atoms are sequentially ionized from the inside out starting with the inner-shell electrons followed by subsequent inner-shell vacancy decay [136]. This stripping of the atoms lead to highly charged clusters with a induced nanoplasma minimizing all photon-depending ionization effects.

Summing up, the averaged scattering profiles show a saturation of the absorption in the krypton clusters at x-ray wavelength addressed during the LCLS experiments. In the next section a further analysis based on single cluster scattering is presented to avoid averaging effects. In combination with time-of-flight mass-spectroscopy a detailed study of the reached charge states becomes possible.

4.6.3. Time-of-flight mass-spectroscopy of single clusters

Time-of-flight (TOF) mass spectroscopy is a well established tool for the analysis of reaction products from FEL light-cluster interactions and was introduced in section 3.2.1 on page 56. Exposing clusters to an FEL beam results in highly charged ions and cluster fragments, which are analyzed using a time-of-flight mass detector. As a novelty, this experimental method is combined with single cluster imaging technique to gain new insight into the interaction of high intense FEL radiation and clusters. As discussed in the experimental chapter of this

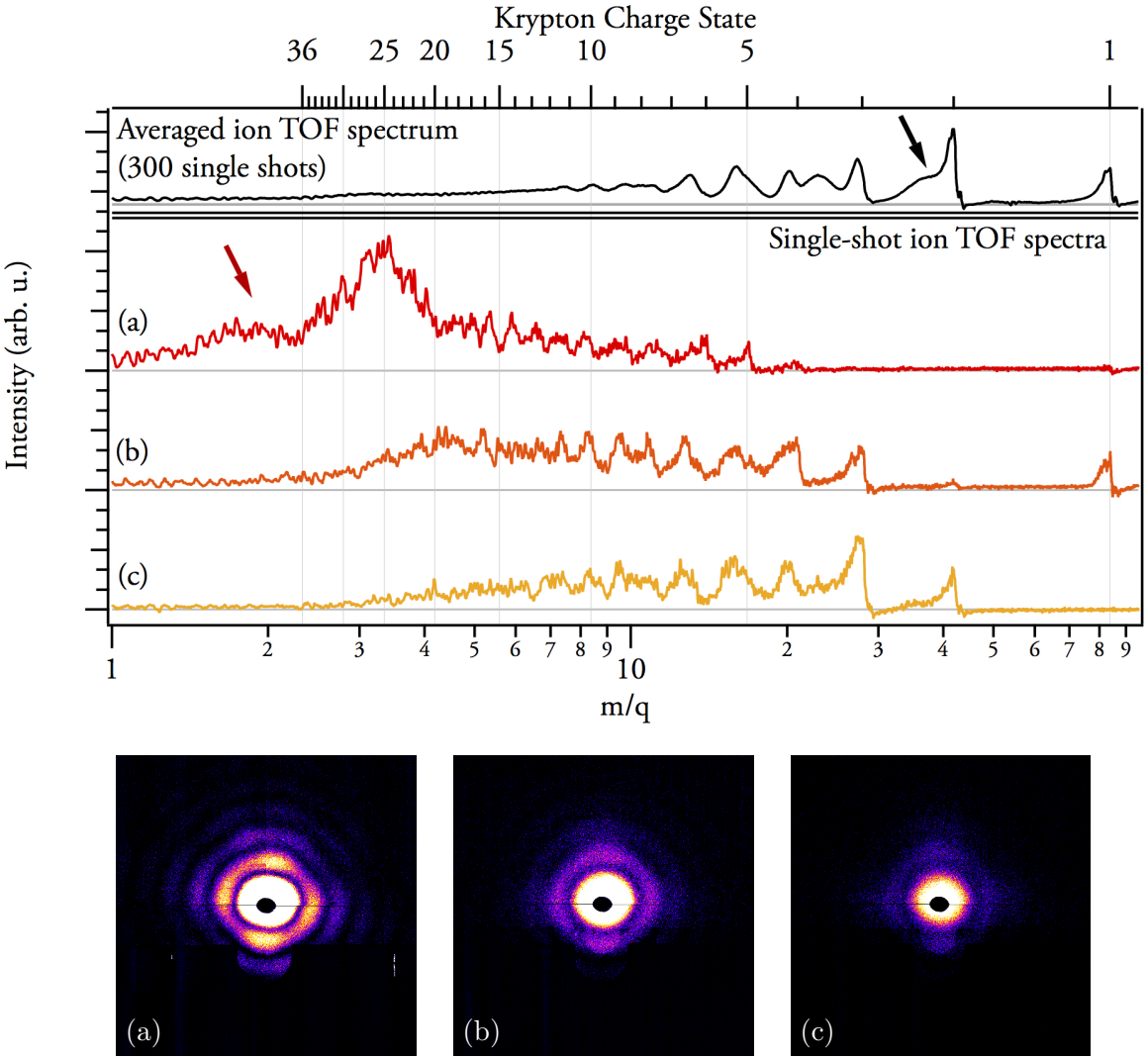

Figure 4.32.: Single shot TOF data recorded from single krypton clusters recorded at 1.7 keV photon energy. The three spectra (a), (b), and (c) are showing a huge change in the detected krypton charge states. While (a) shows high charged states and absence of single charges krypton, (c) marks the opposite. From the scattering pattern (bottom) the intensity is revealed which helps to interpret these patterns. (a) is originating from the center of the FEL focus and (c) at the outer wings. This can be concluded from the intensities of the scattering patterns. The spectrum printed in black is a conventional TOF-spectrum obtained by averaging 300 cluster shots randomly distributed throughout the FEL focus. The TOF-spectrum shows similarity to (c). This shows how single shot data reveals charge states (in (a) and (b)) which cannot be seen in conventional spectroscopy.

work a piezo driven skimmer slit was used for the scattering experiments in order to dilute the cluster beam until the single cluster regime was reached. During the experiments, the single cluster condition was characterized by the appearance of the characteristic ring structure of single spherical clusters in the scattering patterns. By implementing a TOF ion detector into the interaction region simultaneous recording of ion fragments from the same single cluster as achieved. Additionally, the scattering patterns enable further characterization of the clusters, for example the determination of the cluster size. The amount of scattered photons detected, allows conclusions about the position of the cluster in the FEL focus and the FEL shot power intensity. The combination of TOF mass spectroscopy and scattering is denoted "coincidence measurements".

Figure 4.32 illustrates the effects that become visible for single shot, single cluster coincidence measurements. The figure is divided in two parts: at the top four different TOF mass spectra are shown. Below, the corresponding scattering patterns are displayed. The spectra are plotted versus the mass-charge ratio m/q. For comparison reasons the corresponding krypton charge states are also given. The top most TOF mass spectrum shows a conventional spectrum that illustrates a TOF mass spectrum recorded during the LCLS experiments. This spectrum was obtained by averaging 300 data sets containing single cluster scattering patterns of different cluster sizes and different FEL power densities. This simulates the effect of averaging several FEL shots each containing a variety of clusters. This is similar to conventional TOF mass spectroscopy. Similar results are achieved for focal-integrated measurements or cluster size distributions at the LCLS [132]. The most dominant peak in this spectrum is Kr^{2+}. The domination of low charge states with low kinetic ions (back arrow) indicate hydrodynamic expansion of the clusters [137]. Backscattered kinetic ions are absent due to the slit-like design of the entrance aperture of the TOF detector and explain the asymmetry in the kinetic ions. Higher charge states are visible in the data, but they are not very dominant. Ion yields for $q \leqslant 5$ are washed out due to interfering with signal originating from the kinetic ions of lower charge states.

The ion spectrum changes completely when single-shot, single-cluster measurements are considered. This is shown in the spectrums (a), (b), and (c). The corresponding scattering patterns are given below the ion spectroscopy plots and are labeled (a) to (c), accordingly. All data originates from clusters with similar sizes to minimize size effects (cluster radius $r \sim 25 \pm 0.5\,\mathrm{nm}$). Similar distances of the scattering rings in the scattering frames identify the similar cluster sizes. The amount of scattered photons varies greatly from frame to frame, depending on the position of the clusters in the FEL focal waist. Relative to the intensity of the scattering pattern shown in figure (a) one finds that the intensity relations between the different scattering frames is $I_{(\mathrm{b})}/I_{(\mathrm{a})} = 0.35$ and $I_{(\mathrm{c})}/I_{(\mathrm{a})} = 0.12$, respectively. The amount of scattering photons correlates to the energy deposited on the clusters. Variations in the power density affect the single cluster ion spectroscopy data, revealing corresponding changes. In the averaged spectra these changes do not appear due to the clusters being exposed to a variety of different power density. The single cluster measurement for the highest power density (a) shows a maximum ion yield at $q = 25^{+}$. In addition to that, ions up to Kr^{36+} and ions with high kinetic energy (red arrow) were detected. On the basis of that data, it can not be decided if the ions have very high kinetic energy or are in very high charge states. In contrast to that, ions with $q < 5$ are almost absent. In opposite to the characteristics illustrated in (a), measurements with lower power densities show a completely different behavior. In (b) extremely high charge states vanish and lower charge states appear. Considering the last spectrum (c) this trend continues and the spectrum becomes similar to the integrated TOF data shown in black.

The coincidence measurements of imaging and ion spectroscopy from single clusters show a

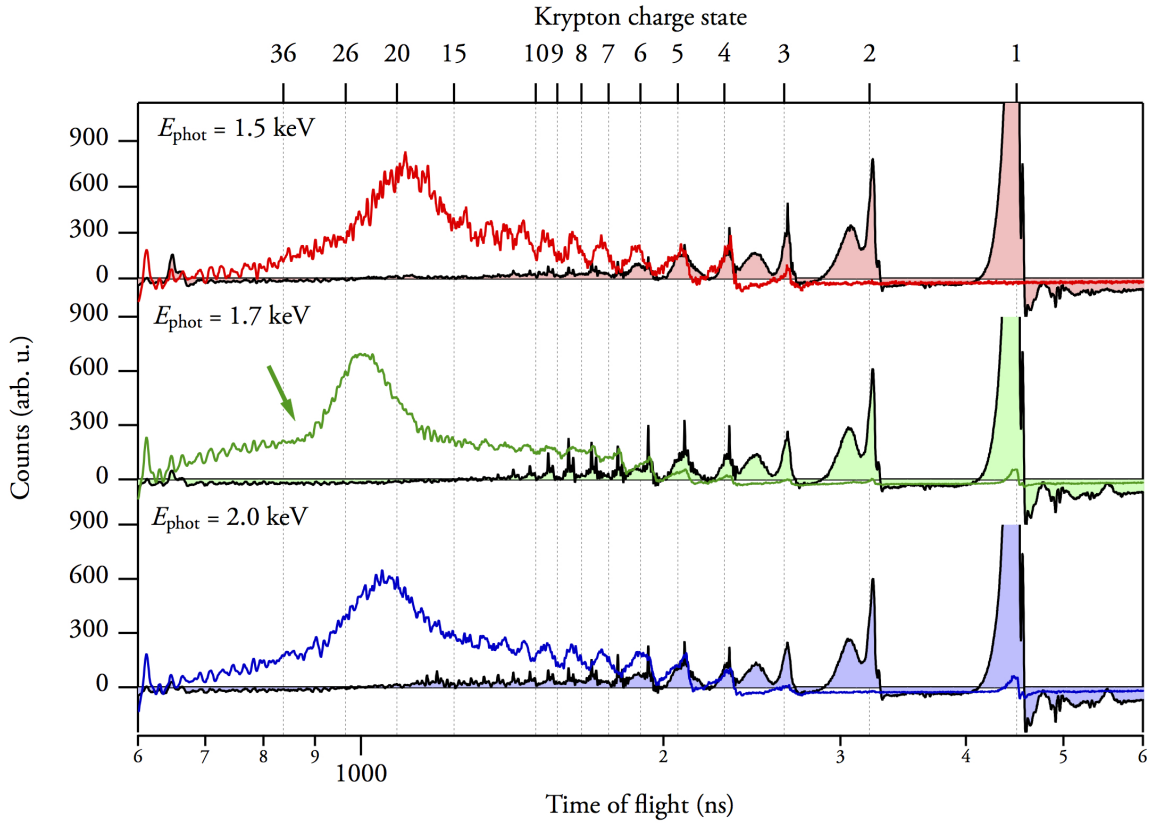

Figure 4.33.: The highest charge states (compare type (c) in figure 4.32) observed for krypton clusters at different photon energies were averaged to generate these ion spectroscopy graphs. Each plot is compared to a focal integrated ion spectrum printed as a black line and filled with the corresponding color. The mean ion yield shifts with the photon energy and at 1.7 keV an increase in kinetic ions is observed (green arrow), indicating an effective ionization process.

strong power dependent ionization process not visible in the average spectrum. The mean charge state increases with increasing power density. This indicates an increase in the energy absorption of the clusters resulting in the high kinetic energy releases found in the data. The absence of low charge states at high power densities (cf. figure 4.32 (a)) indicates an efficient suppression of recombination effects in the laser induced nanoplasma. This is remarkable, as usually less then 1% of photo-activated electrons forming the nanoplasma can leave the increasing coulomb potential of the cluster [65]. An explanation could be that the photons of the FEL induce a high temperature in the plasma, which in consequence suppresses electron-ion recombination effectively. This hypothesis can be supported using plasma simulations. Similar ionization behavior was observed for xenon clusters in the LCLS light pulse, as presented in detail in [14]. There, a plasma simulation is presented which supports the assumption of the high temperatures in the nanoplasma.

The described increased ionization combined with suppressed recombination was found for different cluster sizes and different excitation energies. In this case, cluster size denotes the sizes observable in imaging experiments, namely a cluster radius of $r > 10\,\text{nm}$. However, slight differences are visible comparing the results of excitation energies. These differences are becoming clearer as averaged data is considered. Of course averaging in this context has to be performed carefully in order to preserve effects in the data and not blur them. Hence, averaging contains

only the same cluster size with identical excitation energies. Figure 4.33 shows the averaged ion spectroscopy data from krypton clusters with the highest power density recorded. These are compared for three different FEL photon energies: 1.5 keV, 1.7 keV, and 2.0 keV. Again, these energies are representing measurements below, at, and above an absorption edge of krypton, cf. figure 4.28 and corresponding discussion. Even though total depletion is reached at all excitation energies (see section 4.6.2), slight changes in the maximum ion yield is found to be $q = 19$ at 1.5 keV, $q = 25$ at 1.7 keV, and $q = 21$ at 2.0 keV respectively. Furthermore, the amount of high kinetic ions detected is significantly increased at 1.7 keV photon energy, which is marked with the green arrow.

The shift of the mean maximum charge state at 1.7 keV photon energy can be explained by the increased absorption of krypton at this energy regime due to the corresponding absorption edge. It causes a more efficient heating of the nanoplasma compared to the other excitation energies and results in less efficient recombination during the dispanding of the clusters. This would be visible in higher charge states and faster ions in the detected data. However, it has to be noted that the absorption characteristic shown in figure 4.28 represents neutral krypton. In contrast to that, the cluster remains in ground state only at the very beginning of the laser pulse before the first electrons leave the cluster due to direct ionization. Further investigations on these interactions are needed to gain deeper insight into this ionization process. Again, the role of the nanoplasma for the ionization process has to be studied in greater detail using plasma simulations.

5. Conclusion and outlook

In this work, short intense VUV and x-ray pluses from two free-electron lasers (FEL) were used to image single rare gas clusters in the gas phase. The different experiments were carried out by using two different experimental setups. The experiments using VUV radiation were performed at the "Freie Elektronen Laser in Hamburg" FLASH. For the work at FLASH an experimental setup was designed and build. The setup used a multi layer mirror with a short focal length to achieve high focal intensities in the interaction point of the FEL light and the cluster beam. The Alignment of the mirror was achieved using in-vacuum high precession motors, which combined mirror movement in all directions with a tilting of the mirror. For the detection of the scattered FEL photons a combination of three small pnCCD detectors with single photon sensitivity was used. A build-in time-of-flight ion detector enabled the determination of the power density of the FEL in the interaction region. Comparison with literature [96] revealed power densities up to $2 \cdot 10^{15}\,\mathrm{W/cm^2}$. Essential for the success of the single cluster imaging experiments was a dilution of the cluster beam, obtained by using a skimmer slit with variable width in front of the interaction region. While running scattering experiments the skimmer slit was narrowed until single cluster scattering mode was achieved.

The second set of experiments presented in this thesis were performed at the Linear Coherent Light Source (LCLS) facility, a new free-electron laser operating in the x-ray regime. In collaboration with the CAMP-team [87] coincident measurements of rare gas clusters were performed (cf. [15, 16]). For these experiments large pnCCD detectors for the detection of scattered photons were combined with a time-of-flight ion detector for the recording of charged cluster fragments. Both detectors were used in parallel and recorded data from the same single cluster (coincidence measurements).

A major part of this work was the development of software for data analysis and data acquisition enabling the successful performance of the experiments. The analysis software combines a variety of different techniques in order to achieve maximum flexibility with high performance. Image correction of the recorded scattering patterns was done using Interactive Data Language (IDL), a vectorized, numerical language with a strong focus on image manipulation [109]. Various algorithms like filtering of the scattered frames or specialized peak detection were implemented in C/C++ allowing them to be recompiled on every computer with a suitable compiler. For example, automated cluster size determination using Fraunhofer diffraction was included in the analysis software at LCLS running on the SLAC computing grid. Shell scripts were used for file handling and for automation of the workflow. Based on the experience gathered during the analysis of the scattering experiments a new software program for data acquisition for coincident measurements was developed and tested successfully during experiments at FLASH. The software makes use of multiple threads to acquire the different recording and data handling tasks. A shared memory buffer was used for data exchange. A specialized file format was defined for the storage of the data, which is based on HDF5 technology [107]. This allows fast storage access with file sizes only limited by the hard drive capacity.

The scattering data recorded at FLASH revealed three different types of cluster scattering

patterns. The patterns could be classified by the number of clusters in the interaction region and the separation between the clusters. The most common type of scattering patterns is due to single clusters, which can be identified by the clear ring structure in the frame. Stripe like interference patterns allowed the conclusion that two scattering objects were in the interaction region. These could be separated in "two clusters" and "twin clusters" scattering events. The difference between these events is the distance of the clusters in the interaction region. A few scattering patterns showed a "newton ring" structure originating from scattered photons interfering on the detector, which were scattered from two clusters in the interaction region. A dumbbell shape of two clusters in direct contact results in a scattering pattern similar to a double pinhole scattering experiment and identifies twin clusters. 80% of the recorded data showed single cluster signatures, followed by a surprisingly high amount of twin clusters with about 20% abundance. The appearance of "newton ring" structure caused by two clusters separated by a long distance depends on the width of the skimmer slit and was only rarely observed, as a result of single cluster conditions ($\sim 1\%$). A slight increase of the twin cluster abundance was found for measurements above the vapor pressure curve.

The ring-like structure of single cluster scattering patterns was used to determine the cluster size distribution of a cluster beam using Mie theory. Cluster sizes obtained from individual single cluster scattering patterns were used to create a histogram according to the expansion parameters p_0 and T. From the histograms a mean cluster size for the experimental runs was obtained. This mean cluster size was compared to cluster scaling laws derived by Hagena and modified by Dorchies. The comparison showed good agreement with Hagena's scaling law.

The twin cluster scattering patterns were found for all experimental conditions and across all recorded runs. They were explained as residuals of the cluster growth process. For large clusters further growth is governed by binary collisions and coalescence of the clusters. The data shows twin cluster images with different coalescence states. The twin clusters were imaged milliseconds after their formation proving the stability of these objects. It was proposed that twin clusters survive these period of time since the average temperature of the cluster beam reached during the growth process is so low that small fraction of the clusters are solid. However, the data shows that during the cluster formation the clusters temperature remains close to the size-dependent melting temperature of the clusters. Binary collisions between clusters increase the cluster temperature and evaporation of surface atoms reduces them. From the observed ratios between single and twin cluster images a simulation of the cluster growth process could support that spherical clusters show a temperature above the melting point. This enables them to reorganize into an energetic favorable almost spherical shape. The remaining clusters stay below the melting temperature (at least during the last collisions) and therefore remain in a dumbbell shape originating from a binary cluster-cluster collision.

The simulation of the cluster formation process was achieved by developing a simulation program called "ClusterSim" (CS) which enables observation of the development of an initial size distribution of the clusters over time. This C++ program used collision detection based on a hard sphere model for the formation of twin clusters during the cluster growth. The growth process was simulated by picking clusters from a pool and letting them interact with a certain probability derived from cluster growth theory [8]. The simulation could reproduce the general trent of the cluster size distribution and increase of the mean cluster size. Furthermore, the ratio of single clusters to twin clusters was in agreement with experimental data. Due to computational limitations the simulation was not capable of simulating clusters up to 10^6 atoms but the general agreement shows that the key aspects of the cluster growth process are well described by the simulation.

Probably the ultimate goal for scattering experiments is atomic resolution. In order to achieve that, much shorter wavelengths and high photon density are necessary. An important step towards this regime was the beginning of operation of the LCLS in the hard x-ray regime. The availability of the new FEL wavelength enables new cluster experiments. In this thesis studies on krypton clusters were performed. The experiments were among the first investigations on light-matter interactions in this regime and aimed to develop an understanding of future scattering experiments.

Using the light from LCLS, krypton clusters were studied at energies below and above the krypton L-edge at 1.7 keV. It turned out that the distribution of charge states in the time-of-flight ion spectra are almost the same for excitation below and above the L-edge (at 1.5 keV and 2.0 keV, respectively), being in striking contrast to experiments at low power densities performed at synchrotrons. It was proposed that this unexpected behavior stems from the saturation of absorption. Krypton atoms inside the cluster are sequentially ionized including Auger cascades up to the highest charge states. These are rather insensitive to the initial photon energy since 1.5 keV to 2.0 keV are sufficient to remove all electrons up to $3d$ shell while the remaining $2p, 2s$ and $1s$ electrons of highly charged krypton required much higher energies to be removed.

In addition, the combination of the scattering technique with time-of-flight (TOF) ion spectroscopy was performed at LCLS. These coincidence measurements used the scattering data from single cluster to determine the size of the cluster together with the FEL power density. Ion spectra were recorded from the same cluster producing the scattering image. The combination of both enabled the analysis of single cluster ion spectroscopy data from size-selected clusters. Single cluster measurements allowed the determination of the position of the cluster in the FEL focus. While the position of the cluster in the focus determines the deposed FEL energy on the cluster, drastic changes in the ion yield distributions of krypton clusters were observed in single cluster measurements depending on different focus positions of the clusters. Similar effects are not visible with conventional spectroscopy due to averaging over all different positions of the clusters in the focus. The observation of extremely highly charged ions indicate an efficient suppression of electron-ion recombination effects due to high temperature in the laser induced nanoplasma.

In conclusion, the combination of scattering and spectroscopy techniques, especially in coincidence open a large variety of studies, giving insights into light matter interaction. It is expected that for the future scattering techniques will be a very helpful tool for the study of gas phase nano particles and their dynamics.

Appendix

A. Quantum efficiency of pnCCDs used at LCLS

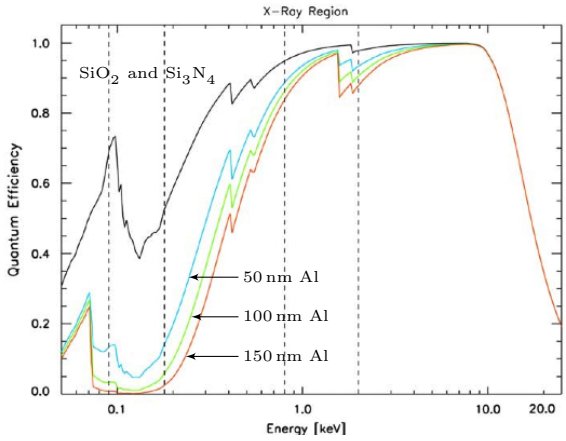

Figure A.1.: Quantum efficiency of the pnCCD detector for different optical filters plotted as a function of energy. Due to the similar design of the detectors the quantum efficiency is comparable to 3.9b on page 51. From [87].

B. Vapor pressure curve of xenon

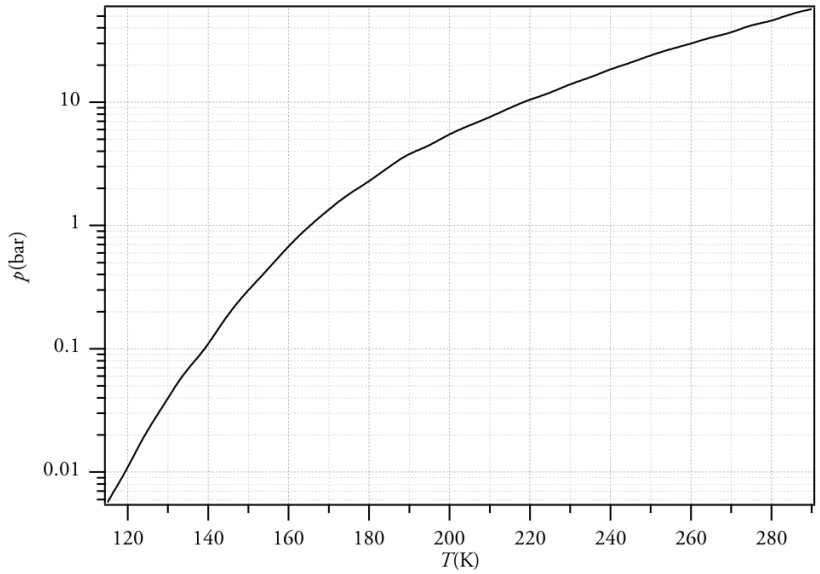

Figure B.1.: Vapor pressure curve of xenon. The experiments at FLASH presented in this work were performed at 220 K. [138]

C. Acqiris Digitizer Thread - source code

FoxIt uses multi threading to perform the task of collecting data from different sources simultaneously. Each thread is an instance of an implemented QThread Object [102]. Each QThread is able to shares data with all other threads in the application but process them independently. Instead of starting its execution in a `main()` function a QThread object uses a `run()` function as its starting point. This listing shows the `run()` function of the thread reading data from the Acqiris Digitizer.

```
// reimplementation of QThread::run()
void acqirisThread::run()
{
    std::cout << "Starting acqiris thread... (takes some time)" << std::endl;
    // Creating local variables for using less locks
    acqiris acqi;
    acqirisData acDataLocal;
    // Copy settings to local variables
    mutex.lock();
    acDataLocal.duplicate(&acData);
    mutex.unlock();
    // This is the shot ID. Here, at the beginning of the run
    // method, the id is reset. It will be increased for
    // every recorded shot by one.
    long ID = 0;
    // Create shared memory, plus an overhead of 16 bytes for ID, etc.
    size_t size = acDataLocal.get_dataSizeInBytes();
    if(!acMemoryShare.create(size + 16)){
        /*PRINT ERROR*/
        return;
    }
    // Check if an Acqiris is connected to the
    // computer and initialize it
    if(!acqi.FindDevices()){
        return;
    }
    acqi.InitializeDevices();
    acqi.Configure(&acDataLocal);
    // Acqiris has been configured with the current settings.
    // Set the settingsChanged variable to false. If it
    // become true again, the Acqiris will be configured again.
    mutex.lock();
    settingsChanged = false;
    mutex.unlock();
    std::cout << "Acqiris online." << std::endl;

    // This loop contains the actual work perfumed by the thread.
    // It will be executed until the stop flag is set.
    forever{
        // Check if we had to stop the loop
        if(stop){
            std::cout << "Shutting down acqiris thread." << std::endl;
            //break out of the loop and shut down Acqiris.
            break;
        }
        // Check if the settings are changed. If yes,
        // copy them to local buffers
        if(settingsChanged){
            mutex.lock();
            acDataLocal.duplicate(&acData);
```

```
            size = acDataLocal.get_dataSizeInBytes();
            settingsChanged = false;
            mutex.unlock();
            // Resize the shared memory. Because this thread
            // is the only one attached to the memory it will
            // be deleted automatically if this thread detaches.
            if(acMemoryShare.isAttached()){
                acMemoryShare.detach();
            }
            if(!acMemoryShare.create(size + 16)){
                /*PRINT ERROR*/
                break;
            }
            acqi.Configure(&acDataLocal);
        }

        // Acquisition and readout:
        // Arm the Acqiris, it will wait for the next hardware trigger.
        // The thread execution will be stopped at this point until
        // a hardware trigger occurs an the data buffer of the Acqiris
        // contains data or if a timeout occurs.
        acqi.Acquire();
        // Flush the data from the device to the machine and copy it
        // to the local thread data. During this step the format
        // of the data is changed in order to match FoxIt requirements.
        acqi.ReadOut(&acDataLocal);

        // Copy the data to the shared memory
        acMemoryShare.lock();
        if(size > acMemoryShare.size()){
            /*PRINT ERROR*/
           acMemoryShare.unlock();
           acMemoryShare.detach();
           break;
        }
        char *to = (char*)acMemoryShare.data();
        const char *from = (char*)acDataLocal.get_dataPointer(0);
        memcpy(to,from,size);
        to = (char*) acMemoryShare.data() + size + 8;
        from = (char*) &ID;
        memcpy(to,from,sizeof(long));
        acMemoryShare.unlock();

        // The data of the recorded shot has been send to the
        // shared memory and will be processed elsewhere.
        // Therefore, the shot ID can be increased for the next
        // shot and this thread is paused until the recored data
        // is processed. This is necessary because processing could
        // be more time consuming then recording a new data set.
        ID++;
        mutex.lock();
        emit acqirisThreadSignal(ID);
        waitCondition.wait(&mutex);
        mutex.unlock();
    // End of forever-loop
    }

    /*SHUTTING DOWN ACQIRIS*/
// End of acqirisThread::run()
}
```

D. Outlook: Future development of FoxIt

Requirements of the acquisition software change with every generation of cluster experiments at FLASH. Even though FoxIt was designed to be as flexible as possible and served as a data acquisition tool in several beam times, changes in the software architecture will provide the flexibility for future generations of cluster experiments at FLASH. This section proposes three changes in future versions of FoxIt in order to meet the requirements of next generation cluster imaging experiments.

A key aspect in upcoming versions of FoxIt will be performance. Pulse repetition rates of FEL machines increase. By the time FoxIt was designed FLASH operated at 5 Hz. Today, the pulse repetition rate has been doubled to 10 Hz. For a data acquisition program (DAQ) this means that the time between recording and storing data to the hard disk has been divided in halve, which also implies that high-performance data processing is required before storing. Most of the tasks required for data processing can be parallelized and hence performed on multi-core processors such as GPUs (graphics processing unit) taking full advantage of modern computers. The current version of FoxIt uses the GPU only for visualization of scattering patterns and scaling of scattering images when application windows are moved and changed in sizes. This ensures a fast responding program, which does not interrupt data recording. FoxIt uses a QGLWidget for this task. The first step for the future of FoxIt would be improving this current implementation and carrying out the entire data processing operations, like online noise reduction, offset correction, or visualization of differences between a reference image and the recorded frame on the GPU. With such an implementation parallelizable tasks like the per-pixel calculation of an offset can be performed for an entire scattering frame at once. An implementation could be based on OpenCL [139, 140].

Another main aspect for future FoxIt releases is an increased flexibility in terms of supporting different experimental setups. This means that drivers that handle the interaction between the application and the hardware should be loaded during runtime of the software. The application could then detect connected equipment during startup and load the corresponding drivers accordingly. An implementation would require a more distinct separation between application logic and interface communication using a factory design pattern [141] for the implementation of dynamically loaded drivers. Such a pattern could be implemented as a second step.

Finally, flexibility could be further improved by introducing a plug-in concept for FoxIt. A MATLAB or Python interface for a quick and easy customization of the workflow can be used to realize this. Corresponding programming language interfaces are available from MathWorks using the MATLAB Engine [142] or using the Boost wrapper classes for Pythons [143], respectively. In both cases the benefit would be that changes in the data processing, e.g. different noise reduction algorithms, can be made without writing C++ code. However, it has to be carefully implemented in order to avoid performance bottlenecks. An alternative would be to used dynamically loaded C++ libraries for workflow customization. This would reduce the runtime performance bottlenecks, which can occur when Python or MATLAB is used, but for the sake of a more complex implementation.

The plug-in concept could furthermore be useful for the implementation of new analysis features, which would help to perform the scattering experiments. For example, a plug-in could be used for online cluster size determination creating a real-time histogram of the cluster sizes. In combination with plug-ins controlling VUV mirror movements, the gas system, and the cluster nozzle this could be used for the development of a fully remote controlled experimental setup.

With that features at hand and a sufficient online analysis of the scattering data, a feed back loop could be implemented which would allow a self-adjusting experimental setup.

With these three development steps future versions of FoxIT can be developed, which will meet the requirements of future generations of cluster experiments at FLASH with increased performance, flexibility in the experimental setups and optimized workflow using plug-ins.

List of Figures

List of Tables

Bibliography

[1] E. W. Becker, Zeitschrift für Physik D Atoms, Molecules and Clusters **3**, 101 (1986).

[2] A. Castleman and P. Jena, Proceedings of the National Academy of Sciences of the United States of America **103**, 10552 (2006).

[3] P. Jena and A. Castleman, Proceedings of the National Academy of Sciences of the United States of America **103**, 10560 (2006).

[4] H. Cheng, X. Li, R. Whetten, and R. Berry, Physical Review A **46**, 791 (1992).

[5] F. Federmann, O. Björneholm, A. Beutler, and T. Möller, Physical Review Letters **73**, 1549 (1994).

[6] O. Björneholm, F. Federmann, F. Fössing, and T. Möller, Physical review letters **74**, 3017 (1995).

[7] C. Bahr et al., *Bergmann Schäfer, Lehrbuch der Experimentalphysik, Vielteilchensysteme, Band 5*, Walter de Gruyter, Berlin, 1992.

[8] J. Soler, N. Garcia, O. Echt, and K. Sattler, Physical Review Letters **49**, 1857 (1982).

[9] W. Ackermann et al., Nature Photonics **1**, 336 (2007).

[10] R. Neutze, R. Wouts, D. van Der Spoel, E. Weckert, and J. Hajdu, Nature **406**, 752 (2000).

[11] H. Chapman et al., Nature Physics **2**, 839 (2006).

[12] H. Wabnitz et al., Nature **420**, 482 (2002).

[13] C. Bostedt et al., Nuclear Instruments and Methods in Physics Research Section A **601**, 108 (2009).

[14] T. Gorkhover et al., Physical Review Letters **108**, 245005 (2012).

[15] D. Rupp, *Ionization and plasma dynamics of single large xenon clusters in superintense XUV pulses*, PhD thesis, Technische Universität Berlin, 2013.

[16] T. Gorkhover, *Ultrafast light induced dynamics of Xe nanoparticles studied with a combination of intense infrared and x-ray pulses*, PhD thesis, Technische Universität Berlin, 2014.

[17] M. Adolph, *Entwicklung von Zwei-Farben Streuexperimenten an Clustern mit weicher Röntgenstrahlung*, Diplomarbeit, Technische Universität Berlin, 2008.

[18] C. Bostedt et al., Physical Review Letters **108**, 093401 (2012).

[19] W. Henkes, Zeitschrift für Naturforschung **16 a**, 842 (1961).

[20] E. W. Becker, K. Bier, and W. Henkes, Zeitschrift für Physik **146**, 333 (1956).

[21] J. T. Lau et al., Physical Review Letters **101**, 153401 (2008).

[22] J. Dahl and S. Liu, Science **299**, 96 (2003).

[23] C. Bostedt et al., Journal of Physics B: Atomic, Molecular and Optical Physics **43**, 194011 (2010).

[24] O. Hagena, Review of Scientific Instruments **63**, 2374 (1992).

[25] J. Farges, M. De Feraudy, B. Raoult, and G. Torchet, Surface Science **106**, 95 (1981).

[26] J. Cuvellier et al., Zeitschrift für Physik D Atoms, Molecules and Clusters **21**, 265 (1991).

[27] A. Bell, J. Mestdagh, and J. Berlande, Journal of Physics D: **26**, 994 (1993).

[28] A. Bush, A. Bell, J. Frey, and J. Mestdagh, The Journal of Physical Chemistry A **102**, 6457 (1998).

[29] A. J. Cox, A. DeWeerd, and J. Linden, American Journal of Physics **70**, 620 (2002).

[30] U. Buck and R. Krohne, The Journal of chemical physics **105**, 5408 (1996).

[31] G. Scoles, D. Brassi, U. Buck, and D. Lainé, editors, *Atomic and Molecular Beam Methods Volume I*, Oxford University Press, New York, 1988.

[32] U. Buck, The Journal of Physical Chemistry **92**, 1023 (1988).

[33] G. Gspann and H. Vollmer, Mass separation in cluster beams by crossed free jets (for cluster particle size determination), in *Rarefied gas dynamics; Proceedings of the Eighth International Symposium, Stanford*, pages 261–267, 1974.

[34] K. Bier and B. Schmidt, Zeitschrift für angewandte Physik **13**, 493 (1961).

[35] R. Becker and W. Döring, Annalen der Physik **416**, 719 (1935).

[36] M. Rao and B. Berne, The Journal of Chemical Physics **68** (1978).

[37] D. Lippmann, W. C. Schieve, and C. Canestaro, The Journal of Chemical Physics **81**, 4969 (1984).

[38] O. Hagena, Physics of Fluids **17**, 894 (1974).

[39] O. Hagena, Zeitschrift für Physik D Atoms, Molecules and Clusters **4**, 291 (1987).

[40] J. Stapelfeldt, *CLULU: ein neues Experiment für Fluoreszenzuntersuchungen an Edelgas-Clustern vom Dimer bis zum Mikrokristall*, PhD thesis, Universität Hamburg, 1990.

[41] O. Hagena and W. Obert, The Journal of Chemical Physics **56**, 1793 (1972).

[42] F. Dorchies et al., Physical Review A **68**, 023201 (2003).

[43] E. Snyder, S. Buzza, and A. Castleman, Physical Review Letters **77**, 3347 (1996).

[44] Y. L. Shao et al., Physical Review Letters **77**, 3343 (1996).

[45] T. Ditmire et al., Nature **398**, 489 (1999).

[46] U. Saalmann, C. Siedschlag, and J.-M. Rost, Journal of Physics B: Atomic, Molecular and Optical Physics **39**, R39 (2006).

[47] U. Saalmann, Journal of Physics B: Atomic, Molecular and Optical Physics **43**, 194012 (2010).

[48] M. Arbeiter and T. Fennel, eprint arXiv:1011.2069 (2010).

[49] I. Last and J. Jortner, Physical Review A **60**, 2215 (1999).

[50] T. Ditmire, T. Donnelly, A. Rubenchik, R. Falcone, and M. Perry, Physical Review A **53**, 3379 (1996).

[51] T. Ditmire et al., Physical Review A **57**, 369 (1998).

[52] C. Deiss et al., Physical Review Letters **96**, 1 (2006).

[53] L. V. Keldysh, Soviet Physics JETP **20**, 1307 (1965).

[54] T. Seideman, M. Ivanov, and P. Corkum, Physical Review Letters **75**, 2819 (1995).

[55] T. Zuo and A. D. Bandrauk, Physical Review A **52**, 2511 (1995).

[56] T. Martchenko, C. Siedschlag, S. Zamith, H. Muller, and M. Vrakking, Physical Review A **72**, 1 (2005).

[57] A. V. Gets and V. P. Krainov, Journal of Physics B: Atomic, Molecular and Optical Physics **39**, 1787 (2006).

[58] R. Santra and C. Greene, Physical Review Letters **91**, 1 (2003).

[59] Z. Walters, R. Santra, and C. Greene, Physical Review A **74**, 1 (2006).

[60] T. Laarmann et al., Physical Review Letters **95**, 3 (2005).

[61] Y. Shima, Physical Review A **12**, 2106 (1975).

[62] C. Siedschlag and J.-M. Rost, Physical Review Letters **93**, 2 (2004).

[63] D. Bauer, Applied Physics B: Lasers and Optics **78**, 801 (2004).

[64] D. Bauer, Journal of Physics B: Atomic, Molecular and Optical Physics **37**, 3085 (2004).

[65] C. Bostedt et al., Physical Review Letters **100**, 12 (2008).

[66] D. Rolles et al., Physical Review A **75**, 3 (2007).

[67] C. Bostedt et al., New Journal of Physics **12**, 083004 (2010).

[68] M. Hoener et al., Journal of Physics B: Atomic, Molecular and Optical Physics **41**, 181001 (2008).

[69] B. Ziaja, H. Wabnitz, E. Weckert, and T. Möller, New Journal of Physics **10**, 043003 (2008).

[70] C. F. Bohren and D. R. Huffman, *Absorption and Scattering of Light by Small Particles*,

Wiley-VCH, 1998.

[71] M. Born and E. Wolf, *Principles of Optics*, Pergamon Press, Oxford, 3^{rd} edition, 1965.

[72] B. Henke, E. Gullikson, and J. Davis, Atomic Data and Nuclear Data Tables **54**, 181 (1993).

[73] G. Mie, Annalen der Physik **330**, 377 (1908).

[74] J. Jackson, *Classical Electrodynamics*, John Wiley & Sons, New York, 2^{nd} edition, 1975.

[75] O. Forster, *Analysis 3 - Integralrechnungen im* $\mathbb{R}^n$ *mit Anwendungen*, Vieweg, Braunschweig, 3^{rd} edition, 1984.

[76] M. Born and E. Wolf, *Principles of Optics*, Pergamon Press, Oxford, 6^{th} edition, 1980.

[77] G. Airy, Transactions of the Cambridge Philosophical Society **5**, 283 (1835).

[78] D. Rupp, *Simulation und Auswertung von Streuexperimenten am Freie-Elektronen-Laser für weiche Röntgenstrahlung* , Diplomarbeit, Technische Universität Berlin, 2008.

[79] P. Emma et al., Nature Photonics **4**, 641 (2010).

[80] D. Attwood, *Soft X-rays and Extreme Ultraviolet Radiation*, Cambridge University Press, Cambridge, 2007.

[81] A. S. Schlachter and F. J. Wuilleumier, *New Directions in Research with Third-Generation Soft X-ray Synchrotron Radiation Sources*, Springer, 1994.

[82] J. Madey, Journal of Applied Physics **42**, 1906 (1971).

[83] D. Deacon et al., Physical Review Letters **38**, 892 (1977).

[84] M. Geitz, A. Kabel, G. Schmidt, and H. Weise, Proceedings of the 1999 Particle Accelerator Conference (Cat. No.99CH36366) , 2507 (1999).

[85] V. Ayvazyan et al., The European Physical Journal D - Atomic, Molecular and Optical Physics **20**, 149 (2002).

[86] V. Ayvazyan et al., Physical Review Letters **88**, 1 (2002).

[87] L. Strüder et al., Nuclear Instruments and Methods in Physics Research Section A **614**, 483 (2010).

[88] N. Meidinger et al., Nuclear Instruments and Methods in Physics Research Section A **512**, 341 (2003).

[89] N. Meidinger et al., Nuclear Instruments and Methods in Physics Research Section A **568**, 141 (2006).

[90] ESA XMMNewton Webpage, http://www.esa.int/esaSC/120385_index_0_m.html (12/29/2011).

[91] MPI eROSITA Webpage, http://www.mpe.mpg.de/erosita (12/29/2011).

[92] N. Meidinger et al., Systematic testing and results of x-ray CCDs developed for eROSITA and other applications, in *Proc. SPIE*, volume 6276, 2006.

[93] N. Meidinger et al., Nuclear Instruments and Methods in Physics Research Section A **565**, 251 (2006).

[94] W. Demtröder, *Experimentalphysik 3*, Springer-Verlag, Berlin, 2^{nd} edition, 2004.

[95] W. C. Wiley and I. H. McLaren, The Review of Scientific Instruments **26**, 1150 (1955).

[96] A. Sorokin et al., Physical Review Letters **99**, 1 (2007).

[97] SIS Simion Webpage, http://simion.com/ (03/01/2012).

[98] H. Thomas, *Wechselwirkung von Edelgas-Clustern mit intensiven Pulsen weicher Röntgenstrahlung vom Freie-Elektronen-Laser FLASH*, PhD thesis, Technische Universität Berlin, 2009.

[99] R. Moshammer, M. Unverzagt, and W. Schmitt, Nuclear Instruments and **108**, 425 (1996).

[100] A. Eppink and D. Parker, Review of Scientific Instruments **68**, 3477 (1997).

[101] R. Andritschke, G. Hartner, R. Hartmann, N. Meidinger, and L. Struder, 2008 IEEE Nuclear Science Symposium Conference Record , 2166 (2008).

[102] Qt reference version 4.7, http://qt-project.org/doc/qt-4.7/ (07/01/2012).

[103] Doxygen documentation, http://www.stack.nl/∼dimitri/doxygen/ (01/05/2012).

[104] S. Goloborodko and G. Grygiel, DESY Hamburg (1997).

[105] Qt reference version 4.7, Signal-Slot documentation, http://doc.qt.nokia.com/4.7-snapshot/signalsandslots.html (09/03/2012).

[106] Qt reference version 4.7, Threading example, http://doc.qt.nokia.com/4.7-snapshot/threads-mandelbrot.html (09/07/2012).

[107] HDF5 reference and documentation, http://www.hdfgroup.org/ (07/17/2012).

[108] D. Rupp et al., New Journal of Physics **14**, 055016 (2012).

[109] IDL, http://www.exelisvis.com/ProductsServices/IDL.aspx (03/01/2012).

[110] ImageJ webpage, http://rsbweb.nih.gov/ij/ (12/13/2011).

[111] Wavemetrics, IgorPro, http://www.wavemetrics.com/ (02/15/2014).

[112] A. Bondi, The Journal of Physical Chemistry **68**, 441 (1964).

[113] K. Luria, W. Christen, and U. Even, The journal of physical chemistry. A **115**, 7362 (2011).

[114] M. Smoluchowski, Z. phys. Chem **92**, 9 (1917).

[115] S. Chapman and T. G. Cowling, *The mathematical theory of non-uniform gases: an account of the kinetic theory of viscosity, thermal conduction, and diffusion in gases*, Cambridge Mathematical Library, Cambridge University Press, 3rd edition, 1991.

[116] L. Ming, N. Markovic, and M. Svanberg, The Journal of Physical Chemistry **101**, 4011 (1997).

[117] M. Kalweit and D. Drikakis, Physical Review B **74**, 1 (2006).

[118] R. Jansen, N. Gimelshein, S. Gimelshein, and I. Wysong, The Journal of chemical physics **134**, 104105 (2011).

[119] M. Matsumoto and T. Nishimura, ACM: Transactions on Modeling and Computer Simulation **8**, 3 (1998).

[120] MTWebPage, http://www.math.sci.hiroshima-u.ac.jp/∼m-mat/MT/emt.html (05/31/2012).

[121] F. Lindemann, Zeitschrift für Physik **11**, 60 (1910).

[122] G. Allen, R. Bayles, W. Gile, and W. Jesser, Thin Solid Films **144**, 297 (1986).

[123] A. Rytkönen, S. Valkealahti, and M. Manninen, The Journal of chemical physics **108**, 5826 (1998).

[124] A. Michels, Physica **28**, 101 (1962).

[125] M. Schmidt and H. Haberland, Comptes Rendus Physique **178**, 327 (2002).

[126] J. Gspann, Zeitschrift für Physik D Atoms, Molecules and Clusters **3**, 143 (1986).

[127] J. Frenkel, *Kinetic Theory of Liquids*, Oxford University Press, 1946.

[128] F. F. Abraham, Reports on Progress in Physics **45**, 1113 (1982).

[129] van de Waal B, Physical review letters **76**, 1083 (1996).

[130] K. Gaffney and H. Chapman, Science **316**, 1444 (2007).

[131] L. Foucar et al., Computer Physics Communications **183**, 2207 (2012).

[132] H. Thomas et al., Physical Review Letters **108**, 133401 (2012).

[133] A. C. Thompson and D. Vaughan, editors, *X-ray Data Booklet*, Lawrence Berkeley National Laboratory, University of California, second edition, 2001.

[134] Jose Crespo, private communications.

[135] H. Iwayama et al., Journal of Physics B: Atomic, Molecular and Optical Physics **42**, 134019 (2009).

[136] L. Young et al., Nature **466**, 56 (2010).

[137] H. Thomas et al., Journal of Physics B: Atomic, Molecular and Optical Physics **42**, 134018 (2009).

[138] AirLiquide, http://encyclopedia.airliquide.com/Encyclopedia.asp?GasID=71 (05/18/2012).

[139] A. Munshi, B. Gaster, T. Mattson, J. Fung, and D. Ginsburg, *OpenCL Programming Guide*, Addison-Wesley, 2012.

[140] The Khronos Group, http://www.khronos.org/ (03/27/2014).

[141] E. Gamma, R. Helm, R. Johnson, and J. Vlissides, *Entwurfsmuster*, Addison-Wesley,

2011.

[142] Mathworks, MatLab, http://www.mathworks.de/ (03/31/2014).

[143] Boost C++ libraries, http://www.boost.org/ (03/31/2014).

Danksagung

An dieser Stelle möchte ich mich bei allen bedanken, die wesentlich zum Gelingen dieser Arbeit beigetragen haben.

Zu allererst möchte ich mich bei Thomas Möller bedanken, der mir ermöglich hat diese Arbeit in seiner Arbeitsgruppe anzufertigen. Seine Betreuung sowie die unzähligen Diskussionen und Ratschläge haben ganz entschieden zum Gelingen dieser Arbeit beigetragen.

Dank gilt auch Christoph Bostedt, der meine Begeisterung für die Forschung an FELs geweckt hat und mir die ganze Zeit über ein leuchtendes Vorbild war. Mein herzliches Dankeschön gilt ihm auch für die Möglichkeit an dem LCLS Beamline Commissioning teilzunehmen.

Bei Tim Laarmann möchte ich mich nicht nur für eine hervorragende Messzeit am FLASH bedanken sondern auch dafür, dass er sich bereit erklärt hat Zweitgutachter dieser Arbeit zu sein.

Für endlose Diskussionen und die nötige Motivation danke ich meinen Mitstreitern Daniela Rupp, Tais Gorkhover und Leonie Flückiger. Außerdem sage ich Danke für umfangreiche Messzeitunterstützung an Sebastian Schorb, David Wolter, Maria Müller, Mario Sauppe, Yevheniy Ovcharenko, Bruno Langbehn und Maria Krikunova. Zu Dank verpflichtet bin ich auch der gesamten AG Möller deren entspannte und produktive Atomsphäre ganz entscheidend zum Gelingen dieser Arbeit beigetragen hat.

Der Betrieb der CAMP-Kammer wäre ohne die ASG-Gruppe nicht möglich gewesen. Besonderes zu Dank verpflichtet bin ich Daniel Rolles, Anton Barty, Lutz Foucar, Benjamin Erk, Benedikt Rudek, Artem Rudenko, Carlo Schmidt und Joachim Ullrich.

Für die pnCCDs möchte ich mich beim MPI-HLL sowie bei PNSensor bedanken. Besonders ohne deren Messzeitteam Robert Hartmann, Nils Kimmel, Peter Holl, Christian Reich, Georg Weidenspointner und Lothar Strüder wäre der reibungslose Betrieb nie möglich gewesen.

Mein besonderer Dank gilt auch der feinmechanischen Werkstatt des IOAP und hier insbesondere Jörn Six, ohne die viele Änderungen in letzter Sekunde nie durchgeführt worden wären.

Ein großer Dank geht auch an die Leute bei FLASH: Rolf Treusch, Sven Toleikis, Svea Kapitzki sowie die vielen helfenden Hände im Hintergund. Auch das Team der DESY Werkstatt hat nicht nur einmal den Tag gerettet. Nicht vergessen möchte ich auch alle SLAC Mitarbeiter, insbesondere John Bozek, Jean-Charles Castagna, Marc Messerschmidt und Michelle Swiggers. Danke für einen großartigen Support!

Für Korrekturen an dieser Arbeit bedanke ich mich herzlich bei Elena Klimpel und Tobias von Stülpnagel.

Schlussendlich bedanke ich mich bei meiner Familie, die mich immer während dieser Arbeit unterstützt hat. Ohne die endlose Geduld, Diskussionen, Unterstützungen und Liebe von Katharina Schössler wäre die Arbeit nicht denkbar. Vielen Dank!